Evolution of X-ray and Optical Properties of Galaxy Clusters

by

Abdulmonem Alshino

A thesis submitted to
The University of Birmingham
for the degree of
DOCTOR OF PHILOSOPHY

Astrophysics and Space Research Group
School of Physics and Astronomy
The University of Birmingham
August 2010

Abstract

This thesis is comprised of X-ray and optical studies of 27 X-ray selected galaxy clusters from the *XMM-LSS* survey. These systems are mostly groups and poor clusters, with temperatures 0.6-4.8 keV, spanning the redshift range 0.05 to 1.05, hence these are some of the highest redshift X-ray selected clusters to have been studied. In the X-ray study, the evolution in the X-ray surface brightness profiles of the hot intracluster plasma is studied. Comparing the profiles with a standard β-model it is found that 54% of the sample possess cuspy (cool) cores. Trends with both temperature and redshift in the outer slope (β) of the X-ray surface brightness and in the incidence of cuspy cores are investigated. Fits indicate that the incidence of cuspy cores does not decline at high redshifts, as has been reported in rich clusters. Rather such cores become more prominent with increasing redshift. It is also found that β has a positive correlation with temperature. In the optical study, *CFHTLS* optical photometry has been used to study the galaxy luminosity functions of 14 members of the sample. Individual luminosity functions (LFs) as well as redshift-stacked and temperature-stacked LFs in three filters, g', r' and z', down to $M = -14.5$ are derived. All LFs were fitted by Schechter functions which well-constrained the faint-end slope, α. Derived values of α ranged from -1.03 to as steep as -2.1. No evidence is found for upturns at faint magnitudes. Evolution in α was apparent in all bands: it becomes shallower with increasing redshift. It is found that at $z \sim 0.3$, α is steeper (-1.67) in the green (g') band than it is (-1.30) in the red (z') band. This colour trend disappears at low redshift, which is attributed to reddening of faint blue galaxies from $z \sim 0.3$ to $z \sim 0$. Also, the total optical luminosity is calculated and is found to correlate strongly with X-ray luminosity and temperature, which is consistent with expectations for self-similar clusters with constant mass-to-light ratio.

Dedication

This work is dedicated to the following very special people:

My tenderhearted grandmother,

my loving parents,

my treasured sisters,

my cherished nephew and nieces,

my soul-mate Mohammed Al-Tamimi

and to my childhood friend Suad Al-Housani.

Acknowledgements

There are a number of people without whom this thesis might not have been written, and to whom I am greatly indebted. Thanks to all members of my family whose steadfast support for me was greatly needed and deeply appreciated. I would like to thank my supervisor Prof. Trevor Ponman for his sage advice, precious help and patient encouragement aided the writing of this thesis in innumerable ways. Special thanks to Florian Pacaud for his friendly appreciated help. I would also thank Habib Khosroshahi for his support and invaluable guidance. I also thank Marguerite Pierre, Jon Willis and Monique Arnaud for the academic support and help.

Thanks are also due to the administration of the University of Bahrain who sponsored a significant part of this work. Finally, I am also very grateful to my beloved friends: Dr. Abdulaziz Al-Otaibi, Dr. Khalid Al-Motrafi, Naif Al-Shamsmari, Khalid Al-Ghamdi, Mohammed Al-Odaib, Tawfeeq Al-Anazi, and Saleh Al-Zufiri for their support and encouragement.

Statement of originality

This thesis is comprised of two introductory chapters (chapters 1 and 2), two main results chapters (chapters 3 and 4) and a conclusion chapter (chapter 5). Chapter 3 is a paper submitted to Monthly Notices of the Royal Society (MNRAS) in March 2010 and accepted in June 2010, with title: "*Evolution of the X-ray profiles of poor clusters from the XMM-LSS survey*". Chapter 4 is a paper that was published in MNRAS in January 2010, in Volume 401, Issue 2, Pages: 941-962, with title: "*Luminosity functions of XMM-LSS C1 galaxy clusters*". I am the first author of both papers. These two papers were kept in their original form with the exception that the references were combined with the rest of the thesis references at the end.

The data used in the first paper (chapter 3), namely, X-ray images, exposure and segmentation maps of the clusters were produced by the *XMM-LSS* pipeline lead by Dr. Marguerite Pierre and performed by Dr. Florian Pacaud. The core program used in the data analysis was originally written by Dr. Florian Pacaud and was significantly modified by myself. A Fortran code used in computing the PSF redistribution matrix was originally written by Dr. Monique Arnaud. The performance of the analysis and results production and the paper writing was carried on by myself with the important guidance and input from my supervisor Prof. Trevor Ponman.

The observations and compilation of the optical catalogues used in the second paper (chapter 4) were performed by and obtained with MegaPrime/MegaCam project team, which is a joint project of CFHT and CEA/DAPNIA, at the Canada-France-Hawaii Telescope (CFHT). The analysis of the data and the writing of the paper was done by myself with essential input from my supervisor Prof. Trevor Ponman and Dr Habib Khosroshahi.

Contents

Chapter 1

General Properties of Galaxy Clusters

1.1 Introduction to clusters

A galaxy is a dynamically bound system that consists of many stars, dust and dark matter. Most of the mass-energy in galaxies (about 95%) is *dark*. It is called dark because it does not emit any form of electromagnetic radiation. The existence of dark matter is inferred indirectly by its gravitational effect. A bright galaxy, like our own Milky Way, consists of a few times 10^{10} stars and has a diameter of ~ 20 thousand parsec (kpc).[1]

Galaxies do not usually occur as isolated mass aggregations in the universe, but normally form groups, covering a wide range from a few or few dozens of galaxies, to large clusters of up to several thousands. These clusters of galaxies are the most massive bound objects in the Universe. According to the hierarchical clustering scenario for the formation of cosmic structure, galaxy clusters originate from the gravity-driven collapse of rare high peaks of primordial perturbations in density (e.g., Peebles 1993, Coles & Lucchin 1995 and Peacock 1999). Clusters are then formed between 10 billion years ago and now.

Typically the term *group* is reserved for clusters with fewer than ∼50 members (galaxies of luminosities $L \gtrsim 10^{10} L_{\odot}$). The main characteristic of a cluster is that it is gravitationally bound and in this sense the term 'group' and 'cluster' are interchangeable: as the group is simply a cluster with relatively fewer members. In this thesis, we use the word *clusters* in its broader sense to refer to any galactic systems regardless of their size. However, in places where we use the word *groups*, we only mean clusters with intracluster medium (ICM) temperature less than 2 keV.

While galaxy clusters have total masses of 10^{14} to 10^{17} $M_{\odot}$, the total mass contained in

[1] $1\text{pc} = 3.09 \times 10^{16}\text{m}$.

less-massive groups is typically around 10^{13} $M_{\odot}$. Galaxy groups usually have diameters around 0.5-2 Mpc and the velocity dispersion is few hundred km s^{-1}. The mass-to-light ratio found in groups of galaxies is typically around 200 in solar units ($M_{\odot}/L_{\odot}$), indicating the presence of large amounts of non-luminous matter or dark matter which accounts for about 23% of the total content of the Universe. 4.6% of this content is in the form of ordinary baryonic matter mainly in the hot intracluster medium and in stars. The remaining 72% of the Universe, is composed of *dark energy*, which is thought to be responsible for the present-day acceleration of the universal expansion. For further details, see for example, Spergel et al. (2007), Jones et al. (2004), Sparke & Gallagher (2007) and Barnes & Murdin (2000). It is worth noting, though, that these ratios have large uncertainties, see e.g., Gonzalez et al. (2007).

One of the most important discoveries in cosmology was Hubble's (Hubble 1929) observation that galaxies are receding from us and that their recession velocities increase in direct proportion to their distances, i.e.

$$v_r \propto r. \tag{1.1}$$

It follows that

$$v_r = \mathrm{H}_0 r, \tag{1.2}$$

where H_0 is the Hubble constant, currently estimated as $\mathrm{H}_0 = 70.5$, (Hinshaw et al. 2009). This relation is called Hubble's law and it shows that the Universe as a whole is expanding. Because of this expansion of the Universe, an object that is farther away will have a larger recession velocity, and thus a larger *redshift*, denoted by the letter z and defined as the shift in the wavelength, λ, of the object's spectrum towards the red side of the spectrum,

$$z + 1 = \frac{\lambda_{\mathrm{observed}}}{\lambda_{\mathrm{emitted}}}. \tag{1.3}$$

Since the light from high-redshift galaxies was emitted when the Universe was younger, we can study galaxy evolution by observing the galaxy population at different redshifts. Statistically, high-redshift galaxies are the progenitors of present-day galaxies and any change in the properties of galaxies with redshift gives us knowledge on the formation and evolution of the galaxy population. Since, the recession velocity of a galaxy can be measured from its redshift, z, the distance to the galaxy simply follows from $r = \mathrm{c}z/\mathrm{H}_0$, assuming $v_r \ll c$. To parametrise

the uncertainty in H_0, it is usually expressed as

$$H_0 = 100h \,\mathrm{km\,s^{-1}Mpc^{-1}}, \tag{1.4}$$

and express all quantities that depend on its value in terms of the reduced Hubble constant, h.

The fact that most galaxies occur in small groups is indicated by galaxy redshift surveys of the nearby universe (Huchra & Geller 1982, Geller & Huchra 1983 and Tully 1987). The low number of luminous galaxies in groups makes deriving the dynamical properties of these groups hard and characterized by high errors. Observing groups with X-ray observatories has enhanced our knowledge of them because many groups host luminous extended X-ray sources. X-ray spectroscopy shows that the emission mechanism is a combination of bremsstrahlung and line emission from highly ionized elements.

Bremsstrahlung radiation is the radiation given off by electrons due to their acceleration caused by the electric field of ions . The word *Bremsstrahlung* is a German word meaning braking radiation, which refers to the way in which electrons are braked when they hit a positively charged target. The incident electrons are free, meaning they are not bound to an atom or ion, both before and after the braking. Consequently, this kind of radiation has a continuous spectrum (unlike line emission) and is sometimes referred to as free-free radiation. If the energy of the incident electrons is high enough, the emitted radiation is mostly X-rays.

Emission lines or bound-bound emissions on the other hand, appear in a spectrum if the source emits specific wavelengths of radiation. This emission occurs when an atom, element or molecule in an excited state returns to a configuration of lower energy. Since every atom, element and molecule has a unique set of energy levels, the emitted photon has a discrete wavelength, and an energy equal to the difference between the initial and final energy levels. Emission lines are usually seen as bright lines, or lines of increased intensity, on a continuous spectrum.

Spatial and spectral analysis of X-ray observations suggest that the potential wells of groups are filled by hot gas. Not all groups contain an X-ray emitting intragroup medium. Actually, some group surveys suggest that 75% of nearby groups host hot X-ray emitting intragroup gas (Ponman et al. 1996).

The properties of groups resemble those of richer clusters, but there are also differences. The velocity dispersions of groups are lower than for clusters, and are comparable to the velocity despersions of individual galaxies. Thus one expects galaxy-galaxy interactions in groups to be

more dominant than in clusters. Also, because of the lower temperature in groups, the X-ray emission is caused mostly by line emission, while in the case of clusters the emission is caused mainly by bremsstrahlung emission.

X-ray astronomy is now recognized as one of the standard branches of observational astrophysics. Studying the physics of the ICM is essential for a deep understanding of galaxy evolution and of large-scale structures. Galaxy evolution processes include collapse of primordial perturbations, accretion of gas and dark matter, outright mergers, shock waves due to inflows or outflows of gas enriched by supernovae, thermal and nonthermal processes associated with particle acceleration. The radiative output of all of these processes includes an X-ray emission component. So the detection of X-ray emission is key to understanding the energetics of the ICM. Also X-ray emission can provide the most sensitive probe of the gravitational potential in groups.

1.2 Morphology of galaxy groups

The morphology of the X-ray emission in galaxy groups provides important insights into the ICM. Usually, the more luminous the group is, the more it has a regular morphology. In this case, the X-ray emission is centred on the dominant optical galaxy, which is usually lies at the centre of the group. Such groups contain a higher portion of E and S0 galaxies than spirals. Hickson Compact Group (HCG) 62 (from Hickson's compilation, Hickson et al. 1982) is an example of this type of group, see Fig. 1.1.

Conversely, less X-ray luminous groups tend to have irregular X-ray emission morphologies, and show little or no symmetry. These groups lack a central galaxy and the X-ray emission is irregularly distributed around several galaxies. They consist of all types of galaxies including spirals. Less luminous groups also have lower intragroup gas temperatures. The clumpy nature of the gas in low-luminosity groups suggests that these systems are not virialised. In addition to a global group potential as a source of detected X-ray radiation, potentials of individual galaxies is thought to play important role in the X-ray emission in low-luminosity environments. Also, shock waves originated by galaxy encounters may raise the gas temperature enough to emit X-rays photons. HCG 90 is an example of irregular low X-ray emission galaxy group with strong galaxy-galaxy gravitational interactions, see Fig. 1.2 (Mulchaey 2000). The mass contained in

an irregular group is usually less than the mass of a regular group.

1.3 Dark matter halos

It is now well established that galaxies reside in extended halos of dark matter (DMHs), see for example, Bond et al. (1991) and Giocoli et al. (2010). According to this paradigm, these dark matter halos form through gravitational instability generated by primordial density perturbations. These perturbations grow linearly until they reach a critical density and then they turn around from the expansion of the Universe and collapse forming virialised DMHs. These DMHs continue to grow through accreting more more dark matter or by merging with other halos.

DMHs are the hosts of galaxies and therefore, properties of these halos affects directly many important properties of the galaxy populations such as the mass function, progenitor mass function, merger rate, clustering properties and even the internal properties of the galaxies. These effects show clearly the importance of understanding the structure and formation of DMHs in order to understand the formation and evolution of galaxies.

The simplest way to model the DMH is to assume the virialised halos resemble isothermal spheres and hence the density profile $\rho(r)$ can be modelled as:

$$\rho(r) \propto r^{-2}. \tag{1.5}$$

The isothermal model is an approximation. Significant deviations from this model may be caused by several effects, for example, collapse may never reach an equilibrium state, especially in the outer regions, non-radial motion may be important and mergers with other halos may seriously invalidate the spherical-collapse model.

Using N-body simulations of structure formation in a CDM Universe, Navarro, Frenk & White (1996) showed that the density profiles of the simulated DMHs are shallower than r^{-2} at small radii and steeper at larger radii. They found that the density profiles to be well described by what has become known as the NFW profile:

$$\frac{\rho_0}{\frac{r}{r_s}(1+\frac{r}{r_s})^2}, \tag{1.6}$$

where the scale radius, r_s, and the characteristic overdensity, ρ_0, are parameters which vary from halo to halo. The logarithmic slope of the NFW profile changes gradually from -1 near

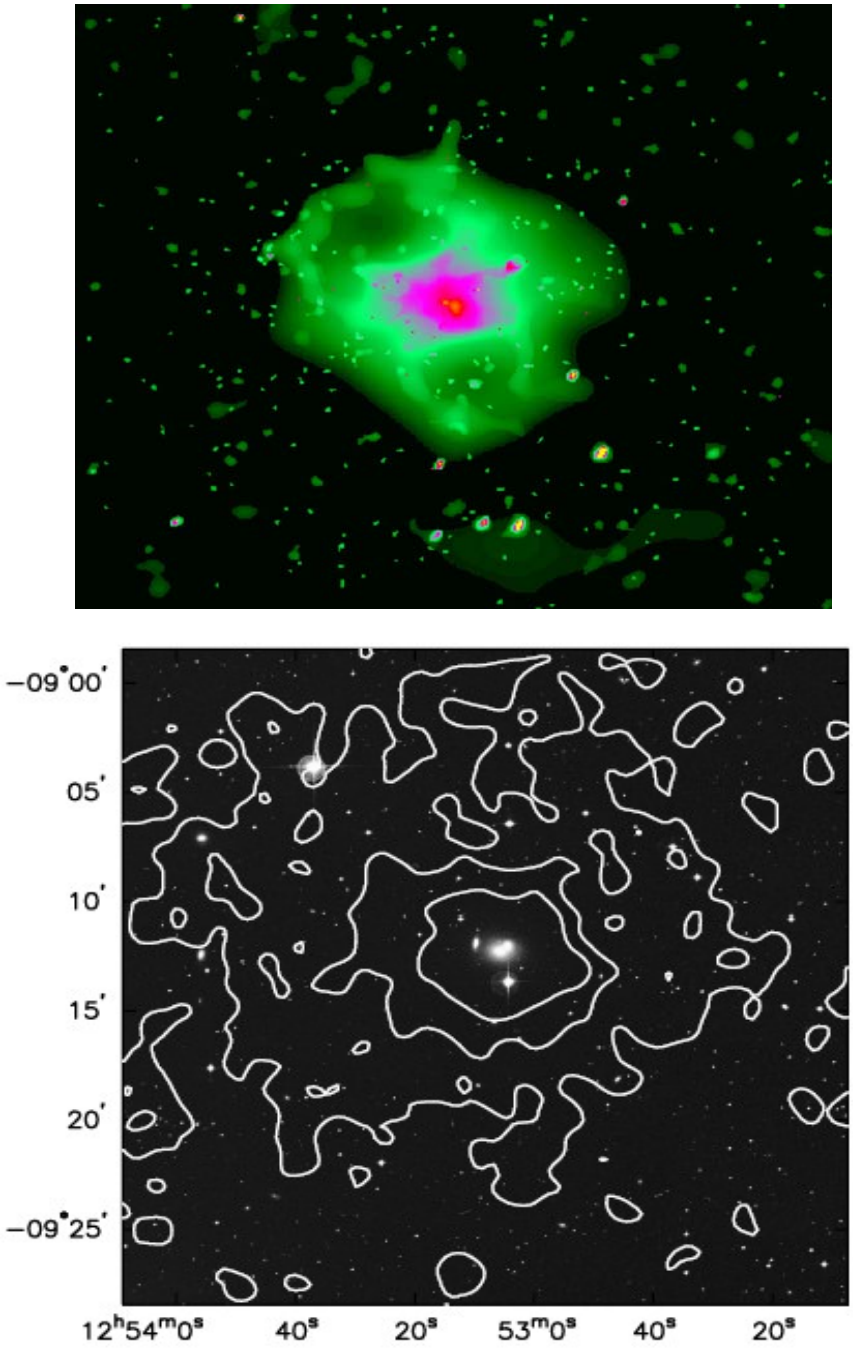

Figure 1.1: Chanda X-ray image of the regular group HCG 62, showing the symmetrical morphology (top panel, Vrtilek et al. 2002) and X-ray contours overlaid on the optical image of the same group (bottom panel, (Mulchaey 2000)).

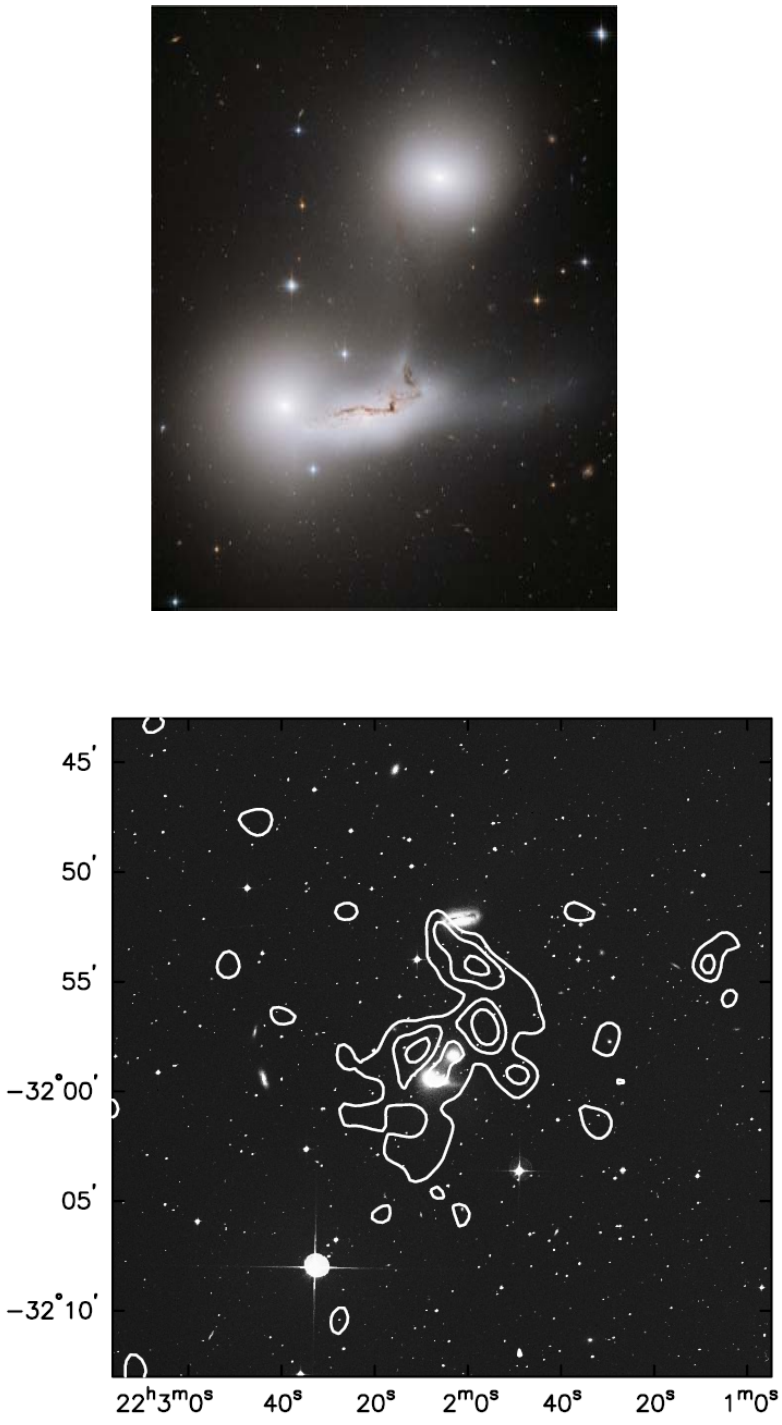

Figure 1.2: Recent optical image of the irregular Hickson Compact Group HCG 90 (top panel, (Sharples et al. 2009)) and X-ray contours overlaid on another optical image (of different scale) of the same group (bottom panel, (Mulchaey 2000)).

the centre to -3 at large radii and only resembles that of an isothermal sphere at radii $r \sim r_s$. In a later paper, Navarro, Frenk & White (1997), found that the NFW profile to be a good representation of the density profiles of DMHs of all masses and in CDM-like cosmologies. This showed the universality of the dissipationless hierarchical formation nature of the halos.

1.4 X-ray surface brightness

The spatial extent of the hot gas within clusters can be estimated by plotting the surface brightness profile from the centre to the radial distance at which the X-ray emission approaches the X-ray background level. For rich clusters the central X-ray brightness is several orders of magnitude higher than the background. On the other hand, this brightness for groups can be as low as only a few times higher than the brightness of the background and the spatial extent of the hot gas in groups is less than that of rich clusters.

The surface brightness profile is often modelled by a theoretical profile known as the β-model. In the past, it was assumed that galaxies and the ICM gas are both isothermal and in hydrostatic equilibrium (Cavaliere & Fusco-Femiano 1976, 1981, Bahcall & Sarazin 1977, 1978, Sarazin & Bahcall 1977, Gorenstein et al. 1978 and Jones & Forman 1984). This assumption is more reasonable in regular clusters than in irregular clusters. Although it is now known that the gas is rarely isothermal, the β-model is generally found to give a reasonable representation of X-ray surface brightness profiles (e.g., Neumann & Arnaud 1999 and Arnaud 2009). The β-model represents the X-ray surface brightness amplitude (I) at a projected distance r from the following equation:

$$I(r) = \frac{I_0}{[1 + (\frac{r}{r_{core}})^2]^{3\beta_{fit}-0.5}} \tag{1.7}$$

where $r_{\rm core}$ is the core radius of the hot gas and β_{fit} is a dimensionless power law index.

If the cluster is isothermal and hydrostatic, then the value of β_{fit} will be equal to the ratio of the specific energy in galaxies to the specific energy in the hot gas, β_{spec}:

$$\beta_{spec} = \mu m_p \sigma^2 / k T_{gas} \tag{1.8}$$

where μ is the mean molecular weight, m_p is the proton mass, σ is the velocity dispersion and T_{gas} is the temperature of the gas. For clusters in equilibrium, the virial theorem shows that σ^2 is proportional to M/r_{vir} of the cluster.

It has been shown (Sanderson & Ponman 2003) that there is no trend in mass-to-light ratio with X-ray temperature. Cluster mass-to-light ratios show a wide scatter about a median value and some of this scatter represents fluctuations around virial equilibrium.

The assumption, in the past, that all clusters can be modelled as isothermal and hydrostatic systems lead to what was referred to as the β-discrepancy. If the assumption that clusters are isothermal and hydrostatic, then the same value is expected for β, regardless of the method used to estimate it. But the method of the surface brightness profile fit typically gives a lower value for β than the value given by the ratio of the specific energy of the galaxies β_{spec}. This β-discrepancy issue has been studied initially on rich clusters (see, for example, Mushotzky 1984, Sarazin 1986, Edge & Stewart 1991 and Bahcall & Lubin 1994) and then applied on groups (e.g., Helsdon & Ponman 2000a).

Now, it is known that these two values of β should differ, unless the cluster is really isothermal and hydrostatic. The typical values of β_{spec} and β_{fit} (which is derived from the surface brightness profile fit) are around 1 and 0.6 respectively. It has been shown (Helsdon & Ponman 2000a) that the surface brightness profiles of groups are significantly flatter than those of galaxy clusters, that is β_{fit} is lower in groups than in clusters. The steepness of the surface brightness profiles of groups, as measured by the parameter β_{fit}, appears to show a trend with mass when combined with cluster data.

In spectral studies of galaxy clusters, it is important to take into account the instrument response. These studies are usually started by choosing a suitable model spectrum with a few adjustable parameters and then the next step is finding the best fit to the observed data. The assumption used in spectral models is that the X-rays are generated by thermal emission from diffuse low-density isothermal gas. The most important parameters in these models are the temperature and the metal abundance in the isothermal plasma.

A widely adopted model in this area is the MEKAL model (Mewe, Gronenschild & van den Oord 1985, Kaastra & Mewe 1993 and Liedahl, Osterheld & Goldstein 1995). As the temperature of the plasma rises, the X-ray emission becomes more dominated by the free-free continuum from hydrogen and helium. But in lower temperature systems as in groups much of the flux is in line emission and bound-free continuum. See Fig. 1.3 as an example of MEKAL spectral fitted data.

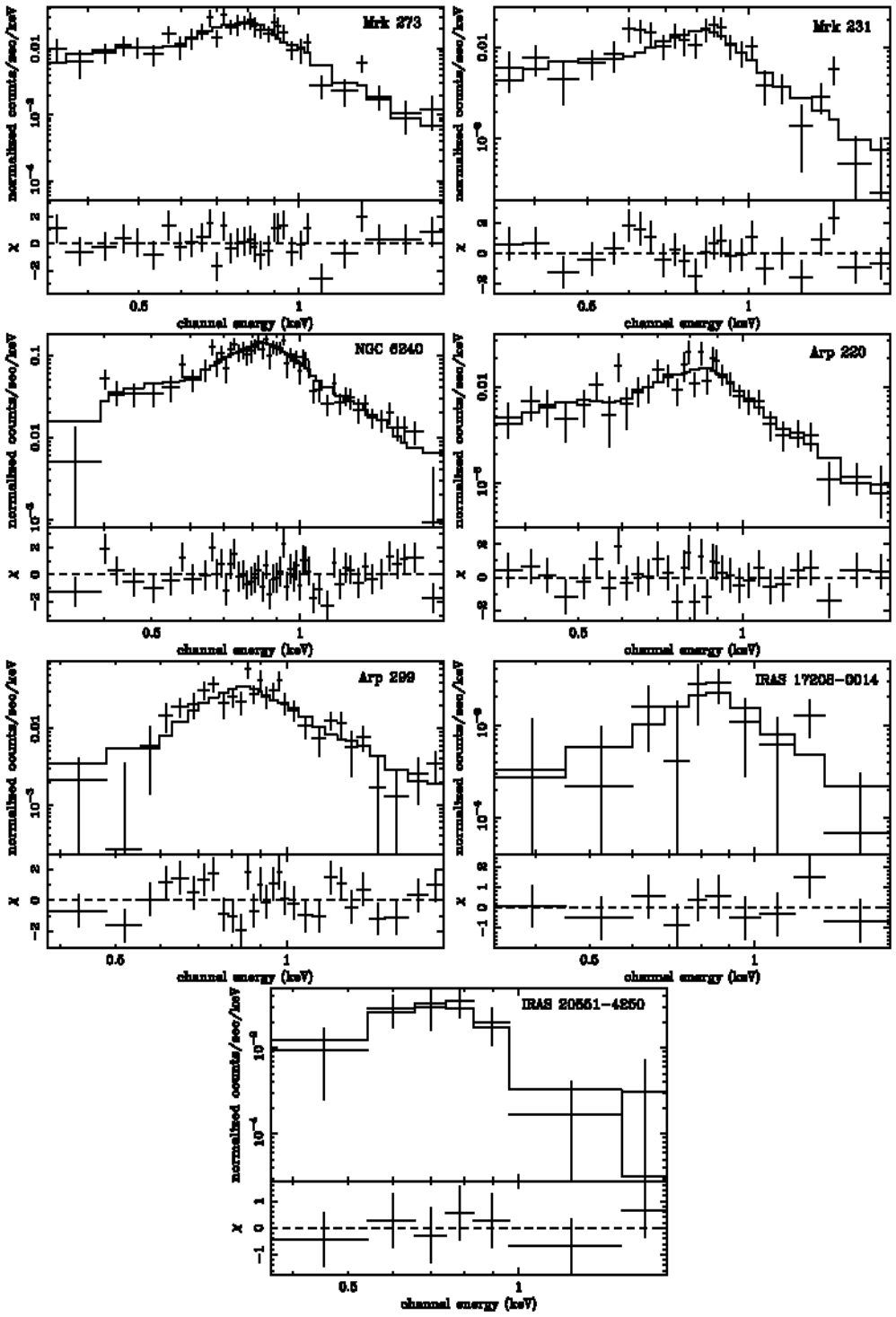

Figure 1.3: A MEKAL model provides a satisfactory fit for the 0.3-2.0 keV spectra of the outer halos of seven ultraluminous infrared galaxies (Huo et al. 2004)

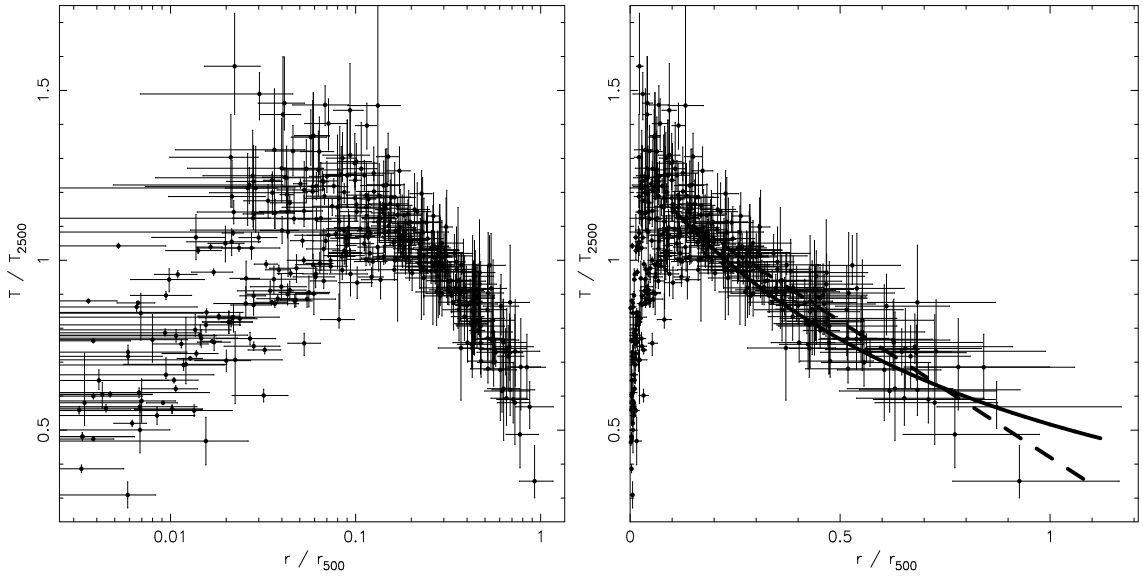

Figure 1.4: Temperature profiles in the logarithmic and linear scales of R_{500} of nearby galaxy groups (Sun et al. 2009)

For groups, the gas temperature ranges from around 0.3 keV to 2.0 keV, which is roughly what is expected given the range of observed velocity dispersions for groups (e.g., Helsdon & Ponman 2000b). Profile of these groups does not show a perfect isothermal system; at the centre of the groups the temperature is a minimum and then it rises to its maximum at intermediate radii of around $0.1 \times R_{500}$ (which is ~ 60 kpc in most cases) and then it drops gradually, whereas the maximum of the X-ray brightness is at the centres of these groups. For some groups, radial profiles indicate the existence of cool cores within these groups. Generally, the assumption of isothermal plasma is fairly good except for the small central cool parts (Vikhlinin et al. 2005 and Sun et al. 2009), see Figure 1.4.

1.5 Scaling relations of galaxy clusters and groups

There has been considerable interest in how the properties of groups differ from those of rich clusters. Clusters are more luminous than groups and hence clusters have been intensively studied and group properties are poorly determined relative to rich clusters. This limits the comparison between groups and clusters. The properties of the hot gas also tend to be more uncertain in poorer systems than in clusters because of the lower X-ray fluxes of groups. It is also noted that the X-ray properties of groups and clusters are often derived over very different

gas density ranges, which further complicates the comparisons between them. Despite these discrepancies, comparisons between groups and clusters and even sometimes between compact and loose groups have provided considerable insights into the nature of groups.

To compare different systems, one should look for differences in properties of the ICM gas and in particular in the correlations involving X-ray luminosity L_X and temperature T. This correlation reflects the relationship between the gas, the potential well and the galaxies it contains. Other important relationships include luminosity and velocity dispersion (σ) correlation, and temperature and velocity dispersion correlation.

L_X correlates strongly with σ, as L_X is $\propto \sigma^{\sim 4}$ (Plionis & Tovmassian 2004, Ortiz-Gil et al. 2004 and Brough et al. 2006). It was shown (Helsdon & Ponman 2000b) that the L_X-σ correlation for groups was basically consistent between loose and compact groups, although it was also noted (Mahdavi et al. 2000) that the relationship may become somewhat flatter for low velocity dispersion systems.

Galaxy cluster formation is often modelled by the spherical collapse picture of mass halos (Gunn & Gott 1972) and simulations of cluster formation indicate that L_X correlates with T as $L_X \propto T^2$ if non-gravitational effects are ignored and the energy emission is dominated by thermal bremsstrahlung (reviewed in Voit 2005a). But, it has been clear for many years that the $L_X - T$ relation for clusters does not follow the $L_X \propto T^2$ expected for systems radiating bremsstrahlung X-rays. Many studies (see, for example, Arnaud & Evrard 1999) have found logarithmic slopes close to 3 in cluster systems. The $L_X - T$ relation appears to be very steep in groups, a study (Helsdon & Ponman 2000b) obtained a slope of 4.5 $\pm$0.6 for a sample of X-ray bright loose groups and 4.3 $\pm$0.5 for a larger sample including both loose and compact groups. This steepening is found in low temperature systems (below 1 keV, see Ponman et al. 1996) and suggests that the deviation of cool groups from the cluster relationship is indeed significant.

Another study (Osmond & Ponman 2004) which is a part of the Group Evolution Multiwavelength Study (GEMS), involved a sample of 45 galaxy groups and gave slope values close to the slope seen in clusters. Their slope value was 2.75 $\pm$ 0.46 which flattened still further to 2.5 $\pm$ 0.42 with L_X values extrapolated to R_{500}. However, in this case, the authors did not use orthogonal regression and a more careful analysis gives a slope of 3.5-4.0 (Ponman, private communication). A recent study (Jeltema et al. 2009) found results consistent with the GEMS

study for both low- and high-redshift groups. See, Fig. 1.5.

The idea of having the same relations of physical properties, including the $L_X - T$ relation for both groups and clusters, is based on the self-similar model. This assumes that the same physics operates on different spatial scales, so that larger systems (clusters) should show scaled-up properties (temperature, luminosity and velocity dispersion) compared to smaller systems (groups) and that the way these quantities change with each other should stay the same. Because this is not what is observed, other physical processes are thought to cause the steeper $L_X - T$ relations in low-mass systems. Non-gravitational processes, such as supernova energy injection, active galactic nuclei and radiative cooling are believed to be the main causes for the observed non-similarity (Ortiz-Gil et al. 2004). The effect of extra heating is not to increase the gas temperature, rather it is to expand the gas and therefore to reduce its density, which decreases the X-ray luminosity (Wu, Fabian & Nulsen 2000). The extra energy should have greater impact on groups because their total masses are smaller than richer clusters and therefore, the extra energy per particle obtained has a relatively larger impact. This makes studying groups, rather than rich clusters, more interesting in terms of the wealth of information these poor systems provides for the understanding of the effects of non-gravitational processes for the galaxy evolution.

Both the temperature of the ICM medium and the velocity dispersion of galaxies provide a measure of the gravitational potential. Therefore, correlation between these two quantities is expected to be similar for both clusters and groups. Groups appear to have similar T-σ relation ($T \propto \sigma^2$) and similar β_{spec} value (~ 1) as for clusters (Helsdon & Ponman 2000b). Fig. 1.6 shows this similarity of T-σ relation for clusters and groups but the group data have larger scatter compared to clusters.

1.6 Evolution of galaxy clusters

In addition to studying anisotropies in the cosmic microwave background radiation, galaxy cluster surveys provide an important means to constrain cosmological parameters. What cosmological models predict is the number density of clusters of a given mass as a function of time. Thus to accurately determine the evolution of space density of clusters, cluster surveys have to have a well-defined selection function over a wide range of redshift in order to see how the mass

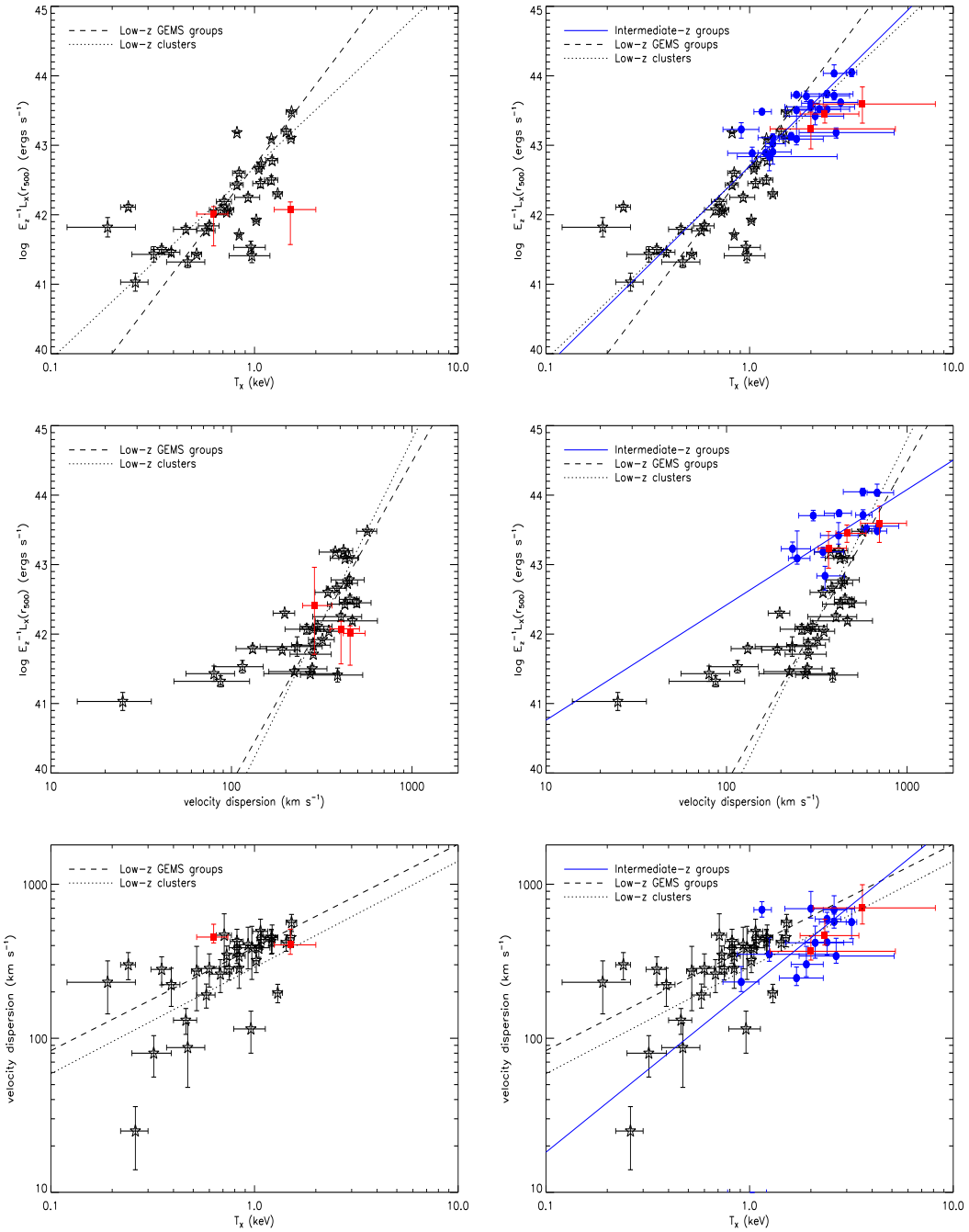

Figure 1.5: From top to bottom: $L_X - T$, $L_X - \sigma$ and $\sigma - T$ scaling relations. Left panels: For low-redshift groups (red squares) compared to X-ray luminous, low-redshift groups from the Group Evolution Multiwavelength Study (GEMS) sample (open stars). Fits show the best-fitting relations for the GEMS groups (dashed line) and low-redshift clusters (dotted line). Right panels: For high-redshift groups (z > 0.7; red squares) compared to X-ray luminous intermediate-redshift groups (0.2 < z < 0.6) from the RDCS and XMM-LSS samples (blue circles) and low-redshift groups from the GEMS sample (open stars). Fits show the best-fitting relations for the intermediate-redshift groups (blue solid line), the low-redshift GEMS groups (dashed line) and low-redshift clusters (dotted line). Source: Jeltema et al. (2009).

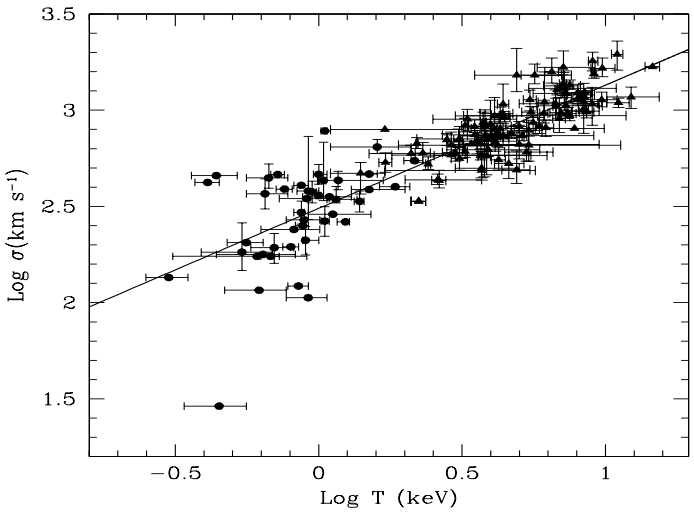

Figure 1.6: Velocity dispersion σ for a sample of groups (circles) and clusters (triangles) versus temperature, T. The solid line represents the best-fit for the cluster sample. The groups are consistent with the cluster relationship, though with a larger scatter (Mulchaey 2000).

function evolves with time. The mass of galaxy clusters cannot be measured directly, instead, it is inferred indirectly from their observable properties. That is why N-body simulations are important, since they show how the cosmological parameters are linked and affected by the mass function.

Cluster mass, M, can be estimated by X-ray measurements of the ICM, such as luminosity L_X and T, using the relationships between these X-ray observables and the total mass. While this is attainable for low and intermediate redshifts, through accurate measurements of the gas density and temperature profiles, high-redshift clusters suffer from low quality data due to their lower signal-to-noise ratios.

For perfectly self-similar clusters with ICM processes driven solely by gravity, Kaiser (1986) derived these scaling relations:

$$T_X \propto M^{2/3}(1+z), \tag{1.9}$$

$$L_X \propto M^{4/3}(1+z)^{7/2} \tag{1.10}$$

and

$$L_X \propto T^2(1+z)^{3/2}. \tag{1.11}$$

These relations can be used to test the breaking of self-similarity caused by non-gravitational

heating and cooling processes. For example, Muanwong, Kay & Thomas (2006) investigated the redshift dependence of X-ray cluster scaling relations using three different models: a radiative model that incorporates radiative cooling of the gas only, a preheating model that additionally heats the gas uniformly at high redshift, and a feedback model which self-consistently heats the gas in proportion to local star formation rate. While all three models were capable of reproducing the observed $L_X - T$ relation at $z = 0$, they predicted substantially different results at high redshift ($z = 1.5$), with the radiative, preheating, and feedback models predicting strongly positive, mildly positive, and mildly negative evolution, respectively. Here, positive (negative) evolution means that the normalisation of the scaling relation at high redshift is higher (lower) than what is predicted from the self-similarity model. The authors attributed these differences to the structure of the intracluster medium. This study highlights the importance of measuring cluster scaling relations to sufficiently high quality over wide redshift ranges.

In his review, Voit (2005a) emphasised that self-similar evolution cannot continue to arbitrary high redshift, given the increasing effects of radiative cooling and feedback from galaxy formation on these relations. Some observational studies presented evidence supporting this. For example, Branchesi et al. (2007) studied 39 clusters with redshift range $0.25 < z < 1.3$ and found that the evolution of the $L_X - T$ relation is consistent with the self-similar prediction for clusters with $z < 0.3$, but negative at higher redshift. Also, Ettori et al. (2004b) found negative evolution in their 28 galaxy clusters which had a redshift range of $0.4 < z < 1.3$. However, positive evolution has also been reported at high redshift. Morandi, Ettori & Moscardini (2007) analysed a sample of 24 clusters ($0.14 < z < 0.82$) and found positive evolution of the $L_X - T$ relation and slightly negative evolution of the $M - T$ and $L_X - M$ relations.

1.7 Cool core and non-cool core clusters

Another interesting property of clusters is whether they have cool cores or not. This bimodality in the properties of the cluster cores and its evolution have been the subject of many in-depth studies, lately. Cool core (CC) clusters have very dense gaseous core regions compared to non-cool core (NCC) clusters. CC clusters have central cooling times significantly lower than the Hubble time. Formerly, it was believed that the ICM in the cores of CC clusters cools and condenses, given the absence of heating mechanisms to compensate the radiated energy, and

therefore these clusters were termed cooling flow clusters. With the advent of the *XMM-Newton* and *Chanda* satellites, the spectral features predicted by the cooling flow picture are not detected in the X-ray spectra in the cores of CC clusters (e.g. Peterson et al. 2001 and Peterson et al. 2003). For reviews of cool cores in clusters, see for example, Fabian 1994, Donahue & Voit 2004 and Peterson & Fabian 2006.

It is now widely accepted that active galactic nuclei (AGN) play a crucial role in suppressing the cooling of the gas by feedback processes. An active galactic nucleus is a compact region at the centre of a galaxy that has a much higher than normal luminosity over at least some portion, and possibly all, of the electromagnetic spectrum. It is so bright that the central region can be more luminous than the remaining galaxy light. Much of the energy output of AGNs is of a non-thermal type of emission, with many AGN being strong emitters of X-rays, radio and ultraviolet radiation, as well as optical radiation.

Although, it is unclear how this energy is distributed in the observed homogeneous way, observations (see e.g., Sanderson, Ponman & O'Sullivan 2006) show that AGN tend to be found in CC clusters. Since AGN feedback may also be linked to self-similarity breaking (Johnson et al. 2009), it is interesting to know how CCs evolve with cosmic time and how the incidence of CC and NCC clusters influence the scaling relations of global properties.

At $z \sim 0$, at least half of the detected clusters harbour CCs (Edge, Stewart & Fabian 1992, White et al. 1997, Chen et al. 2007 and Vikhlinin et al. 2007). At intermediate redshifts ($z \approx 0.15 - 0.4$), Bauer et al. (2005) found that CC appeared still to be common, with an incidence nearly identical to that in luminous low-redshift clusters. At high redshifts, observations suggest that CC clusters are less numerous and/or prominent (Ettori et al. 2004b, Vikhlinin et al. 2007 and Santos et al. 2008). Chen et al. (2007) showed that for the scaling relations, $L_X - T$ and $L_X - M$, CC clusters have a significantly higher normalisation and indicated that this effect is due to an enhanced X-ray luminosity for CC clusters. This can be explained by at least some of the NCC clusters being in dynamically young states compared with CC clusters, and they may turn into cooling core clusters in a later evolutionary stage. For a review of recent studies of CC and non-CC in rich clusters and groups, see section 3.1.

1.8 Galaxies and clusters in the optical band

1.8.1 Morphology-density relation of galaxies

Galaxies within clusters themselves are also subject to evolution. There is a well-known relationship between galaxy morphology and environment (see, e.g., Zwicky 1942 and Sandage 1961). Early-type (elliptical and S0) galaxies tend to be found in high density environments, such as rich clusters, while late-type galaxies (spiral and irregular galaxies) are preferentially located in low density environments, for example, poor groups and fields. Hence, spiral galaxies are rare in the high densities of clusters and are common in fields. Early-type galaxies, on the other hand, are common in clusters and are rarely seen in isolation (Vogt et al. 2004). This morphology-density relation is universal and believed to indicate that galaxy evolution is affected by its environment (Boselli & Gavazzi 2006). Specifically, observations show that star formation is suppressed when galaxies enter high density environments, such as clusters (see, for example, Quilis et al. 2000, Bekki et al. 2002 and Chung et al. 2007). The suppression of star formation results from partial or entire removal of the interstellar gas in galaxies which fuels star formation.

1.8.2 Butcher-Oemler effect

Observational studies show that cluster galaxies at different redshifts have different colours. Butcher & Oemler (1978) were the first to discover that clusters at $z \sim 0.5$ have a larger fraction of blue galaxies compared with similar clusters found in the local universe. This was considered as direct evidence of galaxy evolution in dense environments. The so-called Butcher-Oemler effect was later confirmed by photometric studies (Rakos & Schombert 1995 and Goto et al. 2003) and spectroscopic studies (Dressler & Gunn 1992 and Ellingson et al. 2001). This trend of increasing blue galaxy fraction with increased look back time is an important clue to how galaxies form and evolve. The Butcher-Oemler effect has been interpreted as evidence for a rapid change in galaxies driven by transformation mechanisms such as ram pressure stripping (Gunn & Gott 1972), effects of infalling galaxies from the field regions (Kauffmann 1995 and Ellingson et al. 2001) and galaxy-galaxy interactions within cluster environments (Moore et al. 1996).

1.8.3 Colours of galaxies

The colour of a galaxy reflects the ratio of its luminosity in two passbands. A galaxy is considered red if its luminosity in the redder passband is relatively high to that compared to that in the blue passband. Ellipticals and dwarf galaxies generally have redder colours than spirals and dwarf irregulars. The colour of a galaxy is related to its age and metallicity of its stellar population. Generally, redder galaxies are either older or more metal rich, or both. Ergo, the colour of a galaxy holds important information regarding it stellar population. Also, the galaxy colours carries important information about its star-formation history, since more massive stars (which emit a larger fraction of their total light at short wavelengths than low-mass stars) are in general shorter-lived.

Generally, galaxies come into two different classes. The first is the early-type galaxies. These have relatively old stellar population and are therefore red. The second class is the late-type galaxies which have ongoing star-formation in their disks and are therefore blue. However, there are some exceptions to this colour-morphology relation: a disk galaxy may be red due to extensive dust extinction. Also, an elliptical galaxy may be blue if it has a small amount of recent star formation.

The bimodality of the galaxy population in cluster can be shown in the colour-magnitude diagram (CMD), see Fig. 1.7. This CMD shows that the galaxies are divided into a red sequence and a blue sequence. At the bright end the red sequence (mainly early-type galaxies) dominates and at the faint end the majority of the galaxies are blue (mainly late-type galaxies). It is also worth noting that within each sequence, brighter galaxies appear to be redder, which most likely reflects the fact that the stellar populations in brighter galaxies are both older and more metal rich.

Blanton (2006) compared colours of galaxies in redshift $z \sim 0.1$, from Sloan Digital Sky Survey (SDSS) to another sample at redshift $z \sim 1$ taken from the Deep Extragalactic Evolutionary Probe 2 (DEEP2) to study the evolution of the galaxy colours. He found that galaxies are bluer at $z \sim 1$: the blue sequence by about 0.3 mag and the red sequence by about 0.1 mag, see Fig. 1.8. To evaluate the change in colour, he used simplistic stellar population synthesis models which indicated that the luminous end of the red sequence fades less than passive evolution allows by about 0.2 mag. Given that the stellar population models and flux estimates are correct,

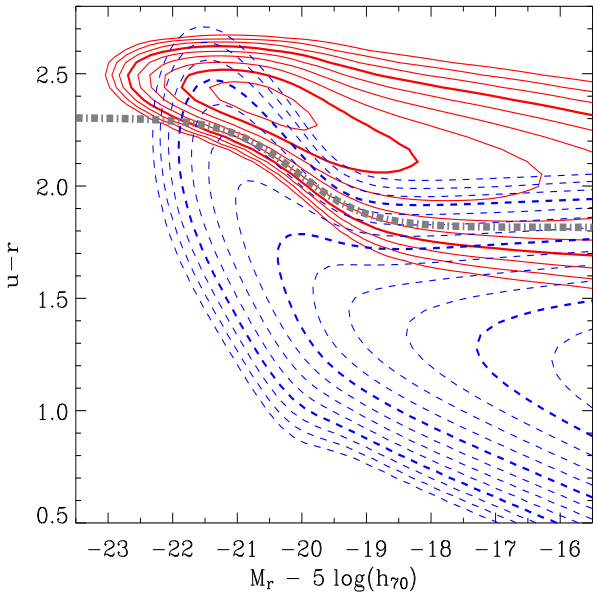

Figure 1.7: The colour magnitude diagram (CMD) of galaxies, showing the red (solid contours) and the blue (dashed contours) cloud. The thick dash-dotted line represents an optimal divider. Source: Blanton (2006).

dry mergers between red galaxies then must create the luminous red population at $z \sim 0.1$. He also concluded that if mergers are catastrophic events, they must be rare for blue galaxies.

1.8.4 Galaxy luminosity function

In the optical part of the spectrum, the luminosity function (LF) of galaxies is often used to study how different types of galaxies are distributed in cluster environments. The LF measures the number of galaxies in a given volume having a certain luminosity range. Galaxies come in a large range of luminosity: from $M_B \sim -7.5$, for example, the faint dwarf elliptical galaxies Drago and Ursa Minor in the local group, to $M_B \sim -22$, for example, the giant elliptical galaxy M87 in the Virgo galaxy cluster.

For a galaxy of redshift, z and apparent magnitude, m, its absolute magnitude is given by

$$M = m - 5\log\left[\frac{\mathrm{d_L(z)}}{10\mathrm{pc}}\right] - \mathrm{K(z)}, \tag{1.12}$$

where $d_L(z)$ is the luminosity distance (in parsecs) which is a function of redshift z. The $K(z)$ is the magnitude *K correction* and is required to correct the observed flux into a fixed rest-frame band, so that the absolute magnitudes are the same for identical galaxies at different redshifts.

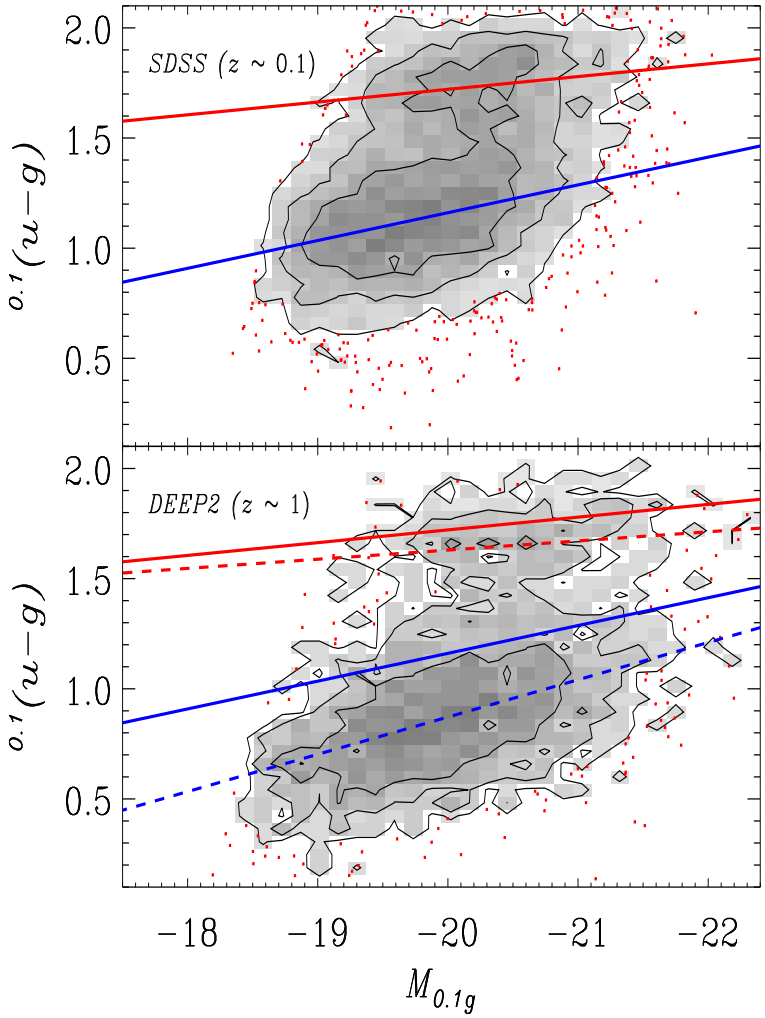

Figure 1.8: SDSS-predicted (top) and observed (bottom) distribution of colour and absolute magnitude. The prediction assumes no change in the galaxy population between redshifts $z = 0.1$ and $z = 1$. The upper solid line in each panel indicates the locus of the red sequence in the SDSS prediction. The lower solid line indicates the locus of the blue sequence in the SDSS prediction. The dashed lines in the bottom panel indicate the corresponding loci in the DEEP2 data. The red sequence is far less well populated relative to the blue sequence at redshift $z = 0.1$ than it is at redshift $z = 0.1$. In addition, the red and blue sequences are both bluer at high redshifts than at low redshifts, Blanton (2006).

The luminositys of a galaxy is related to the absolute magnitude by

$$2.5\log(\mathrm{L}/\mathrm{L}_{\odot}) = \mathrm{M}_{\odot} - \mathrm{M}. \tag{1.13}$$

The LF is an important tool for the study of galaxy formation and evolution. By tracing how LFs of clusters change with time, valuable information can be inferred about the evolution of physical processes that convert mass into light, e.g. star formation and about the mechanisms that change the morphology of the galaxies. Also, comparison of LFs at different cosmological times probes the evolution of the mean galaxy population and constrain the formation times of galaxy clusters (see for example, De Propris et al. 1999 and Strazzullo et al. 2006).

The most popular parameterisation to fit LFs is the Schechter function (Schechter 1976) which is a function of luminosity, L (or equivalently, absolute magnitude, M):

$$\phi(L)dL = \phi^*(L/L^*)^{\alpha}e^{(-L/L^*)}d(L/L^*) \tag{1.14}$$

or equivalently,

$$\phi(M)dM = 0.4ln(10)\phi^*e^{-X}X^{1+\alpha}dM, \tag{1.15}$$

where $X = 10^{-0.4(M-M^*)}$, ϕ^* is the characteristic number density and M^* (L^*) is the characteristic magnitude (characteristic luminosity) whcih is also reffered to as the *knee*, and follows a power law at fainter luminosities. The faint-end slope is given by $-(1+\alpha)$, decreasing for $\alpha > -1$, increasing for $\alpha < -1$ and flat for $\alpha = -1$.

The parameter, M^*, in the Schechter function is sensitive to the evolution of massive galaxies ($M > M^*$) and it is known now that these galaxies form their stars and assemble their masses at high redshift (e.g., Muzzin et al. 2008) which is consistent with the picture of *downsizing* (stars in more massive galaxies tend to have formed earlier and over a shorter time spans, e.g., Perez-Gonzalez et al. 2008). On the other hand, the α parameter in the Schechter function is sensitive to the population of dwarf galaxies in galaxy clusters.

Unlike the bright end of LF, the evolution of the faint end is hard to study, mainly because the number of faint galaxies detected decreases sharply with increasing redshift. It is expected that the faint-end slope of LFs reflects the steep value ($\alpha \sim 2$) which emerges from the cold dark matter (CDM) halo model at recombination time, and that the slope eventually flattens as dwarf galaxies are destroyed in dense environments and finally merge to form larger galaxies (Khochfar et al. 2007). In this theoretical study, the authors show a measurable dependence of

the faint-end slope of the galaxy luminosity function on redshift. But, most of this dependence is seen over a relatively large redshift range, $\Delta z \geq 2$ which makes it difficult to confirm by observation.

From the Schechter function, one can express the galaxy mean number density, n_g, and the galaxy mean luminosity density, L_{tot} in the Universe as:

$$n_g \equiv \int_0^\infty \phi(L) dL = \phi^* \Gamma(\alpha + 1), \tag{1.16}$$

and

$$L_{tot} \equiv \int_0^\infty \phi(L) L dL = \phi^* L^* \Gamma(\alpha + 2), \tag{1.17}$$

where $\Gamma(x)$ is the gamma function.

Since the morphologies of the galaxies are strongly correlated with their colours, luminosity functions should also depend on the galaxy morphology. Fig. 1.9 shows schematically how the luminosity function decomposes into the contributions from galaxies of different types. The bright-end of the LF is dominated by ellipticals, while the spiral galaxies dominate the intermediate luminosity range. At the faint end, LF is more dominated by irregulars and dwarf ellipticals. The LFs of spirals, S0s and ellipticals are peaked around some characteristics luminosities and follow roughly a Gaussian form rather than a Schechter function. Both irregulars and dwarf ellipticals have Schechter-type LFs. The faint-end slope is steeper for dwarf ellipticals than for irregulars. The dwarf ellipticals may be responsible for the faint-end upturns of the LFs of red galaxies. For a thorough updated discussion of the origin and evolution of the faint end of galaxy LFs, see in this thesis sections 4.4.1 to 4.4.5.

Some studies (e.g., Krick et al. 2008) found a deficit of faint galaxies on the red sequence in clusters at $z \sim 1$, implying that more massive galaxies have evolved in clusters faster than less massive galaxies, and that the less massive galaxies are still forming stars in clusters such that they have not yet settled onto the red sequence. Other studies (Crawford, Bershady & Hoessel 2009) found little evidence for evolution of the faint-end slope in their cluster sample with redshift range $0.5 < z < 0.9$. But even if the red sequence is truncated, this does not necessarily mean that the faint-end slope becomes less steep at high redshifts since the dwarf galaxies on the red sequence may be in the blue cloud until their star formation ends.

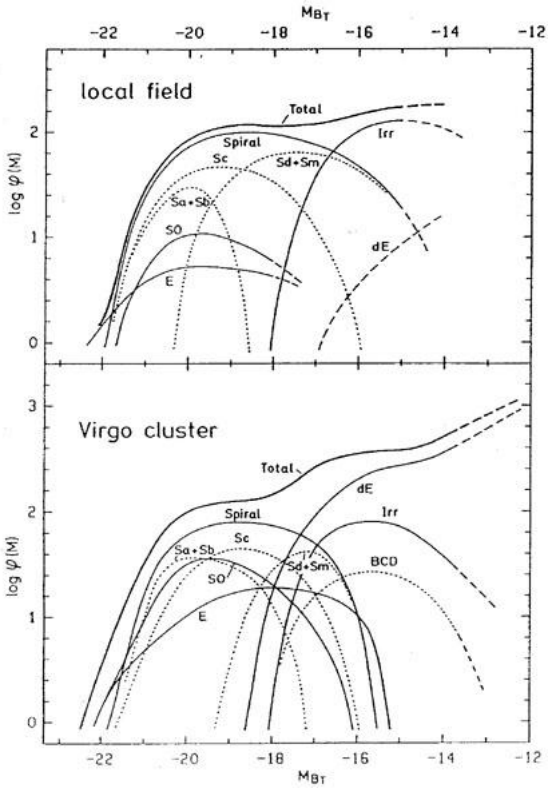

Figure 1.9: Morphology dependence of the galaxy luminosity function. The top panel shows the LF for galaxies in the local field and the bottom panel is for the galaxies in Virgo cluster, Binggeli et al. (1988).

1.9 About this thesis

In this thesis, evolution of X-ray and optical properties of poor galaxy clusters are explored. To achieve this goal, a sample of 27 X-ray selected clean galaxy clusters is used for the investigation. These clusters are mostly groups and poor clusters with temperature of 0.6 to 4.8 keV and have a wide redshift range: 0.05 to 1.05.

The fact that most of our sample are poor systems gives us a better chance to gain important information about the non-gravitational processes which are more effective in groups environments than in richer environments and are crucial for understanding galaxy evolution. This large redshift range enables us to explore how the cluster properties, like spatial structure of the ICM and distribution of dim and luminous galaxies, change with time (redshift). Trends with temperature will also investigated.

In chapter 2, a description of *XMM-LSS* survey is presented. After a brief outline of the *XMM-Newton* satellite, important aspects of the project is introduced focusing on the scientific implications of this multiwavelength survey.

In chapter 3, based on satellite X-ray images, spatial analysis of the ICM of clusters is

studied. By studying the X-ray emitted by the hot plasma in clusters, we should learn more about the effects of gravitational and non-gravitational processes responsible for producing the ICM structure. The observations show that gas is not cooling at clusters' cores as expected from the observed core X-ray luminosities. This tells us that there must heating source(s), probably from the feedback of from AGN, to compensate for the energy loss by radiation. This is probably the same process that is responsible for the quenching of start formations in young galaxies. The physics in clusters cores is very complicated and it is not yet well understood, as no simulations to date have fully give a complete picture of heating and cooling processes there. In chapter 3 of this thesis, we look at how cool cores and the shape of the X-ray profile changes with redshift and temperature; in turn this gives us important clues to the crucial physical processes.

Chapter 4 is an optical study of 14 members of the *XMM-LSS* survey clusters. Since clusters provide us with samples of galaxies of the same age and with similar histories, clusters in different mass and temperature ranges, are considered as tools to learn more about galaxy evolution, e.g. their star formation history and when they accreted most of their baryonic and dark mass. In the optical part of the electromagnetic spectrum, it is harder than the X-ray part to relate the different physical process in clusters to directly observed quantities and semi-analytical models are starting to give us new insights. In chapter 4 of this thesis, we look at the distribution of galaxy luminosities in clusters and see how this changes with both redshift and temperature. This area of research is particularly controversial when it comes to the faintest galaxies in the clusters. In this chapter, Schechter function is fitted to the derived background-subtracted luminosity functions (LFs) of the clusters in three optical passbands: g', r', and z' of the Canada-France-Hawaii Telescope Legacy Survey (CFHTLS). Individual as well as temperature-stacked and redshift-stacked LFs are studied to explore correlations of the Schechter function fitted parameters with both temperature and redshift. Colour trends with redshift and trends of the total optical luminosity with temperature and X-ray luminosity are also explored in this chapter.

Finally, the main conclusions and possible further work are briefly presented in chapter 5.

Chapter 2

The XMM-LSS Project

In this chapter, we present an overview of the XMM-Newton large scale structure (*XMM-LSS*) survey. We start by a short description of the XMM-Newton satellite followed by a brief outline of the survey. In section 2.3, we demonstrate the multi-wavelength aspects of this project and in section 2.4, we show how *XMM-LSS* is capable of probing the evolution of clusters properties. Original and current statuses of the project are presented in section 2.5. Section 2.6 is devoted to present some of the important and recent scientific results of *XMM-LSS*. The cleanest galaxy cluster sample detected by this survey, C1 clusters, are described in section 2.7. Finally, in section 2.8, we go through the optical follow-up, CFHTLS survey associated with *XMM-LSS*.

2.1 XMM-Newton, the satellite

The X-ray Multi-Mirror Newton (XMM-Newton) satellite is the largest spacecraft ever launched by the European Space Agency (ESA). It is 4 tonne, 10 m long and was launched at the end of 1999 by an Ariane-5 vehicle from the European launch base in Kourou, French Guiana. The satellite is dedicated to exploring the Universe in the soft-X-ray portion of the electromagnetic spectrum, that is energy band between 0.1 and 10 keV (0.08-8 nm). This range covers most of the energy range of the hot intracluster gas which is between 0.1 and 15 keV (0.08-12 nm). XMM-Newton is also capable of detecting the spectra of cosmic X-ray sources down to a few times 10^{-16} erg cm^{-2} s^{-1}. The satellite has effective collection area of 4500 cm^2 at 1 keV and 1000 cm^2 at 10 keV. It is capable of performing sensitive medium-resolution spectroscopy with resolving powers between 100 and 700 over the energy band 0.35-2.5 keV (Barré, Nye & Janin 1999, Bagnasco et al. 1999 and Jansen 1999).

The XMM-Newton satellite is configured modularly and is composed of four main elements, see Fig. 2.1:

- The focal plane assembly, consisting of the focal plane platform which carry the focal-plane instruments: two Reflection Grating Spectrometer (RGS) readout cameras, a p-n (PN) European Photon Imaging Camera (EPIC) and two EPIC Metal Oxide Semi-conductor (MOS) imaging detectors
- The telescope tube
- The mirror support platform
- The service module.

The EPIC cameras can perform sensitive imaging observations over the telescope's field of view (FOV) of 30 arcmin with moderate spectral resolution (E/$\triangle$E around 20-50). The PN and MOS CCD cameras have FWHM point spread functions (PSF) of 6.6 and 6.0 arcsec at 1.5 keV, respectively.[1] The orbit of XMM-Newton is highly elliptical, allowing maximum time above the radiation belts, that is higher than 40000 km and it is geosynchronous, with a period that is multiple of 24 hours, giving optimal coverage from dedicated ESA ground stations.

2.2 Outline of the XMM-LSS project

The XMM Large Scale Structure survey (XMM-LSS) is a medium deep large area survey. Associated with this is a multi-wavelength survey that covers all main parts of the electromagnetic spectrum. A previous X-ray satellite, ROSAT (1990-1999), conducted a large scale structure survey of galaxy clusters: REFLEX survey (Trümper 1992). The primary goal of XMM-LSS survey is to extend this ROSAT survey up to redshift of $z \sim 1$ while keeping the precision of earlier studies, and then to use these observations to determine how X-ray gas and galaxy clusters evolved as a function of redshift.

To achieve its goal, the XMM-LSS survey was constrained to give the best possible estimation of two quantities: of the cluster-cluster correlation function which is a quantitative measure of clustering for comparison with evolutionary theories, and the cluster number density. The project[2] is lead by Dr. Marguerite Pierre.[3]

[1] http://xmm.vilspa.esa.es/external/xmm_user_support/documentation/technical/Mirrors/index.shtml
[2] http://vela.astro.ulg.ac.be/themes/spatial/xmm/LSS/index_e.html
[3] Service d'Astrophysique, CEA Saclay, 91191 Gif sur Yvette, France.

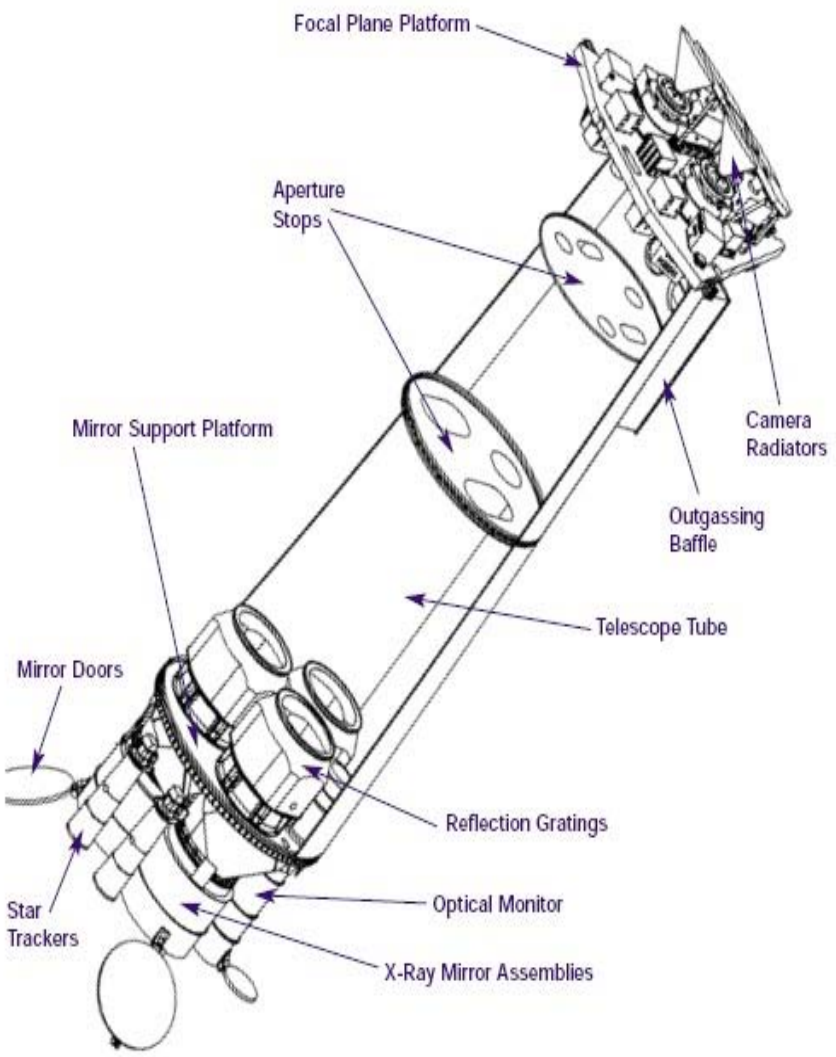

Figure 2.1: XMM-Newton Structure (Barré, Nye & Janin 1999).

The results of any survey is limited by the precision of the instrumentation used to perform it and each new generation of observatories brings advances over its predecessors. The REFLEX survey had a sample of 460 clusters to a nominal flux limit of 3×10^{-12} erg cm^{-2} s^{-1} (in the ROSAT band, 0.1-2.4 keV) (Guzzo et al. 1999). Among the next generation of X-ray satellites, after ROSAT, is XMM-Newton which has the ability to detect extended X-ray sources to higher redshift and with increased sensitivity. XMM-LSS survey has a sensitivity of $\sim 3 \times 10^{-15}$ erg cm^{-2} s^{-1} for pointlike sources in the 0.5-2 keV band. This sensitivity is about three orders of magnitude more than REFLEX and makes XMM-LSS survey much deeper than the previous surveys.

Moreover, the XMM-LSS survey is a multi-wavelength survey that comprises other parts of the electromagnetic spectrum: optical, IR, radio and UV. With these characteristics, the XMM-LSS survey can achieve an accurate estimation of cluster number density and other key parameters to probe the evolution of galaxies, large-scale structure and star and AGN formation as a function environment and of redshift up to $z \sim$1. A suitable area in sky has been allocated for the survey: an area centred on $\alpha = 2^h18^m00^s$, $\delta = -7°00'00''$ (J2000) with neutral hydrogen column of $1.4 \times 10^{20} < N_H$ (cm^{-2}) $< 3.5 \times 10^{20}$. An overview of this area in presented in Fig. 2.2. Other surveys in the same area are also shown (Pierre et al. 2004).

The scientific goals of the survey include:

- Probe X-ray and optical evolutionary properties of clusters and quasi-stellar objects (QSOs). This is a main and important goal of the survey. My work in this thesis –presented in the next two chapters– is concentrated on analysing and fitting spatial properties of the clusters detected in the XMM-LSS pointings and on the optical follow-up survey which partially covers the sky area of the XMM-LSS survey. The results of these projects will help in constructing a database of clusters information that should enable us to track the evolution of clusters' properties with redshift and temperature. This data may also tell us how clusters evolve and what physical processes drives this evolution.

- Map the large scale structures as outlined by clusters of galaxies out to a redshift of $\sim$ 1. This will show the structure of the spatial distribution of deep potential wells up to high redshifts.

- Compute the correlation function of clusters of galaxies in two redshift bins $0 < z < 0.5$ and $0.5 < z < 1$.
- Map the spatial distribution of AGN and QSOs within the cosmic web as determined by the cluster population. This will lead to a deeper understanding of the physics of AGN and the effect of initial density perturbation and galaxy interactions.
- Determine the correlation function of AGN and QSOs.
- Investigate the existence of X-ray bright galaxy clusters between $1 < z < 2$.
- Compare the cosmic topology inferred from X-rays with the mass distribution determined by the galaxy distribution and the associated weak lensing survey in the optical study. This will provide crucial information about bias mechanisms as a function of redshift.

2.3 Multi-wavelength aspects of the XMM-LSS project

Along with the X-ray band survey, XMM-LSS is associated with surveys in other electromagnetic bands. These surveys are important in several respects. While optical information remains the primary database for X-ray source identification, the contribution from other wave bands may be critical. For example, in the far infra-red domain, many heavily absorbed X-ray QSOs, not visible in the optical, are expected to show up. To have a full understanding of the physics of the evolution and formation of clusters, it is necessary to have multi-wavelength data which provide an overview of different physical processes within clusters. The design of the XMM-LSS provides substantial advantages for complementary observations and the project has developed many collaborations at other wavelengths. The applications of other wavelength surveys are summarized below and presented in Table 2.1.

Optical: The imaging of XMM-LSS area is part of the Canada-France-Hawaii Telescope Legacy Survey (CFHTLS).[4] It provides optical multi-colour imaging counterpart of the X-ray sources in at least three colours. Data pipelines and processing have been developed by the TERAPIX (Traitement Elementaire, Reduction et Analyse des PIXels)[5]. Also, the MegaCam

[4] http://www.cfht.hawaii.edu/Science/CFHLS/
[5] http://terapix.iap.fr/

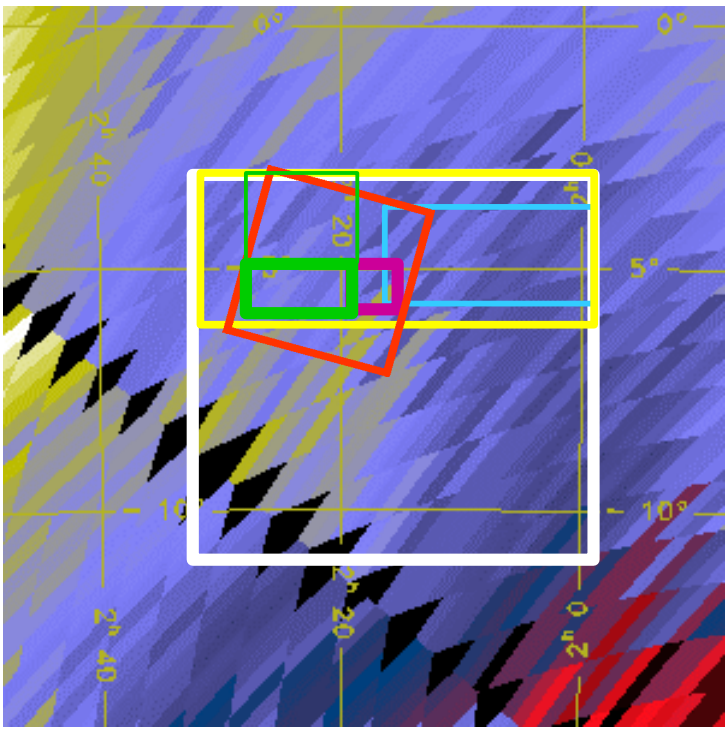

Figure 2.2: Large white square indicating the location of the XMM-LSS survey is overlaid on a map of N_H ($1.4 \times 10^{20} < N_H$ (cm^{-2}) $< 3.5 \times 10^{20}$). The survey area surrounds two deep XMM surveys based on guaranteed time: the XMM Subaru Deep Survey and the XMM Medium Deep Survey (XMDS) which is also corresponding to the VIRMOS-DESCART Deep Survey (VVDS deep). The area overlap greatly assists in quantifying the completeness of the survey. Also indicated are the positions of the associated DESCART-VIRMOS Deep Survey (VVDS wide), the SWIRE SIRTF Legacy Survey, the Galex survey and the NOAO deep survey (Pierre et al. 2004).

Observatory/Instrument	Coverage	Band	Final Sensitivity
XMM/EPIC	~ 20 deg^2	[0.2-10] keV	$\sim 3-5 \times 10^{-15}$erg cm^{-2} s^{-1}[a]
CFHT/CFH12K (VVDS Deep)	2 deg^2	B, V, R, I	26.5, 26.0, 26.0, 25.4[b]
CFHT/CFH12K (VVDS Wide)	3 deg^2	V, R, I	25.4, 25.4, 24.8[b]
CFHT/MegaCam	72 deg^2	u*, g′, r′, i′, z′	25.5, 26.8,26.0, 25.3, 24.3[c]
CTIO 4m/Mosaic	~ 16 deg^2	R, z′	25, 23.5[d]
UKIRT/WFCAM	8.75 deg^2	J, H, K	22.5, 22.0, 21.0[e]
VLA/A-array	110 deg^2	74 MHz	275 mJy/beam[f]
VLA/A-array	5.6 deg^2	325 MHz	4 mJy/beam[g]
OCRA	all XMM-LSS	30 GHz	100 μJy[h]
AMiBA	70 deg^2	95 GHz	3.0 mJy[i]
SPITZER/IRAC (SWIRE Legacy)	8.7 deg^2	3.6, 4.5, 5.8, 8.0 μm	7.3, 9.7,27.5, 32.5 μJy[j]
SPITZER/MIPS (SWIRE Legacy)	8.9 deg^2	24, 70, 160 μm	0.45, 6.3, 60 mJy[k]
Galex	~ 20 deg^2	1305-3000 Å	~ 25.5[l]

Table 2.1: XMM-LSS X-ray and associated surveys (Pierre et al. 2004).

Notes:
[a] For pointlike sources in [0.5-2] keV
[b] AB$_{Mag}$, 5″ aperture
[c] S/N = 5 in 1.15″ aperture
[d] 4 σ in 3″ aperture
[e] Vega$_{Mag}$
[f] 30″ resolution; deeper observations planned
[g] 6.3″ resolution
[h] 5σ, detection limit
[i] 6σ, detection limit
[j] 5σ
[k] 5σ
[l] AB$_{Mag}$

data will form the basis of a weak lensing analysis. The cosmological constraints resulting from these data can then be compared to those provided by the X-ray data on the same region. Deep NIR imaging of $z > 1$ cluster candidates found in the XMM-LSS is used to confirm the sources before carrying spectroscopic studies. Finally, in the UV band, the XMM-LSS field is a part of the Galaxy Evolution Explorer (GALEX) project[6], which is a NASA UV imaging and spectroscopic survey mission designed to study star formation process and its evolution over redshift range $0<z<2$.

Radio: XMM-LSS survey is important for a number of issues concerning the relation of powerful radio galaxies and the overall mass distributions in the Universe, including: radio sources as tracers of large scale structure, the environment of radio sources and distant radio halos. In addition, this follow-up is a useful indicator of galactic nuclear or star-formation activity. The complete survey region is being mapped using the VLA at 74MHz and 325MHz.

Infrared: Infrared studies are also a part of the XMM-LSS project. The Spitzer Wide-area Infra-Red Extragalactic (SWIRE)[7] programme covers about 9 deg^2 of the XMM-LSS in 7 MIR and FIR wavebands from 4 to 160 μm. This is an important X-ray/IR combination to be studied. This study will address the question of how star formation in cluster galaxies depends on distance from the cluster centre, on the strength of the gravitational potential, and on the density of the intracluster medium. The FIR study along with other wavelength bands including the X-ray, optical and radio bands, will provide a deeper understanding of the nature of heavily obscured objects, as well as the first coherent study of biasing mechanisms as a function of distance and redshift.

Spectroscopy: The spectroscopic properties of all identified X-ray sources in the range $0<z<1$ are to be studied. In the subsequent stages of the spectroscopic follow-up, it is planned to undertake spectroscopic programmes that will focus on individual objects, and include high resolution spectroscopy, measurements of cluster velocity dispersions, QSO absorption line surveys, as well as NIR spectroscopy of the XMM-LSS X-ray selected clusters.

[6] http://www.srl.caltech.edu/galextech/galex.htm
[7] http://swire.ipac.caltech.edu/swire/swire.html

2.4 Scientific implications of XMM-LSS for evolution of clusters

2.4.1 Galaxy surveys and cosmology

Clusters of galaxies are now used as tools to probe the properties of the observed universe. According to the theory of the formation of cosmic structures, they formed by the gravitational collapse of rare high peaks of primordial density perturbations in the early universe, see for example, Peebles (1993). Then, they grew by accretion at a rate governed by the initial density fluctuation spectrum, the cosmological parameters, the nature and amount of dark matter as well as the nature of the dark energy (e.g. He & Wang 2008). One of the essential cosmological parameters is the matter density parameter, Ω_m which is defined as $\overline{\rho}/\rho_c$, where $\overline{\rho}$ is the cosmic mean matter density and ρ_c is the critical density of the Universe.

The 3-dimensional space distribution and number density of galaxy clusters as functions of cosmic time constrain cosmological parameters and provide the best tool to infer the large scale structure (LSS) of the cosmos (Kofman, Gnedin & Bahcall 1993, Bahcall & Cen 1993, White et al. 1993 and Rines & Geller 2008). High- and low-density universes show very different evolutionary behaviour, so that the space density of distant clusters can be used as a powerful tool to test different cosmological theories.

What cosmological models actually predict is the number density of clusters of a given mass at varying redshifts. The cluster mass can only be estimated indirectly from observed quantities. Studies of evolution in clusters have also included the evolution in blue galaxy fraction, emission line fraction and lenticular S0-type galaxy fraction (e.g. Gerke et al. 2007).

The spatial extent of clusters can be inferred from their X-ray emission. The LSS study results inferred from clusters are independent of Cosmic Microwave Background (CMB) and supernova (SN) studies since they do not rely on the same physical processes. With a cosmological model and a large statistical sample of clusters, one can have information linking cluster physics, non-linear phenomena involved in cluster evolution, and scaling relations. Also, cluster number counts as a function of both redshift and X-ray luminosity yield important tests of models of the mass-luminosity relation and on cosmological models of dark energy.

Evolution studies in respect of both structure and luminosity are in agreement with models of hierarchical structure formation in a flat low density universe with matter density $\Omega_m \sim 0.3$

and amplitude of mass fluctuations on 8 Mpc scale, $\sigma_8 \sim$ 0.7-0.8 (Rosati, Borgani & Norman 2002). In parallel, optical surveys have developed from sky survey plates to deep multi-colour CCD imaging. Detecting clusters at high redshift ($z \gtrsim 0.8$) is hampered by the relatively bright background resulting in low signal-to-noise ratio and one has to use the photometric redshift data. However, given the limitations on the accuracy of such methods and various underlying hypotheses about galaxy evolution, this usually yields large numbers of high-z candidates, many of them simply being portions of cosmic filaments seen in projection. One will thus always require in default of extensive optical spectroscopic campaigns, an ultimate confirmation from the X-ray band, to assess the presence of deep potential wells.

While galaxy cluster surveys were initiated by Abell in 1958 (Abell et al. 1958) with an over-the-whole-sky survey in the optical band, the first X-ray sky survey was carried out using the Uhuru X-ray satellite, Giacconi et al. (1972). This survey revealed a clear association between rich clusters and bright X-ray sources and established that X-ray clusters were bright (10^{43-45} erg s^{-1}) extended sources in the X-ray band. It also showed that the X-ray emission was thermal and originated in a hot diffuse gas trapped in the gravitational potential of the cluster (Gursky et al. 1971).

Few years later, the HEAO-1 X-ray Observatory (Rothschild et al. 1979) performed an all-sky survey with much improved sensitivity (3×10^{-11} erg cm^{-2} s^{-1}) compared to Uhuru and provided the first flux-limited sample of extragalactic X-ray sources in the [2-10] keV band (Piccinotti et al. 1982). Most of the detected clusters were among the Abell catalogue. The systematic search for clusters underwent a boost of activity in the X-ray band with the Einstein Observatory which had better angular resolution and fainter flux limit by a factor of two than previous observatories. This allowed confused sources detected earlier to be resolved with greater details.

The Extended EINSTEIN Medium Sensitivity Survey (MSS) provided ∼730 serendipitous X-ray sources extracted from pointed observations down to a flux limit of 1.5×10^{-13} erg cm^{-2} s^{-1} in [0.3-3.5] keV band. Later, this survey identified a sample of 67 clusters in the $0.14 < z < 0.6$ range, (Gioia et al. 1990) suggesting, for the first time, a mild evolution in the cluster number density. Several follow-up studies for the MSS survey have been undertaken such as the Canadian

Network for Observational Cosmology (CNOC) survey[8] (see e.g., Yee et al. 1996).

In 1990, the ROSAT All-Sky-Survey (RASS) became the first imaging survey that covers the entire sky and therefore, was considered an important data resource for any LSS research. The REFLEX survey also provided valuable information for cosmological studies down to 3×10^{-12} erg cm^{-2} s^{-1} in the [0.2-2.4] keV band and detecting clusters out to $z \sim 1.2$ (see for example, Böhringer 2001, Burenin et al. 2007 and Krumpe et al. 2010). A summary of X-ray cluster surveys is shown in Fig. 2.3.

Using the XMM-Newton satellite, the Representative XMM-Newton Cluster Structure Survey (REXCESS)[9] is aiming to calibrate the scaling relations for a statistical sample of clusters, selected by X-ray luminosity alone. The REXCESS sample consists of deep X-ray observations of ~ 30 nearby ($z < 0.2$) galaxy clusters. To best assess the scaling relations, the selection has been designed to provide a close to homogeneous coverage of the X-ray luminosity range. The chosen luminosity regime, $L_X = 0.407 - 20 \times 10^{44} h_{50}^{-2}$ erg/s in the [0.1-2.4] keV rest-frame band, provides clusters with estimated temperatures above 2 keV. For recent results of REXCESS, see (Pratt et al. 2007, Pratt et al. 2009 and Haarsma et al. 2010).

XMM-Newton is a powerful X-ray telescope when compared with instruments used in earlier surveys. XMM-Newton has a high sensitivity, considerably better PSF than the RASS (FWHM $\sim 6''$ on axis) and large field of view ($30'$), making it a powerful tool for the study of extragalactic LSS (Strüder et al. 2001). Furthermore, the high galactic latitude field observed with XMM-Newton at medium sensitivity ($\sim 0.5 - 1 \times 10^{-14}$ erg cm^{-2} s^{-1}) is clean, as it contains primarily two types of objects, namely QSOs (pointlike sources) and clusters (extended sources) well above the confusion limit. In addition, if clusters more luminous than around 3×10^{44} erg s^{-1} are present at high redshift, they can be detected as extended sources out to z$\simeq$ 2 using XMM-Newton. All of these powerful capabilities make XMM-Newton ideal for an LSS survey, for more details, see Pierre et al. (2004).

The sensitivity of the XMM-LSS survey allows the entire cluster population to be detected out to a redshift of 0.6, and will unveil the nearby cluster population. With increasing redshift, XMM-LSS is less sensitive to low mass systems and therefore, the low-z and high-z samples to be used for the study of the LSS will pertain to different cluster mass ranges. But this does

[8] http://www.astro.toronto.edu/ cnoc/index.html
[9] http://rexcess.extragalactic.info/home.html

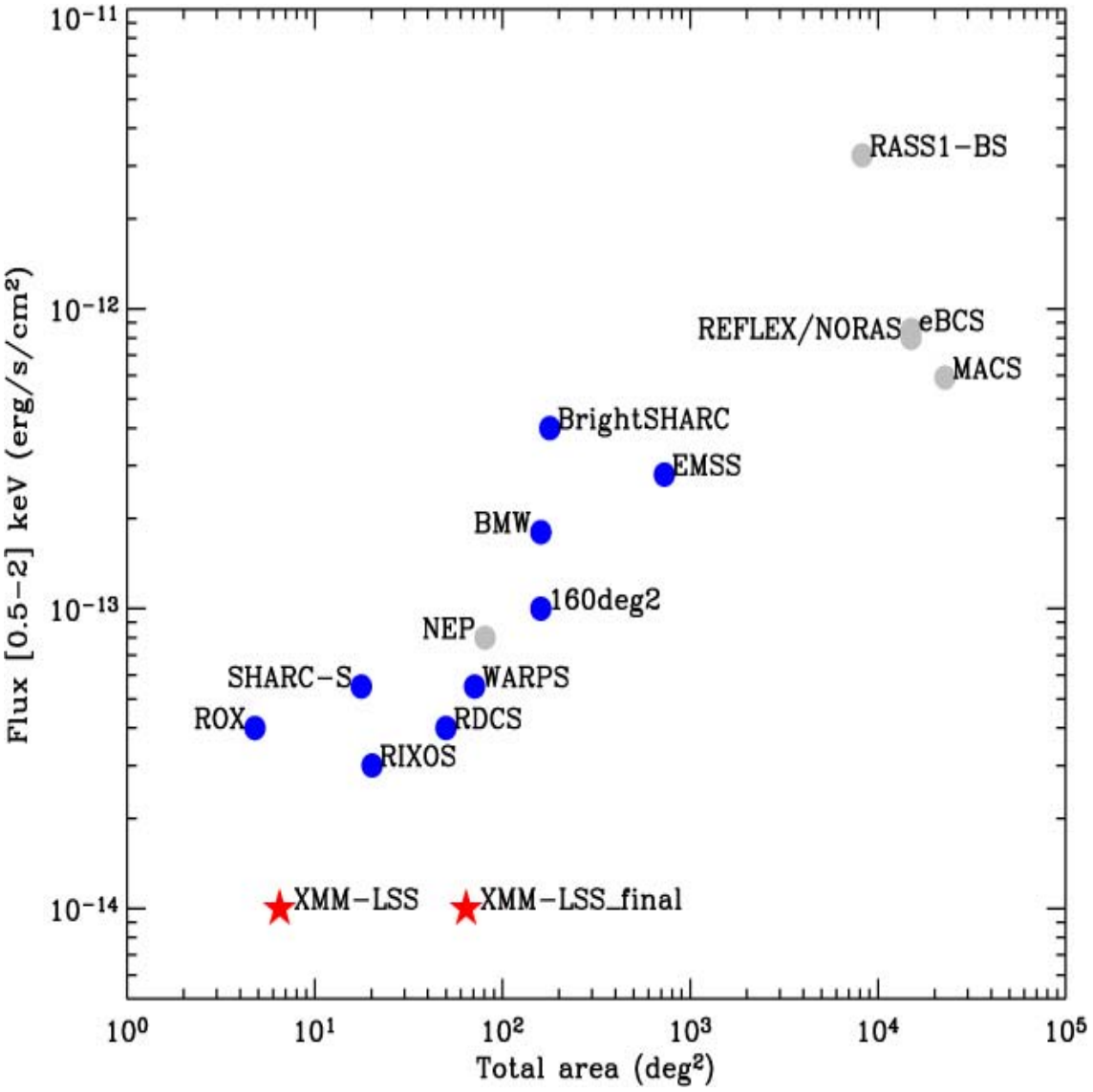

Figure 2.3: Overview of the existing X-ray cluster surveys as a function of area and flux. The area plotted is the maximum area of each survey; the flux plotted is the flux at which the survey area is half the maximum. The light filled circles indicate surveys covering contiguous area, while the blue circles represent serendipitous surveys; the stars show the position of the XMM-LSS surveys, Pierre et al. (2004).

not prevent the derivation of strong cosmological constraints. The results of the XMM-LSS high-z survey can be compared to the corresponding results of the REFLEX survey. Moreover, given the large volume sampled at high redshift, the XMM-LSS is well suited to constraining the abundance of distant massive clusters.

2.4.2 Importance of low-mass clusters (groups)

Groups (clusters with ICM temperature equal to or less than 2 keV) are more important for the evolution of galaxies and large-scale structures than massive clusters (with ICM temperature more than 2 keV). Galaxy formation is a prolonged procedure which may include many processes such as the collapse of primordial perturbations, accretion of baryonic and dark matter, total merging of distinct galaxies and outflows of gas and energy from AGN and supernovas. Most galaxies perform these transactions in group environments. Groups themselves are unstable; while the galaxies in a group are forming, the group itself may be separating out from the Hubble flow, collapsing under the influence of gravity, accreting new galaxies and merging with other groups to form clusters and superclusters. Most of the XMM-LSS detected systems actually fall in the group regime and that makes it a suitable survey to study the evolution of galactic systems.

In general, clusters consist of galaxies and intracluster medium, and the physical processes governing the evolution of these two components are different. Galaxy evolution is driven mainly by galaxy-galaxy gravitational interactions such as stripping and merging. While gas evolution, on the other hand, is driven by non-gravitational processes, like radiative cooling, SN energy and metal injections and feedback from galaxy formation. If these non-gravitational processes are not taken into account, then cluster models predict self-similar evolutionary scenarios, see for example Voit, Kay & Bryan (2005).

To determine how well a model predicts the true properties of a cluster, accurate measurements of cluster mass and baryon-to-dark-matter ratio are needed. Since mass measurements are difficult, observables such as X-ray luminosity, L_X, and temperature, T, are used as estimators for cluster mass by linking the observable with mass through a simple scaling relation, see section 1.5, above. Studying X-ray properties of galaxy clusters probes the way non-gravitational processes affect the mass-temperature relation and baryon-to-dark-matter ratio as

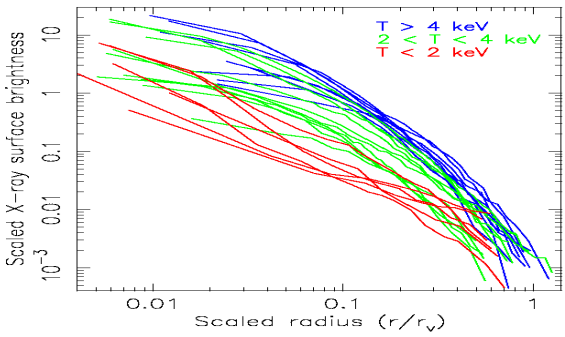

Figure 2.4: Scaled X-ray surface-brightness profiles overlaid to show departures from similarity in galaxy systems of different temperatures (Ponman, Cannon & Navarro 1999).

well as how these scaling relation evolve with time (redshift). It has been shown (Ponman, Cannon & Navarro 1999) that lower-temperature galaxy systems have different surface-brightness profiles from higher-temperature systems, which has been taken as evidence for the effect of non-gravitational processes and for the breaking of self-similarity in evolution, see Fig. 2.4.

Self-similarity is also broken because of the entropy threshold for radiative cooling within the age of the universe. As clusters grow in mass with time as predicted by the hierarchal structure formation scenario, merger causes shocks that increase the entropy of the gas. Without radiative cooling and non-gravitational heating, this entropy increase would yield a self-similar entropy distribution in the gas. But the existence of cooling leads to a break in the self-similarity. Also, departure from self-similarity will be observed if the cooling gas forms supernovae or feeds Active Galactic Nuclei (AGNs), see Voit (2005b).

Also, the cooling threshold affects the evolution of the $L_X - T$ relation of clusters. As the redshift increases, we notice an increasingly larger proportion of the gas in self-similar clusters lies below the cooling threshold and is therefore subject to condensation and feedback. This breaks the self-similarity in high-redshift clusters and hence X-ray observations of these clusters can test this picture.

XMM-LSS is a project that has all the capabilities to study evolution of galaxy clusters .

The XMM-LSS project is detecting faint and distant clusters of low mass, quite comparable in mass to clusters in the local universe. This allows a direct comparison of galaxy properties in similar systems. Prior to XMM-LSS, detailed spectroscopic and purely photometric studies have concentrated mostly upon X-ray systems displaying luminosities $L > 3 \times 10^{43}$ ergs s^{-1}, corresponding to $T \geq 2$ keV. The XMM-LSS survey is capable of adding X-ray groups with $T < 2$ keV at comparable redshifts to existing, higher temperature, X-ray clusters surveys, thus providing a consistent baseline of X-ray selected groups over a large redshift interval.

The few studies which have been conducted into group evolution have been based on optically selected group samples. X-ray selection has been widely accepted to be superior as to clusters selection, since it is less vulnerable to projection effects, and preferentially identifies genuinely collapsed systems. These benefits are even more important for galaxy groups than for clusters. The wide area, medium deep coverage of XMM-LSS provides the ideal sample for detecting collapsed groups at moderate redshifts, in a statistically well-controlled way.

In addition to providing secure evidence that groups are genuine, X-ray surface brightness and temperature permit estimates of mass and virial radius to be computed, allowing systems to be stacked so that radial variations in galaxy properties can be studied. Effects of the group environment can be separated from evolutionary effects by comparing galaxy properties in group and field environments and also comparing XMM-LSS samples with the properties of galaxies in lower redshift groups.

Further, trends as a function of X-ray luminosity can be identified by comparing XMM-LSS samples to higher luminosity X-ray systems observed at comparable redshifts. Baryons, which comprise nearly 16% (Peterson & Fabian 2006) of the mass content of the universe, dynamically follow the dominant dark matter during the collapse of matter that formed clusters. The intracluster material is heated by the adiabatic process of compression and by shocks caused by high-velocity motions during virialization. Efficient methods of identification can be achieved by observing clusters in the X-ray band and hence these observations can be applied in the studies of the evolution of clusters.

Also, the temperature data can be used to infer the depth of the cluster gravitational potential. For these reasons, most cosmological studies based on clusters have used X-ray selected

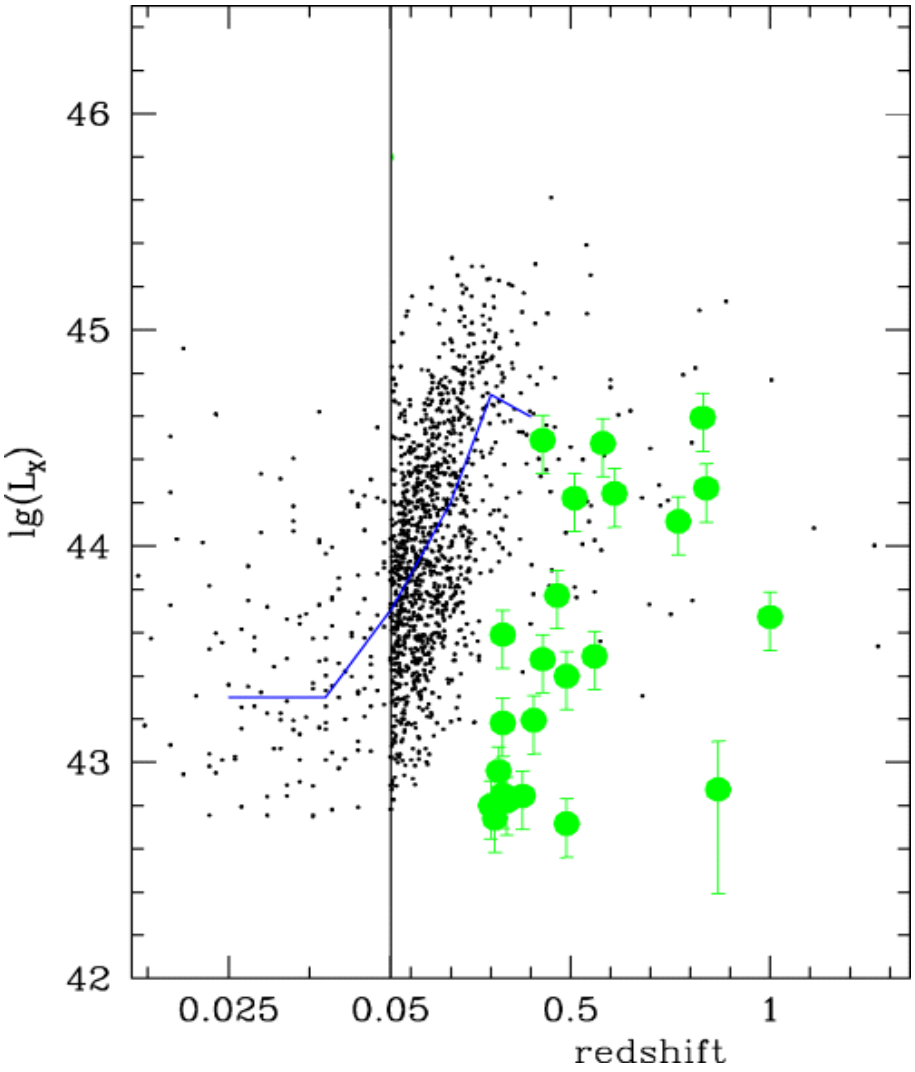

Figure 2.5: X-ray luminosity of about 1300 clusters drawn from literature (small black points) and XMM-LSS clusters (filled green circles with error bars). The blue curve is an adaptively smoothed running median of literature points (Andreon et al. (2004)).

samples. X-ray studies of galaxy clusters provide an efficient way of mapping the overall structure and evolution of the universe. Also, X-ray studies are important means of understanding their internal structure and the overall history of cosmic baryons.

Many intermediate redshift clusters are optically selected, with the risk of biasing the optical properties of galaxies. Therefore, selecting them independently of the optical, will limit the risk of bias. This can be done with the XMM-LSS. Fig. 2.5 shows individual X-ray luminosities of more than 1300 clusters of galaxies (black points) drawn from literature. Their median X-ray luminosity (blue line) increases with redshift (Andreon et al. 2004).

The high sensitivity of the XMM-LSS survey allows it to detect very low-mass galaxy groups

to high redshifts but a more complete understanding of these trends will be possible with the compilation of a statistically complete sample of galaxy clusters anticipated within the continuing XMM-LSS survey.

2.5 Original and current XMM-LSS coverage

Originally, this survey consists of XMM-Newton satellite exposures covering an area of 8×8 deg^2 region. Refregier et al. (2002) expected, for the favoured ΛCDM model, about 600-1200 clusters at $0 < z < 0.5$ and about 200-700 at $0.5 < z < 1$, the uncertainty being dominated by the errors on σ_8 and Ω_m. Some of these clusters are expected to be very clean from contaminations of point-like sources and others are expected to have lower quality. This redshift dependence of the XMM-LSS cluster counts was expected to measure σ_8 and Ω_m with a precision of about 6% and 18% (95% CL), respectively. The uniform coverage over a wide contiguous area, with an extensive spectroscopic follow-up, would allow to measure the correlation function in several redshift bins out to $z = 1$.

Currently the survey covers a sky area of $\sim 10\,\mathrm{deg}^2$ and consists of dozens of 10-ks pointings. Within $\sim 5\,\mathrm{deg}^2$ of this area, there are around 30 Class one (C1) detected clusters. The XMM-LSS C1 cluster sample is a well-controlled X-ray selected and spectroscopically confirmed cluster sample. The C1 clusters are the best class of clusters detected by the survey in terms of quality. The criteria used to select the members of this sample guarantee negligible contamination of point-like sources. The pointings are separated by $20'$, they have a point source sensitivity of $\sim 5 \times 10^{-15}$ erg cm^{-2} s^{-1} in the [0.5-2] keV band.

2.6 Some XMM-LSS recent scientific results

Andreon et al. (2005) performed a search for clusters of galaxies at $z \sim 1$ and above, using data from 2.9 square degrees of XMMNewton images. They selected 19 X-ray potentially extended sources without any counterparts in deep optical images, and therefore these clusters were candidates for high-redshift systems. Most of these clusters were also imaged in Near-IR, R and z' passbands. Photometric observations confirmed that nine of these clusters as genuine high-redshift clusters. The brightest galaxy members of the high-redshift clusters have luminosity

compatible with $z \sim 1$ and the galaxies on the colour magnitude diagram have the right colour to be early-type galaxies at $z \sim 1$. Spectroscopic observations confirmed the redshift value of six of these clusters; three of them had redshifts in the range of $0.81 < z < 0.92$, while the redshifts of the other remaining three clusters were 0.8-0.9, 1.0 and 1.3.

With the Andreon et al. (2005) discovery, the number of high-redshift clusters with X-ray emission has approximately doubled. One of the high-redshift cluster had very low likelihood of extension, but it is still a cluster, suggesting caution in using likelihood of extension at low X-ray counts in their sample. The number density of observed high-redshift clusters, inferred from this study, was about 1.7 squared deg for clusters with X-ray flux above 2.5×10^{-15} erg cm^{-2} s^{-1} in the energy band [0.52] keV, which was the flux of the faintest considered source in their sample. The 68 per cent confidence interval, assuming a Poissonian probability distribution function, was [1.0, 2.9]. This estimate was a lower limit, because not all sources in the considered area had been scheduled for NIR observations.

In their XMM-LSS study, Bremer et al. (2006) reported a discovery of XLSS J022303.0043622 cluster. The redshift of this cluster was 1.22 which made it the most distant system discovered in the survey to the date of that study. This cluster was identified from its X-ray properties and selected as a high redshift candidate from its optical and Near-IR characteristics in the XMM-LSS region. They also presented multiband imaging and spectroscopy information of the discovered system. They spectroscopically confirmed seven galaxies with redshifts of 1.22 within an arcminute of the X-ray centre of the cluster. The cluster had a bolometric X-ray luminosity of 1.1×10^{44} erg s^{-1}, which was fainter than most other known high-redshift X-ray selected clusters. The cluster appeared to have a compact centre, with 15 luminous galaxies within 15 arcsec of the centre and only a further eight in an annulus between 15 and 30 arcsec from its centre.

The spectroscopic data of this distant cluster showed that the galaxies were similar to passive ellipticals. This made the authors conclude that the bulk of the star formation in the galaxy population of this cluster occurred at least 1.5 Gyr, at $z > 2$. The colours and magnitude information also showed that stellar masses were comparable with those of massive galaxies in clusters at low redshift, indicating that massive cluster galaxies may be in place at $z > 1$ and passively evolve at lower redshift with little star formation or growth by possible galaxy mergers.

Valtchanov et al. (2004) reported the discovery of five high-redshift ($z > 0.6$) X-ray selected clusters as part of the XMM-LSS project. The redshifts of the discovered clusters are 0.6128 (XLSSC 1), 0.7722 (XLSSC 2), 0.8378 (XLSSC 3), 0.87 (XLSSC 4) and 1.0 (XLSSC 5). For three of them they had sufficient spectroscopically confirmed member galaxies that an estimate of the velocity dispersion was possible: 867 km s^{-1} (XLSSC 1), 524 km s^{-1} (XLSSC 2) and 780 km s^{-1} (XLSSC 3). The scaling relations between L_X, T and σ_v were found to follow the low redshift values, within the limits of the measurement errors. One cluster, XLSSC 5, showed a complex structure and was speculated that most likely it was actually two clusters in projection. Some galaxies included in the spectroscopic data for this cluster might reside in a possible filament connecting the two clusters.

Most of discovered clusters in Valtchanov et al. (2004) study are weak, extended X-ray sources and consequently would have been difficult to classify in typical deep ROSAT/PSPC pointings because of the insufficient photon statistics in addition to the worse point spread function. By this discovery, XMM-LSS was starting to fill the cluster database with significant number of objects at high redshift from the middle of the mass function. This was considered a great improvement upon ROSAT based surveys which had limited capabilities of detecting low-mass clusters, the realm of systems where non-gravitational physics (like pre-heating and feedback) were presumably more important in galaxy evolution.

2.7 Class 1 clusters of XMM-LSS

2.7.1 Detection and properties of C1 clusters

Pacaud et al. (2007) presented 29 galaxy clusters from the XMM-LSS. These are well-controlled cluster sample observed in 51 XMMNewton pointings covering about 5 deg^2 of XMM-LSS area. Their fluxes in the [0.52] keV band ranging from 1 to 50 $\times 10^{-14}$ erg s^{-1} cm ^{2}. This cluster sample was constructed from a two-dimensional X-ray parameter space guarantee no contamination by point-like sources and observations were performed in a rather very uniform way (1020 ks exposures). Most of the pointings (the B pointings) have a nominal exposure time of 10^4s, while the rest (G pointings) are deeper guaranteed time of 2×10^4s for each, see Fig. 2.6.

The C1 sample have redshifts in the ranges of 0.05-1.05 with a pronounced peak around z $\sim$

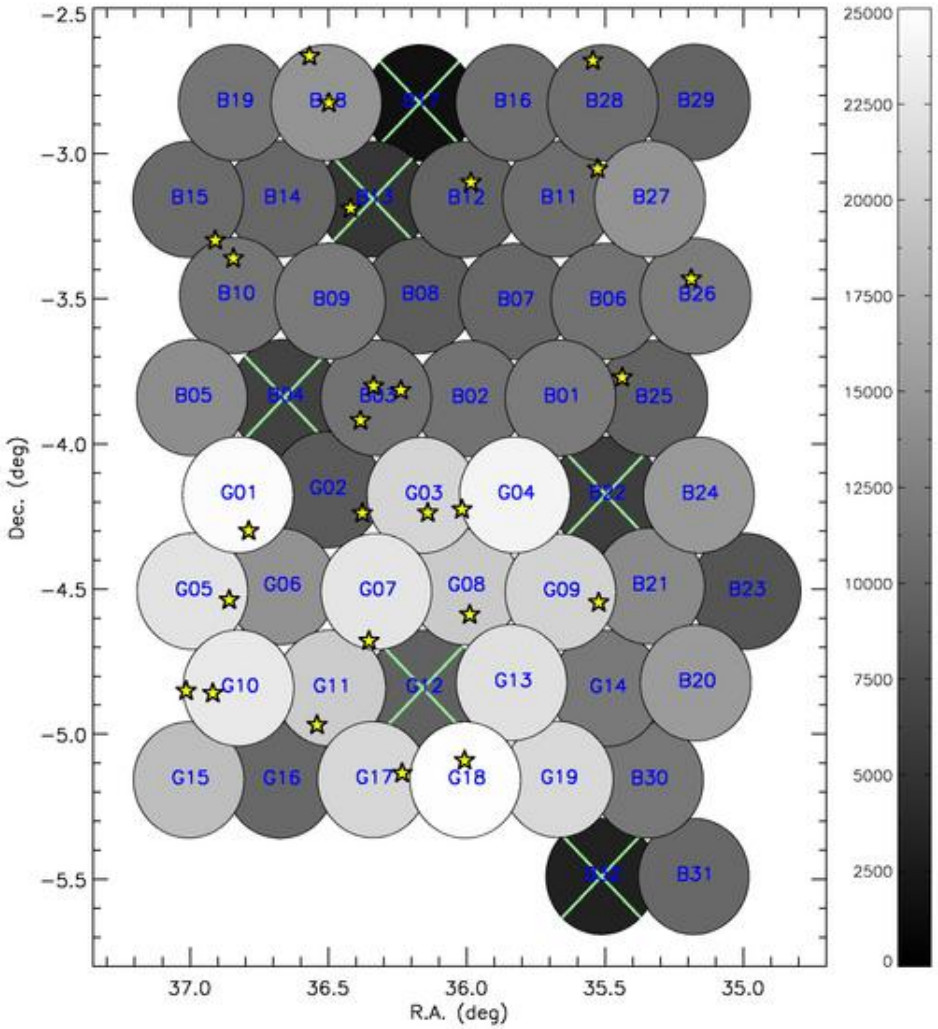

Figure 2.6: C1 clusters pointings. The colour scale indicates the on-axis exposure time of each pointing in seconds. Pointings marked by a cross are strongly affected by flares and were be re-observed, Pacaud et al. (2007).

0.3. Nearly half of the clusters have a temperature ≤ 2 keV (groups). Thanks to the sensitivity and relatively good PSF (compared to previous generation of X-ray telescopes) XMM-Newton systematically unveils for the first time the z $\sim$ 0.3 cluster population on large scales with this temperature range.

The C1 X-ray images were generated from filtered event lists using the XMM-SAS task EVSELECT. As described in the detection pipeline in Pacaud et al. (2006), the images were first filtered using a wavelet multiresolution algorithm was specifically designed to properly account for the Poisson noise in order to smooth the background and lower the noise level, while keeping unchanged the relevant information. Then SEXTRACTOR software was used to extract a very deep primary source catalogue from the filtered X-ray images of the clusters. Also, the properties of clusters were checked by a maximum-likelihood profile fitting programme

to characterise extended sources in images.

Spectroscopic Data were used to estimate the temperature of the clusters. This is the procedure which was followed to measure the temperature, taken from Pacaud et al. (2007) with very little rephrasing: Spectra were extracted in a circular aperture around each source. The corresponding background emission was estimated within a surrounding annulus having inner radius large enough for the cluster contribution to be considered negligible. Preliminary modelling of the cluster surface brightness profile allowed the determination of the optimal extraction radii in terms of the S/N. The resulting spectra were fitted using XSPEC to a thermal plasma model (APEC) assuming a fixed hydrogen column density set to the Galactic value. The metal abundance of the gas was held fixed during the fitting process at 0.3 times the solar abundance. The cluster spectra were constructed imposing a minimum requirement of five background photons per bin in order to avoid the apparent bias we identified in XSPEC temperature estimates when using the Cash statistic on very sparse spectra. Our simulations showed that this procedure provides quite reliable temperature measurements (±10-20 per cent) for ∼13 keV clusters having only a few hundred counts. We further investigated the impact of fixing the metal abundance at 0.3 $Z_{\odot}$, by computing best-fitting temperatures obtained using extreme mean abundances of 0.1 and 0.6 $Z_{\odot}$. In most cases, the temperatures fell within the 1σ error bars from our initial fit.

R_{500} values of C1 clusters (conventionally defined as the radius within which the mean cluster mass density is 500 times the critical density of the Universe at the cluster redshift) were also derived in Pacaud et al. (2007) in order to compute the integrated X-ray luminosities within this radius. The R_{500} values were calculated using

$$\mathrm{R_{500}} = 0.375 \times \mathrm{T}^{0.63} \times \mathrm{h_{73}(z)^{-1}Mpc}, \tag{2.1}$$

where T is the ICM temperature in keV and h_{73} is the Hubble constant in units of 73 $\mathrm{kms^{-1}Mpc^{-1}}$. This formula was originally derived from M-T relation of Finoguenov, Reiprich & Böhringer (2001). The basic properties of C1 clusters are in Table 3.1 and their X-ray contours overlaid on optical images are in Appendix A.

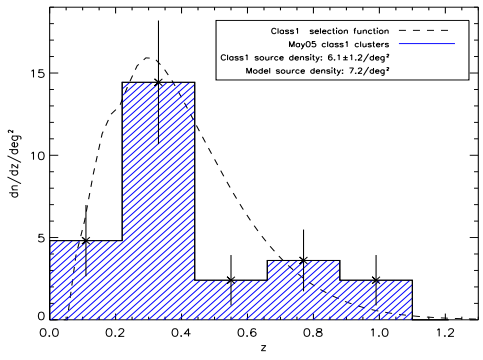

Figure 2.7: Redshift distribution of the observed C1 clusters. The dotted line corresponds to the predictions from a simple halo model in a ΛCDM cosmology, Pacaud et al. (2006).

2.7.2 Selection function of C1 clusters

Simulations provided the necessary basis for the computation of the selection functions of the XMM-LSS. These functions allow to derive detection probabilities as a function of source core radius and count rate for any exposure time, background level and position on the detector, see Fig. 2.8. The probability of detecting a cluster of a given flux and extent for any a Xmm-LSS pointing is derived by applying an analytic correction to the 10^4s simulations, scaling as a function of exposure time the signal-to-noise ratio (S/N) produced by such a cluster. The selection function for the XMM-LSS survey is obtained by integrating the contributions from all pointings.

The expected redshift distribution for both samples is shown in Fig. 2.7 where the results of the selection function are compared with the redshift distribution of the observed C1 clusters. The agreement is very satisfactory and the data suggest a deficit of clusters around a redshift of 0.5, probably induced by a cosmic void. The assumed cosmological model is a ΛCDM cosmology and a constant core radius of 180 kpc for the galaxy clusters.

2.8 Canada-France-Hawaii Telescope Legacy Survey (CFHTLS)

2.8.1 General description

A part of the sky are of the XMM-LSS is observed as an optical follow-up program by *Canada-France-Hawaii Telescope Legacy Survey* (CFHTLS). CFHTLS is a joint Canadian-French program to make e the Canada-France-Hawaii Telescope (CFHT) wide field imager and to address

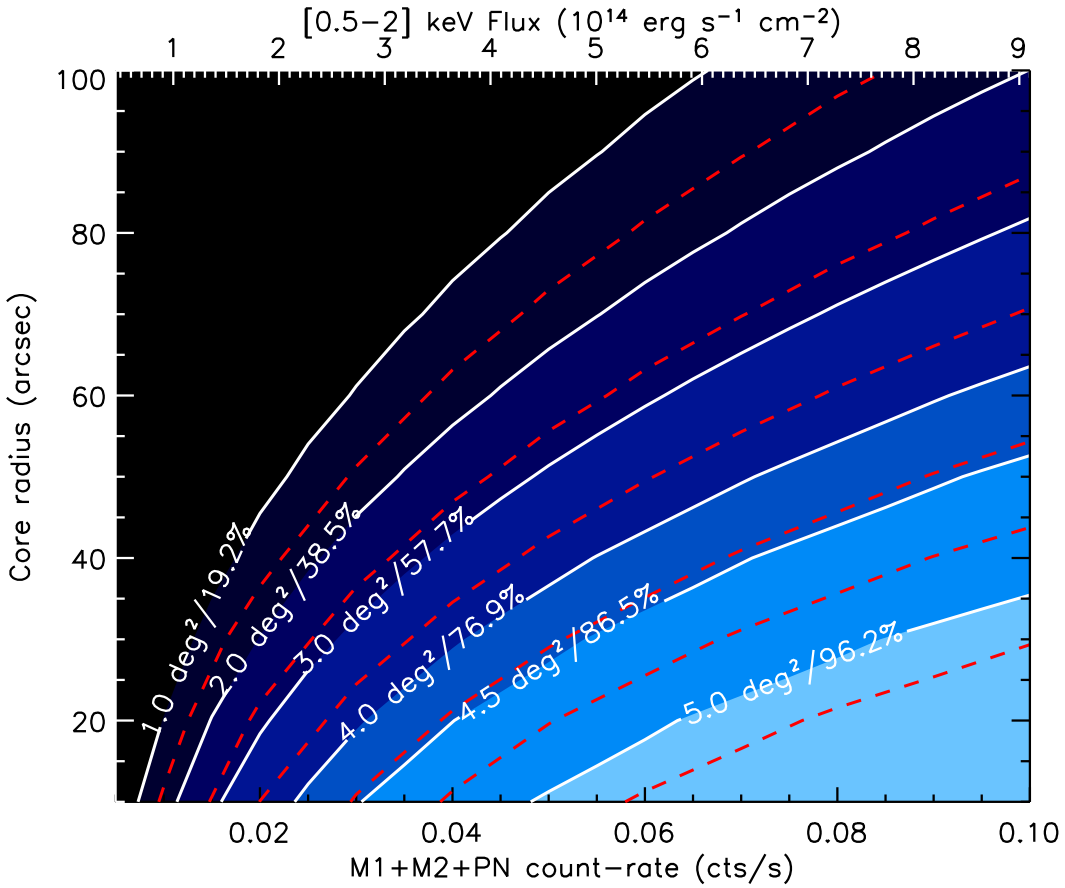

Figure 2.8: XMM-LSS coverage displayed in a two-dimensional parameter space: the sky coverage is a function of both cluster flux and extent. The dashed lines are the result of extensive 10-ks simulations. The slightly shifted white lines are the analytical corrections accounting for exposure variations across the surveyed area. Extent values correspond to the core radius of a β-model with $\beta = 2/3$. The count rate to flux conversion assumes a 2-keV spectrum at $z = 0$, Pacaud et al. (2007).

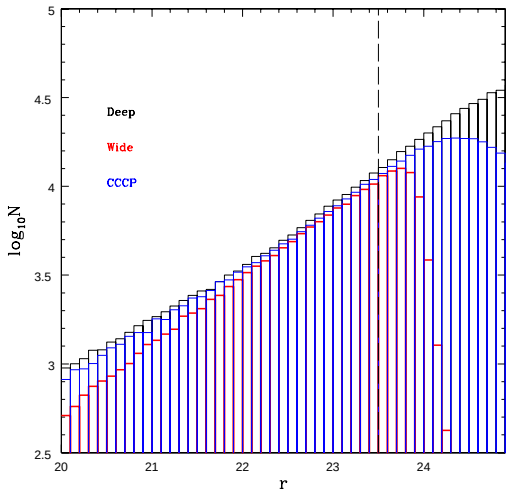

Figure 2.9: Number counts as a function of 3 arcsec diameter r-band magnitudes in representative Canadian Cluster Comparison Project (CCCP) and CFHTLS Wide Megacam fields are compared to number counts in representative CFHTLS Deep Megacam fields. The vertical dashed line indicates r = 23.5 and is the faintest magnitude employed in the following analysis, Urquhart et al. (2009).

a number of fundamental problems in astronomy. The CFHT, operational sine 1979, hosts a 3.6 meter optical and infrared telescope. The observatory is located atop the summit of Mauna Kea, a 4200 meter, dormant volcano located on the island of Hawaii.

Megaprime, equipped with *MegaCam*, the wide-field optical imaging facility at CFHT, was used to observe the XMM-LSS C1 clusters. MegaCam is consists of 362048 × 4612 pixel CCDs (a total of 340 megapixels), covering a full 1 degree × 1 degree field-of-view with a resolution of 0.187 arcsecond per pixel to properly sample the 0.7 arcsecond median seeing offered by the CFHT at Mauna Kea.

Of the 19 deg^2 of CFHTLS Wide data available in the W1 survey area (see Fig. 2.10), 4 deg^2 overlap with the sky area of the C1 clusters. 17 out of 29 C1 clusters were covered and observed by MegaCam in five passbands (u^*, g', r',i' and z') down to a nominal magnitude limit of $i' = 24.5$, see Fig. 2.9. For comparison, the magnitude limits (95% detection repeatability for point sources) of the Sloan Digital Sky Survey (SDSS) of $i' = 21.3$[10].

2.8.2 Reduction of the optical CFHTLS data

The data reduction of the optical survey is described in Hoekstra et al. (2006) and outlined here. The detrending (debiasing and flatfielding) was done using the Elixir pipeline developed

[10]http://www.sdss.org/dr7/

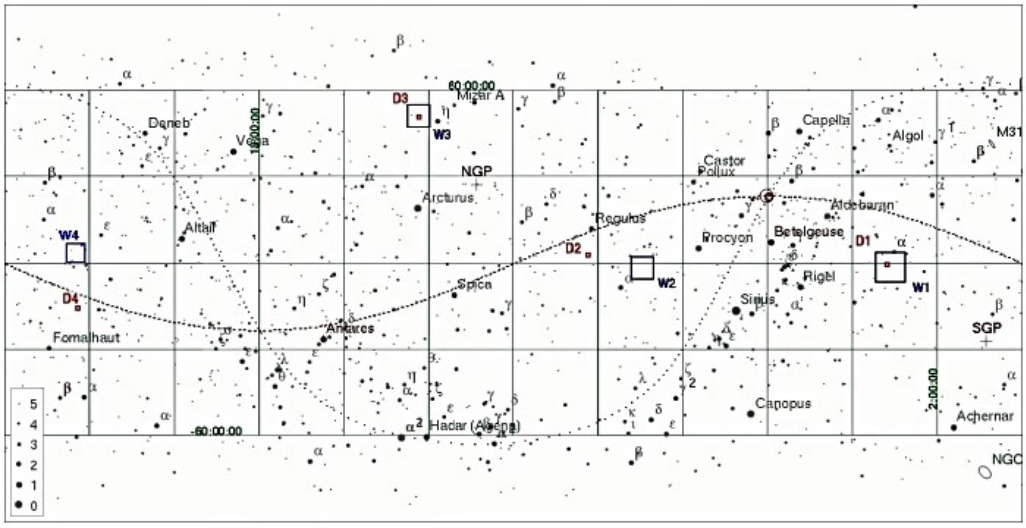

Figure 2.10: The four deep fields are spread across the year and their peak of visibility match roughly the following periods: D1/W1, D2/W2, D3/W3 and D4/W4.

at CFHT which also provided photometric zero points. The photometric calibrations were based on observations of standard stars during the observing run. The magnitudes of a large number of objects in the images were examined to check the stability of the photometric zero point and scale the images to the brightest image. the corrections were found to be small.

To refine the astrometry, Hoekstra et al. (2006) retrieved a red image from the second-generation Digital Sky Survey (POSS II) for each pointing and the astrometry of the POSS II image was calibrated using the USNO-A2 catalogue. SExtractor was used to generate catalogues of sources with accurate astrometry, with a number density significantly higher than the USNO-A2 catalogue. One of the advantages of the POSS II images is that they have been taken more recently, thus reducing the effects of proper motions of the stars.

Then the new astrometric catalogue is matched to each of the MegaCam images. The exposures have been taken with different offsets, in order to fill the gaps between the chips. The matched catalogues were combine for each exposure into a master catalogue, which contained the average positions of the matched objects. This master catalogue was used to derive the final second-order astrometric solution for each chip. This procedure ensured that in the overlapping area, the objects in each exposure are accurately matched to the same position. For more details on our method of data reduction of the optical catalogues, see section 4.2.2.

Chapter 3

Evolution of the X-ray Profiles of XMM-LSS C1 Clusters

In this chapter, a sample consisting of 27 X-ray-selected galaxy clusters from the X-ray Multi-Mirror Large-Scale Structure (XMMLSS) survey is used to study the evolution in the X-ray surface brightness profiles of the hot intracluster plasma. These systems are mostly groups and poor clusters, with temperatures 0.6-4.8 keV, spanning the redshift range 0.05 to 1.05. Comparing the profiles with a standard β-model motivated by studies of low-redshift groups, we find 54 per cent of our systems to possess a central excess, which we identify with a cuspy cool core. Fitting β-model profiles, allowing for blurring by the XMM point spread function, we investigate trends with both temperature and redshift in the outer slope (β) of the X-ray surface brightness, and in the incidence of cuspy cores. Fits to individual cluster profiles and to profiles stacked in bands of redshift and temperature indicate that the incidence of cuspy cores does not decline at high redshifts, as has been reported in rich clusters. Rather such cores become more prominent with increasing redshift. β shows a positive correlation with both redshift and temperature. Given the β-T trend seen in local systems, we assume that temperature is the primary driver for this trend. Our results then demonstrate that this correlation is still present at z $\gtrsim$ 0.3, where most of our clusters reside.

3.1 Introduction

Clusters of galaxies, as the largest virialised gravitationally-bound products of the process of hierarchical structure formation, are powerful probes for both testing cosmological models and tracing structural evolution (e.g. Voit 2005a). One of the most important properties of galaxy

clusters is their mass. Since cluster mass cannot be directly observed, it is studied indirectly through observables such as X-ray radiation emitted by the intracluster medium (ICM) which represents 80% of the total baryonic component of galaxy clusters at z=0 (Ettori et al. 2004a) and accounts for about 10% of the total (including dark) mass content of clusters (Sarazin 1986). The study of the ICM can provide important insights into the evolution and dynamics of cluster and their member galaxies.

Observationally, there are two distinct classes of clusters: cool core (CC) clusters with dense gaseous core regions in which gas temperature drops inwards, and non-cool core (NCC) clusters with shallower core profiles which often exhibit more internal structure (e.g., Jones & Forman 1984; Ota & Mitsuda 2004; Peres et al. 1998 and Schuecker et al. 2001). Cool core clusters have sharply peaked X-ray emission at their centres due to the rise in central gas density which accompanies the central cooling. However, the gas is not observed to cool to very low temperatures at the rates naively expected from the observed core X-ray luminosities, and a consensus has now emerged that this is due to the effects of feedback from a central active galactic nucleus, which limits the effects of cooling through processes which are still not very well understood. For reviews of cool cores in clusters, see for example, Fabian 1994, Donahue & Voit 2004 and Peterson & Fabian 2006.

In the local Universe, some studies have found that nearly two thirds of clusters have cool cores (e.g. Peres et al. 1998, White et al. 1997 and Vikhlinin et al. 2007). However, other studies gave different values: Edge, Stewart & Fabian (1992) found a CC fraction as high as 90%, while the results of Chen et al. (2007) indicated that 49% of local clusters host cool cores. These differences relate to both the selection of the cluster sample, and the way in which cool cores are identified within them.

The evolution of cooling within clusters provides an important probe of the history of cosmic feedback (Voit 2005a). At intermediate redshifts ($z \approx 0.15 - 0.4$), Bauer et al. (2005), using a sample of 38 X-ray-luminous clusters, found that cool cores appeared still to be common, with an incidence nearly identical to that in luminous low-redshift clusters. Consequently, they suggested that heating and cooling processes must have stabilised in massive clusters since $z \sim 0.4$.

At higher redshifts, Vikhlinin et al. (2007) reported that the fraction of clusters with cuspy X-ray cores dropped from ∼70% at $z \sim 0$ to ∼15% at $z > 0.5$. Santos et al. (2008) compared

the fraction of clusters with non-cool cores, moderate cool cores and strong cool cores in nearby ($0.143 \leq z \leq 0.3$) and high redshift ($0.7 \leq z < 1.4$) clusters. These authors detected a significant fraction of clusters harbouring moderate cool cores out to z=1.4, similar to the fraction in their low-redshift sample. However, they noticed an absence of clusters with strong-cool cores at redshift $z > 0.7$.

Regarding the spatial distribution of the ICM, Cavaliere & Fusco-Femiano (1976) introduced the β-model profile, motivated by the distribution expected for an isothermal plasma in hydrostatic equilibrium with a virialised mass distribution. Although it is now known that the gas is rarely isothermal, the β-model is generally found to give a reasonable representation of X-ray surface brightness profiles (e.g. Neumann & Arnaud 1999). However, an additional central component is usually required to fit the inner regions of CC clusters (e.g. Pratt & Arnaud 2002), and detailed studies of surface brightness profiles of clusters extending to large radii have shown that the logarithmic slope continues to increase slowly towards larger radii (e.g. Vikhlinin, Forman & Jones 1999, Croston et al. 2008 and Maughan et al. 2008). It is less clear whether this progressive steepening is also present in galaxy groups. For example, Rasmussen & Ponman (2004) traced the surface brightness out to R_{500} in two rich groups and found them to be well fitted by simple β-models the whole way.

For β-model fits, the β parameter, which characterises the outer slope of the surface brightness profile, has a value of $\approx 2/3$ for rich clusters (Jones & Forman 1984) and lower values for poor clusters and galaxy groups (Finoguenov, Reiprich & Böhringer 2001, Helsdon & Ponman 2000a and Horner et al. 1999). Several studies have shown that β has a mild positive trend with the average temperature of the ICM in nearby clusters (Vikhlinin, Forman & Jones 1999, Croston et al. 2008 and Maughan et al. 2008) and that the value in poorer galaxy groups is lower (i.e. flatter surface brightness slope) than that in clusters (Osmond & Ponman 2004). In terms of evolution, a study of Chandra data for 115 clusters spanning the range $0.1 < z < 1.3$ by Maughan et al. (2008) shows some indication that the β-T correlation is weaker for clusters at $z > 0.5$.

Low-mass galaxy clusters or groups, with ICM temperatures less than 2-3 keV, play an important role in the evolution of galactic systems because they lie at a transition between the field environment and rich cluster environments, and also because non-gravitational processes

have a larger impact in groups than in rich clusters (e.g., Zabludoff & Mulchaey 1998, Ponman, Sanderson & Finoguenov 2003 and Sun et al. 2009). However, these poor systems, and in particular the evolution of their properties, have received rather little attention. This is mainly due to the difficulty in detecting and studying them, especially at large redshifts, due to their faint X-ray emission and small complement of galaxies.

For these reasons, research on the evolution of galactic systems in the regime of groups and poor clusters has only started recently, as a result of improvements in observing capabilities in both the X-ray and optical. By comparing optically-selected systems at $0.3 \leq z \leq 0.55$ with nearby groups, Wilman et al. (2005a) showed that the fraction of group members undergoing significant star formation increases strongly with redshift out to $z \sim 0.45$. However, the study of X-ray selected groups by Jeltema et al. (2007) showed a contrary result: they did not observe significant evolution in the morphology or star formation of the galaxy populations in their $0.2 < z < 0.6$ groups compared to low-redshift X-ray luminous groups. They argued that this discrepancy could be due to different selection methods, since optically-selected systems are typically lower in mass and contain more spiral galaxies and therefore a stronger evolution in the galaxies is expected. They also found that their moderate redshift groups had galaxy populations similar to clusters at the same redshift; in particular, a large fraction of early-type galaxies and a low fraction of galaxies with significant star formation. However, in contrast to the situation in low redshift X-ray bright groups, a significant fraction of these intermediate redshift groups were found (Mulchaey et al. 2006, Jeltema et al. 2007) to have no bright early-type galaxy at the centre of the X-ray emission, or to have a central galaxy with multiple nuclei. This was taken as evidence for the dynamical youth of many of these groups.

The small number of studies which have addressed the evolution in the X-ray properties of galaxy groups have found little convincing evidence for any. Jeltema et al. (2006), in a multiwavelength study of six galaxy groups and poor clusters at intermediate redshift (0.2-0.6), found that they appear to follow the scaling relations between luminosity, temperature, and velocity dispersion defined by low-redshift groups and clusters. This is also true (Jeltema et al. 2009) for three higher redshift poor clusters from the AEGIS survey. A study of evolution in the L-T relation based on the present XMM-LSS cluster sample by Pacaud et al. (2007), taking into account the selection function of the survey, found that the range of models consistent with the

data included self-similar evolution, and also (marginally) a no-evolution model. Finoguenov et al. (2007) extracted a larger sample of 72 clusters (mostly poor ones) from the XMM-Newton observations of the COSMOS field, and found no evidence for evolution in the luminosity function of these systems out to $z \sim 1$, though the quality of their data did not permit them to study the morphology of the X-ray emission.

Motivated by the the paucity of information available for the evolution of the ICM in the important environment of low-mass galaxy clusters, we aim in this study to shed light on the spatial distribution of the ICM in X-ray selected clusters covering a wide redshift range ($z \sim 0-1$), paying special attention to trends in the slope and central cuspiness of the X-ray emission.

The chapter is constructed as follows: in section 3.2, we describe the data and briefly introduce the properties of the cluster sample; then we describe the data reduction used to produce X-ray surface brightness profiles. In section 3.3, we present our results, starting with the individual cluster profiles, and then profiles of redshift-stacked and temperature-stacked clusters. In section 3.4, we discuss the implication of our results and compare them with other studies. Finally, in section 3.5, we summarise our conclusions.

Throughout this chapter, we adopt the cosmological parameters from the five-year WMAP data presented by Hinshaw et al. (2009), namely: $H_0 = 70.5$ km s^{-1} Mpc^{-1}, $\Omega_m = 0.27$, $\Omega_\Lambda = 0.73$.

3.2 Data

3.2.1 The sample

Our sample is based on the 29 Class 1 (C1) clusters from the X-ray Multi-Mirror Large-Scale Structure (XMM-LSS) survey. The XMM-LSS C1 cluster sample is a well-controlled X-ray selected and spectroscopically confirmed cluster sample. The criteria used to select the members of this sample guarantee negligible contamination of point-like sources. The observations of the clusters were performed in a homogeneous way (10-20 ks exposures). For full details of the C1 sample, see Pacaud et al. (2007). Detailed information on the selection function of the C1 sample can be found in Pacaud et al. (2006).

The C1 sample is dominated by groups and poor clusters with temperatures of $0.63 \leq T \leq 4.80$

keV, spanning a redshift range $0.05 \leq z \leq 1.05$. Typically, we have a few hundreds X-ray counts for each cluster, with only a few having over a thousand detected photons. Two of the 29 clusters with less than 80 counts had to be excluded from our analysis because their data were inadequate for useful profiles to be extracted. The excluded clusters are XLSSC clusters 39 and 48. Hence our sample consists of 27 clusters. Cluster 47, with 81 counts, was a marginal case. We were unable to constrain a fit to its individual profile, but its data were included in the analysis of the stacked profiles. Key properties of the sample are presented in Table 3.1.

XLSSC number	R.A. (J2000)	Dec. (J2000)	Redshift	T (keV)	R_{500} (Mpc)	β Fitted $r_{\rm core}$	$r_{\rm core}/R_{500}$	β Fixed $r_{\rm core}$	Central Excess Factor (f_c)	Counts
11	36.5413	-4.9682	0.05	0.64	0.290	$0.45^{+0.03}_{-0.02}$	$0.08^{+0.03}_{-0.03}$	$0.47^{+0.01}_{-0.02}$	1.14 ± 0.14	795
52	36.5681	-2.6660	0.06	0.63	0.285	$0.69^{+0.07}_{-0.05}$	$0.14^{+0.03}_{-0.02}$	$0.62^{+0.02}_{-0.01}$	0.95 ± 0.09	561
21	36.2345	-5.1339	0.08	0.68	0.297	$0.65^{+0.27}_{-0.09}$	$0.04^{+0.03}_{-0.02}$	$1.34^{+0.29}_{-0.22}$	1.04 ± 0.12	87
41	36.3777	-4.2391	0.14	1.34	0.440	$0.47^{+0.02}_{-0.01}$	$0.05^{+0.02}_{-0.01}$	$0.51^{+0.01}_{-0.01}$	1.70 ± 0.22	656
50	36.4233	-3.1895	0.14	3.50	0.804	$0.78^{+0.06}_{-0.05}$	$1.12^{+0.10}_{-0.09}$	$0.37^{+0.01}_{-0.01}$	0.59 ± 0.07	4387
35	35.9507	-2.8588	0.17	1.20	0.394	$0.44^{+0.05}_{-0.04}$	$0.13^{+0.07}_{-0.06}$	$0.42^{+0.02}_{-0.02}$	0.67 ± 0.37	422
25	36.3531	-4.6776	0.26	2.00	0.533	$0.58^{+0.05}_{-0.04}$	$0.07^{+0.02}_{-0.02}$	$0.65^{+0.03}_{-0.02}$	1.42 ± 0.18	683
44	36.1411	-4.2347	0.26	1.30	0.399	$1.37^{+4.48}_{-0.61}$	$0.63^{+0.25}_{-0.31}$	$0.50^{+0.03}_{-0.02}$	1.02 ± 0.41	276
51	36.4982	-2.8265	0.28	1.20	0.518	$1.81^{+***}_{-0.84}$	$0.77^{+0.12}_{-0.31}$	$0.47^{+0.05}_{-0.03}$	2.18 ± 1.09	160
22	36.9165	-4.8576	0.29	1.70	0.471	$0.57^{+0.02}_{-0.02}$	$0.04^{+0.01}_{-0.01}$	$0.71^{+0.02}_{-0.02}$	1.46 ± 0.16	1234
27	37.0143	-4.8510	0.29	2.80	0.653	$0.70^{+0.16}_{-0.10}$	$0.40^{+0.13}_{-0.10}$	$0.45^{+0.02}_{-0.01}$	0.86 ± 0.23	653
8	36.3370	-3.8015	0.30	1.30	0.396	$0.53^{+0.11}_{-0.07}$	$0.04^{+0.04}_{-0.03}$	$0.67^{+0.08}_{-0.06}$	1.54 ± 0.47	160
28	35.9878	-3.0991	0.30	1.30	0.399	$0.43^{+0.08}_{-0.05}$	$0.08^{+0.09}_{-0.06}$	$0.45^{+0.04}_{-0.04}$	3.65 ± 1.42	245
13	36.8586	-4.5380	0.31	1.00	0.340	$0.58^{+1.25}_{-0.14}$	$0.06^{+0.20}_{-0.05}$	$0.73^{+0.20}_{-0.12}$	1.54 ± 1.01	120
18	36.0087	-5.0904	0.32	2.00	0.521	$0.94^{+0.76}_{-0.22}$	$0.19^{+0.14}_{-0.06}$	$0.68^{+0.04}_{-0.04}$	1.02 ± 0.27	89
40	35.5272	-4.5431	0.32	1.60	0.442	$0.44^{+0.04}_{-0.02}$	$0.01^{+0.02}_{-0.01}$	$0.55^{+0.05}_{-0.04}$	2.70 ± 0.74	223
10	36.8435	-3.3623	0.33	2.40	0.574	$0.57^{+0.08}_{-0.05}$	$0.08^{+0.05}_{-0.03}$	$0.61^{+0.03}_{-0.02}$	1.94 ± 0.35	327
23	35.1894	-3.4328	0.33	1.70	0.457	$0.54^{+0.03}_{-0.03}$	$0.05^{+0.01}_{-0.01}$	$0.65^{+0.03}_{-0.03}$	1.19 ± 0.27	394
6	35.4385	-3.7715	0.43	4.80	0.838	$0.68^{+0.03}_{-0.03}$	$0.19^{+0.02}_{-0.02}$	$0.570^{+0.003}_{-0.011}$	0.84 ± 0.09	1394
36	35.5280	-3.0539	0.49	3.60	0.676	$0.60^{+0.06}_{-0.04}$	$0.08^{+0.03}_{-0.02}$	$0.67^{+0.03}_{-0.02}$	1.37 ± 0.22	481
49	35.9892	-4.5883	0.49	2.20	0.493	$2.20^{+***}_{-0.92}$	$0.38^{+0.04}_{-0.13}$	$0.67^{+0.06}_{-0.05}$	1.59 ± 0.55	157
1	36.2367	-3.8131	0.61	3.20	0.584	$0.62^{+0.05}_{-0.04}$	$0.11^{+0.02}_{-0.02}$	$0.62^{+0.02}_{-0.02}$	2.25 ± 0.30	595
2	36.3844	-3.9200	0.77	2.80	0.493	$0.83^{+0.57}_{-0.18}$	$0.09^{+0.08}_{-0.04}$	$0.92^{+0.14}_{-0.11}$	3.03 ± 0.68	136
47	35.5461	-2.6783	0.79	3.90	0.592					81
3	36.9098	-3.2996	0.84	3.30	0.518	$0.48^{+0.05}_{-0.04}$	$0.03^{+0.02}_{-0.02}$	$0.64^{+0.07}_{-0.05}$	1.15 ± 0.54	193
5	36.7854	-4.3003	1.05	3.70	0.489	$2.42^{+***}_{-1.33}$	$0.33^{+0.05}_{-0.17}$	$0.80^{+0.13}_{-0.09}$	2.46 ± 0.94	130
29	36.0172	-4.2251	1.05	4.10	0.524	$0.76^{+0.37}_{-0.16}$	$0.11^{+0.08}_{-0.05}$	$0.76^{+0.07}_{-0.06}$	1.86 ± 0.59	233

Table 3.1: List of the properties of the C1 galaxy clusters sample sorted according to their redshifts (Pacaud et al. 2007) with the fitted parameters of the 26 successfully constrained clusters. The β and $r_{\rm core}$ values in the seventh and eighth columns are for the the β-model with both $r_{\rm core}$ and β freely fitted. The β values in the ninth column are for the β-model with fixed $r_{\rm core}$=0.105 $\times$ R_{500}. All errors are 1σ errors. Clusters 47 failed to converge but its data were not excluded from the stacked analysis. The central excess factor, f_c (tenth column), is calculated by dividing the observed surface brightness by the predicted surface brightness (from the fitted model) for the innermost radial bin, that is 0.05 $\times$ R_{500}. If f_c is greater than 1 then this is considered as an indication that the cluster has a cool core and vice versa. The stars (***) denote unconstrained errors.

3.2.2 Data analysis

To construct the X-ray surface brightness profiles for each cluster, we used three X-ray FITS images, three exposure maps and one segmentation map, all produced using the production pipe line described in Pacaud et al. (2006). The images were taken by the MOS1, MOS2 and PN imagers on board the XMM-Newton satellite in the energy band [0.5-2.0] keV with exposure times ranging from 10 to 20 ks. The exposure maps are FITS images containing the vignetting-corrected exposure of the clusters as a function of the sky position. A single segmentation map, generated by SExtractor was used for each cluster to remove contaminating sources.

The right ascension (RA) and declination (Dec) values of the centres were determined as outlined in Pacaud et al. (2006). But when we examined the X-ray profiles of the clusters, some showed dips at the centre. For these clusters, we mosaicked the three images, smoothed the resulting image and took the coordinates of the pixel with the maximum photon counts and modified the cluster centre accordingly. The modified centres at most are only ∼14 arcseconds from the original values but remove the central dips in the profiles. The clusters with modified centres have XLSSC numbers: 50,28,40,1,47 and 5. The RAs and Decs in Table 3.1 are the modified centres and the original coordinates can be found in Table 1 in Pacaud et al. (2007).

Since the angular size of our clusters is small, background removal using a local estimate works well. The background was taken from an annulus extending from $2\times R_{500}$ to $3\times R_{500}$ about each cluster, where R_{500} is the radius within which the mean cluster mass density is 500 times the critical density of the Universe at the cluster redshift. As in Pacaud et al. (2007), the R_{500} values were calculated using

$$R_{500} = 0.388 \times T^{0.63} \times h_{70.5}(z)^{-1}\mathrm{Mpc}, \tag{3.1}$$

where T is the ICM temperature in keV and $h_{70.5}$ is the Hubble constant in units of 70.5 $\mathrm{kms}^{-1}\mathrm{Mpc}^{-1}$. This formula was originally derived from M-T relation of Finoguenov, Reiprich & Böhringer (2001).

Two background components were evaluated: the photon background component and the particle background component. These were separated using the fact that photons are vignetted, whilst particles are not. Hence the relationship between count rate and effective area for pixels in the background annulus gives an estimate of the photon background component from the slope, and of the particle background component from the intercept.

Surface brightness profiles were extracted from a standard set of annuli (as a fraction of R_{500} to facilitate later stacking), extending to $3\times R_{500}$. For each annulus we removed the particle background and computed the the vignetting-corrected count rate (in ct/s/pix) and its error. The MOS1, MOS2 and PN profiles, generated in this way were then combined, and their errors added in quadrature. Profiles were extracted up to $3\times R_{500}$ where they flattened and reached the photon background values. The final column in Table 3.1 is the total X-ray counts within $3\times R_{500}$ after subtracting from it both the photon and the particle background.

The X-ray cameras on the XMM-Newton satellite have a point spread function (PSF) of ~ 6 arcsec FWHM, see Strüder et al. (2001) and Turner et al. (2001). Correction for PSF blurring is important to avoid biased estimation of the parameters of the cluster's radial profile, especially, the core radius, $r_{\rm core}$. We applied the PSF correction method used by Arnaud et al. (2002) (and described in detail therein) which analytically computes a photon redistribution matrix (RDM) based on the properties of the three XMM-Newton cameras and depends on the energy band used and off-axis angle between the centre of the camera and the cluster position. The PSF matrices for the three cameras were weighted by the source counts in each camera and combined to produce a matrix appropriate to the coadded profiles.

We fitted the surface brightness profile with a β-model (Cavaliere & Fusco-Femiano 1976)

$$S(r) = S_0(1 + (r/r_{\rm core})^2)^{-3\beta+0.5}, \tag{3.2}$$

where S_0 is central brightness (cts/s/pix) and $r_{\rm core}$ is the core radius (in units of R_{500}). The model was blurred with the PSF redistribution matrix, and fitted to the surface brightness data. The best values of $r_{\rm core}$ and β were estimated by computing the minimum χ^2 value on an adaptively refined $r_{\rm core}$–β grid. 1σ errors were computed for $r_{\rm core}$ and β, and 1σ, 2σ and 3σ error regions computed in the $r_{\rm core}$–β plane for each fit.

As will be seen below, a number of systems show a central excess above the fitted β-model. Such a central cusp suggests the possible presence of a cool core. Since a central excess may distort the β-model fit, we attempted to fit a model with the central bin excluded, but given the limited statistical quality of our data, loss of the central bin resulted in poorly behaved fits in many cases. We therefore adopted the approach of fitting a β-model with core radius fixed at a value (as a fraction of R_{500}) motivated by the observed profiles of local groups in which detailed modelling of the surface brightness has been possible. A central excess above this model then

indicates the presence of a cuspy core.

The fixed value of the core radius we adopt as a canonical value for poor clusters is taken from Helsdon & Ponman (2000a), who studied 24 X-ray-bright galaxy groups. For half of their sample they found that two-component β-models were required to give acceptable fits to the surface brightness distribution. The outer component represented the intragroup gas, whilst core emission could be distinguished by a clear shoulder in the profile in many cases, and was fitted by the inner β-model component. The median value of $r_{\rm core}$ for the outer component in the 12 clusters was found to be 60 kpc. Correcting to our value of H_0, this median $r_{\rm core}$ would be 42.6 kpc. The 12 systems in Helsdon & Ponman (2000a) had an average temperature of 1.07 keV. To calculate this $r_{\rm core}$ as a fraction of R_{500}, we used the $R_{500}(T)$ equation above, which gives $r_{\rm core}$=0.105 $\times$ $\rm R_{500}$. This value of $r_{\rm core}$ was therefore used in our fixed-core fits.

To quantitatively determine whether a profile of a cluster (or a stacked set of clusters) has a central brightness excess, and therefore a CC, we define the central excess factor (f_c) as the ratio between the observed surface brightness and predicted surface brightness (from the fitted fixed-core model) for the innermost radial bin, at $r = 0.05\times$ $\rm R_{500}$. If f_c is greater than 1 then this was considered as an indication that the cluster has a CC and vice versa. The error on f_c is derived simply from the error on the innermost surface brightness value. We checked the effects of excluding the central bin for the fixed-core fits. This has little effect on the fitted β value, but in cases where there is a central excess, it results in a somewhat lower normalisation for the fitted model, and hence a slightly (up to 10%) higher value of f_c.

3.2.3 Stacked profiles

The statistical quality of our individual profiles is limited, so we stacked the observed profiles of clusters with similar redshifts and temperatures, producing higher quality profiles which might highlight any trends with temperature or redshift.

Since each cluster has a different $\rm R_{500}$, we extracted the profiles in fixed radial bins in units of $\rm R_{500}$ up to 3$\times\rm R_{500}$. The range from (0-1)$\times\rm R_{500}$ was divided into 20 equally spaced bins, from (1-2)$\times\rm R_{500}$ into 15 equally spaced bins and the range from (2-3)$\times\rm R_{500}$ into 10 equally spaced bins. These different bin widths allow for the decline in flux with radius whilst keeping the inner bins sufficiently fine to resolve the core. This distribution of bins was chosen after some

experimentation to obtain the best fit constraints.

Before the stacking, the profiles were multiplied by the scale factor:

$$\frac{1}{A \times B \times C}, \tag{3.3}$$

where

$$A = \mathrm{R}_{500} \tag{3.4}$$

to account for the cluster line of sight depth,

$$B = \left(\frac{\rho_c(z)}{\rho_c(z=0)} \right)^2 \tag{3.5}$$

to correct for the change in critical density of the Universe and

$$C = (1+z)^{-4} \tag{3.6}$$

to eliminate the effect of cosmological dimming. The aim of the scaling is to allow for the effects of variable cluster depth and for cosmological factors, so that all profiles would be similar (to within the rather weak temperature dependence of the X-ray emissivity) in the case where clusters are simple self-similar systems, evolving with the critical density of the Universe.

The profiles for each component cluster were then added bin by bin and their errors quadratically summed to generate a stacked profile. The photon background values for each cluster were scaled by the same factors as the source profiles, before being combined. This coadded photon background was then included in the fitted model as a fixed background level. The PSF redistribution matrices were weighted by the scaled count rate for each cluster before being combined to produce a composite matrix.

3.3 Results

3.3.1 X-ray surface brightness profiles of individual C1 clusters

Most individual C1 clusters profiles fit successfully with a free–r_{core} β-model, and nearly all have well-constrained fixed–r_{core} β-model fits. The profile of cluster 47, with only 81 counts, is the only one for which we could not achieve a useful β-model fit. For clusters 51 (160 counts), 49 (157 counts) and 5 (130 counts), although best fit models were obtained, the upper bound of the free–r_{core} β values were not constrained, and no r_{core}–β contour plots could be produced.

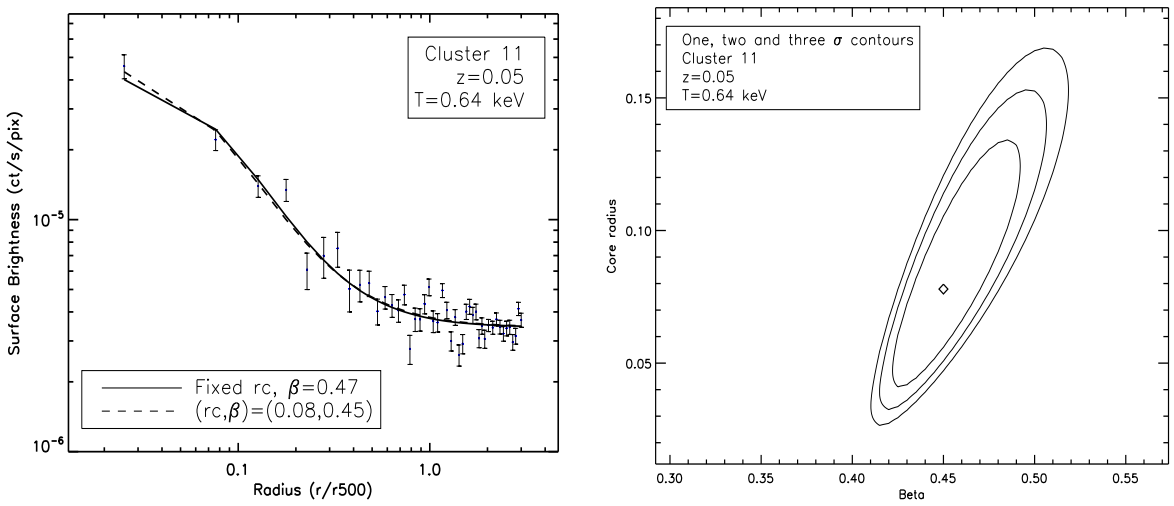

(a) Cluster 11

Figure 3.1: X-ray surface brightness profiles of the individual C1 clusters with redshift $0.05 \leq z \leq 0.17$, ordered according to redshift and the associated $1\sigma, 2\sigma$ and 3σ contours. The dashed lines are the fitted β-model profiles with both $r_{\rm core}$ and β freely fitted, while the solid lines are for the fitted profiles with free β and $r_{\rm core}$ fixed to $0.105 \times {\rm R}_{500}$.

The surface brightness profiles with fits and associated 1σ, 2σ and 3σ error contours for individual clusters with redshift ranges 0.05-0.17, 0.26-0.33 and 0.43-1.05 are shown in Fig. 3.1, 3.2 and 3.3 respectively, and numerical results are given in Table 3.1. The profile of cluster 50 is unusual; it has a remarkably large $r_{\rm core}$ value, of $1.12\times{\rm R}_{500}$ (see Fig. 3.1), and an elongated spatial extension indicating a cluster in a state of merging, with a highly unrelaxed core.

Amongst the 26 clusters with constrained fixed-$r_{\rm core}$ fits, 21 (81%) possess CCs according to the criterion outlined above (i.e. $f_c > 1$), whilst the remaining five (19%) are non-cool core (NCC) ($f_c < 1$) systems, as shown in Table 3.1. However, for some of these, the classification must be regarded as uncertain, since the error bar on f_c crosses unity. This is the case for 7 (from the 21) CC systems, and 2 (of the five) NCC clusters. Hence, at the 1σ level, 54% (14 out of 26) of our clusters show a central excess in surface brightness which may indicate the presence of a cool core.

The median value of β for free-$r_{\rm core}$ fits to the 26 clusters is 0.61. A similar median value (β=0.63) is obtained from the fixed–$r_{\rm core}$ fits. As for the $r_{\rm core}$, its median value is $0.08\times{\rm R}_{500}$. As expected, this is rather smaller than the canonical value of $0.105\times{\rm R}_{500}$ for the group scale component of the emission, due to the influence on the fits of cuspy cores in many systems.

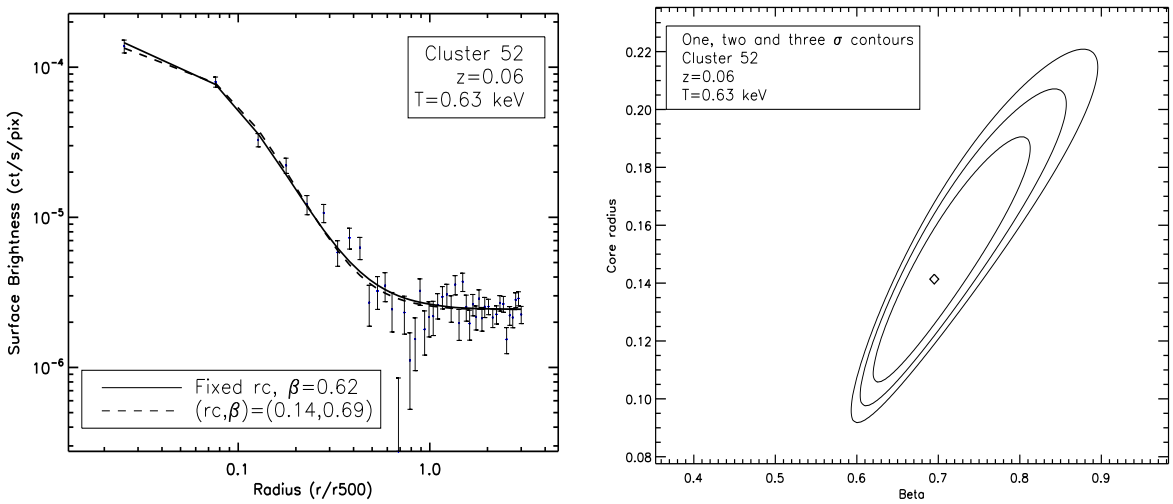

(b) Cluster 52

Figure 3.1: (*continued*)

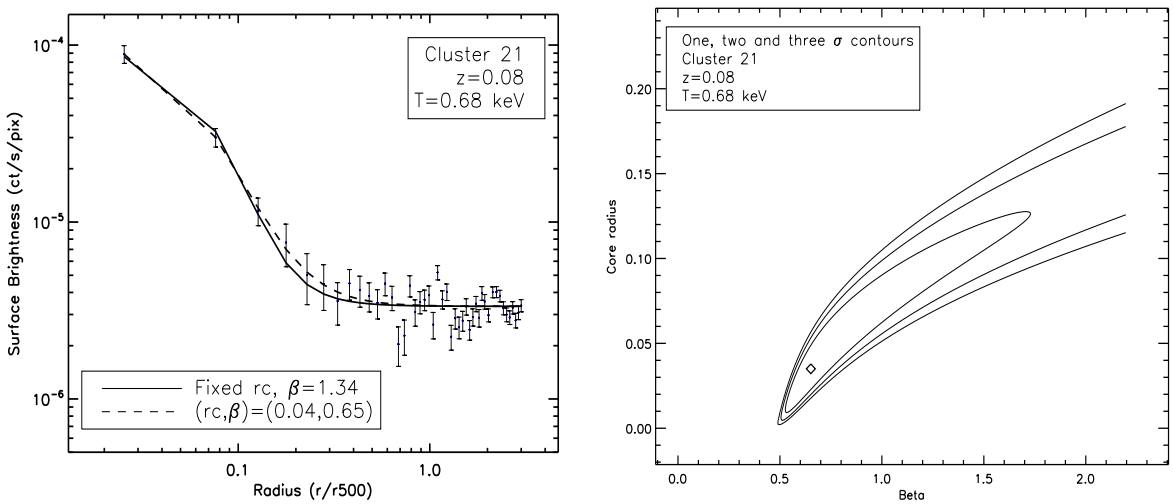

(c) Cluster 21

Figure 3.1: (*continued*)

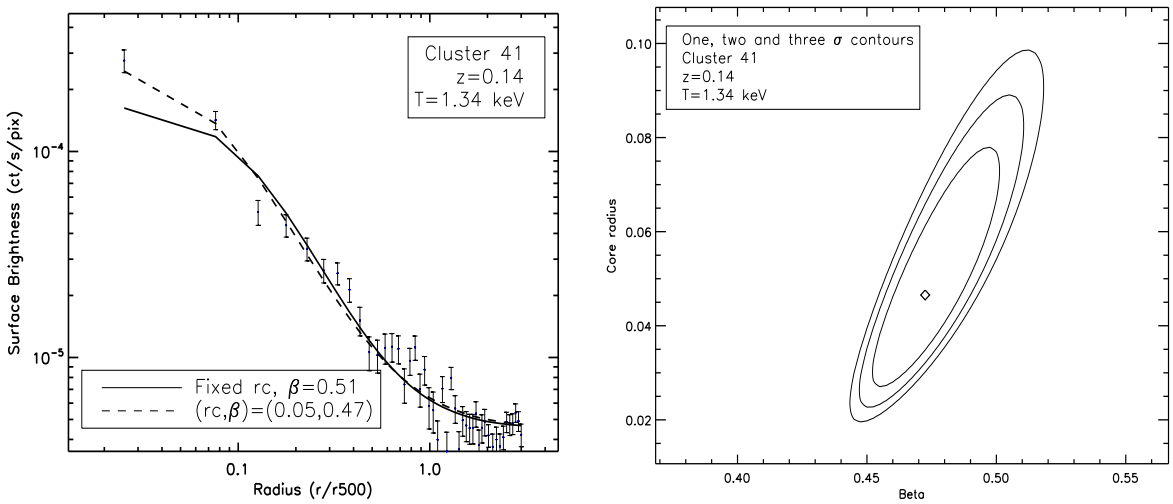

(d) Cluster 41

Figure 3.1: (*continued*)

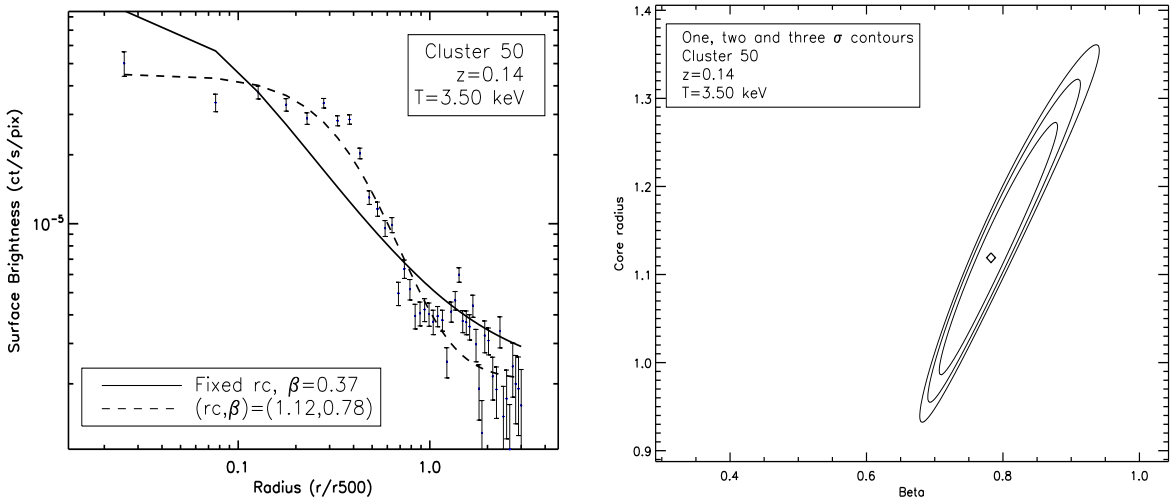

(e) Cluster 50

Figure 3.1: (*continued*)

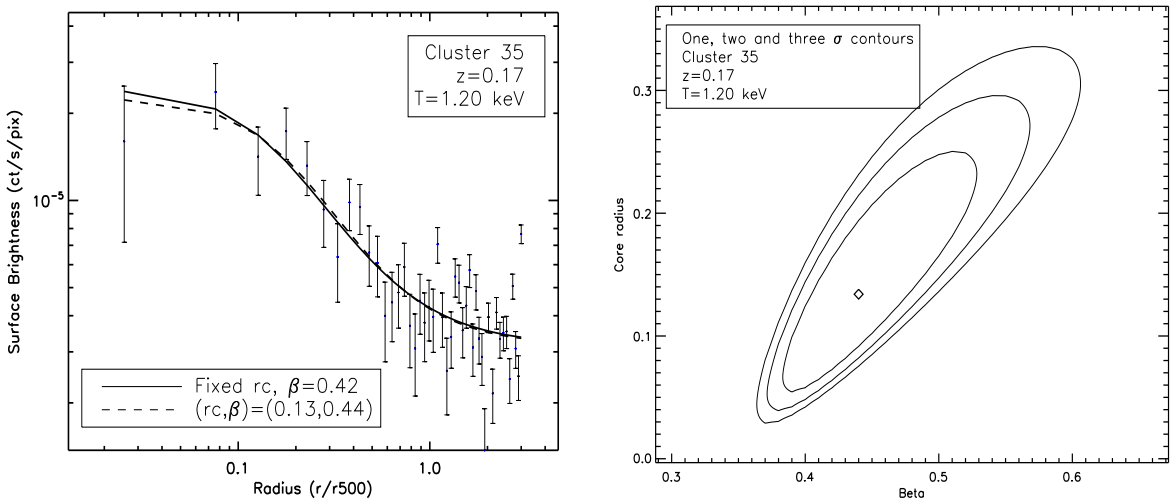

(f) Cluster 35

Figure 3.1: (*continued*)

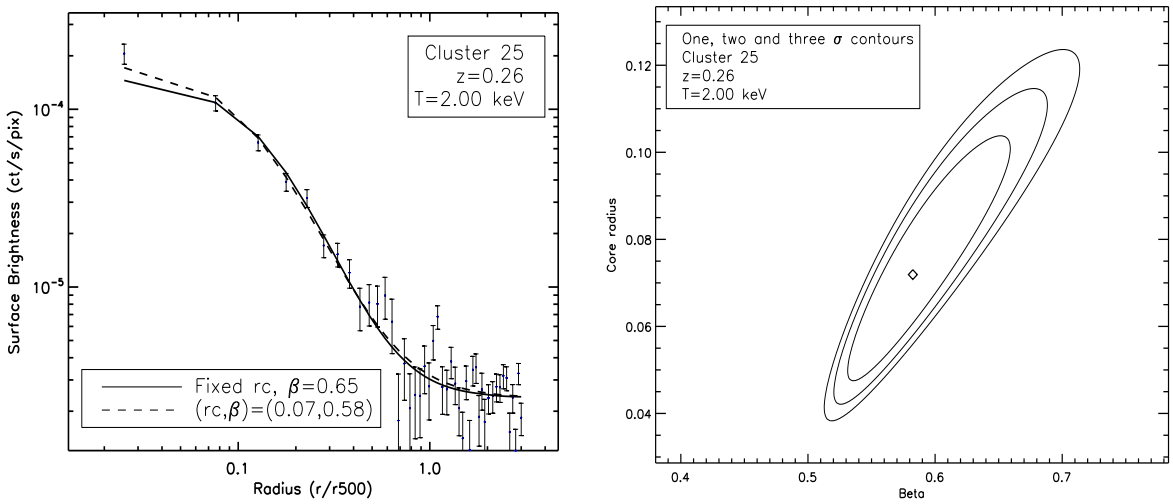

(a) Cluster 25

Figure 3.2: X-ray surface brightness profiles of the individual C1 clusters with redshift $0.26 \leq z \leq 0.33$, ordered according to redshift and the associated constrained $1\sigma, 2\sigma$ and 3σ contours. The dashed lines are the fitted β-model profiles with both $r_{\rm core}$ and β freely fitted, while the solid lines are for the fitted profiles with free β and $r_{\rm core}$ fixed to $0.105 \times \mathrm{R}_{500}$.

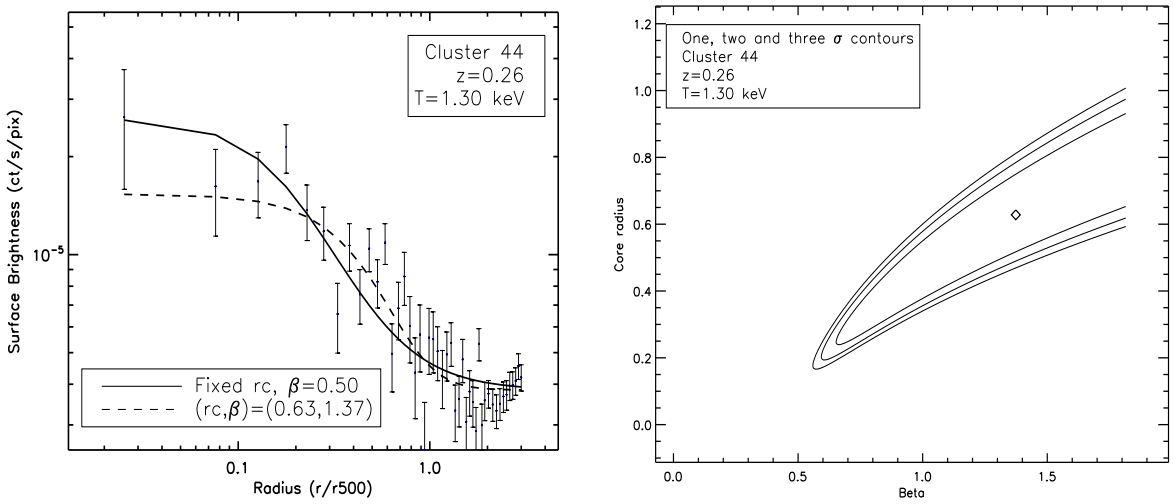

(b) Cluster 44

Figure 3.2: (*continued*)

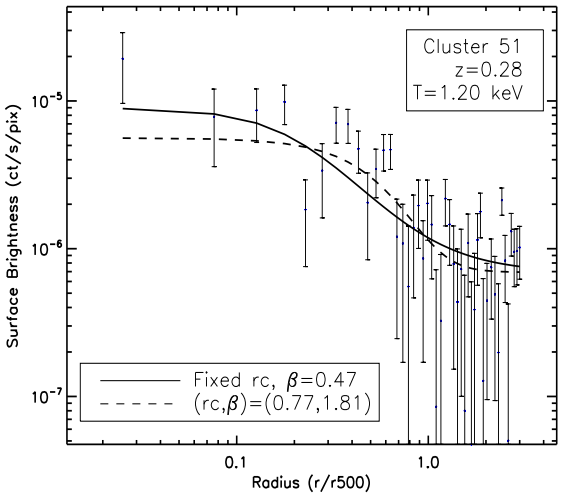

(c) Cluster 51

Figure 3.2: (*continued*)

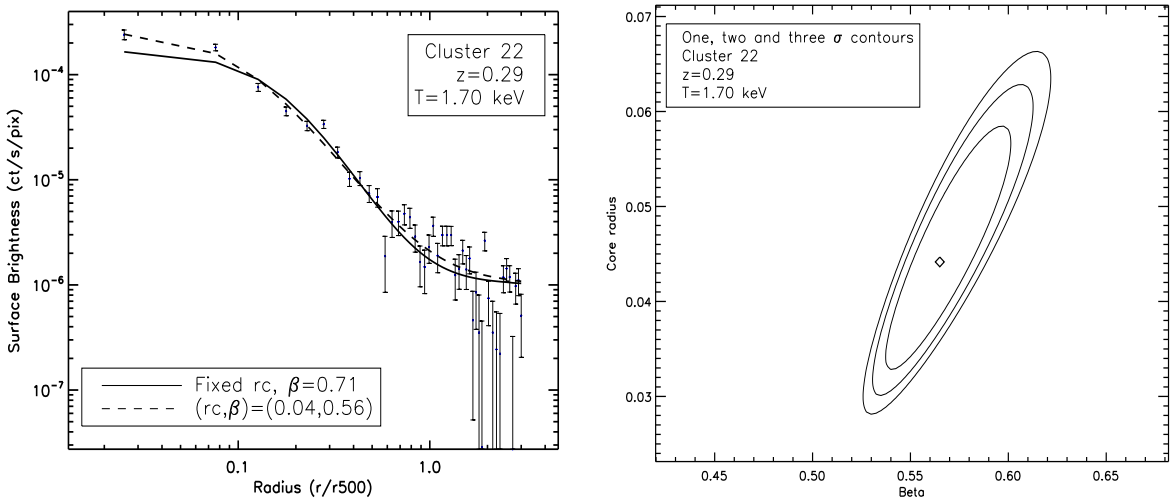

(d) Cluster 22

Figure 3.2: (*continued*)

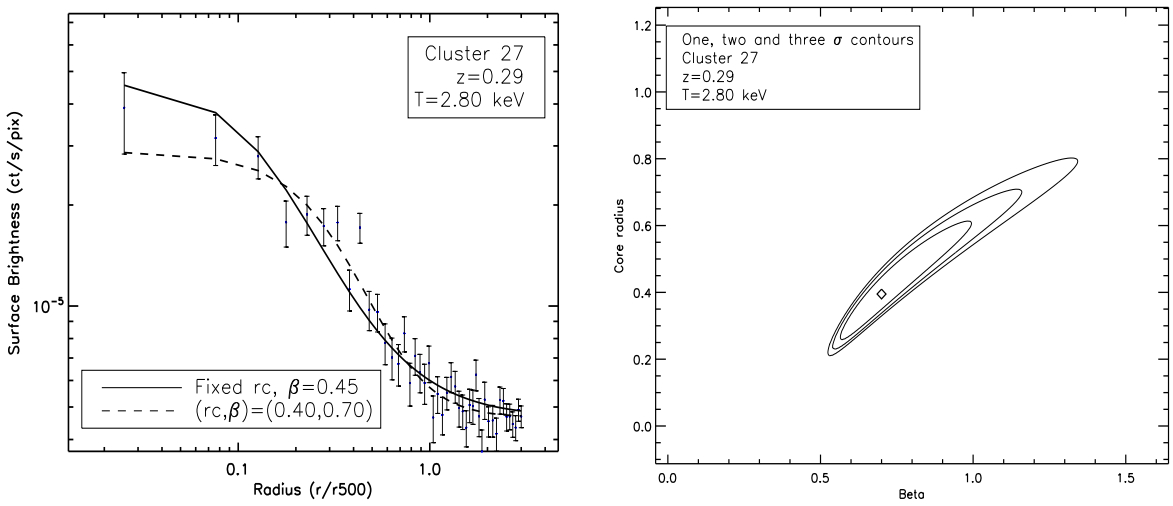

(e) Cluster 27

Figure 3.2: (*continued*)

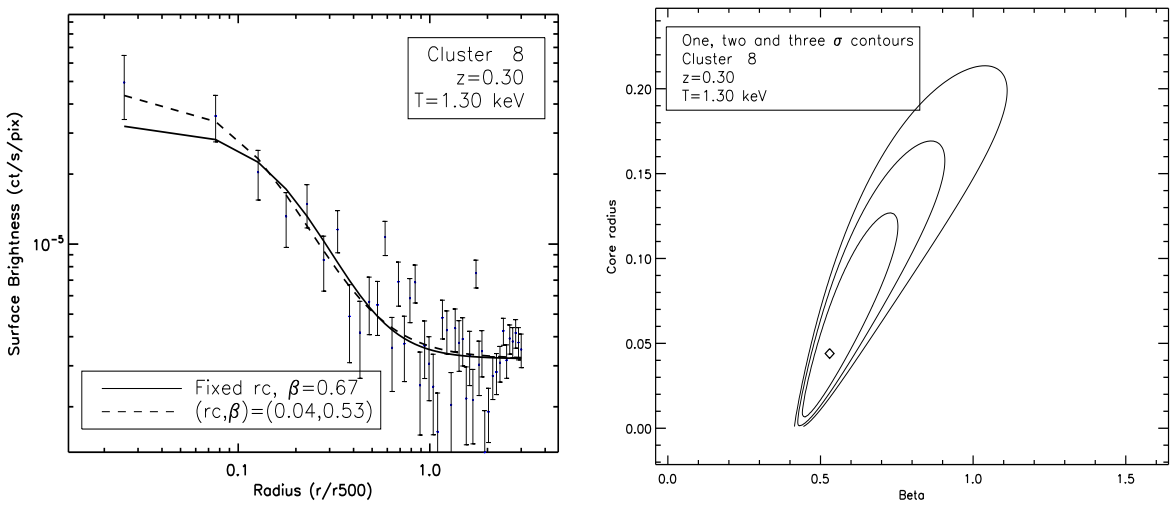

(f) Cluster 8

Figure 3.2: (*continued*)

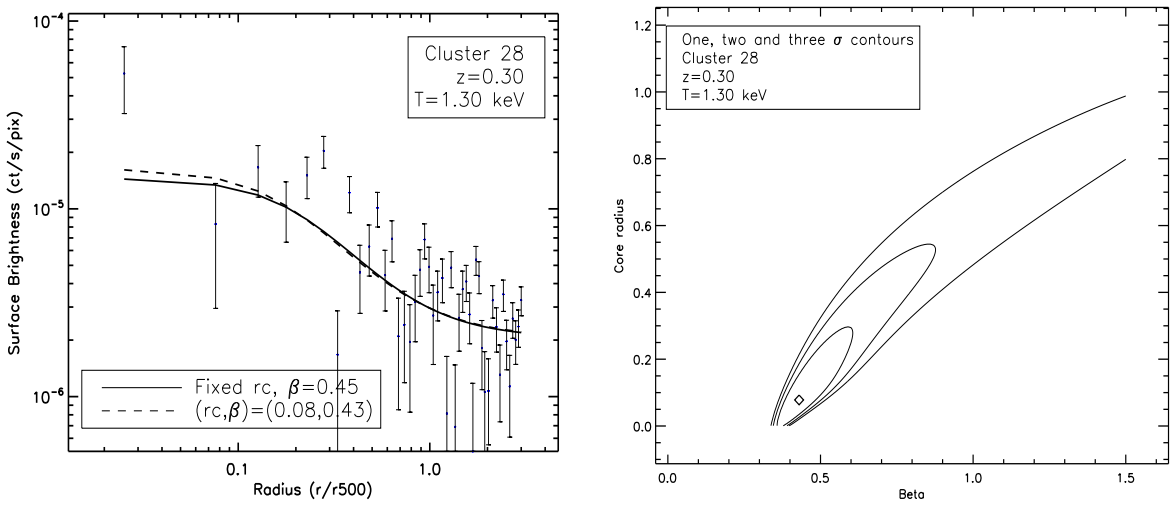

(g) Cluster 28

Figure 3.2: (*continued*)

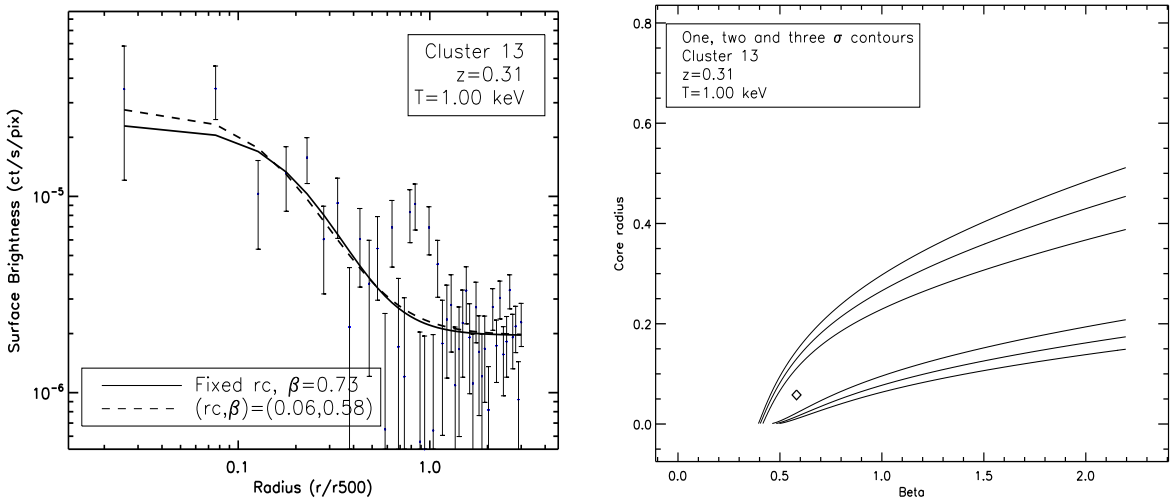

(h) Cluster 13

Figure 3.2: (*continued*)

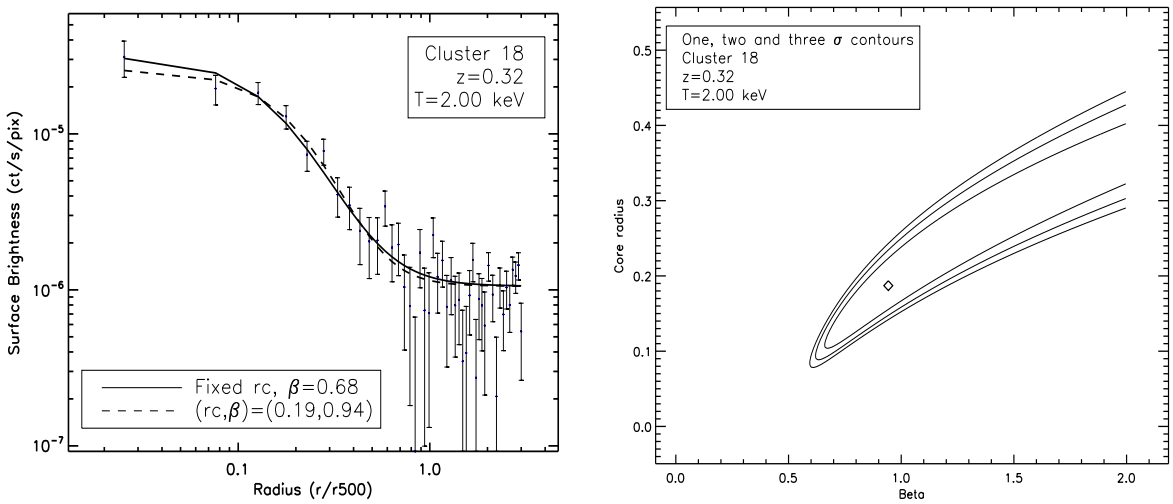

(i) Cluster 18

Figure 3.2: (*continued*)

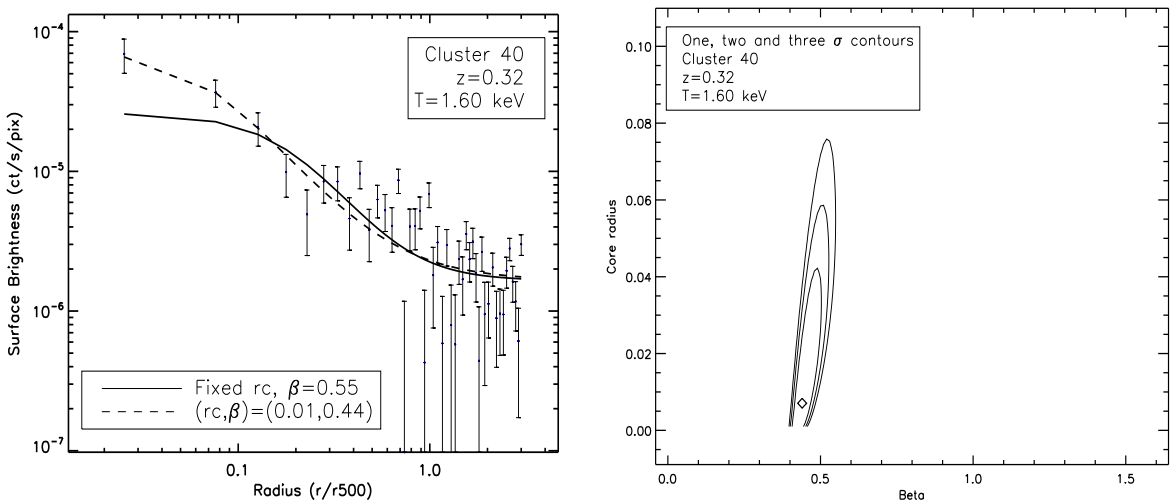

(j) Cluster 40

Figure 3.2: (*continued*)

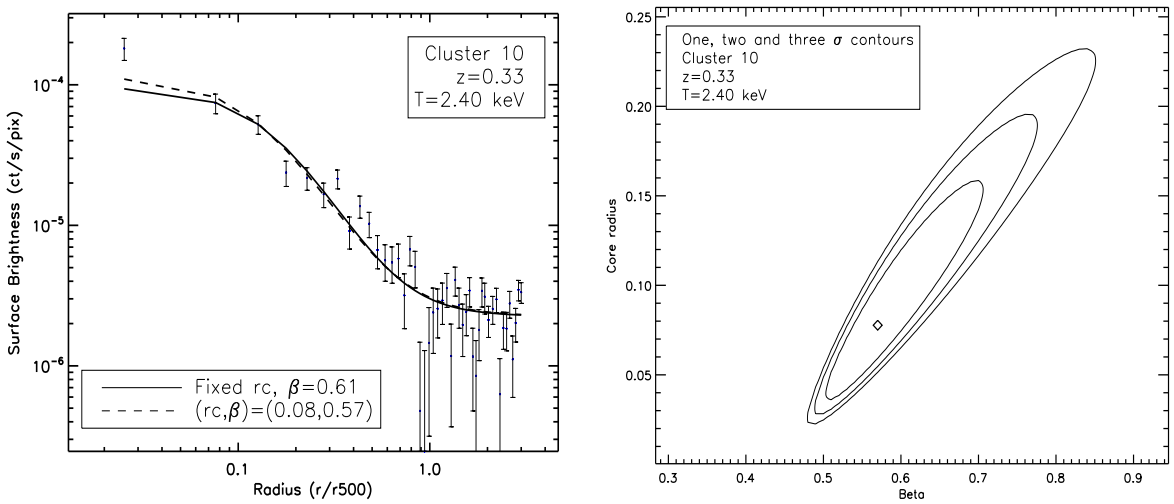

(k) Cluster 10

Figure 3.2: (*continued*)

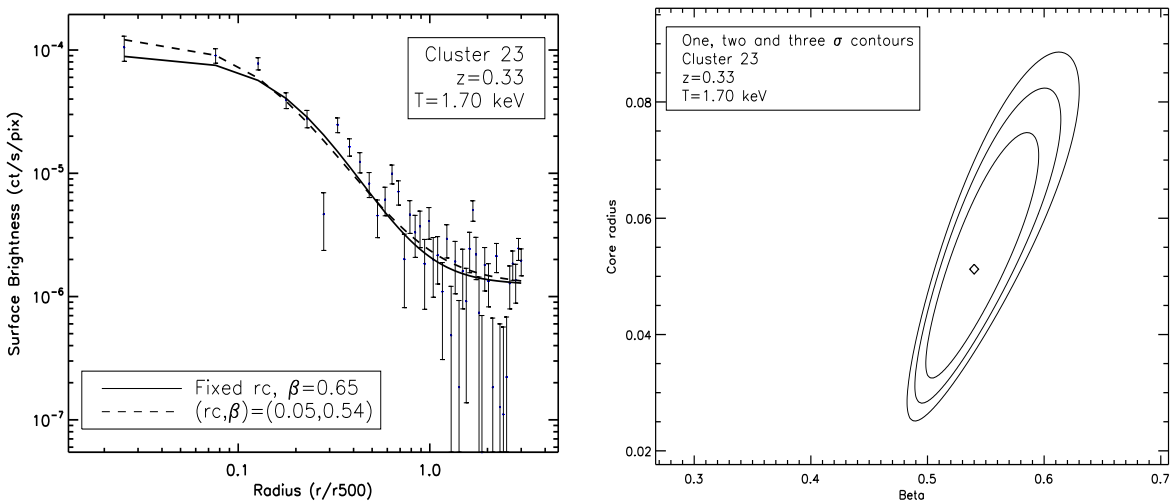

(l) Cluster 23

Figure 3.2: (*continued*)

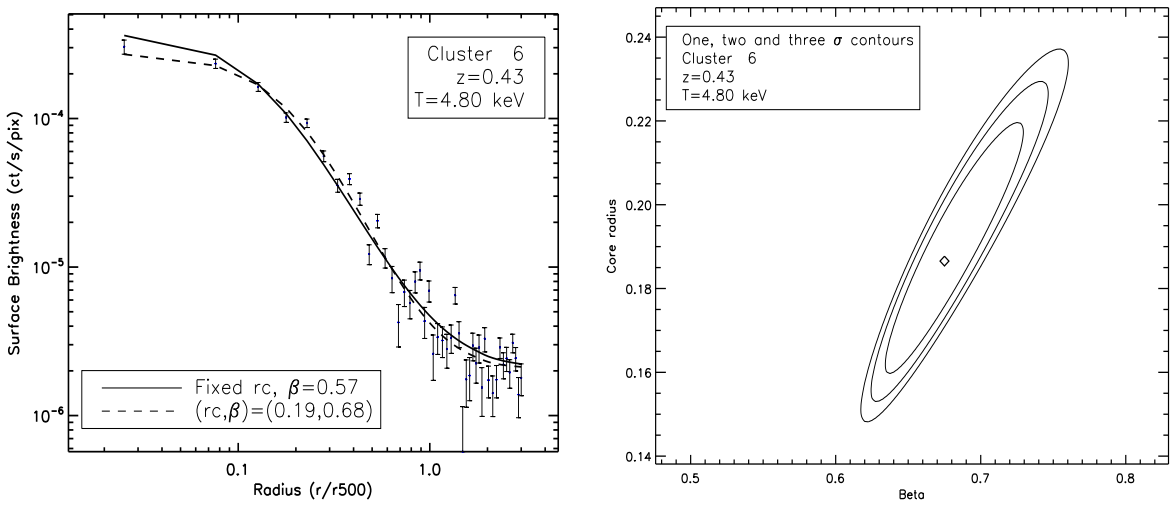

(a) Cluster 6

Figure 3.3: X-ray surface brightness profiles of the individual C1 clusters with redshift $0.43 \leq z \leq 1.05$, ordered according to redshift and the associated constrained $1\sigma, 2\sigma$ and 3σ contours. The dashed lines are the fitted β-model profiles with both $r_{\rm core}$ and β freely fitted, while the solid lines are for the fitted profiles with free β and $r_{\rm core}$ fixed to $0.105 \times {\rm R}_{500}$.

3.3.2 X-ray surface brightness profiles of redshift-stacked clusters

The C1 clusters span a redshift range of 0.05 to 1.05. To probe how the X-ray surface brightness profiles evolve with redshift, we divided the C1 sample into three redshift ranges: 0.05-0.17 (low–z), 0.26-0.33 (intermediate–z) and 0.43-1.05 (high–z). The low–z set consists of 6 clusters with an average redshift of 0.11 and a temperature range from 0.63 to 3.50 keV (average 1.33 keV). Only one of these (cluster 50) has $T > 2$ keV. Twelve clusters fall in the intermediate–z stacked set, with average redshift and temperature of 0.30 and 1.69 keV respectively. The high–z set contains 9 clusters spanning a redshift range 0.43 to 1.05 (average 0.72) and having temperatures from 2.20 to 4.80 keV (average 3.51 keV). The profiles and the error contours of the three stacked sets are presented in Fig. 3.4 and the fitted parameters for the free and fixed β-model fits with 1σ errors are shown in the first three rows of Table 3.2.

The central excess factor, f_c is seen to increase with redshift; for the low–z stack it is 1.30, increasing to 1.56 and 1.95 for the intermediate and high z systems respectively. Table 3.2 also shows that β (for both free and fixed $r_{\rm core}$ fits) increases with redshift, whilst the $r_{\rm core}$ values are essentially constant.

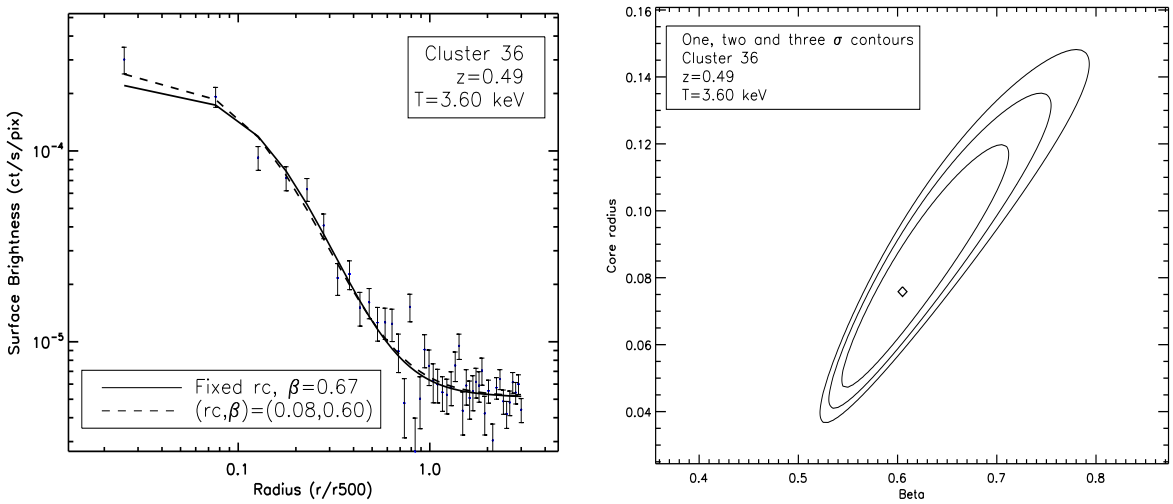

(b) Cluster 36

Figure 3.3: (*continued*)

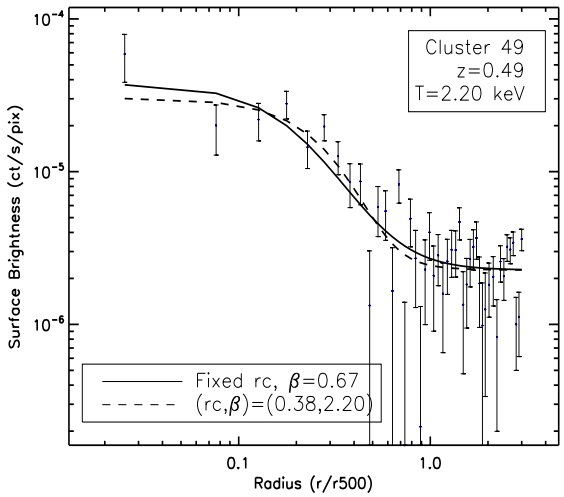

(c) Cluster 49

Figure 3.3: (*continued*)

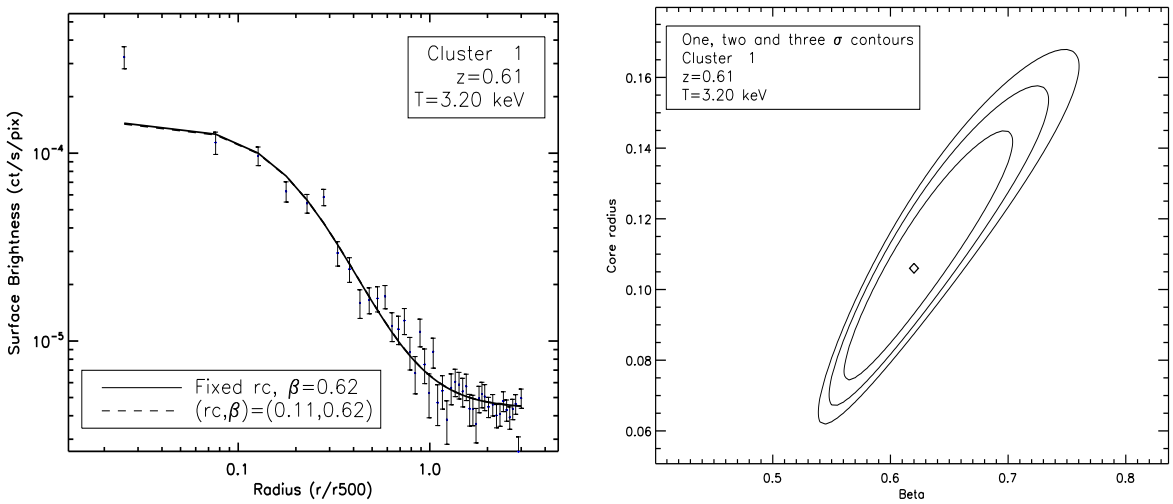

(d) Cluster 1

Figure 3.3: (*continued*)

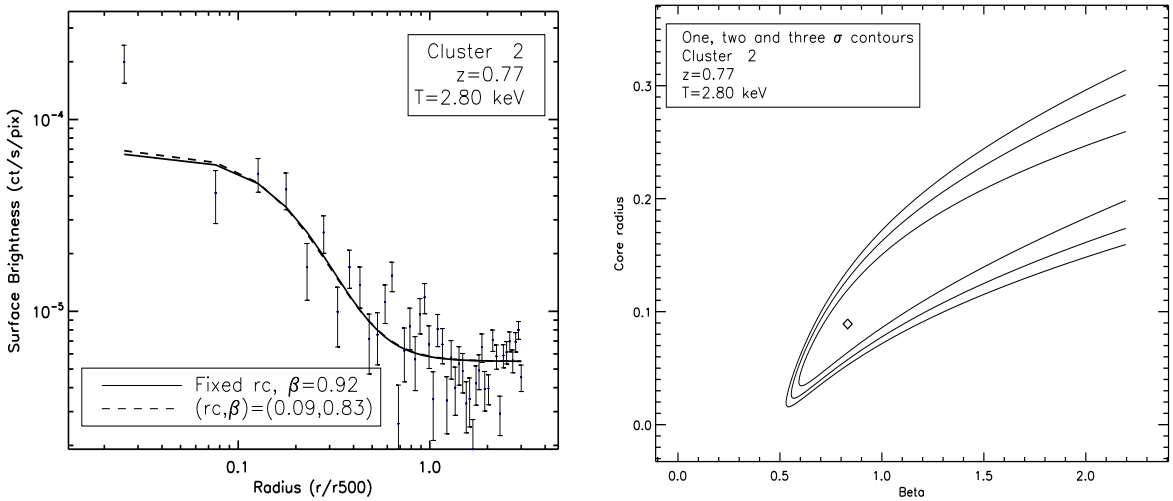

(e) Cluster 2

Figure 3.3: (*continued*)

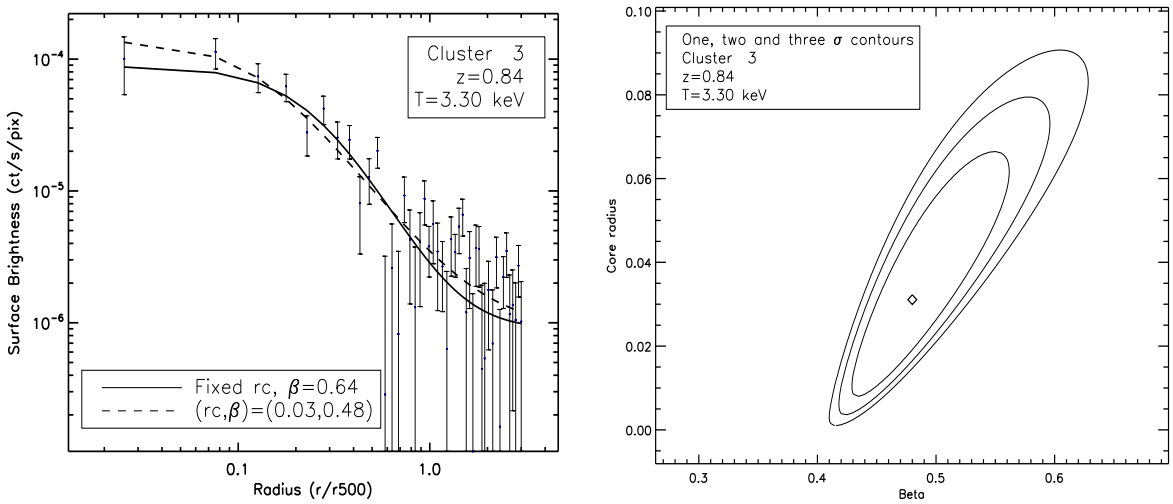

(f) Cluster 3

Figure 3.3: (*continued*)

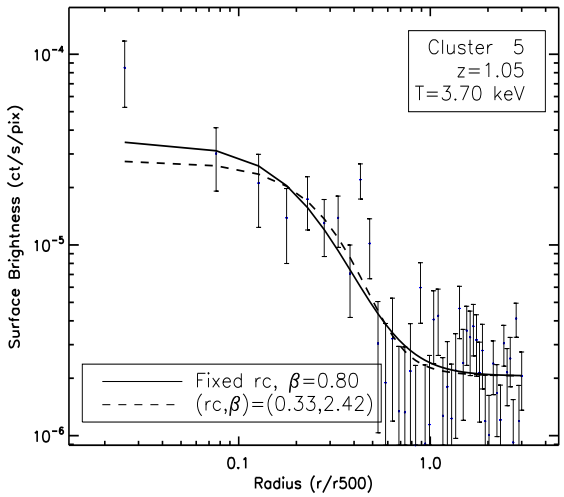

(g) Cluster 5

Figure 3.3: (*continued*)

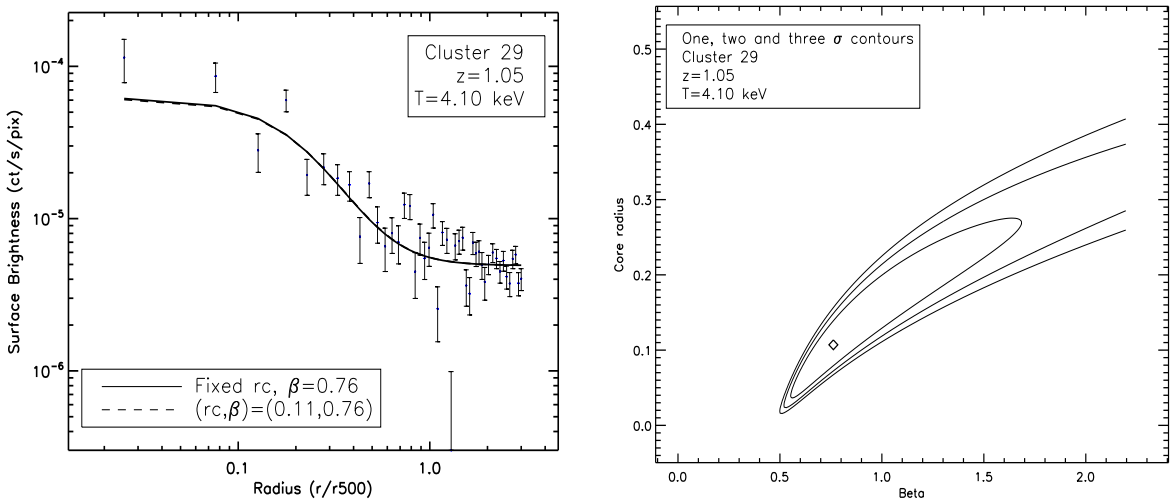

(h) Cluster 29

Figure 3.3: (*continued*)

Range	Stacked Clusters XLSSC	Average z	Average T (keV)	β Fitted $r_{\rm core}$	$r_{\rm core}/R_{500}$	β Fixed $r_{\rm core}$	Central Excess Factor (f_c)
Redshift-stacked clusters (all clusters)							
z:0.05-0.17	11,52,21,41,50,35	0.11	1.33	$0.46^{+0.01}_{-0.01}$	$0.07^{+0.01}_{-0.01}$	$0.49^{+0.003}_{-0.006}$	1.30 ± 0.09
z:0.26-0.33	25,44,51,22,27,8,28,13,18,40,10,23	0.30	1.69	$0.51^{+0.01}_{-0.01}$	$0.06^{+0.01}_{-0.01}$	$0.590^{+0.009}_{-0.011}$	1.56 ± 0.11
z:0.43-1.05	6,36,49,1,2,47,3,5,29	0.72	3.51	$0.60^{+0.06}_{-0.04}$	$0.07^{+0.02}_{-0.02}$	$0.70^{+0.02}_{-0.03}$	1.95 ± 0.25
Temperature-stacked clusters (all clusters)							
T:0.63-1.34	52,11,21,13,35,51,8,28,44,41	0.20	1.06	$0.49^{+0.03}_{-0.02}$	$0.07^{+0.02}_{-0.02}$	$0.52^{+0.02}_{-0.01}$	1.48 ± 0.14
T:1.60-2.80	40,22,23,18,25,49,10,2,27	0.38	2.13	$0.65^{+0.08}_{-0.05}$	$0.07^{+0.02}_{-0.02}$	$0.79^{+0.03}_{-0.04}$	2.17 ± 0.28
T:3.20-4.80	1,3,50,36,5,47,29,6	0.68	3.76	$0.60^{+0.07}_{-0.05}$	$0.07^{+0.02}_{-0.02}$	$0.69^{+0.02}_{-0.03}$	1.81 ± 0.27
Redshift-stacking for clusters with narrow temperature range: 1.20-1.34 keV							
z:0.14-0.26	41,35,44	0.19	1.28	$0.49^{+0.03}_{-0.03}$	$0.10^{+0.03}_{-0.03}$	$0.490^{+0.012}_{-0.008}$	1.49 ± 0.18
z:0.28-0.30	51,28,8	0.29	1.27	$0.56^{+0.11}_{-0.07}$	$0.14^{+0.07}_{-0.05}$	$0.52^{+0.02}_{-0.03}$	1.98 ± 0.45
Temperature-stacking for clusters with narrow redshift range: 0.23-0.33							
T:1.00-1.60	13,51,44,28,8,40	0.30	1.28	$0.54^{+0.07}_{-0.04}$	$0.11^{+0.05}_{-0.04}$	$0.53^{+0.02}_{-0.02}$	1.83 ± 0.32
T:1.70-2.80	22,23,25,18,10,27	0.30	2.10	$0.55^{+0.02}_{-0.01}$	$0.07^{+0.01}_{-0.01}$	$0.620^{+0.013}_{-0.006}$	1.39 ± 0.10

Table 3.2: Results of the β-model fit for the redshift-stacked and temperature-stacked clusters for all clusters and for redshift and temperature subsets. The β and $r_{\rm core}$ values in the fifth and sixth columns are for the β-model with both $r_{\rm core}$ and β freely-fitted. The β values in the seventh column are for the β-model with fixed $r_{\rm core}$. All errors are 1σ errors.

3.3.3 X-ray surface brightness profiles of temperature-stacked clusters

The full temperature range of our C1 sample (0.63 to 4.80 keV) was divided into three subsets. The coolest set (0.63 keV $\leq$T$\leq$ 1.34 keV) contains ten clusters with average T=1.06 keV and average z=0.20. There are nine clusters in the second set (1.60 keV $\leq$T$\leq$ 2.80 keV) with averages T=2.13 keV and z=0.38, and the hottest set (3.20 keV $\leq$T$\leq$ 4.80 keV) contains eight clusters with average temperature and redshift of 3.76 keV and 0.68 respectively. The stacked profiles and the associated 1σ,2σ and 3σ contours are shown in Fig. 3.5 and the fitted parameter values in Table 3.2.

All three temperature-stacked sets show evidence for CCs, with $f_c > 1$. However, f_c does not show a monotonic trend with temperature as was the case for the redshift-stacked clusters. The intermediate-temperature set shows the strongest central excess, with f_c=2.17$\pm$0.28. Similarly, the β values, for both fixed and free $r_{\rm core}$ fits, do not show a monotonic trend across the full T range of our sample, although it is clear that the hotter systems ($T > 1.5$ keV) have β values significantly higher than the groups in our coolest bin. The core radius, $r_{\rm core}$ appears remarkably stable in these stacked clusters, fitting at a value 0.07$\times$R$_{500}$. This is also essentially the case for the redshift-stacked clusters, in which the high and low redshift stackes fitted at $r_{\rm core}$= 0.07$\times$R$_{500}$ whilst the intermediate-redshift stack gives $r_{\rm core}$=0.06$\times$R$_{500}$, which is the same within errors.

3.4 Discussion

3.4.1 X-ray surface brightness profiles of $z \sim 0.3$ clusters

Pacaud et al. (2007) show (see their Fig. 3) that the redshift distribution of the C1 clusters, which spans the redshift range 0.05 to 1.05, has a pronounced peak around $z \sim 0.3$. More than 40% (12 systems) of our clusters are concentrated in the relatively small redshift range $0.26 \leq z \leq 0.33$. The average temperature of these 12 clusters is 1.69 keV. Their average M_{500} is 3.96 $\times 10^{13} M_{\odot}$. This puts them in the realm of groups or poor clusters. To our knowledge, this is the best sample of X-ray selected groups at $z \sim 0.3$ studied to date, and hence our individual and stacked X-ray profiles of these clusters provide the best available X-ray profile of low-mass clusters at intermediate redshift, and should be useful for future comparative studies. The individual X-ray profiles with the the $r_{\rm core}$–β contours for these cluster are shown in Fig.

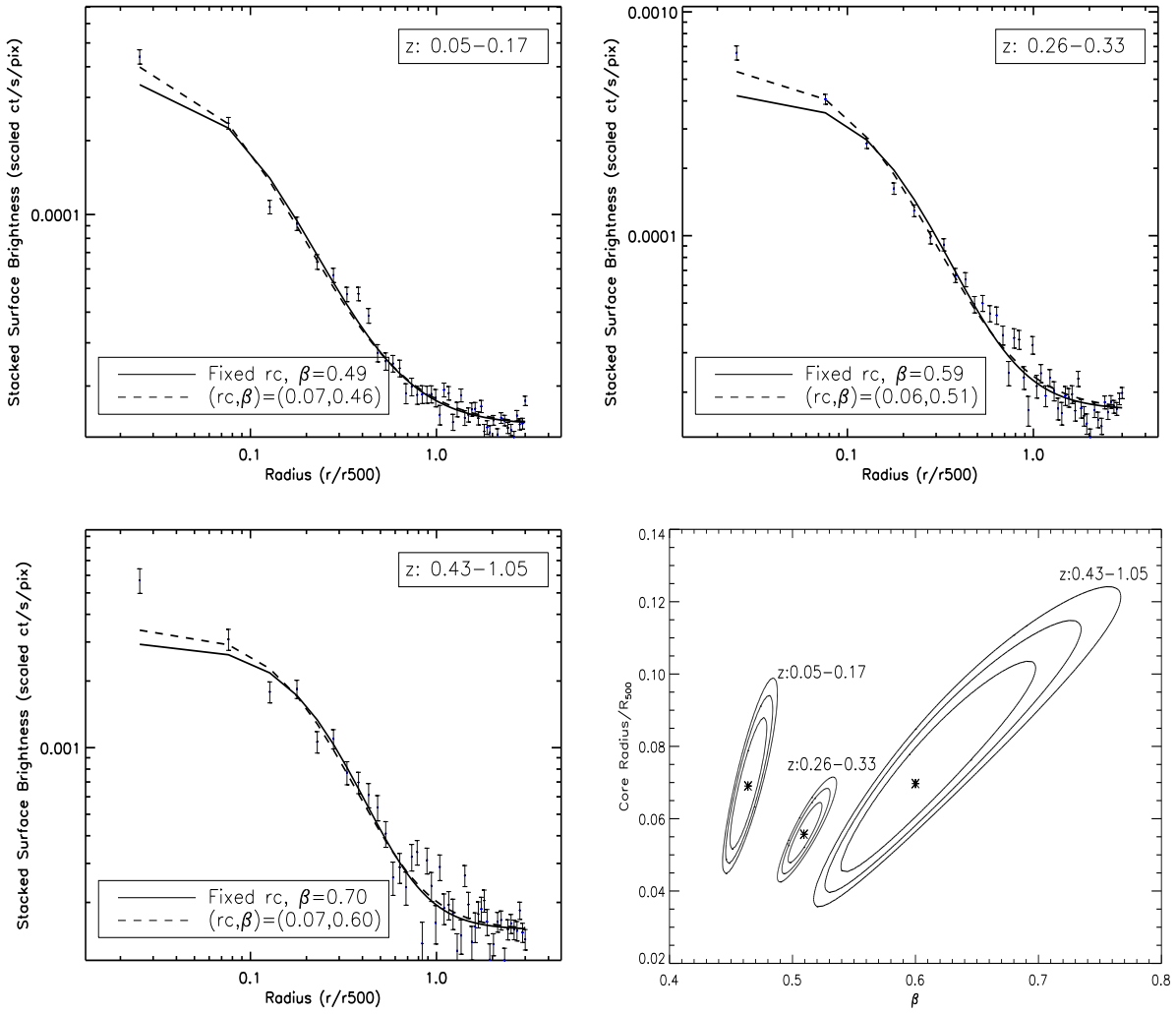

Figure 3.4: X-ray surface brightness profiles of the redshift-stacked C1 clusters with the associated $1\sigma, 2\sigma$ and 3σ contours of the free $r_{\rm core}$ fit. The dashed lines are the fitted β-model profiles with both $r_{\rm core}$ and β freely fitted, while the solid lines are for the fitted profiles with free β and $r_{\rm core}$ fixed to $0.105 \times {\rm R}_{500}$.

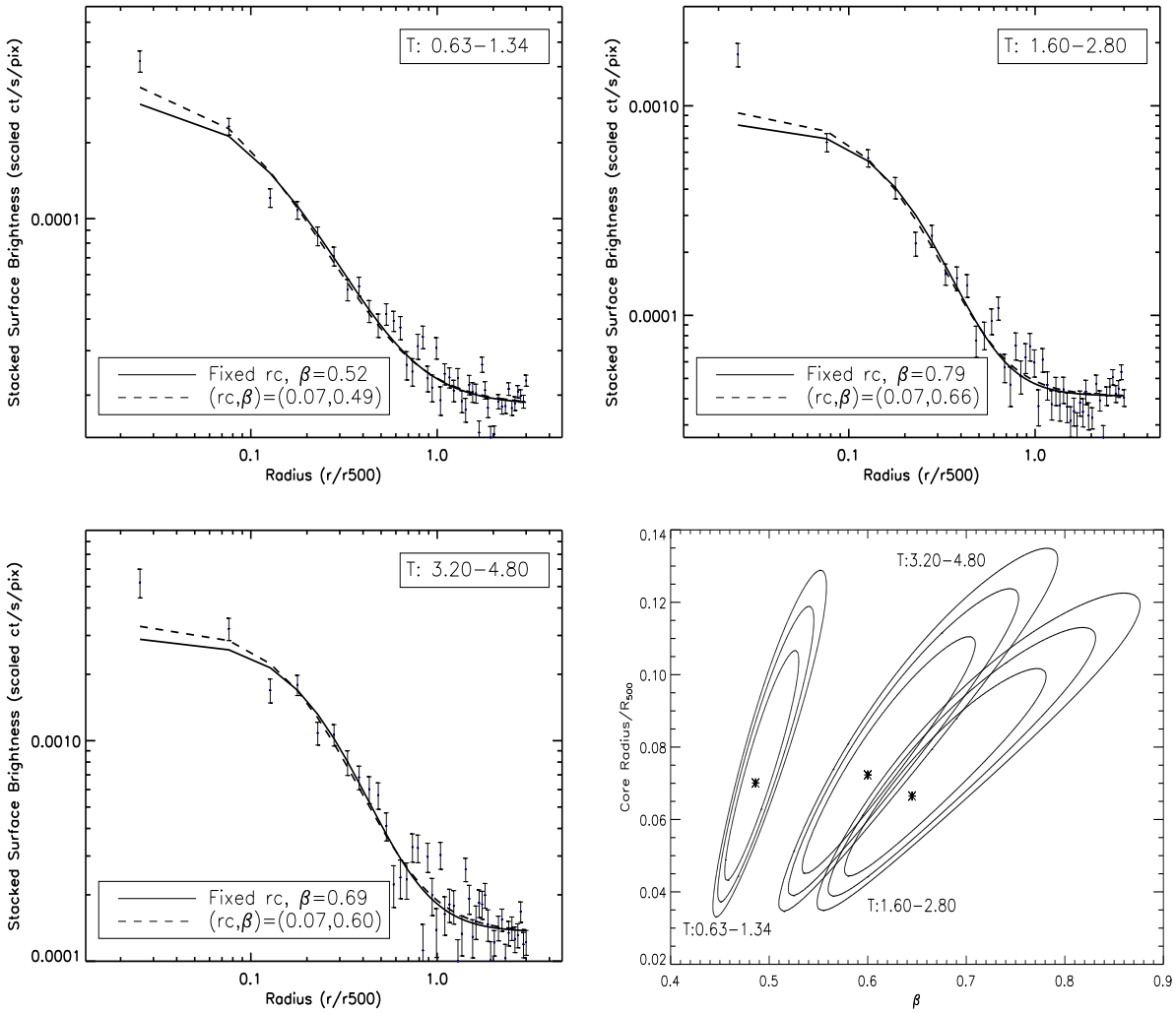

Figure 3.5: X-ray surface brightness profiles of the temperature-stacked C1 clusters with the associated $1\sigma, 2\sigma$ and 3σ contours of the free $r_{\rm core}$ fit. The dashed lines are the fitted β-model profiles with both $r_{\rm core}$ and β freely fitted, while the solid lines are for the fitted profiles with free β and $r_{\rm core}$ fixed to $0.105 \times {\rm R}_{500}$.

3.2 and the stacked profile is the second panel in Fig. 3.4.

The free-$r_{\rm core}$ fit to the stacked profile for these clusters gives $\beta = 0.51$ (see Table 3.2, second row) which is in agreement with studies of low redshift groups (see for example, Helsdon & Ponman 2000a and Mulchaey et al. 2003). Helsdon & Ponman (2000a) attributed the fact that the slopes of group surface brightness profiles are flatter than the canonical slope (β=0.67) for clusters, as a result of the effects of feedback from galactic winds on the intergalactic medium. The stacked data show a central excess, with $f_c = 1.56 \pm 0.11$, indicating that these systems typically possess CCs. The individual profiles of $z \sim 0.3$ clusters in Fig. 3.2, also support this results; the central excess factor, f_c is greater than unity for 7 of the 12 clusters (25,51,22,8,28,40 and 10) and an additional 4 clusters (44,13,18 and 23) have best fit $f_c > 1$, but with error bars crossing unity. So, we conclude that 58-92% of our systems at $z \sim 0.3$ have CCs. The fitted $r_{\rm core}$ for the stacked profiles is $0.06 \times R_{500}$.

3.4.2 Trends of f_c and β with redshift and temperature

The main results of our analysis are the presence of trends in the value of β, and in the incidence of cuspy cores, with redshift and temperature. Our C1 clusters, as for any deep cluster survey, suffer from *Malmquist* selection effects, which result in increasing mean cluster luminosity with redshift, due to the fact that higher redshift clusters are more difficult to detect than nearby ones – see Fig. 3 in Pacaud et al. (2007). Given the well-known correlation between X-ray luminosity and temperature, there is a corresponding tendency for more distant clusters in our sample to be hotter. This correletaion between z and T within our sample, makes it difficult to establish whether our observed trends in β and f_c are evolutionary effects, or whether they represent changes in cluster properties with system mass (and hence temperature).

We attempt to address this issue in two ways: firstly, we can examine whether the trends we see (in both individual and stacked clusters) are stronger with respect to T or z. Secondly, we use the group of clusters at $z \sim 0.3$; subdividing these by temperature allows us to check for trends with T at essentially a single redshift. Similarly, we also extract a subset of our clusters which cover a rather narrow temperature range, but a larger spread in z.

Trends of f_c

To investigate whether the trends we see in the redshift-stacked sets are affected by the T-z correlation in our sample, we select six clusters with similar temperatures (T=1.20 to 1.34 keV) but a relatively wide spread in redshift (z=0.14 to 0.30). These are then divided into two subsets, each consisting of three systems: the first has $0.14 \leq z \leq 0.26$ (average z=0.19) and mean temperature $\bar{T}$=1.28 keV, the second has $0.28 \leq z \leq 0.30$ (average $z = 0.29$) and $\bar{T}$=1.27 keV. The fit results for these subsets are shown in Fig. 3.6 and in Table 3.2.

Similarly, we divided the twelve $z \sim 0.3$ clusters, which span a temperature range of 1.0-2.8 keV, into two temperature bins: 1.0-1.6 keV and 1.7-2.8 keV with six clusters in each. See Fig. 3.7 and the last two rows in Table 3.2 for the results of stacking these subsets. The 1.0-1.6 keV clusters have an average redshift $z = 0.30$ and average temperature $\bar{T}$=1.28 keV, while the 1.7-2.8 keV clusters have the same average redshift $z = 0.30$ and $\bar{T}$=2.1 keV.

The results from these subsets, shown in Fig. 3.6 and 3.7, reinforce the impression from Fig. 3.4 and 3.5 that the increase in profile cuspiness is a function of z rather than T. In fact, the temperature-stacked subset (Fig. 3.7) actually shows a *decline* in f_c with temperature, whilst in the redshift-stacked subset it increases from 1.49 for the $0.14 \leq z \leq 0.26$ clusters to 1.98 for the $0.28 \leq z \leq 0.30$ clusters (Fig. 3.6).

We also tested the f_c–z behaviour in the individual profiles. In Fig. 3.8, we plot f_c against redshift for the individual C1 clusters. The figure shows that the high–z clusters tend to have larger-than-unity values of f_c more often than clusters at lower redshift. We tested for a correlation in this plot, using the Pearson correlation coefficient, which has a value 0.40 for 26 points, corresponding to a Student t value of 2.12, which shows a poitive correlation at over 95% significance (2-tailed test). To visualise the trend more clearly, we grouped adjacent data points into three bins and computed their weighted mean and the standard error. These binned results are shown as diamonds, though it should be noted that resulting values are sensitive to the choice of bin boundaries.

In contrast, the f_c-temperature plot in Fig. 3.9, shows no monotonic trend in f_c with T, with a Pearson correlation coefficient of 0.01. The binned values (diamonds) agree well the temperature-stacked results discussed earlier, where we noticed that intermediate-temperature clusters had the highest central excess.

The present work is the first study of the *evolution* of CCs within galaxy groups, although previous work (e.g., Helsdon & Ponman 2000a) has shown that CCs are common in X-ray bright groups at low redshift. Richer clusters have received much more study. CC clusters are found to be common at low and moderate redshifts, see Bauer et al. (2005), but Vikhlinin et al. (2007) found only a very small fraction of clusters at $z > 0.5$ to have cuspy X-ray brightness profiles, which were taken as an indication of cool cores. Santos et al. (2008) found moderate CC clusters out to $z = 1.4$, but noted an absence of *strong* CCs at redshifts higher than 0.7.

Our results therefore suggest that groups behave differently to clusters, in that cuspy cores are actually *more* prominent at higher z in these poorer systems. How can we understand this difference? One possibility is that the central excess seen in groups at moderate-high z is not due to CCs at all, but to the presence of central Active Galactic Nuclei (AGN). We can immediately rule out the possibility that the effect is due to just a few groups with bright AGN contaminating our stacked profiles by noting (cf. Fig. 3.8) that a central excess is seen in the *majority* of systems at $z > 0.3$. Hence, any effect from central AGN would have to be widespread and moderate.

There would be significant spectral differences between central excesses generated by CCs and AGN, since the thermal emission from cool cores is much softer than the X-ray spectra of AGN. The limited statistics for individual clusters in our sample do not permit us to investigate whether the core emission is soft or hard. However, this can be investigated using the stacked data. We therefore repeated the stacking analysis for intermediate- and high-z clusters using X-ray images derived from the hard energy band, 2.0-4.5 keV. The results are shown in Fig. 3.10. Comparing with the corresponding soft (0.5-2.0 keV) band profiles in Fig. 3.4, we notice the disappearance of the central excess above the β-model in the hard-energy profiles in both the intermediate and high redshift stacks. This provides strong evidence that this central excess does not arise from AGN in cluster cores.

Assuming that the cuspy profiles really do indicate the presence of CCs, the observation of such cores in groups at high redshift can help to constrain the reasons for their absence in high z clusters. The decline in CC clusters with redshift could result from disruption of CCs due to the higher merging rates at high redshifts (e.g., Cohn & White 2005 and Jeltema et al. 2005) or from the effects of preheating (McCarthy et al. 2004), which can raise the gas entropy and prevent

cooling. In the latter case, the impact of a given entropy boost will be larger in cooler systems (see e.g. Borgani et al. 2005), especially at high redshift, so one would expect if anything to see a *drop* in the incidence of CCs within groups at high z, at least as large as pronounced as that in richer clusters.

The hypothesis that CCs are destroyed by cluster mergers appears more promising, since this effect might be stronger in more massive systems. For example, Burns et al. (2008) find that CCs are more common in low mass clusters, and attribute the lack of CCs in more massive systems to their destruction by early mergers in systems destined to grow into large clusters. On the other hand, these authors caution that their model does not reproduce the observed reduction with redshift in CCs within massive clusters. In fact, no numerical simulations have yet succeeded in adequately reproducing the properties of cluster cores.

Trends of β

Whilst it seems quite clear, as discussed above, that the trend in central cuspiness is primarily related to redshift, rather than temperature, the situation with regard to β is not so straightforward. In the stacked datasets, comparison of Fig. 3.4 and 3.5 suggest that the relationship with redshift is stronger: β rises monotonically through the three redshift intervals, whilst in temperature the only clear result is that the cool systems have lower β. In contrast, the fits to individual clusters (Fig. 3.11 and 3.12) show a more pronounced trend with temperature than with redshift. The stacked subsets of the narrow temperature and redshift ranges (Fig. 3.7 and 3.6) produce ambiguous results: β increases with temperature if $r_{\rm core}$ is fixed, but with z if $r_{\rm core}$ is left free to fit.

So, on the basis of our data alone, we are unable to say whether the general trend in β is driven by the temperature or the redshift. However, evidence from studies of low redshift groups and clusters is very relevant here. Such studies provide clear evidence of a positive correlation between β and temperature in local systems systems – e.g., Osmond & Ponman (2004) and Fig. 7 in the study of Croston et al. (2008), who analysed clusters with redshift < 0.2. Combining these previous results with ours, favours a trend in β with temperature (and hence cluster mass) rather than an evolutionary effect. Our results then demonstrate that this trend is still present in groups and clusters at $z \sim 0.3$.

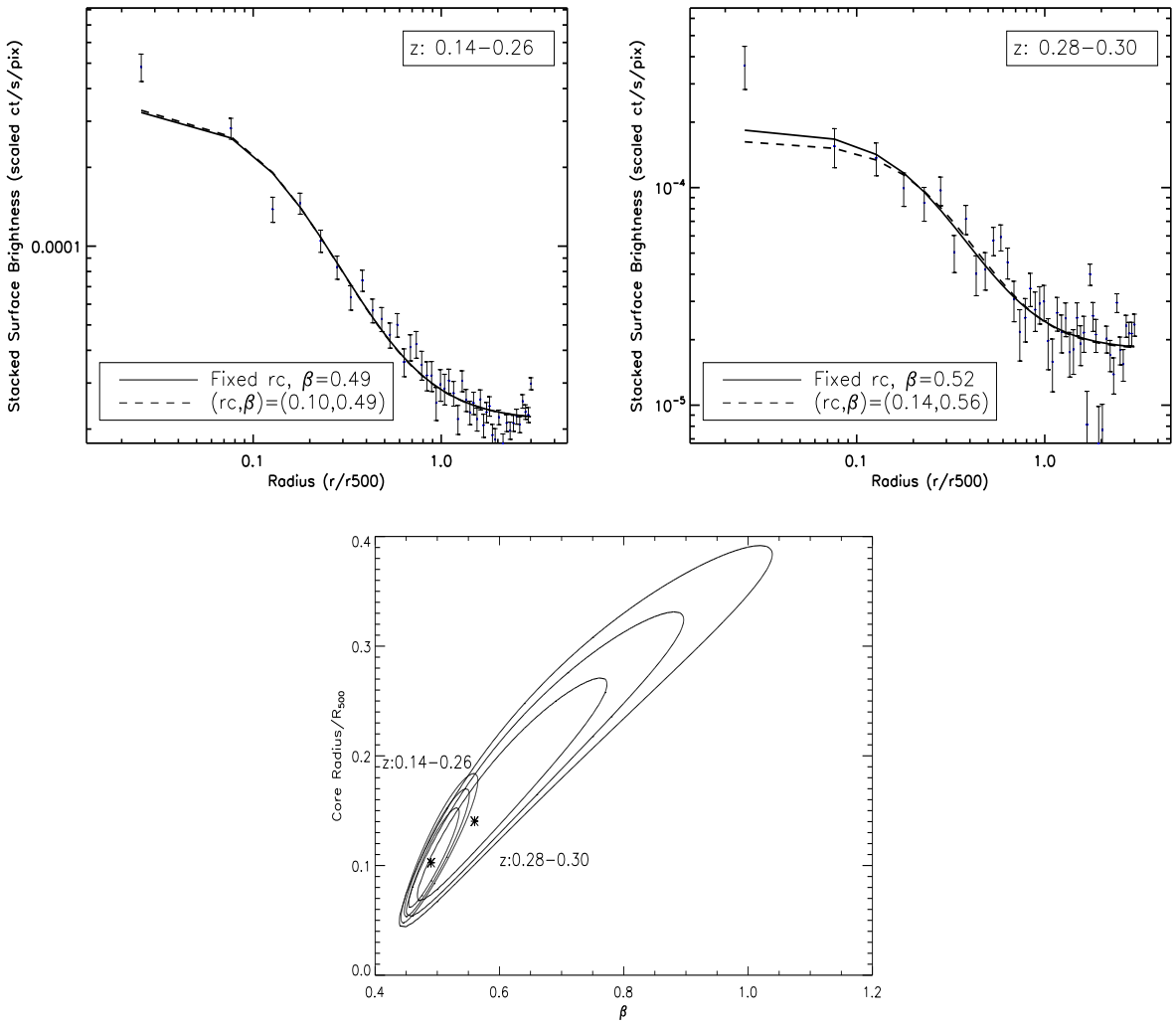

Figure 3.6: X-ray surface brightness profiles of stacked C1 clusters with narrow temperature range (1.20-1.34 keV), grouped into two redshift bins: $0.14 \leq z \leq 0.26$ (top panel) and $0.28 \leq z \leq 0.30$ (middle panel). The bottom panel is the $1\sigma, 2\sigma$ and 3σ contours. The dashed lines are the fitted β-model profiles with both $r_{\rm core}$ and β freely fitted, while the solid lines are for the fitted profiles with free β and $r_{\rm core}$ fixed to $0.105 \times {\rm R}_{500}$.

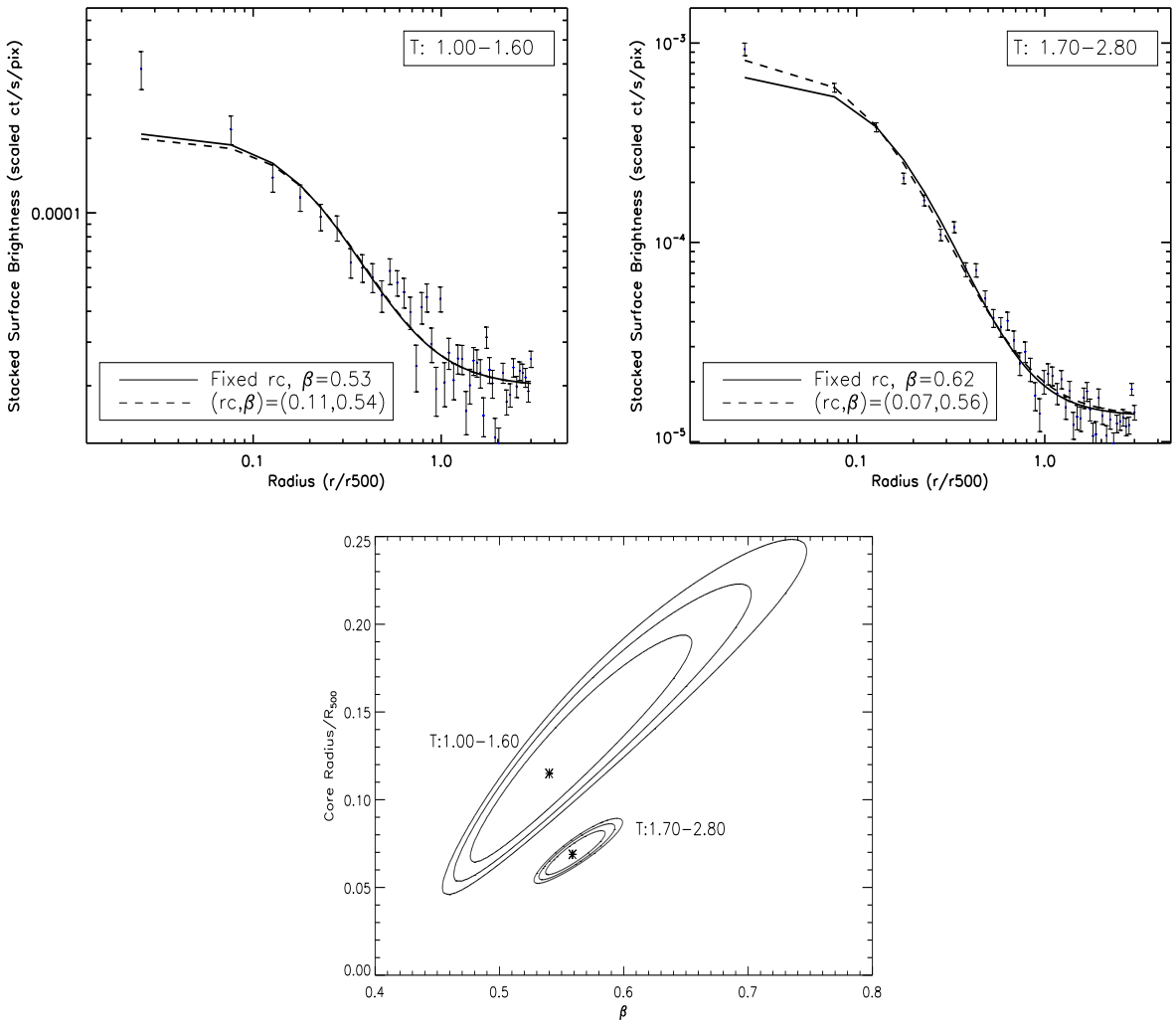

Figure 3.7: X-ray surface brightness profiles of stacked C1 clusters with narrow redshift range (0.23-0.33), grouped into two temperature bins: 1.00-1.60 keV (top panel) and 1.70-2.80 keV (middle panel). The bottom panel is the $1\sigma, 2\sigma$ and 3σ contours. The dashed lines are the fitted β-model profiles with both $r_{\rm core}$ and β freely fitted, while the solid lines are for the fitted profiles with free β and $r_{\rm core}$ fixed to $0.105 \times {\rm R}_{500}$.

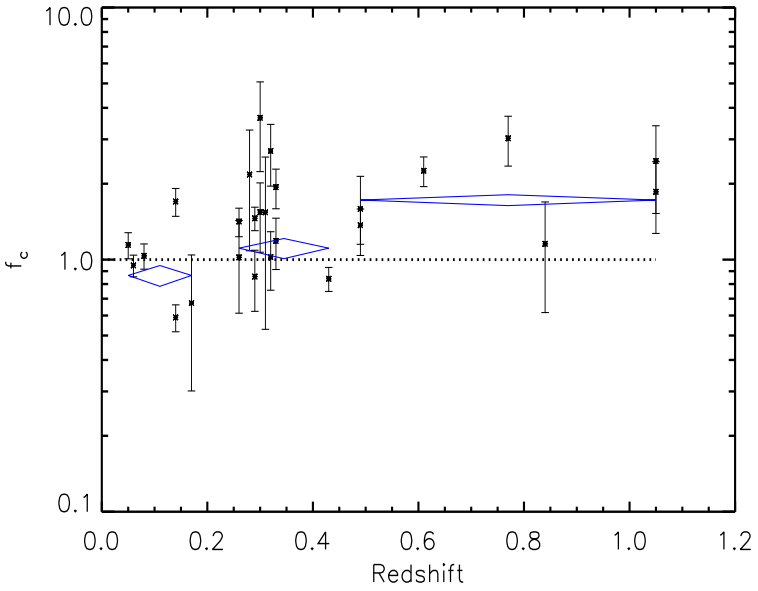

Figure 3.8: Central excess factor, f_c (of the fixed $r_{\rm core}$ fits) plotted against redshift of the individual C1 clusters. f_c is defined as the ratio of the observed surface brightness to the predicted (model) surface brightness within $0.02\times R_{500}$ (first radial bin). A value of f_c above 1 is an indication of a cool core cluster and vice versa. The positions and sizes of the diamonds represent the weighted means and the standard errors of the weighted means of the points as described in text and Appendix B.

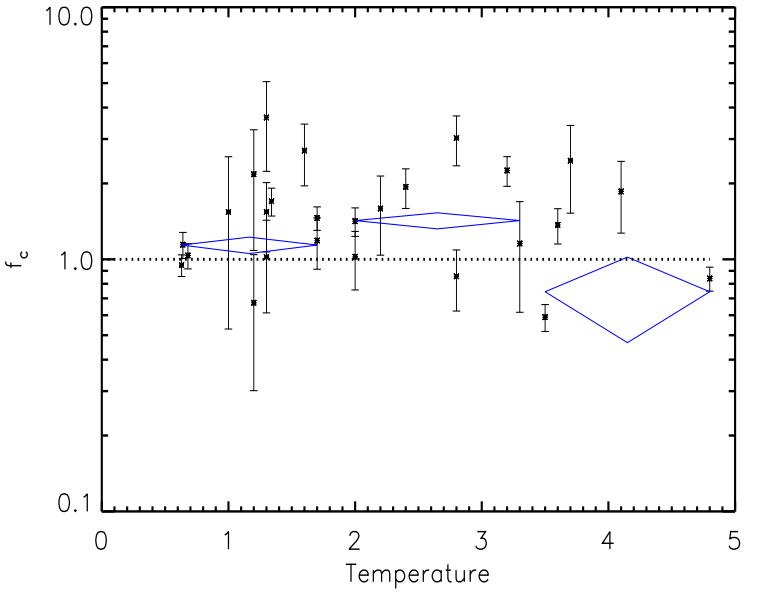

Figure 3.9: Central excess factor, f_c (of the fixed $r_{\rm core}$ fits) plotted against temperature of the individual C1 clusters. The positions and sizes of the diamonds are calculated as described in Appendix B.

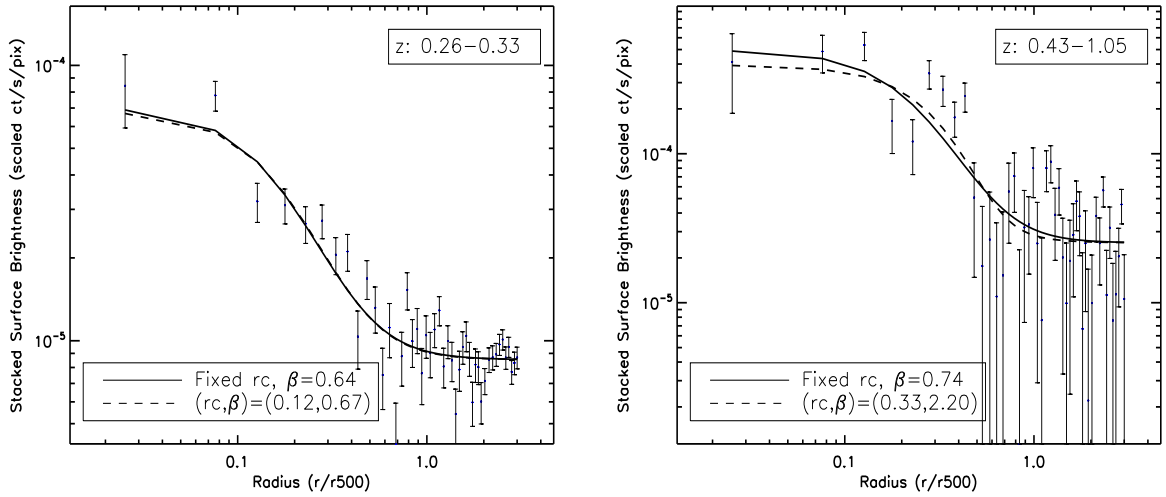

Figure 3.10: Stacked profiles for the intermediate- and high-redshift cluster subsamples extracted from hard band (2.0-4.5 keV). These can be compared directly with the corresponding soft band stacks shown in Fig. 3.4, and shown that the central excess above the fixed-$r_{\rm core}$ β-model is not present in the hard band.

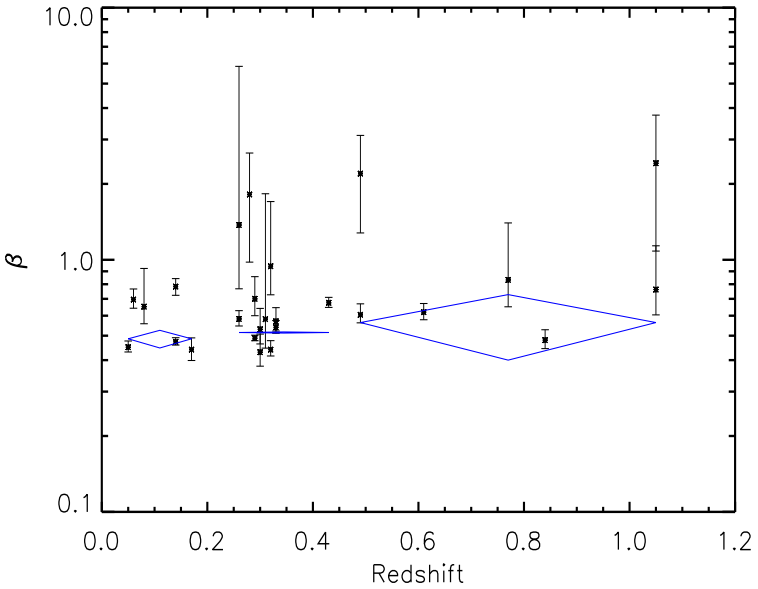

Figure 3.11: β values (of the free $r_{\rm core}$ fits) versus redshift of the individual C1 clusters. The positions and sizes of the diamonds are calculated as described in Appendix B.

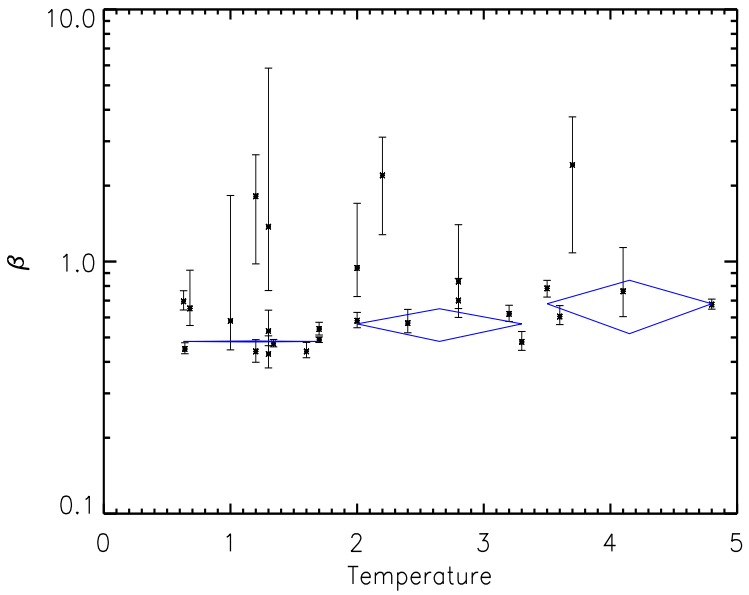

Figure 3.12: β values (of the free $r_{\rm core}$ fits) versus temperature of the individual C1 clusters. The positions and sizes of the diamonds are calculated as described in Appendix B.

3.5 Summary and conclusions

In this chapter, we used *XMM-Newton* observations of 27 X-ray selected galaxy clusters spanning the redshift range ($0.05 \leq z \leq 1.05$) to study the spatial properties of their ICM. Most of these clusters fall in the realm of low-mass clusters or groups, with ICM temperatures from 0.63 to 4.80 keV. The XMM data provide typically a few hundreds X-ray source counts. We extracted and vignetting-corrected the profiles to $3\times R_{500}$ where they flattened and reached the photon background values, which were estimated locally for each cluster.

In addition to the individual profiles, we also stacked the profiles into three redshift and temperature bins. To explore the effects of *Malmquist bias*, we further stacked clusters with similar redshifts/temperatures into two subsets each with different averaged temperature/redshift. Both individual and stacked profiles were fitted with blurred (to account for the PSF errors of the *XMM-Newton* cameras) β-models with both free and fixed core radii. The fixed-$r_{\rm core}$ β-model fits were used to test whether a profile showed evidence of a cuspy core, making this study the first to probe the evolution of CCs out to $z \gtrsim 0.3$ within poor clusters.

Our main conclusions are:

- We find that 54% of our sample show evidence for cool cores, in the form of a central

excess (at $> 1\sigma$ significance) above a standard β-model.

- For the free-$r_{\rm core}$ fits to individual clusters, the median value of β is 0.61, and the median $r_{\rm core}$ is $0.08\times R_{500}$.

- For the fixed-$r_{\rm core}$ fits to individual clusters, the median β is 0.63.

- Twelve systems in our sample (with $\bar{T} = 1.69$ keV) have $z \sim 0.3$, allowing us to characterise the X-ray surface brightness profiles of intermediate redshift X-ray selected groups. The free-fit parameters to the stacked data from these 12 systems gives $\beta = 0.51 \pm 0.01$ and $r_{\rm core}=0.06 \pm 0.01\times R_{500}$. This stacked profile indicates the presence of CCs ($f_c = 1.56 \pm 0.11$), with 7 of the 12 systems showing a significant central excess in their individual profiles.

- Stacked and individual profiles for our sample of poor galaxy clusters show that the CCs do not disappear at high redshift, but rather become more prominent, though one would like to confirm this result with higher spatial resolution observations.

- The slope parameter, β, shows a positive trend with both redshift and temperature in our data. Combining this results with previous findings, we incline towards a trend with temperature (and hence mass) rather than redshift. The present study then demonstrates for the first time, that the β-T trend seen at low z is also present in groups and clusters at $z \gtrsim 0.3$.

Chapter 4

Luminosity Functions of XMM-LSS C1 Clusters

In this chapter, CFHTLS optical photometry has been used to study the galaxy luminosity functions of 14 X-ray selected clusters from the XMM-LSS survey. These are mostly groups and poor clusters, with masses (M_{500}) in the range 0.6 to 19 $\times 10^{13} M_{\odot}$ and redshifts $0.05 \leq z \leq 0.61$. Hence, these are some of the highest redshift X-ray selected groups to have been studied. Lower and upper colour cuts were used to determine cluster members. We derive individual luminosity functions (LFs) for all clusters as well as redshift-stacked and temperature-stacked LFs in three filters, g', r' and z', down to $M = -14.5$. All LFs were fitted by Schechter functions which constrained the faint-end slope, α, but did not always fit well to the bright end. Derived values of α ranged from -1.03 to as steep as -2.1. We find no evidence for upturns at faint magnitudes. Evolution in α was apparent in all bands: it becomes shallower with increasing redshift; for example, in the z' band it flattened from -1.75 at low redshift to -1.22 in the redshift range z =0.43-0.61. Eight of our systems lie at $z \sim 0.3$, and we combine these to generate a galaxy LF in three colours for X-ray selected groups and poor clusters at redshift 0.3. We find that at $z \sim 0.3$, α is steeper (-1.67) in the green (g') band than it is (-1.30) in the red (z') band. This colour trend disappears at low redshift, which we attribute to reddening of faint blue galaxies from $z \sim 0.3$ to $z \sim 0$. We also calculated the total optical luminosity and found it to correlate strongly with X-ray luminosity ($L_X \propto L_{OPT}^{2.1}$), and also with ICM temperature ($L_{OPT} \propto T^{1.62}$), consistent with expectations for self-similar clusters with constant mass-to-light ratio. We did not find any convincing correlation of Schechter parameters with mean cluster temperature.

4.1 Introduction

Most of our knowledge of galaxies is based on observations of the local Universe, although distant Universe observations have also provided a wealth of information. Statistical studies of galaxies at high redshift are mostly limited to rich galaxy clusters mainly due to observational limitations. Galaxy clusters are important cosmological environments where key galaxy transformation such as stripping and strangulation occur. However, in the hierarchical formation of structure rich clusters are the latest structures to be formed. Lower mass systems or galaxy groups may have been the place where galaxies experience a substantial degree of evolution through processes such as mergers and tidal interaction, as a result of the higher efficiency of these processes in the lower velocity dispersion environment of groups.

The galaxy luminosity function (LF) – the number of galaxies per unit volume in the luminosity interval L to $L + dL$ – has been widely used to study the formation of galaxies and the evolution of galaxy populations with redshift. It is also an excellent statistical tool for describing how different environments influence the properties of galaxies.

Both the bright end (Bower et al. 2006, Naab & Burkert 2007) and the faint end (Marzke et al. 1994, Khochfar et al. 2007) of the LF have been the subject of in-depth studies, as they offer strong observational constraints for models of galaxy formation and evolution. While the bright end of the LF is affected by AGN feedback (Bower et al., 2006), the faint-end slope is predominantly influenced by feedback from supernovae (Dekel & Silk 1986), and provide a direct indicator of the significance of dwarf galaxies, which are expected to behave differently in rich and poor clusters. Multi-colour LFs, in particular, probe the history of the faint galaxy population, including its star formation history – see for example, Adami et al. (2007).

The vast majority of studies of the galaxy LF give faint-end slopes in the range ~ -1 to ~ -2. Most of these have limited magnitude depth ($M > -16$) and recent deep studies are mostly confined to rich local clusters (See Table 1 in Popesso et al. 2005a and Table A.1 in Boué et al. 2008 and references therein). These studies not only disagree on the value of the faint-end slope, but they also disagree on the exact form of it, as some studies (e.g. Gonzàlez et al. 2006) found upturns; a single Schechter function was not an adequate fit to the faint end, and a double Schechter function was required to give a reasonable fit. The existence of these upturns is very sensitive to the method used to determine galaxy membership, with some approaches including

spurious galaxies or excluding genuine cluster members due to their low surface brightness.

The evolution of the faint-end slope is hard to study, mainly because the number of faint galaxies detected decreases sharply with increasing redshift. Liu et al. (2008) found that the faint-end slope of a field galaxy population became shallower with increasing redshift (up to $z = 0.5$) for all galaxy spectral types. However, to account for the photometric redshift errors of the galaxies, they weighted the galaxies as probability-smoothed luminosity distribution at the redshift at which they were measured. This places an important caveat on the interpretation of their data, and hence on their results. On the other hand, simulations by Khochfar et al. (2007) show a measurable dependence of the faint-end slope of the galaxy luminosity function on redshift. However, most of this dependence is seen over a relatively large redshift range, $\Delta z \geq 2$. Furthermore, it is hard to discriminate galaxy environments in such studies.

X-ray surveys remain one of the most popular methods of finding galaxy systems. Due to the strong density dependence of X-ray emissivity, X-ray cluster selection is much less vulnerable to contamination along the line-of-sight than optical methods. The XMM-Large Scale Survey (XMM-LSS) (Pierre et al. 2004), a contiguous X-ray survey, has a well-defined selection function which is used to produce a sample of galaxy groups to study their intracluster medium and galaxy properties at medium to high redshift. Pacaud et al. (2007) have presented a study of a sample of 29 galaxy systems from the XMM-LSS survey, drawn from an area of 5 deg^2 out to a redshift of z = 1.05. The cluster distribution peaks around z = 0.3 and T=1.5 keV, half of the objects being groups with a temperature below 2 keV.

In this chapter, we use the XMM-LSS optical follow-up observations to study the evolution of the galaxy luminosity function in galaxy groups and poor clusters since $z \approx 0.6$. Given the observational biases – distant groups are more massive and hotter – we study whether the redshift dependencies are weaker or stronger when the intrinsic properties of the systems, for instance, intracluster medium temperature, are taken into account.

By using a deep ($m_{g'} = 24$) optical survey of X-ray selected galaxy clusters up to redshift of $z = 0.61$, we aim in this chapter to clarify the debate on the faint-end slope of the LFs of low-mass ($M_{500} \leq 20 \times 10^{13} M_{\odot}$) galaxy clusters (or groups), and to explore the existence of any dips, or upturns at the faint end, and to establish whether the slope shows trends with redshift or intracluster medium temperature. Comparison with previous results can help to elucidate the

universality of galaxy cluster LFs. Furthermore, the scaling relation of total optical luminosity with temperature and X-ray luminosity for our cluster sample can shed light on the mass-to-light ratios of low-mass systems when compared to rich clusters.

The chapter is constructed as follows: In section 4.2, we describe the optical catalogue used to calculate the LFs. Then, we describe the data reduction and the method used to construct the colour-magnitude diagrams (CMD) and the subsequent LFs, and the technique adopted for the background subtraction. In section 4.3, we describe our results, starting with the individual cluster LFs, and then the redshift-stacked clusters and temperature-stacked clusters. In section 4.4, we discuss our results and compare them with other studies. Finally, in section 4.5, we summarise our conclusions.

Throughout this chapter, we adopt the cosmological parameters estimated by Spergel et al. (2007), namely: $H_0 = 73$ km s^{-1} Mpc^{-1}, $\Omega_m = 0.24$, $\Omega_\Lambda = 0.76$.

4.2 Data

4.2.1 Observations

Optical photometry of the XMM-LSS survey was obtained from the Canada-France-Hawaii Telescope Wide Synoptic Legacy Survey[1], referred to as the CFHTLS Wide survey. Data were obtained in five passbands (u^*, g', r',i' and z') down to a nominal magnitude limit of $i' = 24.5$. Of the 19 deg^2 of CFHTLS Wide data available in the W1 survey area, 4 deg^2 overlap with the X-ray selected cluster catalogue presented by Pacaud et al. (2007). Hence our photometric data are drawn from four $1^\circ \times 1^\circ$ catalogues derived from the survey data.

The data used in this chapter are based upon the reduction procedure outlined in Hoekstra et al. (2006). Source extraction and photometry were performed using `SExtractor v2.5.0` (Bertin & Arnouts 1996). Zero point information for sources detected in the CFHTLS Wide field survey W1 area was extrapolated from common sources detected in the Sloan Digital Sky Survey equatorial patch which overlaps the southern edge of the W1 area.

XMM-LSS Class 1 (C1) clusters are a well-controlled X-ray selected and spectroscopically confirmed cluster sample. The criteria used to construct the sample guarantee negligible contamination by point-like sources. The observations of the clusters were performed in a homogeneous

[1]See http://www.cfht.hawaii.edu/Science/CFHLS/

XLSSC number	R.A. (J2000)	Dec (J2000)	Redshift	T (keV)	L_X $10^{43} ergs^2$	r_{500} (Mpc)
11	36.5413	-4.9682	0.05	0.64	0.11	0.290
21	36.2345	-5.1339	0.08	0.68	0.11	0.297
41	36.3777	-4.2391	0.14	1.34	2.4	0.440
25	36.3531	-4.6776	0.26	2.0	4.6	0.533
44	36.1411	-4.2347	0.26	1.3	1.2	0.399
22	36.9165	-4.8576	0.29	1.7	6.2	0.471
27	37.0143	-4.8510	0.29	2.8	4.8	0.653
8	36.3370	-3.8015	0.30	1.3	1.2	0.396
13	36.8586	-4.5380	0.31	1.0	1.3	0.340
40	35.5232	-4.5464	0.32	1.6	1.6	0.442
18	36.0087	-5.0904	0.32	2.0	1.3	0.521
6	35.4385	-3.7715	0.43	4.8	60.3	0.838
49	35.9892	-4.5883	0.49	2.2	4.3	0.493
1	36.2381	-3.8157	0.61	3.2	33.2	0.584
2	36.3844	-3.9200	0.77	2.8	19.6	0.493
29	36.0172	-4.2251	1.05	4.1	48.3	0.524
5	36.7885	-4.3000	1.05	3.7	17.1	0.489

Table 4.1: List of the 17 C1 galaxy clusters covered by CFHTLS optical survey and their properties sorted according to their redshifts (Pacaud et al. 2007). The three highest redshift clusters (2,29 and 2) though covered by the survey, were not included in our analysis because their data were too poor to yield useful fits.

way (10-20 ks exposures). For full details of the C1 sample, see Pacaud et al. (2007). The main properties of the sample are shown in Table 4.1. Detailed information on the C1 selection process can be found in Pacaud et al. (2006). 17 out of the 29 XMM-LSS C1 clusters are covered by the CFHTLS Wide field survey. The dropped clusters are random and therefore, this should not produce any bias in the results. In this chapter, we study the luminosity functions of 14 of these 17 clusters – dropping the three with the highest redshifts (clusters with XLSSC numbers 2,29, and 1) because their photometric data is too poor to allow useful constraints to be obtained.

4.2.2 Analysis

Galaxies were detected by SExtractor (Bertin & Arnouts 1996). Luminosity functions (LFs) were produced in three of the five CFHTLS (u^*, g', r',i' and z') filter bands, namely, g', r' and z'. To determine the completeness of the LFs, we took into account the limiting apparent magnitude in each field. The completeness limits for each filter was determined using the apparent magnitude LFs of all data (down to the faintest magnitudes available) for each C1 cluster individually.

Variations in seeing and exposure time across the CFHTLS fields used here are small, and it was found that for each filter there was a common completeness limit at which all LFs started to drop below the faint end power law slope. Note that the LF turn-up reported by some authors (see section 4.4.2), which could potentially introduce an error into this method for estimating completeness, falls beyond the faint limit of our LFs (e.g. at -16 in g' band), except in our three closest clusters, and hence cannot seriously bias our estimates of the completeness limits. The completeness threshold magnitudes for the three filters g', r' and z' were found to be 24, 23.5 and 23, respectively. These values are also consistent with results based on comparison of the number counts per field to deeper data from the CFHTLS Deep Field and CCCP Megacam observations (Urquhart et al. 2009).

Each entry in the catalogues is associated with a FLAG value which indicates the degree of reliability of the data. Flag is a short integer, and a value of 0 denotes good data. The more unreliable the data is, the higher the FLAG value becomes. We included all catalogue entries with FLAG ≤ 3, which includes sources with very close and bright neighbours or some bad pixels and sources which are originally blended with other sources. This may admit some problematic galaxies but this is better than excluding many genuine cluster members, because many clusters contain significant number of blended sources. Factors that may raise the FLAG to > 3 include sources with saturated pixels, truncated sources, incomplete or corrupted data and sources with memory overflow during deblending or extraction. Catalogue entries with FLAG > 3 constitute only $\simeq 5\%$ of the total number of entries, and were all removed. Many of the removed entries are fainter than the threshold magnitude and hence would have been removed anyway.

Each entry in the catalogue also includes a stellarity class value, STAR, with values ranging from 0 to 1. The lower its value, the more likely the detected object is a galaxy. Data points with different STAR values were checked by IRAF and their radial profiles were examined to see if they matched the typical profile of a star or a galaxy. Typically, objects with STAR $>$ 0.85 were found to be stars, whilst those with < 0.85 were galaxies. Therefore, only catalogue entries with STAR values of 0.85 or less were included when constructing the LFs.

Spectral temperatures of the XMM-LSS clusters, and the resulting values of R_{500} (which allow for the evolution in critical density with redshift), were measured by the Saclay team (Pacaud et al. 2007). To construct colour-magnitude diagrams, we selected all galaxies within

a circle of radius, $R^* = 1.5 \times R_{500}$ of the clusters. The R_{500} values were computed as explained in Alshino et al. 2010. This radius limit, R^*, represents an estimate of R_{200}. Colour-magnitude diagrams were produced for all 14 clusters for colour bands: g', r' and z'. The factor, 1.5 does not have a large effect on the fitted parameters of the Schechter function; we compared the results of $1.0 \times R_{500}$ to $1.8 \times R_{500}$ and found that the faint-end slope, α, was only changed within its 1 σ errors.

The CMD were used to colour select galaxies which might be cluster members, hence reducing the background due to interlopers. The colours used for this were $u^*_2 - g'_2$ versus $g'_{\rm kron}$, $g'_2 - r'_2$ versus $r'_{\rm kron}$, and $i'_2 - z'_2$ versus $z'_{\rm kron}$ for the three filters respectively, where the subscript *2* refers to the 2 arcsec aperture used in the magnitude measurements. To define and select cluster members in the CMD, we defined upper and lower colour cuts and only galaxies between these two lines were used to produce the LF, as galaxies outside these limits were most likely not cluster members. To define these two colour cuts, we first defined the red sequence line in the CMD and then pushed this line up and down to allow for statistical errors, and for the likely range of galaxy colours.

To define the red sequence line, we first defined the slope and then its Y-intercept. We checked that the BCGs lay at the centre of the X-ray emission in all clusters, and then calculated the red sequence slope in each case by fitting a straight line to the bright galaxies in the CMD. Bright galaxies are defined as those with magnitude ranging from that of the brightest cluster galaxy, $m_{\rm BCG}$, to a magnitude of $m_{\rm BCG} + 3$, inclusive. We found that the slope of the red sequence line for the 14 C1 clusters showed a mild trend with redshift: it was steeper for high-redshift clusters. A similar trend was observed by Gilbank et al. (2008) and attributed to a deficit of faint red galaxies at high redshifts, consistent with the galactic downsizing picture.

We divided our cluster sample into two redshift ranges: low-redshift clusters ($z < 0.2$) and intermediate-redshift clusters ($0.2 \leq z \leq 0.61$). Clusters from each group share a common red sequence line slope with a small variation. The common slope for the low-redshift range was -0.007 and -0.025 for the second range. Instead of using a different red sequence slope for each cluster, we used the common slope of the redshift groups for all clusters belonging to that redshift group.

The Y-intercepts of the red sequence lines were different for each galaxy cluster and depended

on the average colour of the bright galaxies as defined above. To fix the value of the intercept for each cluster, the red sequence line was normalised so as to pass through the point in the CMD which has a magnitude of $m_{\rm BCG}+1.5$ and colour equal to the average colours of the bright galaxies. This point and the value of the slope completes the definition of the red sequence line.

Both upper and lower colour cuts have the same slope as the red sequence line. In order to define the upper colour cut, we have to determine the upper (red) limit to the cluster red sequence. We took into account the statistical scatter of the colours of the faintest galaxies on the red sequence. These galaxies are defined as those inside a 1.0×0.1 (magnitude by colour units) box in the CMD centred on the faint end of the red sequence line (see Fig. 4.1). The size of this box was chosen to include the faintest galaxies most probably belonging to the red sequence after studying the CMD of the C1 sample. The expected scatter of these galaxies, σ, is calculated by averaging their colour errors, that is the Y-axis errors in the CMD. The upper colour cut, is then taken to be the red sequence line pushed upward by 2σ. By taking into account this scatter, we ensure that almost all genuine cluster red sequence galaxies should fall beneath the red cut, since the statistical error on the brighter galaxies will be smaller.

Similarly, the lower (blue) colour cut is the red sequence line pushed downward in the CMD. In this case, the shift has to account for both statistical scatter, and for the fact that late-type cluster galaxies are intrinsically bluer than red sequence galaxies. The shift was therefore taken to be $-(2\sigma + \triangle)$. Where $\triangle$ is the theoretical colour difference between ellipticals and spirals. This was estimated using a simple model which calculates what colour late-type galaxies would have when redshifted by different amounts, as described in King & Ellis (1985). $\triangle$ is a function of redshift only and the redshift of the galaxy cluster was used to determine its value. This method of estimating $\triangle$ ignores any intrinsic evolution in the colour offset between red and blue cluster galaxies. However, the detailed COMBO-17 study of Bell et al. (2004) (see their Fig. 1) shows that the colour difference between blue and red sequence cluster galaxies changes little over the redshift range (0-0.7) spanned by our clusters. Fig. 4.1 shows an example of our use of colour cuts for selection of cluster galaxies.

Of course, background and foreground galaxies will still contaminate the sample after the colour cut has been applied, and this contamination must be estimated and removed statistically. For this purpose we used all data in the catalogue to which a given galaxy cluster belonged. In

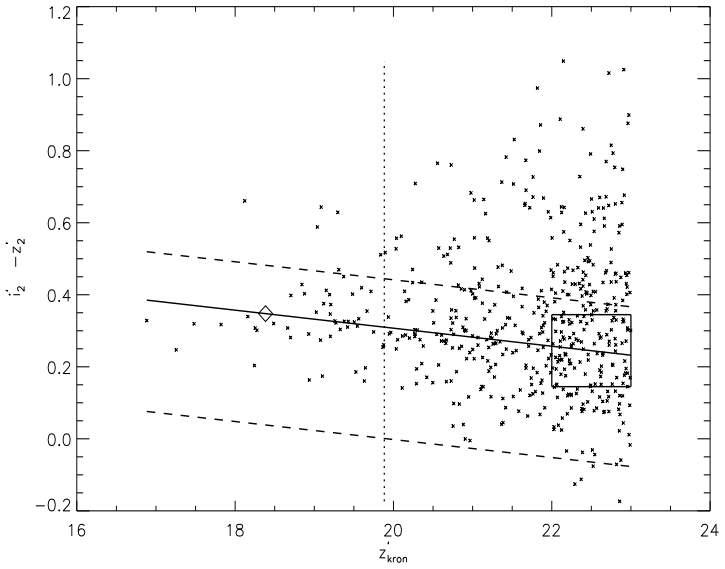

Figure 4.1: Colour-magnitude diagram of cluster 25 (redshift=0.26). All galaxies (crosses) on the left of the vertical dotted line are the bright galaxies with magnitude $\leq m_{\rm BCG} + 3$. The red sequence line (the solid line) is defined by the point (diamond) with magnitude of $m_{\rm BCG} + 1.5$ and colour equal to the average colours of all bright galaxies and by the slope of -0.025. The statistical scatter, σ, is estimated by the average colour errors of the galaxies within the 1.0×0.1 box on the faint end of the red sequence line. In the case of cluster 25, $\sigma = 0.07$. The dashed lines are the upper and lower colour cuts. The upper colour cut is the red sequence line pushed upward by 2σ and the lower colour cut is the red sequence line pushed downward by $2\sigma + \triangle$, where $\triangle = 0.175$ for redshift of 0.26. See text for definition of $\triangle$.

addition to simple Poisson fluctuations, uncertainties in removing background and foreground galaxies arise from large scale structure. To quantify the extra fluctuations arising from this, we proceeded as follows. The whole catalogue $1^\circ \times 1^\circ$ area was divided into smaller blocks with areas comparable to that of the cluster in question. Any of these blocks covered mostly (60% or more, by area) by a galaxy cluster, were considered to be dominated by a cluster and hence were discarded from the background calculation. Blocks covered by clusters to an extent less than 60%, were not discarded but the portion covered by the R^* circle of any galaxy cluster was removed, so the final blocks used have somewhat different areas.

For each background block, an LF was produced in just the same way as for the cluster itself. The same values of the upper and lower red sequence limits of the galaxy cluster in question, were applied to all its background block areas, so galaxies beyond those limits were removed. The application of colour cuts to both source and background fields reduces the noise level in both of them, and hence in the final background-subtracted LF.

We then divided each background block LF by its area, added them and normalised the resulting single LF to the area of the galaxy cluster in question. The error bars on the averaged background LF were calculated from the scatter of the individual block LFs contributing to it. This method of estimating the background has some advantages over the more conventional background estimation method using an outer annulus around the galaxy cluster, since it uses a large background region, and the error estimate allows for the variance arising from the large scale structure. Finally, for each cluster we subtracted its composite background LF from the cluster LF, and propagated the errors.

Apparent magnitudes were converted to absolute magnitudes, using the distance for each cluster, and applying K-corrections calculated from Table 3 (for Hubble type E) in Frei & Gunn (1994). The use of early-type K-corrections is common in cluster studies, and justified by the dominance of early-type galaxies in clusters. However, if there were a systematic trend in early-type fraction with magnitude, then this could lead to some distortion of the LF slope. To quantify the maximum possible effect, we note that, using the tables in Frei & Gunn (1994), the K-correction for Hubble type E at z=0.6 for z' is 0.37 while it is 0.05 for Hubble type Im). Assuming (very conservatively) a systematic change from a 100% early-type to 100% late-type population across the faint end slope of our LFs, the impact of a differential error of 0.3

magnitudes on our determination of α would still only amount to $\Delta\alpha \approx 0.04$, which is small compared to the trends in α which represent some of our main results. The tables in Frei & Gunn (1994) apply to SDSS filters, which differ slightly from the corresponding MegaCam filters. The resulting differences in K-corrections are much smaller than the differences between early-type and late-type galaxies (about 0.03 at z=0.1 and 0.06 at z=0.6), and will have negligible effect on our derived LF slopes.

Finally, the data were binned into bins of width 0.5 magnitude (experiments showed that this bin size was a good choice in terms of fit quality and parameter confidence regions), and the resulting LFs were then fitted by a Schechter function model (Schechter 1976),

$$\phi(M)dM = 0.4ln(10)\phi^* e^{-X} X^{1+\alpha} dM, \tag{4.1}$$

where $X = 10^{-0.4(M-M^*)}$, M^* is the characteristic magnitude, ϕ^* is the characteristic number density and α is the faint-end slope, Lin et al. (1996). Contour plots of the 1σ, 2σ and 3σ confidence levels of α and M^* were also produced. The errors in the text and tables refer to the 1σ errors. We also calculated the total optical luminosity L_{OPT} of each cluster by integrating the fitted Schechter function from $5 \times M^*$ to -16.

In addition to single LFs for each galaxy cluster in our sample, we produced stacked luminosity functions. The radius used to determine the volume is the R^* of the cluster. Before stacking different clusters together, to correct for the evolution in the critical density of the Universe, we multiply the LF by

$$\frac{\rho_c(z=0)}{\rho_c(z=z_{cl})}, \tag{4.2}$$

where z is the redshift, ρ_c is the critical density of the Universe, a function of z, and z_{cl} is the redshift of the cluster. This correction is necessary for high-redshift clusters if stacked with low-redshift clusters to scale the galaxy density in each cluster to the density at redshift=0. The faintest magnitude bin is not necessarily the same for each cluster and to account for this, we divided the total number of galaxies in each magnitude bin by the summed volume of galaxy clusters that contributed to that bin only. The stacked LFs should enable us to study the evolution of the LF with redshift and to explore any differences between clusters of different temperature.

4.3 Results

4.3.1 Individual cluster luminosity functions

The values of α and M^* and L_{OPT} of the individual C1 clusters are presented in Table 4.2. The LF plots with the associated 1σ, 2σ and 3σ contours in the M^*-α plane for passbands r' and z' are shown in Appendices C.1 and D.1 respectively. For some of the C1 clusters, the fitting failed to constrain some of the parameters, M^* in particular, due to poor statistics or the lack of any well-defined turnover in the LF at the bright end. For these clusters the LF and best fit are presented without any accompanying confidence contour plot. These LFs are placed at the bottom of the Figs. For clusters with unconstrained M^*, L_{OPT} was also not constrained, because its value depends on both α and M^*. Therefore, we excluded these clusters in the part of the analysis related to L_{OPT}.

The average values of α for our sample of clusters are -1.70 ± 0.10, -1.64 ± 0.04 and -1.43 ± 0.03 for the g', r' and z' passbands respectively. The correlations between L_{OPT}, α and M^* and redshift, temperature (T) and the X-ray luminosity (L_X) taken from Pacaud et al. (2007), were tested using Pearson's correlation coefficient. These coefficients are computed from the ratio of the covariance of the tested variables, X and Y, to the square root of the product of the variances of these variables, i.e.

$$r = \frac{COV(X,Y)}{\sqrt{VAR(X) * VAR(Y)}}. \tag{4.3}$$

This correlation coefficient measures the linear correlation, if it is 1 or -1 then the two variables are perfectly positively or negatively linearly correlated, respectively. To compute the upper and lower 1 σ errors on the correlation coefficient r, we used Fisher's Z transformation: $Z = \tan^{-1} r$. The strongest correlations found are those between L_{OPT} and T and between L_{OPT} and L_X, both of which are expected from the scaling relations of galaxy clusters. In our sample, they both have a correlation coefficient of at least 0.9, see Table 4.3.

Because higher redshift clusters are more difficult to detect than nearby ones, they will tend to be more massive and hence hotter than typical nearby clusters, see Fig. 3 in Pacaud et al. (2007). This (*Malmquist*) selection effect is present in any deep cluster survey. To account for the $T-z$ correlation arising from this selection effect in the C1 sample, for each correlation coefficient between a quantity and T or z, we have also calculated the partial correlation coefficient between

the same two quantities, which attempts to remove any part of the correlation which arises due to the intrinsic trend in T with z within our sample.

For this we used an Interactive Data Language (*IDL*) routine, *p_correlate.pro* to compute the partial correlation coefficient. This uses the following method, which to be concrete we explain using the example of the correlation between α and redshift. Let α and redshift z are the variables of primary interest, whilst temperature T is a third variable whose effects we wish to remove. First, the routine calculates the residuals after regressing α on T; these are the parts of α that cannot be predicted by T. Likewise, it calculates the residuals after regressing z on T. Finally, the partial correlation coefficient between α and z, adjusted for T, is the correlation between these two sets of residuals.

The results of our correlation analysis for the unstacked clusters, are tabulated in the top section of Table 4.3. The correlation coefficients between the faint-end slope, α of the individual clusters and redshift are 0.44±0.27 for the r' band and 0.54±0.25 for the z' band. These coefficients, including the coefficient for the g' band, get stronger after the application of the partial analysis and the errors on the coefficients become smaller. This strongly suggests evolution of α with redshift in our sample.

We will further scrutinise this possibility in the section of redshift-stacked clusters, because stacking LFs of clusters with similar redshifts should lower scatter in the data and provide a means to probe possible trends. M^* also shows a negative correlation with redshift and with temperature but these correlations become insignificant in a partial correlation analysis.

4.3.2 Global scaling relations

The relationships between the global cluster properties, L_{OPT}, L_X and T provide a probe of cluster self-similarity. L_{OPT} is strongly correlated to the temperature of our clusters – the correlation coefficients between L_{OPT} and T are 0.95±0.06, 0.96±0.04 and 0.97±0.03 for the g', r' and z' bands respectively, whilst the partial correlation coefficients for the same quantities, factoring out the effects of z, are 0.87±0.16, 0.89±0.11 and 0.92±0.06, see third row in Table 4.3. The removal of the z effects has lowered the values of the coefficients but they are still high and significant. Correlation between L_{OPT} and L_X is also quite strong: 0.92±0.11 (g' band), 0.93±0.07 (r' band) and 0.90±0.08 (z' band).

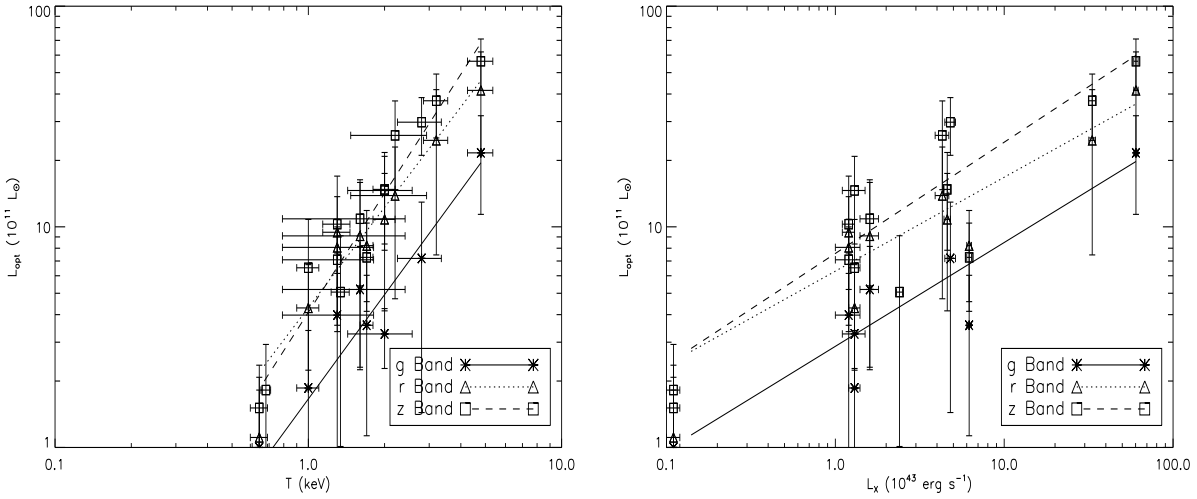

Figure 4.2: Correlation diagrams of L_{OPT} versus X-ray gas temperature, T (left panel) and L_{OPT} versus X-ray luminosity, L_X (right panel) of C1 clusters for passbands g' (stars), r' (triangles) and z' (squares). Clusters with unconstrained M^* and hence unconstrained L_{OPT} were excluded.

In Fig. 4.2, we plot L_{OPT} versus T (left panel) and L_{OPT} versus L_X (right panel). We calculate the slopes for these plots using the *Fortran* package *ODRPACK* (Akritas et al. 1996), which uses numerical orthogonal distance regression method to minimise perpendicular distances between points and the fitted line. One advantage of this is that the slope value will not change if the quantities in question switch axes. In addition, *ODRPACK* takes into account errors on both X-values and Y-values which are available for L_{OPT}, T and L_X.

The logarithmic slopes for the $L_{OPT}-T$ relation for the three filters g', r' and z', respectively are $1.57 \pm 0.17, 1.51 \pm 0.17$ and 1.79 ± 0.12, giving an average value of 1.62 ± 0.11. For the $L_{OPT} - L_X$ relation, the slopes are $0.47 \pm 0.07, 0.43 \pm 0.08$ and 0.50 ± 0.07, and the average value is 0.47 ± 0.05. Note that the slopes do not differ significantly for the three filters, except the slope of L_{OPT} versus T in the z' filter. Such relations between L_{OPT} on one hand, and L_X and the gas temperature on the other, are expected because richer and hence more luminous clusters have deeper gravitational potential wells which in turn raise the ICM temperature and its X-ray output by adiabatic compression and shocks generated by supersonic motion. We will discuss this further in Sec. 4.7.

The correlation coefficients between L_{OPT} and redshift are high (all above 0.8), but when the effects of temperature are removed they become insignificant in at least two of the filter set, therefore, this correlation is most likely due to selection effects, *Malmquist effect*, and does not

reflect any genuine relationship between L_{OPT} and z. Correlations between α and M^* and T, z and L_X were also computed, but none of those showed significantly high values.

Following the above analysis of trends in the properties of individual clusters, we now perform a stacking analysis, grouping clusters first by redshift, and then by temperature. This provides LFs of higher statistical quality, enabling the behaviour to be examined in greater detail.

4.3.3 Redshift-stacked clusters

The 14 C1 clusters span a redshift range 0.05 to 0.61. This range was divided into five redshift bins: 0.05-0.14, 0.26-0.26, 0.29-0.29, 0.30-0.32 and 0.43-0.61. The number of clusters in each bin ranges from two to four. The redshift ranges of these bins were chosen according to two criteria: first, the redshift range of the combined clusters was not too large, and second we required adequate data quality in each bin, to allow a well-constrained Schechter function fit. We kept the number of bins to at least five because a smaller number of bins increases the errors on the correlation coefficients. Plots of the redshift-stacked data with fitted Schechter functions for the three photometric bands are shown in Figs 4.3, 4.4 and 4.5, and results of the fits are given in Table 4.4.

The faint-end slope, α of the Schechter function of the stacked data shows an evolutionary trend, becoming less steep with increasing redshift. Three of the redshift bins (0.26-0.26, 0.29-0.29 and 0.30-0.32) have very similar redshifts and in general the α values for these three bins agree within their errors.

The Pearson and partial correlation coefficients were calculated for α and z, see Table 4.3. The coefficients are high (≥ 0.88) but with relatively large errors, mainly due to the small number of bins. The partial correlation analysis lowered the values of the coefficients and enlarged the errors. Evidence for evolution in α is seen in all three bands, arising primarily from the fact that the faint-end slope is steeper ($\alpha = -1.75$ to -1.8) in the low z bin than in the higher redshift bins.

One obvious concern in probing evolutionary trends in the Schechter function fits is that the fitted magnitude range decreases systematically with redshift, due to the apparent magnitude limit of our data. A second effect which might bias α is that within a given redshift bin, the contributing clusters are probed down to different absolute magnitudes, according to their

distance. Hence at the faint end, clusters may progressively drop out of the stacked LF. This is especially the case for the lowest and highest redshift bin, which are both much broader that the three bins at $z \approx 0.3$.

To show the scale of this latter effect, we have drawn a vertical dotted line on each of the stacked LF plots to show the faintest magnitude to which *all* clusters in the bin contribute. To the right (fainter side) of this line, one or more of the clusters in the redshift bin drop out of the stacked data.

To check whether the trend of α with redshift is robust against these two effects, we carried out tests on the stacked data, by progressively removing the faintest magnitude bin in the stacked LFs and re-fitting. In general, we found no significant change in the fitted values of α (which changed only within their errors), or in the α-z correlation when the LFs were truncated at the vertical dashed line, or when the LFs for all redshift bins were fitted to the same limiting absolute magnitude (which is set by the most distant systems). There was one exception to this. The three clusters in the highest redshift band (clusters 1, 6 and 49) all have α values (albeit with large errors) steeper that the shallow slope of -1.31 which fits to the stacked data in the g' band for this high redshift bin. As the faintest bins, to the right of the dashed line in the plot of Fig. 4.3 (e), are progressively removed, the fitted slope steepens. Hence the flat slope of -1.31 must be regarded as unsafe, and the very high α-z correlation in g' band, given in Table 4.3, is probably overestimated. Rather, we have a situation in all three photometric bands, where the faint-end slope is steeper at $z < 0.2$ than it is at higher redshift.

To visualise the behaviour of the faint-end slope in terms of both redshift and colour, we plot the faint end of the fitted luminosity functions for the three bands in Fig. 4.6 using green for g' band, red for r' band and black for z' band. For this plot, we have divided the sample into three redshift bins: low (0.05-0.14), intermediate (0.26-0.32) and high (0.43-0.61), denoted by different line styles. All LFs have been renormalised to have $\phi = 1$ at M=-19.5.

The figure shows how the faint end slope steepens towards low z. It also illustrates colour trends in α. At low redshift (solid lines), the slopes are very similar (though the curves are separated due to their different values of $M*$), whilst at intermediate redshift (dashed lines), the slope shows a strong trend with colour.

The values of α in Table 4.4 also show a trend with colour. The faint-end slope of z-stacked

clusters becomes steeper as we move from z' (red side) band to g' (blue side). This trend is very obvious in the second, third and fourth redshift bins ($0.29 \leq z \leq 0.32$) and much less obvious and maybe absent (within the errors) in the first bin($z \leq 0.14$), see Fig. 4.7 in which we plotted the values of α for the three bands for the lower- and intermediate redshift bins. The increase in the faint-end slope of the Schechter function in the bluer bands means that at the faint side of the colour-magnitude diagram the blue galaxies outnumber red ones.

To explore this we produced K-corrected colour-magnitude diagram (Figure 4.8) of $g'_2 - z'_2$ versus absolute $r_{\rm kron}$ magnitude for $0.29 \leq z \leq 0.32$ (six clusters: 8,13,18,22,27 and 40) in which this trend is most obvious, and the same plot for the first redshift bin, $0.05 \leq z \leq 0.14$ in which no such trend is apparent. Fig. 4.8 clearly demonstrate how the distribution of cluster galaxy colours changes from $z \sim 0$ to $z \sim 0.3$. In the g' band the evolution of α is much stronger, especially after removing the effects of the temperature (partial correlation). These trends in α show that the fraction of blue faint galaxies at $z \sim 0.3$ was larger than it is now, and suggests that these galaxies have reddened and moved upward in the CMD – i.e. they have become less active.

The Schechter function characteristic magnitude M^* in the redshift-stacked clusters showed a negative correlation with redshift. The correlation coefficients between M^* and redshift are high but less significant than those between α and redshift. However, when the partial calculations were carried out, these coefficients dropped and became consistent with zero. Hence the trend in M^* with z appears to be due to a selection effect: hotter clusters are more luminous, and so are more easily detected at high redshift, and these brighter clusters also tend to have brighter M^* (Zandivarez et al. 2006).

XLSSC number	g Band	r Band	z Band
		α	
1	-1.94±0.23	-1.59±0.2	-1.06±0.17
6	-1.61±0.16	-1.7±0.09	-1.31±0.09
8	-1.53±0.37	-1.39±0.2	-1.15±0.16
11	-1.67±0.09	-1.8±0.05	-1.71±0.04
13	-1.63±0.63	-1.5±0.07	-1.51±0.08
18	-1.21±0.88	-1.76±0.13	-1.53±0.12
21	-2.01±0.11	-1.89±0.06	-1.77±0.06
22	-1.62±0.26	-1.19±0.19	-1.16±0.15
25	-2.10±0.12	-1.73±0.09	-1.57±0.08
27	-1.78±0.14	-1.85±0.12	-1.56±0.10
40	-1.03±0.30	-1.55±0.13	-1.27±0.09
41	-1.84±0.07	-1.86±0.09	-1.67±0.08
44	-1.75±0.12	-1.47±0.07	-1.44±0.09
49	-1.99±0.38	-1.65±0.16	-1.36±0.12
		$M*$	
1	-34.65±***	-23.7±0.91	-23.47±0.32
6	-20.96±0.43	-23.24±0.50	-22.98±0.23
8	-21.42±2.11	-21.79±0.83	-22.55±0.69
11	-20.61±1.50	-21.81±1.84	-21.13±0.73
13	-19.78±1.22	-22.19±0.37	-24.31±0.73
18	-19.66±1.43	-31.09±***	-22.23±0.41
21	-30.21±***	-29.02±***	-21.16±0.80
22	-20.26±0.84	-20.62±0.39	-22.15±0.50
25	-29.29±***	-22.66±0.78	-22.98±0.52
27	-22.22±1.32	-33.02±***	-23.52±0.76
40	-21.30±0.78	-22.95±0.96	-23.21±0.50
41	-30.57±***	-32.20±***	-23.38±1.50
44	-33.23±***	-22.79±0.53	-23.42±0.62
49	-31.66±***	-23.06±0.82	-23.72±0.46
		L_{OPT} 10^{11} $L_{\odot}$	
1	57.51±***	24.66±17.20	37.27±11.98
6	21.64±10.25	41.53±20.52	56.29±14.72
8	3.98±3.63	3.07±1.92	7.09±3.74
11	1.00±0.82	1.11±0.97	1.51±0.85
13	1.86±1.53	12.93±4.75	23.17±12.84
18	1.27±0.99	107.34±***	14.61±6.25
21	0.94±***	4.19±***	1.82±1.11
22	3.58±2.45	4.22±1.64	7.27±3.13
25	10.95±***	10.81±6.65	14.78±6.95
27	7.19±5.75	42.62±***	14.81±8.72
40	5.20±2.95	10.10±6.79	12.87±5.47
41	12.99±***	12.21±***	5.06±4.05
44	95.01±***	9.45±4.25	13.28±6.70
49	17.41±***	13.86±9.14	25.97±11.23

Table 4.2: Results of the Schechter function fitting of the LFs of the 14 C1 galaxy clusters. For some clusters, the $M*$ values were not constrained by the fitting program and the errors of these unconstrained $M*$ are starred. Also, the errors of the corresponding L_{OPT} values are starred, since the computation of L_{OPT} depends on both α and $M*$.

Quantities	g' Band P.C. Coeff.	r' Band P.C. Coeff.	z' Band P.C. Coeff.
Individual non-stacked C1 clusters			
L_{OPT},L_X	0.92±0.11	0.93±0.07	0.90±0.08
L_{OPT},T	0.95±0.06	0.96±0.04	0.97±0.03
L_{OPT},T,z (Partial)	0.87±0.16	0.89±0.11	0.92±0.06
L_{OPT},z	0.82±0.21	0.83±0.16	0.86±0.10
L_{OPT},z,T (Partial)	0.28±0.44	0.36±0.36	0.61±0.22
α,L_X	-0.08±0.30	0.23±0.30	0.64±0.21
α,T	0.01±0.29	0.05±0.30	0.54±0.25
α,T,z (Partial)	0.00±0.29	-0.37±0.28	-0.17±0.30
α,z	0.01±0.29	0.44±0.27	0.54±0.25
α,z,T (Partial)	0.20±0.30	0.67±0.20	0.65±0.21
M^*,T	-0.32±0.43	-0.57±0.31	-0.48±0.26
M^*,T,z (Partial)	-0.47±0.41	-0.15±0.37	-0.02±0.29
M^*,z	-0.06±0.43	-0.57±0.31	-0.48±0.26
M^*,z,T (Partial)	0.25±0.44	0.00±0.36	0.00±0.29
Redshift-stacked			
α,z	0.97±0.10	0.88±0.29	0.89±0.29
α,z,T (Partial)	0.91±0.24	0.65±0.58	0.51±0.65
M^*,z	-0.86±0.33	-0.87±0.31	-0.71±0.53
M^*,z,T (Partial)	-0.21±0.67	-0.58±0.62	-0.33±0.68
Temperature-stacked			
α,T	0.10±0.64	0.31±0.68	0.75±0.49
α,T,z (Partial)	-0.44±0.67	-0.85±0.35	-0.45±0.67
M^*,T	-0.46±0.67	-0.26±0.67	0.67±0.56
M^*,T,z (Partial)	0.20±0.67	-0.46±0.67	0.25±0.67

Table 4.3: Pearson's correlation coefficients (P.C. Coeff.) of individual C1 clusters, redshift-stacked clusters and temperature-stacked clusters for the three-filter set (g', r' and z'). 'X,Y,Z (Partial)' denotes partial correlation coefficient of quantities X and Y with effects of quantity Z removed, to be compared with the line directly above it, where correlation coefficient of the same quantities X and Y is presented without partial analysis.

Redshift-Stacked								
z-Range	Average T (keV)	Clusters-Stacked	α (g' Band)	α (r' Band)	α (z' Band)	M^* (g' Band)	M^* (r' Band)	M^* (z' Band)
0.05-0.14	0.89	11,21,41	-1.79±0.05	-1.75±0.03	-1.75±0.02	-20.15±0.51	-20.69±0.48	-22.03±0.54
0.26-0.26	1.65	25,44	-1.66±0.10	-1.55±0.07	-1.48±0.07	-21.05±0.36	-22.86±0.48	-23.31±0.46
0.29-0.29	2.25	22,27	-1.67±0.13	-1.54±0.10	-1.30±0.10	-20.76±0.47	-21.90±0.46	-22.25±0.35
0.30-0.32	1.48	8,13,18,40	-1.59±0.22	-1.47±0.07	-1.27±0.07	-20.56±0.58	-21.99±0.25	-22.54±0.21
0.43-0.61	3.40	1,6,49	-1.31±0.09	-1.46±0.08	-1.22±0.06	-21.40±0.26	-22.99±0.31	-23.49±0.18
Temperature-Stacked								
T-Range (keV)	Average z	Clusters-Stacked	α (g' Band)	α (r' Band)	α (z' Band)	M^* (g' Band)	M^* (r' Band)	M^* (z' Band)
0.64-1.00	0.15	11,13,21	-1.67±0.05	-1.80±0.02	-1.79±0.02	-20.11±0.45	-22.97±0.58	-25.68±2.13
1.30-1.34	0.23	8,41,44	-1.57±0.05	-1.54±0.05	-1.42±0.04	-21.12±0.30	-22.32±0.31	-23.05±0.28
1.60-2.20	0.34	18,22,25,40,49	-0.90±0.10	-1.26±0.05	-1.18±0.04	-19.64±0.20	-21.71±0.18	-22.85±0.17
2.80-3.20	0.45	1,27	-1.45±0.08	-1.22±0.07	-1.15±0.05	-22.24±0.44	-22.78±0.28	-23.58±0.20
4.80-4.80	0.43	6	-1.61±0.16	-1.70±0.09	-1.31±0.09	-20.96±0.43	-23.24±0.50	-22.98±0.23

Table 4.4: Results of the Schechter function fitting of the redshift-stacked and temperature-stacked clusters for the three-filter set (g', r' and z').

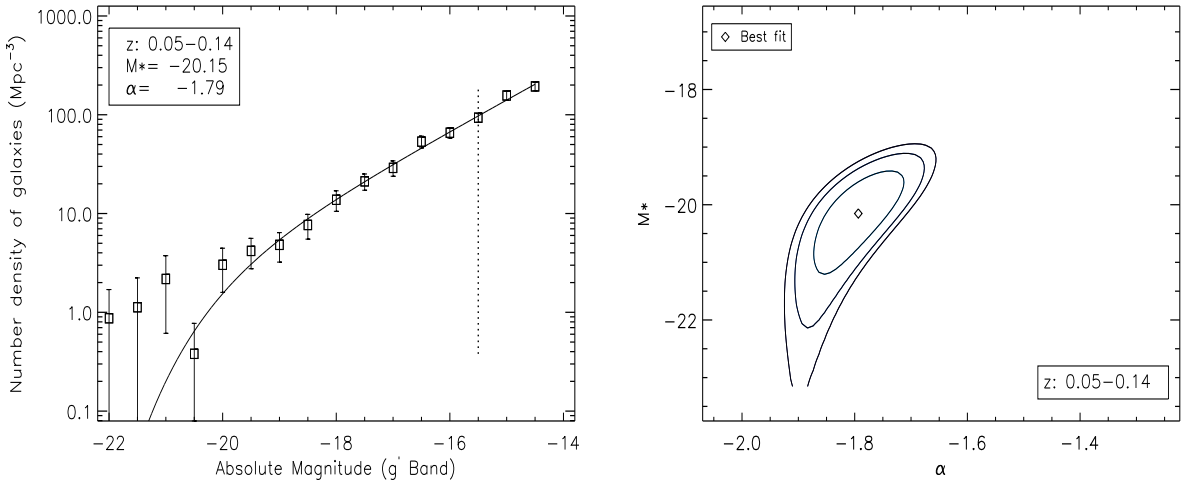

(a) Redshift: 0.05-0.14 (g' band)

Figure 4.3: LFs of the stacked clusters for 5 redshift ranges and the associated 1σ, 2σ and 3σ contours for g' band. All stacked clusters contributed to all magnitude bins are at the left side (brighter side) of the vertical dotted line which is at the faintest common magnitude bin of the clusters. Whereas at the right side (fainter side) of it, some clusters did not have data in some magnitude bins because they already reached their faintest magnitude limit.

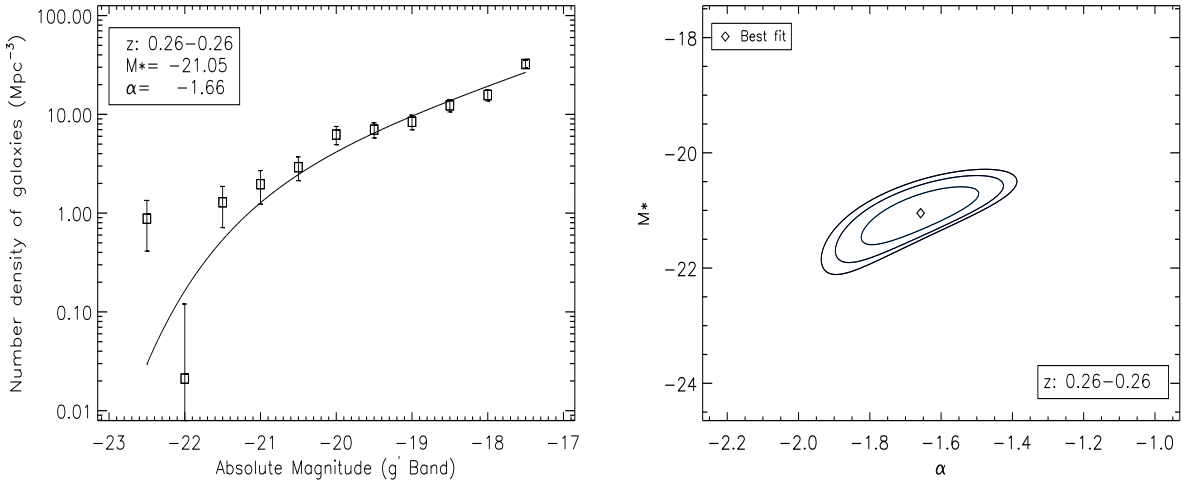

(b) Redshift: 0.26-0.26 (g' band)

Figure 4.3: (*continued*)

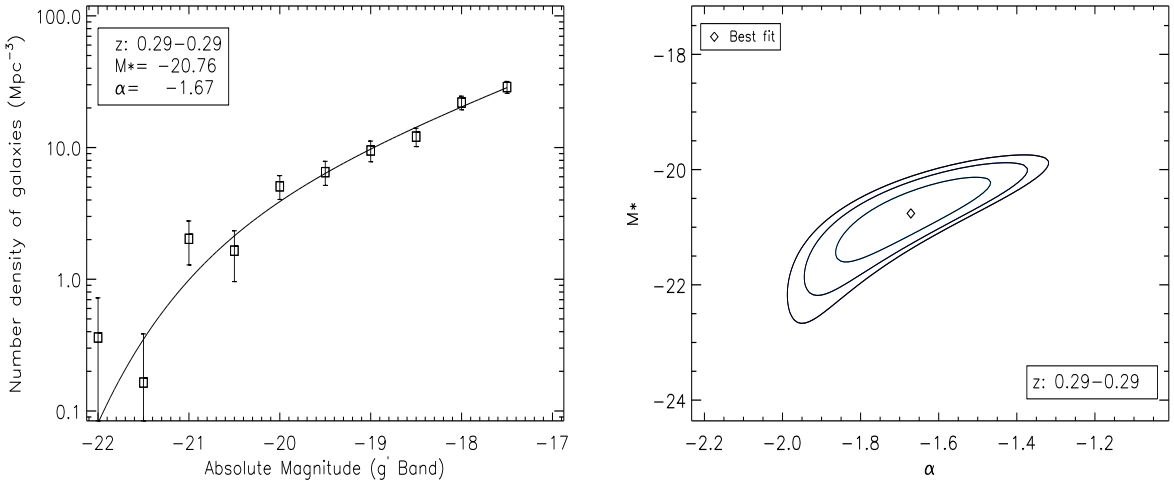

(c) Redshift: 0.29-0.29 (g' band)

Figure 4.3: (*continued*)

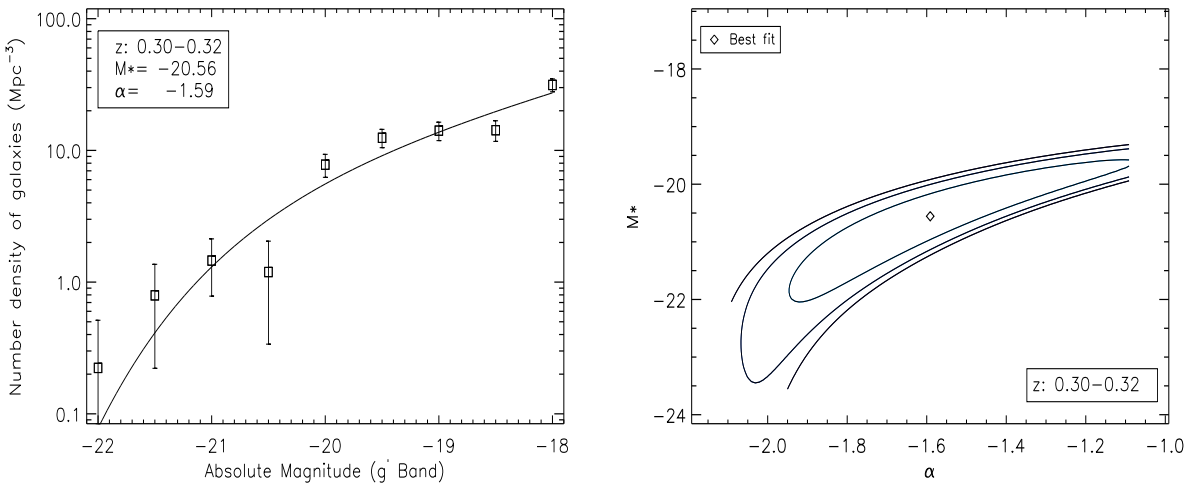

(d) Redshift: 0.30-0.32 (g' band)

Figure 4.3: (*continued*)

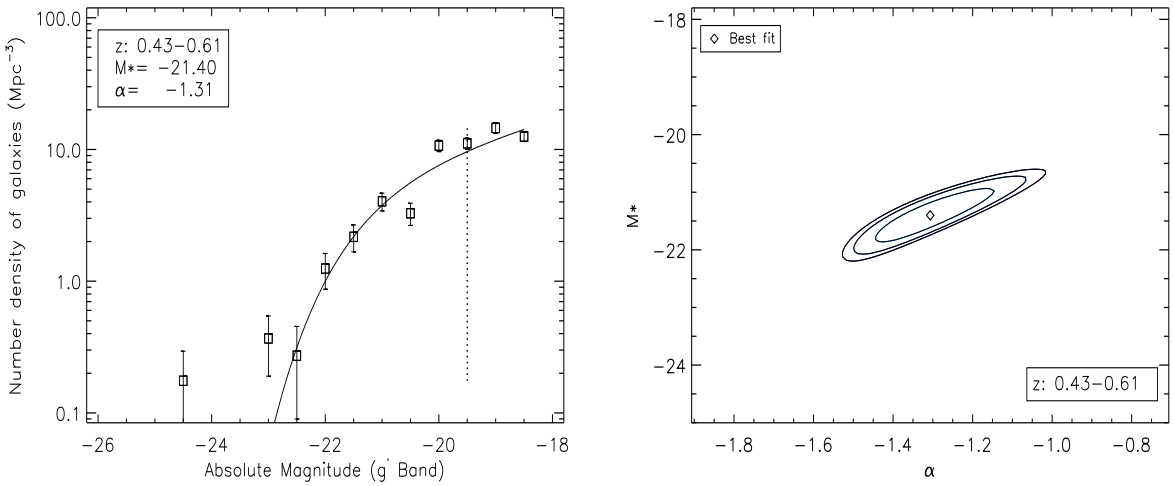

(e) Redshift: 0.43-0.61 (g' band)

Figure 4.3: (*continued*)

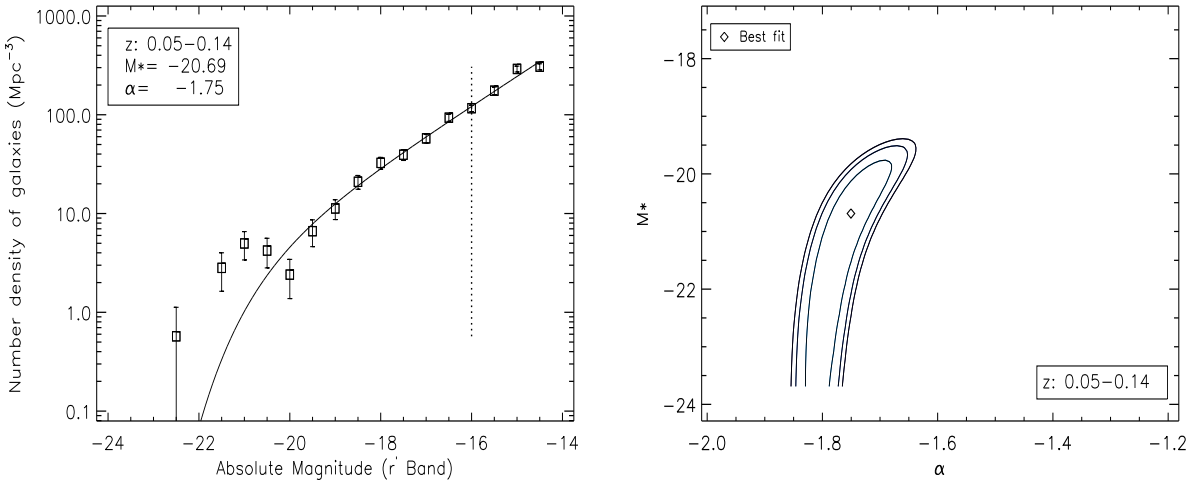

(a) Redshift: 0.05-0.14 (r' band)

Figure 4.4: LFs of the stacked clusters for 5 redshift ranges and the associated 1σ, 2σ and 3σ contours for r' band. All stacked clusters contributed to all magnitude bins are at the left side (brighter side) of the vertical dotted line which is at the faintest common magnitude bin of the clusters. Whereas at the right side (fainter side) of it, some clusters did not have data in some magnitude bins because they already reached their faintest magnitude limit.

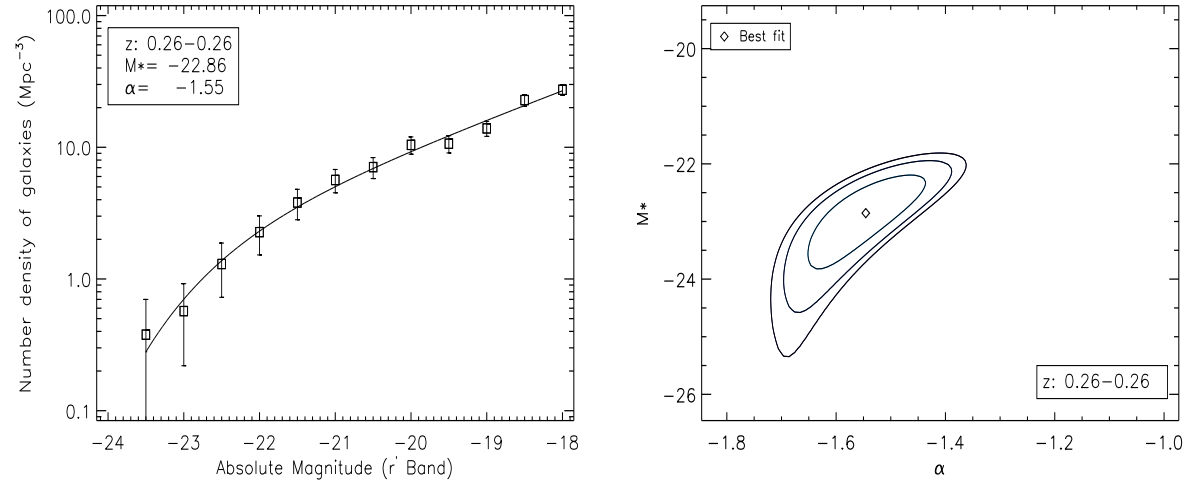

(b) Redshift: 0.26-0.26 (r' band)

Figure 4.4: (*continued*)

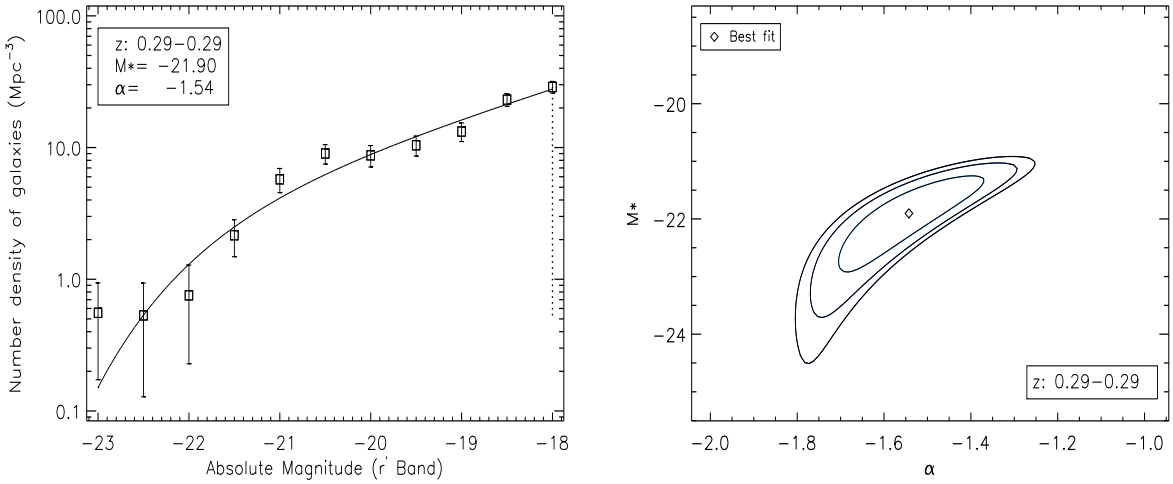

(c) Redshift: 0.29-0.29 (r' band)

Figure 4.4: (*continued*)

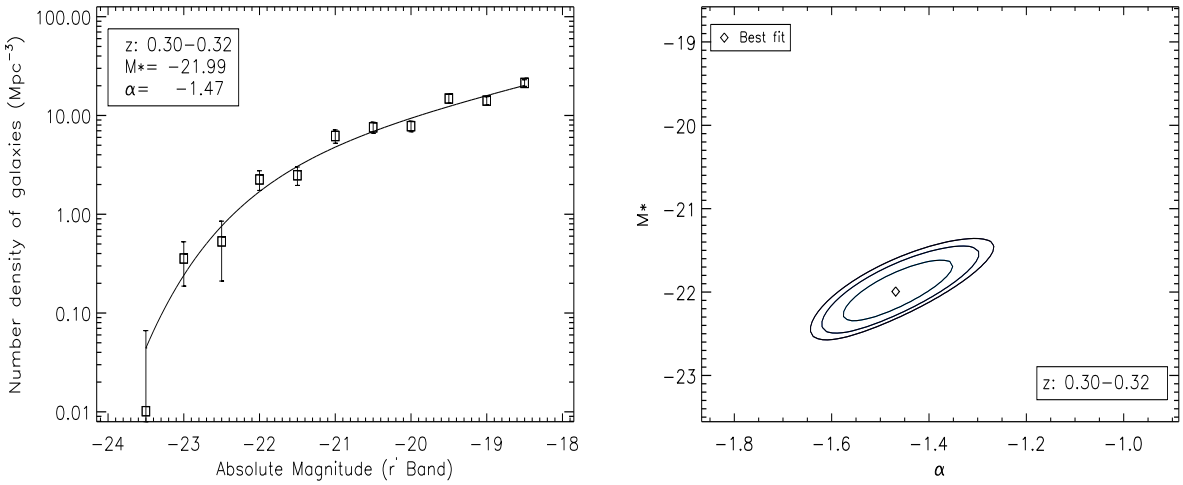

(d) Redshift: 0.30-0.32 (r' band)

Figure 4.4: (*continued*)

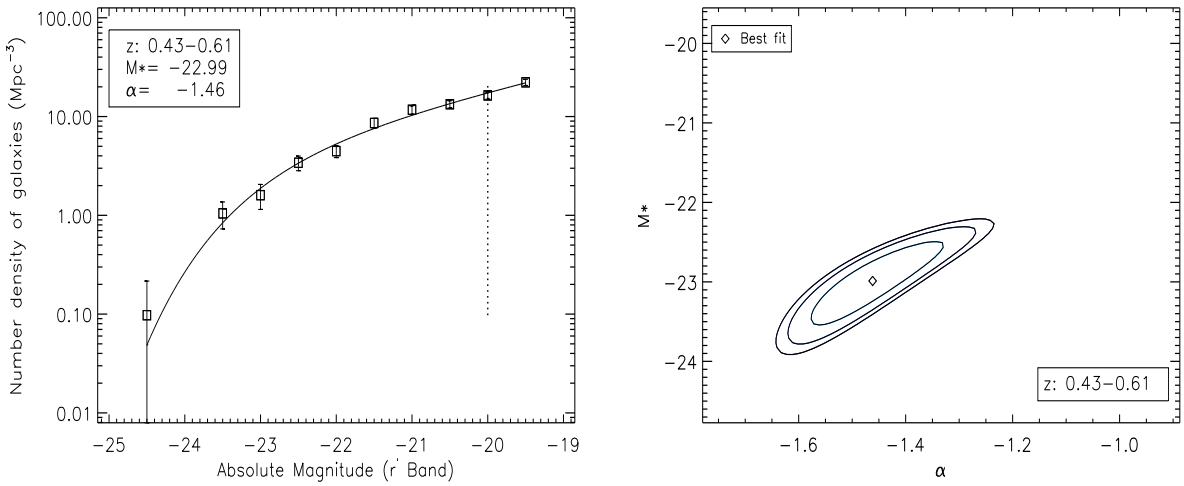

(e) Redshift: 0.43-0.61 (r' band)

Figure 4.4: (*continued*)

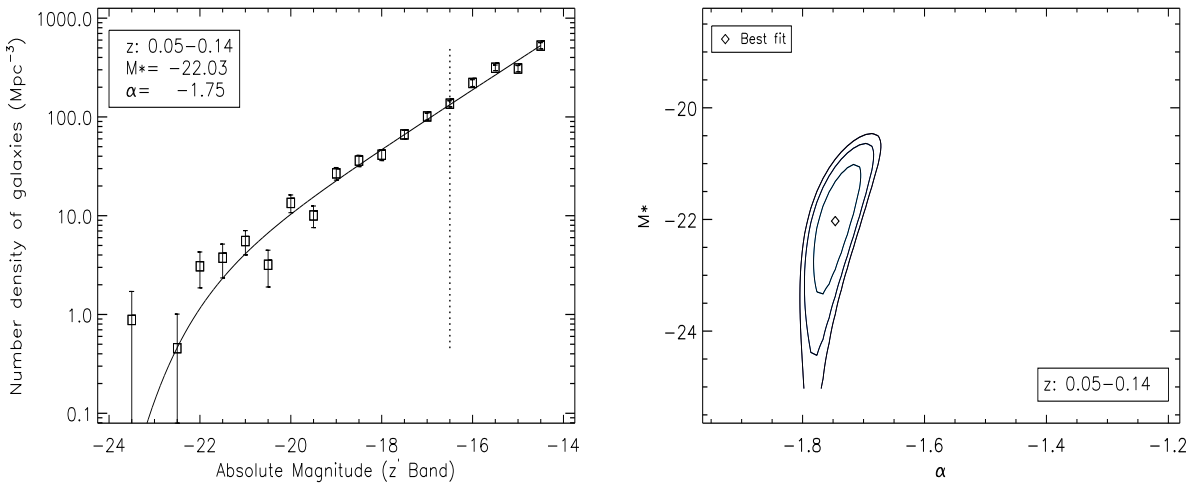

(a) Redshift: 0.05-0.14 (z' band)

Figure 4.5: LFs of the stacked clusters for 5 redshift ranges and the associated 1σ, 2σ and 3σ contours for z' band. All stacked clusters contributed to all magnitude bins are at the left side (brighter side) of the vertical dotted line which is at the faintest common magnitude bin of the clusters. Whereas at the right side (fainter side) of it, some clusters did not have data in some magnitude bins because they already reached their faintest magnitude limit.

4.3.4 Luminosity functions of $z \sim 0.3$ clusters

Eight amongst the 14 C1 clusters, more than half of our sample, lie within the narrow redshift range 0.26 to 0.32. These clusters are representative of low-mass clusters at intermediate redshifts - a population which dominates the XMM-LSS cluster dataset. Stacking these clusters together provides the best available composite LF for X-ray selected poor clusters at $z \sim 0.3$, which should be valuable for future comparative studies. The LFs and their associated error contours are shown in Figs 4.9, 4.10 and 4.11.

These clusters range in temperature from 1.3 to 2.8 keV. Schechter fits give α values -1.66 ± 0.11, -1.50 ± 0.05 and -1.36 ± 0.05, and M^* values -21.07 ± 0.38, -22.21 ± 0.22 and -22.83 ± 0.17, for the g', r' and z' bands respectively. Their faint-end slopes are shallower than the local clusters ($z \leq 0.14$) but steeper than higher-redshift ($z \geq 0.43$) ones. The colour trend of α is very obvious and seems to be a characteristic of $z \sim 0.3$ clusters compared to other clusters in other redshift bins, as mentioned above. Wilman et al. (2005a) studied a sample of poor clusters at redshift $z \sim 0.4$ selected from the CNOC2 galaxy redshift survey. Comparing this optically selected sample with nearby clusters, they found that the fraction of passive galaxies declines with redshift, which is consistent with our finding of larger population of faint blue galaxies at

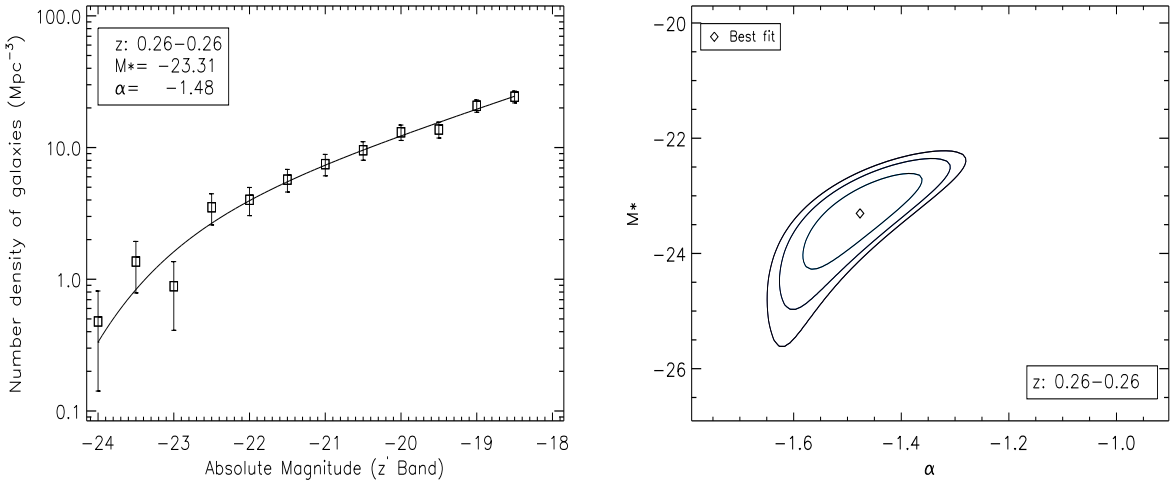

(b) Redshift: 0.26-0.26 (z' band)

Figure 4.5: (*continued*)

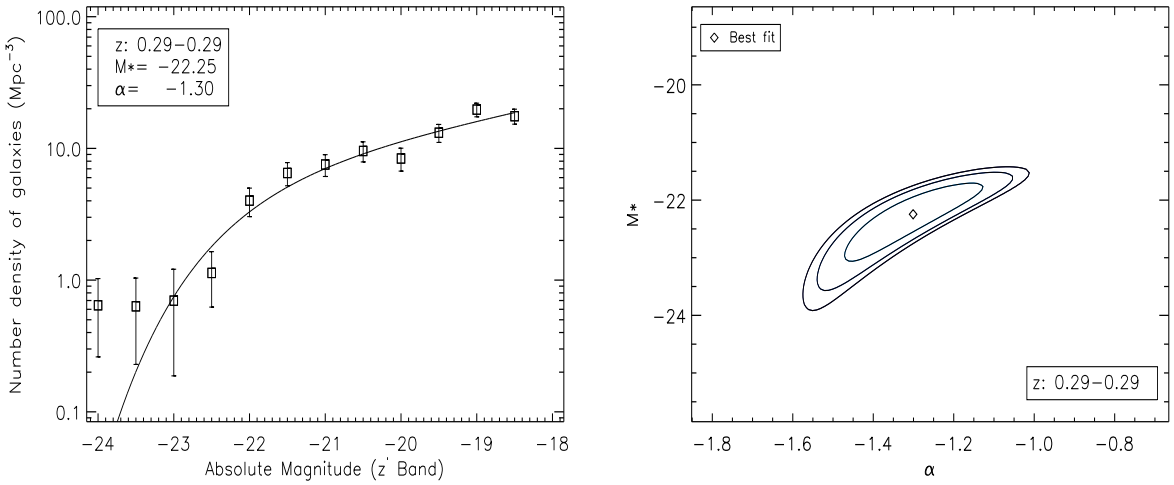

(c) Redshift: 0.29-0.29 (z' band)

Figure 4.5: (*continued*)

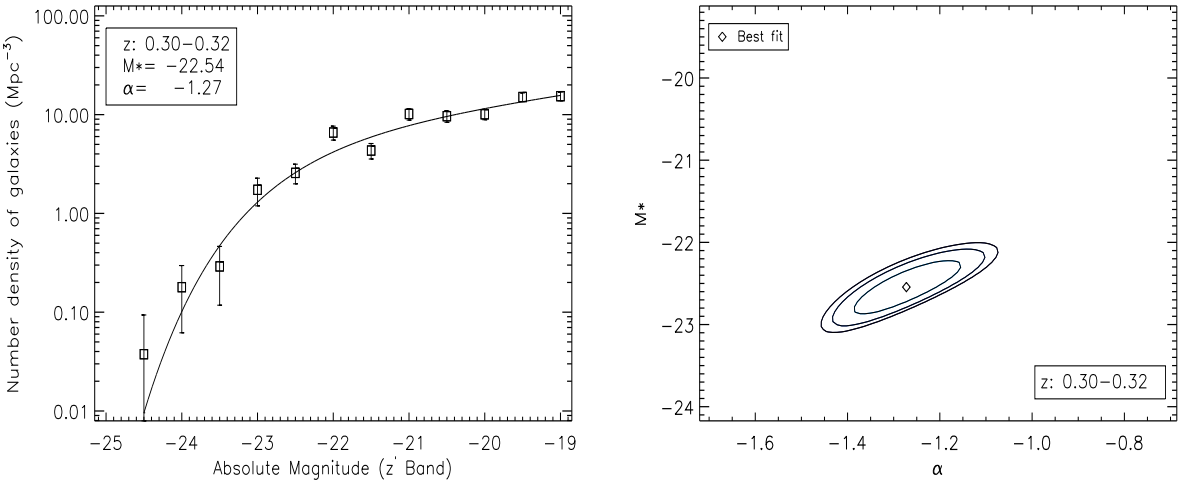

(d) Redshift: 0.30-0.32 (z' band)

Figure 4.5: (*continued*)

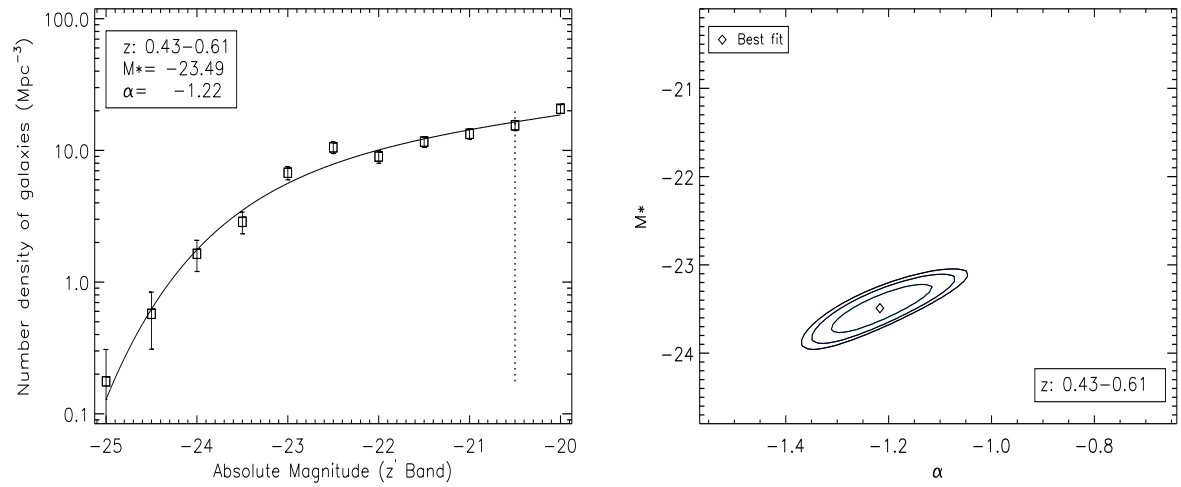

(e) Redshift: 0.43-0.61 (z' band)

Figure 4.5: (*continued*)

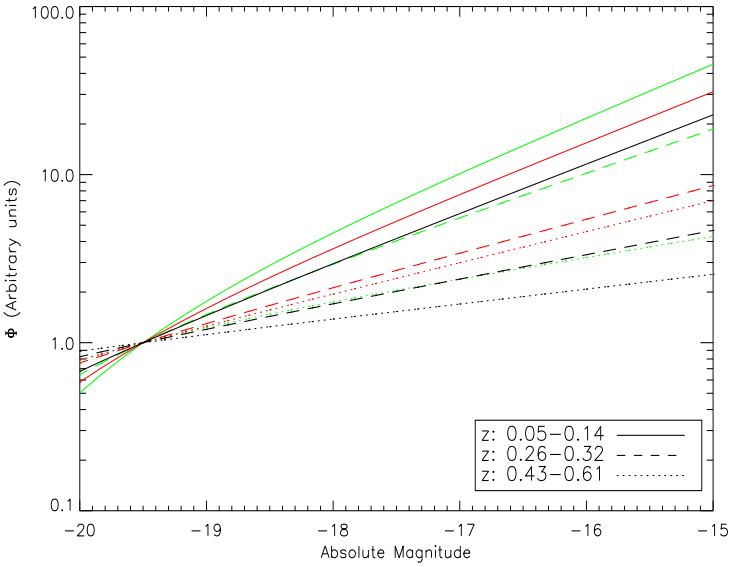

Figure 4.6: The faint end of the fitted LFs of the C1 sample grouped into three redshift bins: low (0.05-0.14, solid lines), intermediate (0.26-0.32, dashed lines) and high (0.43-0.61, dotted lines). Colours represent the filter bands: green for g', red for r' and black for z'. All LFs were normalised to have $\phi = 1$ at M=-19.5 for easy comparison. The faint end slopes become shallower with increasing redshifts. Also, at intermediate redshift (dashed lines), the slope shows a trend with colour, becoming steeper towards the blue. This colour trend largely vanishes at low redshifts (solid lines).

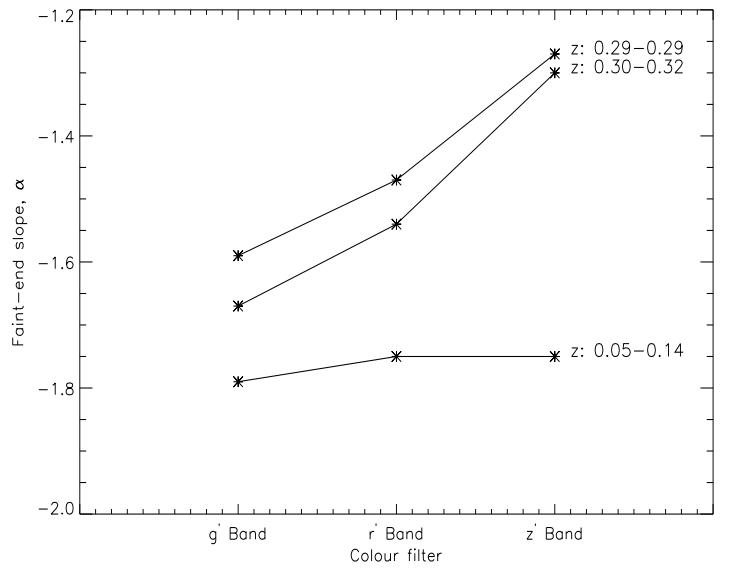

Figure 4.7: The faint-end slope of the fitted Schechter function in g', r' and z' bands for local clusters with redshift 0.05 to 0.14 and for intermediate redshift ($0.29 \leq z \leq 0.32$) clusters.

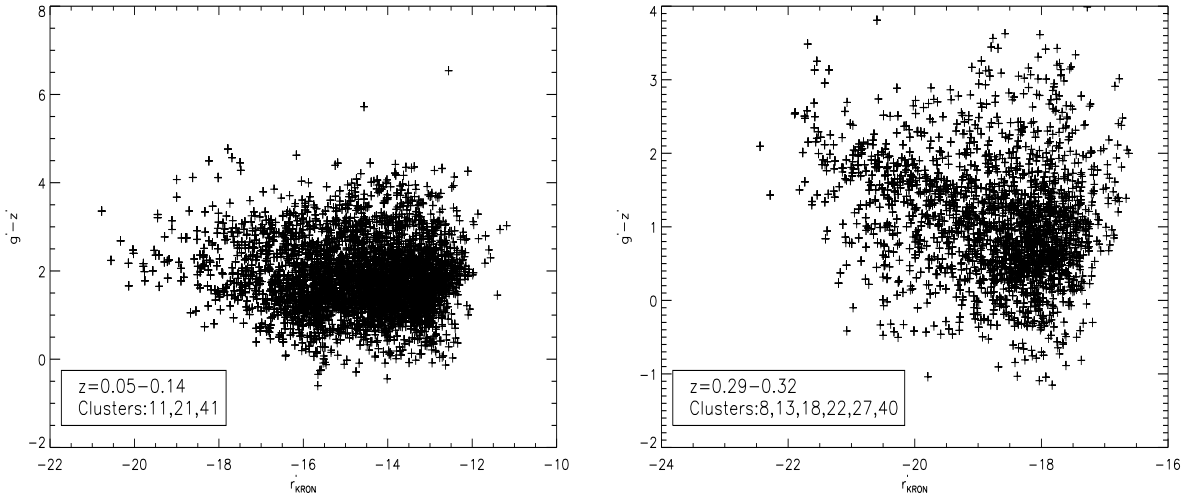

Figure 4.8: Colour-magnitude diagram: $g' - z'$ versus r' (K-corrected) for low-redshift (z=0.05-0.14) clusters and intermediate-redshift (z=0.29-0.32) clusters.

$z \sim 0.3$. However, these authors did not study the LF of their intermediate redshift groups.

In a recent study, Harsono & De Propris (2009) presented composite LFs of six rich ($T \sim$ 7-9 keV) clusters with redshifts ranging from 0.14 to 0.40 (averaging to 0.246) in the B, g, V, r, i and z bands. The LFs were well fitted by a single Schechter function with α values for g, r and z bands as follows: -1.31 ± 0.04, -1.33 ± 0.03 and -1.45 ± 0.02 and the corresponding M^* values were -20.94 ± 0.17, -21.95 ± 0.29 and -22.26 ± 0.30. Their M^* values are in reasonable agreement with ours, but their slopes are shallower, and show no trend with colour. However, their data were limited to 20-40% of the area within R_{200}, and they suggest that the lack of any upturn in the slope at faint magnitudes may be related to this – the extra faint galaxies responsible for the upturn being associated with a population infalling into clusters. In contrast, our data extend to $1.5 \times R_{500}$, which is approximately equal to R_{200}.

4.3.5 Temperature-stacked clusters

The 14 C1 clusters span a temperature range of 0.64 to 4.80 keV This was divided into five subranges: 0.64-1.00, 1.30-1.34, 1.60-2.20, 2.80-3.20 and 4.80-4.80, using the same criteria, discussed above, which were used for stacking into redshift bins. The highest temperature bin consists of only one cluster because after removing the three high-redshift clusters (2,5 and 29), the temperature difference between the two highest temperature clusters was too large to stack them together, and the LF of the highest temperature cluster, cluster 6 (T=4.80 keV) was of

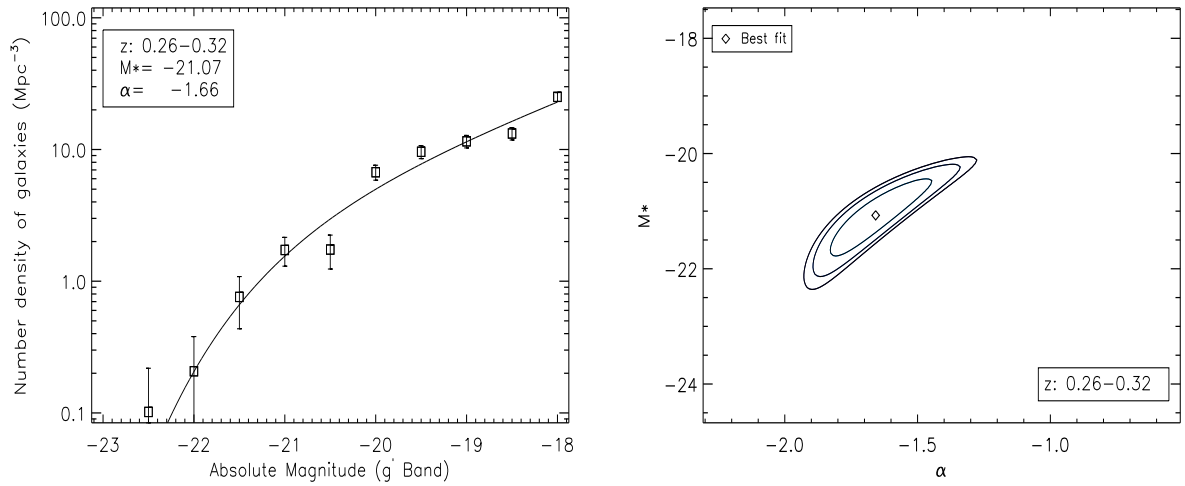

Figure 4.9: LFs of the eight stacked C1 clusters with redshift 0.2 to 0.4 and their associated 1σ, 2σ and 3σ contours of confidence levels for α and M^* in the g' band.

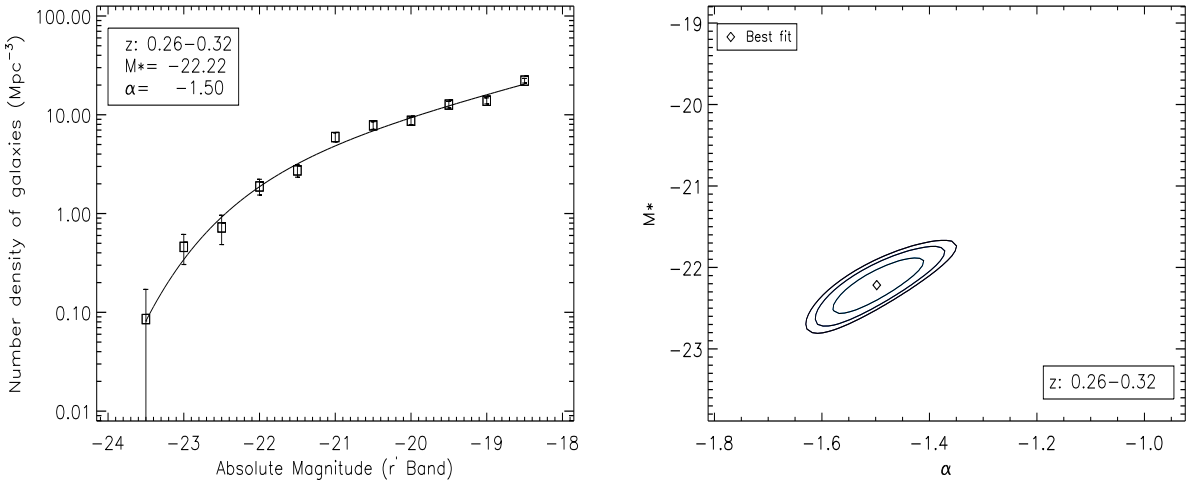

Figure 4.10: LFs of the eight stacked C1 clusters with redshift 0.2 to 0.4 and their associated 1σ, 2σ and 3σ contours of confidence levels for α and M^* in the r' band.

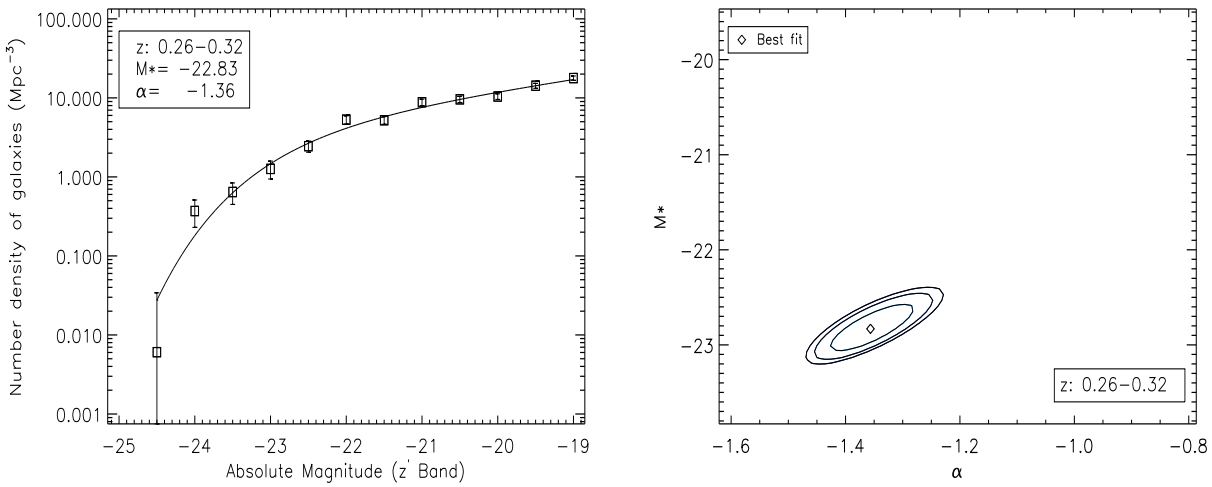

Figure 4.11: LFs of the 8 stacked C1 clusters with redshift 0.2 to 0.4 and their associated 1σ, 2σ and 3σ contours of confidence levels for α and M^* in the z' band.

sufficient quality that it provides useful constraints on its own. The second highest temperature bin consists of two clusters and the rest have at least three clusters.

The correlation coefficients of α with temperature are not high enough to establish any trend, especially when we take into consideration the reverse in sign of the coefficients after the partial correlation calculation, see Table 4.3. But in Table 4.4 the highest temperature bin contains only one cluster (cluster 6) and the other bins show some indication that α increases (slope decreases) with temperature, especially in bands r' and z'. Further investigation is needed to arrive at more conclusive results about the α tend with temperature. As to M^*, the stacked results do not show any trend with temperature. The LFs of the temperature stacked data are shown in Figs 4.12, 4.13 and 4.14.

Some previous studies (see for example, Miles et al. 2004) found that galaxy clusters with low X-ray luminosity (comparable to the coolest clusters in our C1 sample) exhibit dips in their LFs. In our data, some of the temperature stacked LF plots (4.12, 4.13 and 4.14), especially those with high temperature ($\geq$ 2.8 keV) showed signs of dips in the faint end of the LF. It can be hard to distinguish between scatter of the data points and a genuine dip in the LF.

To test the genuineness of these dips we fitted a Schechter function minus a Gaussian function defined by three parameters (central magnitude, width and depth) to these temperature stacked LFs. The two fits, with and without the Gaussian were statistically compared using their χ^2 values, and an F-test applied to assess the significance of the improvement resulting from

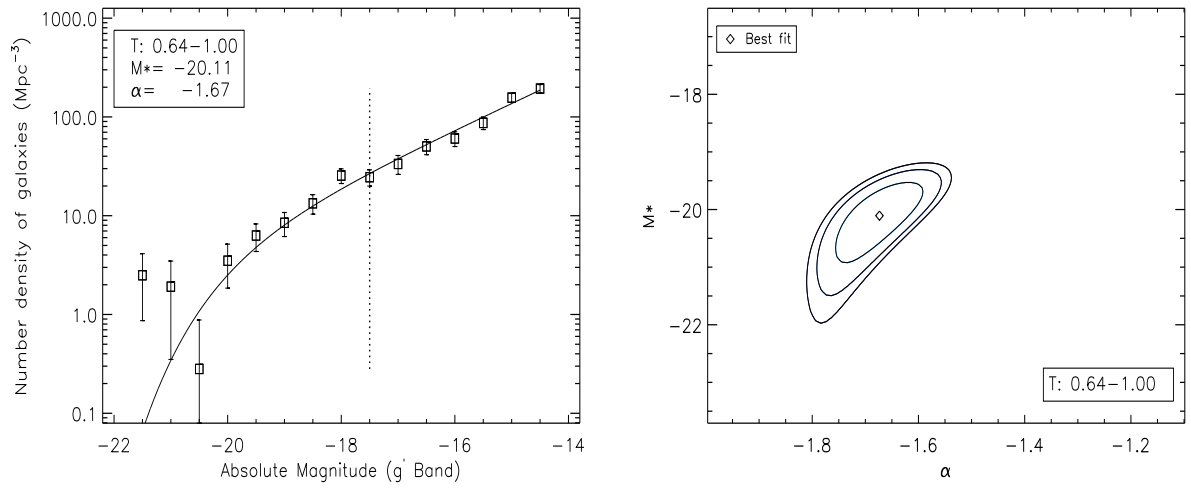

(a) Temperature: 0.64-1.00 (g' band)

Figure 4.12: LFs of the stacked clusters for 5 temperature ranges and the associated 1σ, 2σ and 3σ contours for g' band. All stacked clusters contributed to all magnitude bins are at the left side (brighter side) of the vertical dotted line which is at the faintest common magnitude bin of the clusters. Whereas at the right side (fainter side) of it, some clusters did not have data in some magnitude bins because they already reached their faintest magnitude limit.

inclusion of the dip. In some cases the dip improved the fit at a confidence level of more than 90%. See, for example Fig. 4.15.

However, careful examination of the stacked LF and the individual clusters LFs in these cases suggested that the dip is produced by the stacking of clusters with different faintest magnitude limits, rather than lying within the magnitude range shared by all the combined clusters. This was found to be true for all stacked LFs that showed a statistical improvement in fit on inclusion of a Gaussian dip. We therefore conclude that our data show no evidence for real dips in the optical LFs of the C1 clusters.

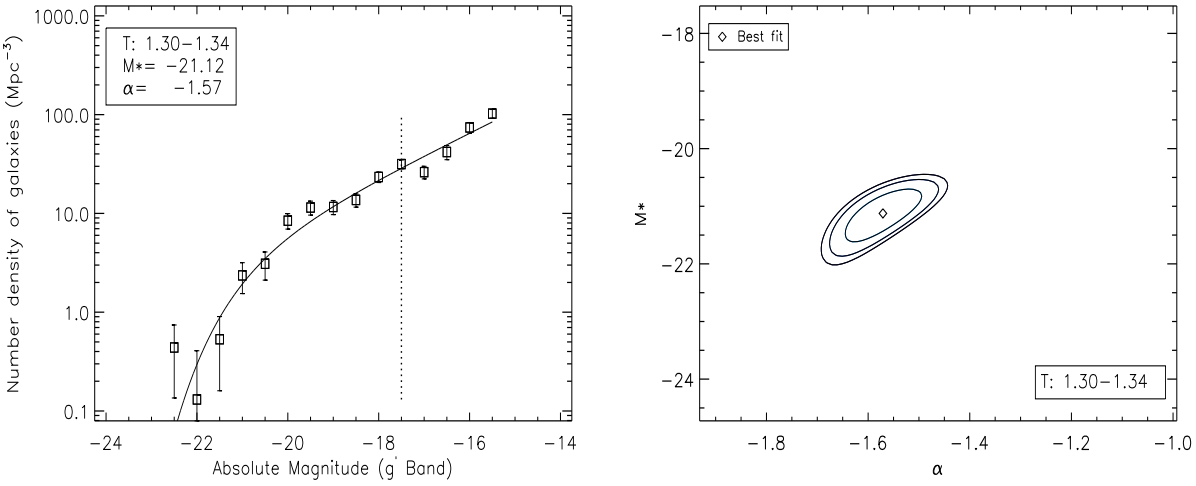

(b) Temperature: 1.30-1.34 (g' band)

Figure 4.12: (*continued*)

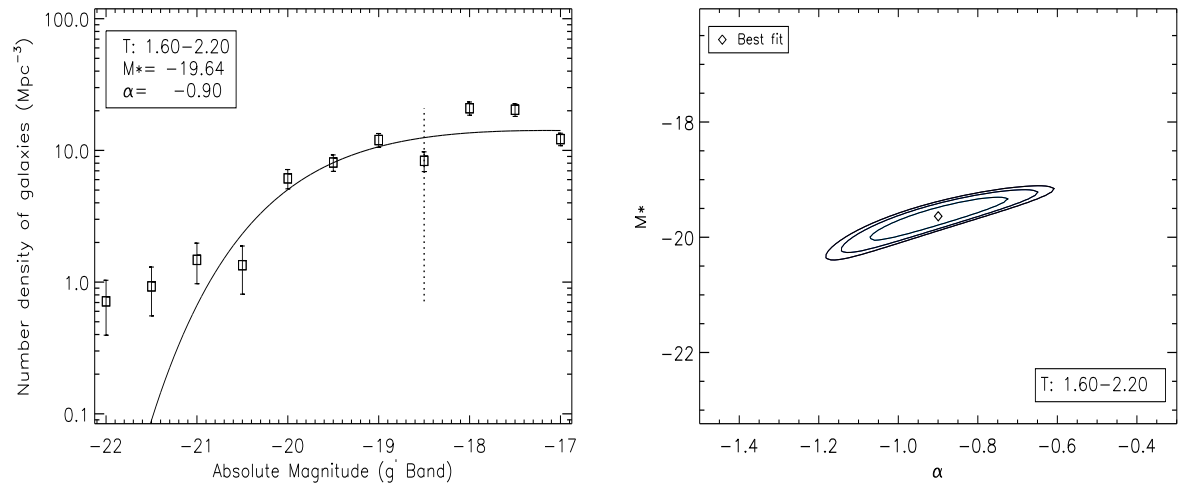

(c) Temperature: 1.60-2.20 (g' band)

Figure 4.12: (*continued*)

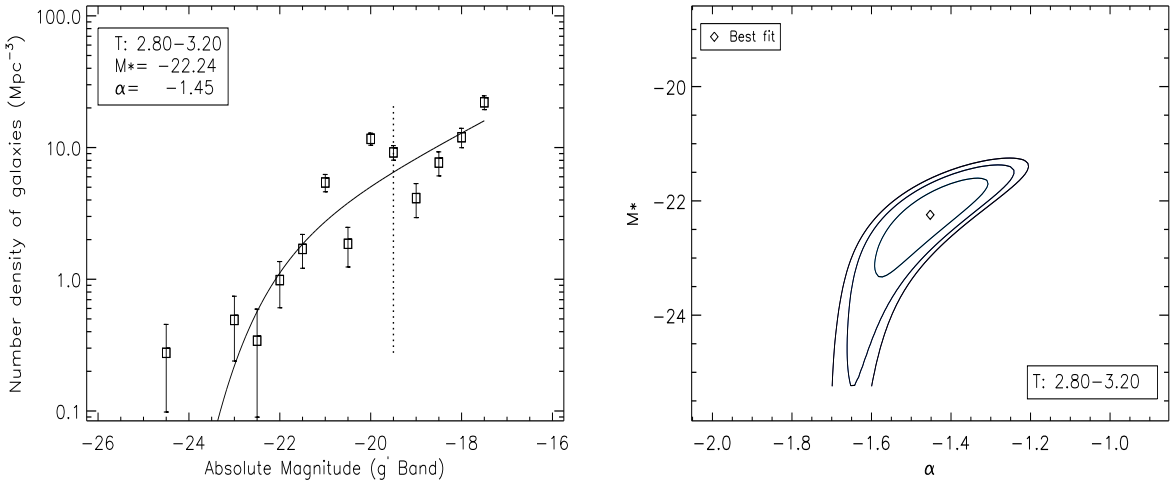

(d) Temperature: 2.80-3.20 (g' band)

Figure 4.12: (*continued*)

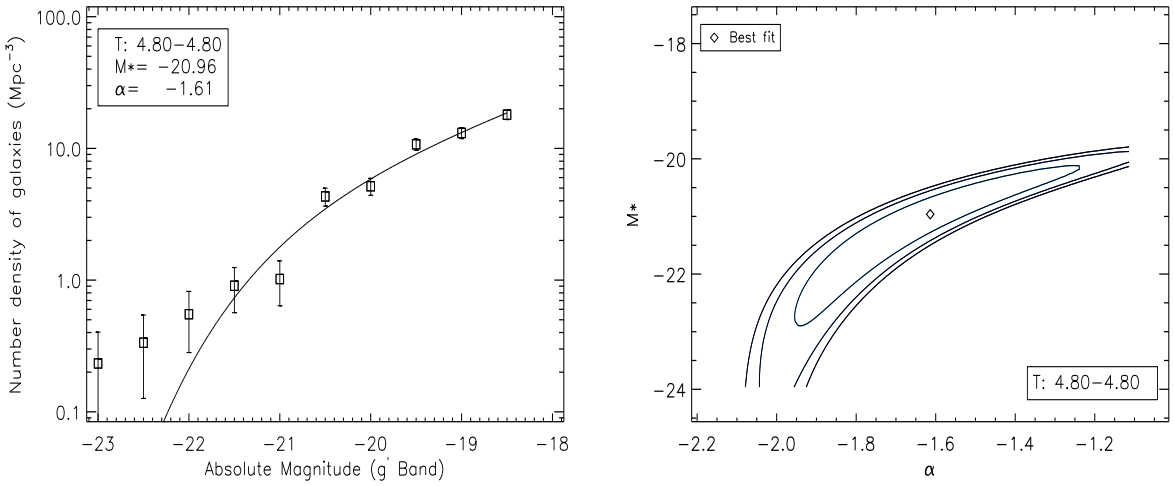

(e) Temperature: 4.80-4.80 (g' band)

Figure 4.12: (*continued*)

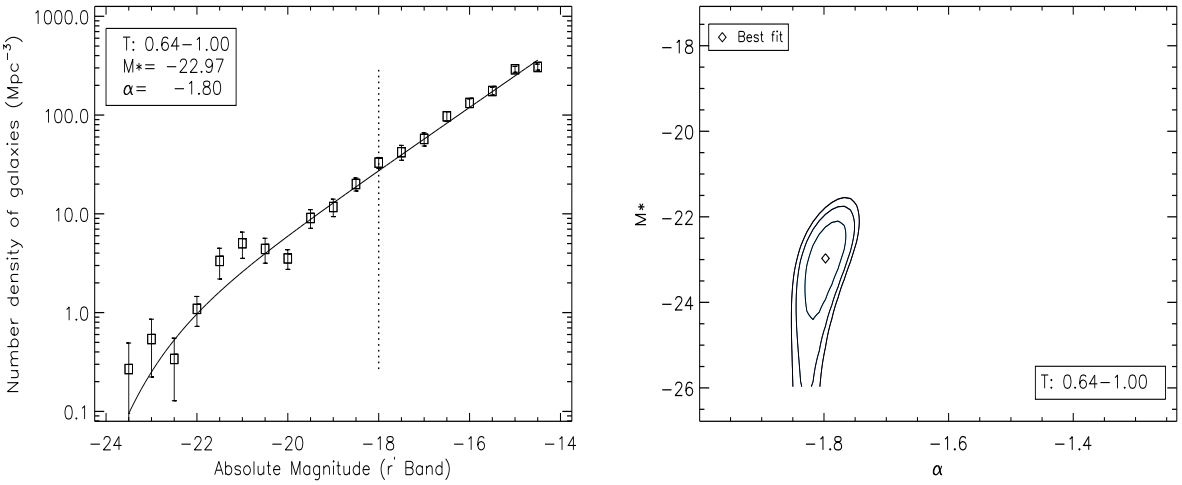

(a) Temperature: 0.64-1.00 (r' band)

Figure 4.13: LFs of the stacked clusters for 5 temperature ranges and the associated 1σ, 2σ and 3σ contours for r' band. All stacked clusters contributed to all magnitude bins are at the left side (brighter side) of the vertical dotted line which is at the faintest common magnitude bin of the clusters. Whereas at the right side (fainter side) of it, some clusters did not have data in some magnitude bins because they already reached their faintest magnitude limit.

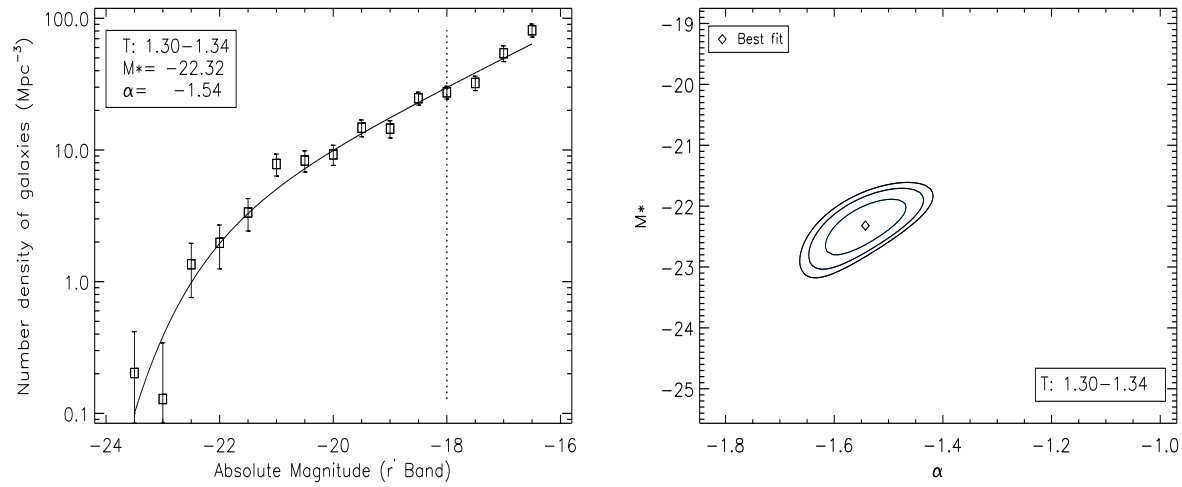

(b) Temperature: 1.30-1.34 (r' band)

Figure 4.13: (*continued*)

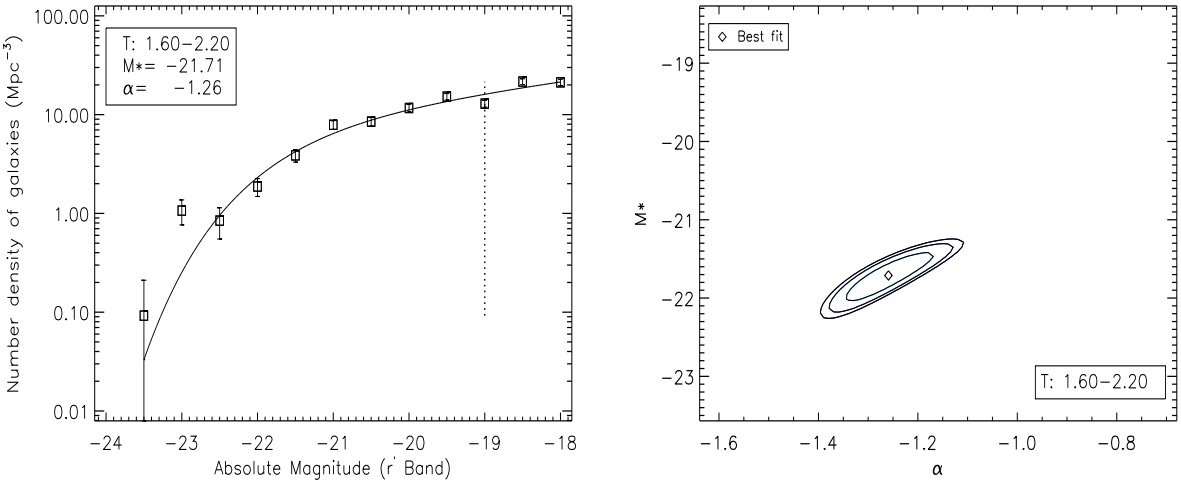

(c) Temperature: 1.60-2.20 (r' band)

Figure 4.13: (*continued*)

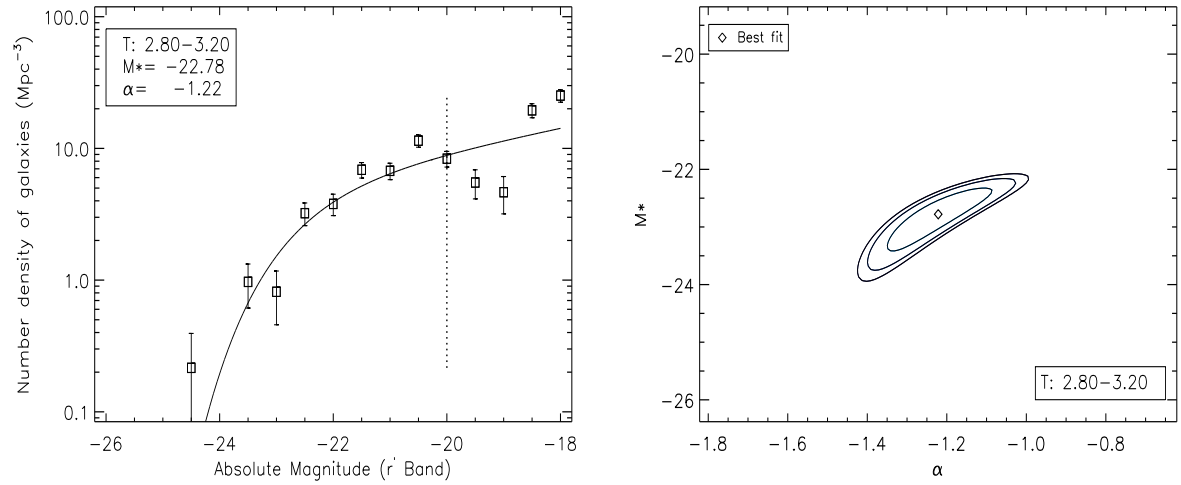

(d) Temperature: 2.80-3.20 (r' band)

Figure 4.13: (*continued*)

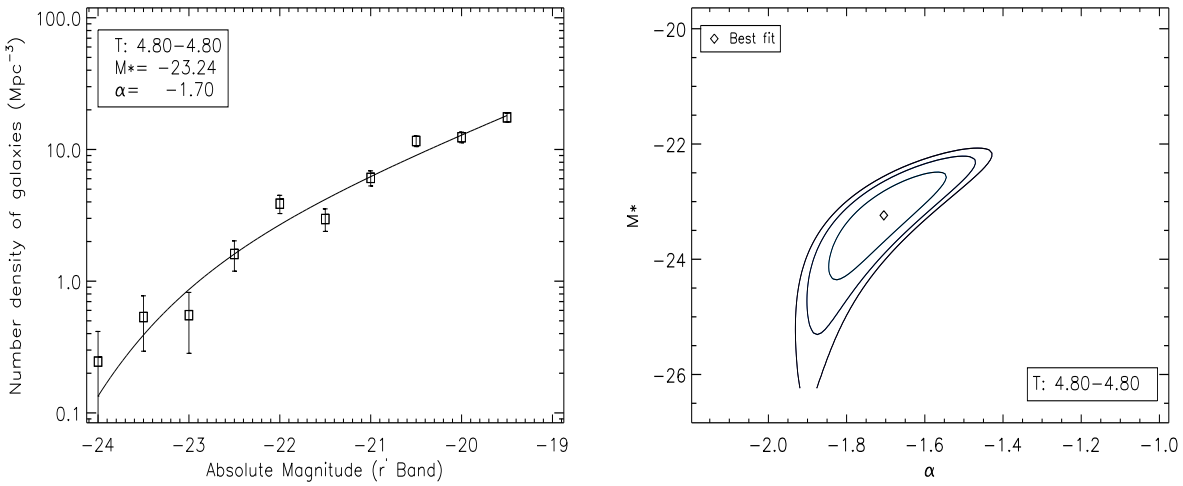

(e) Temperature: 4.80-4.80 (r' band)

Figure 4.13: (*continued*)

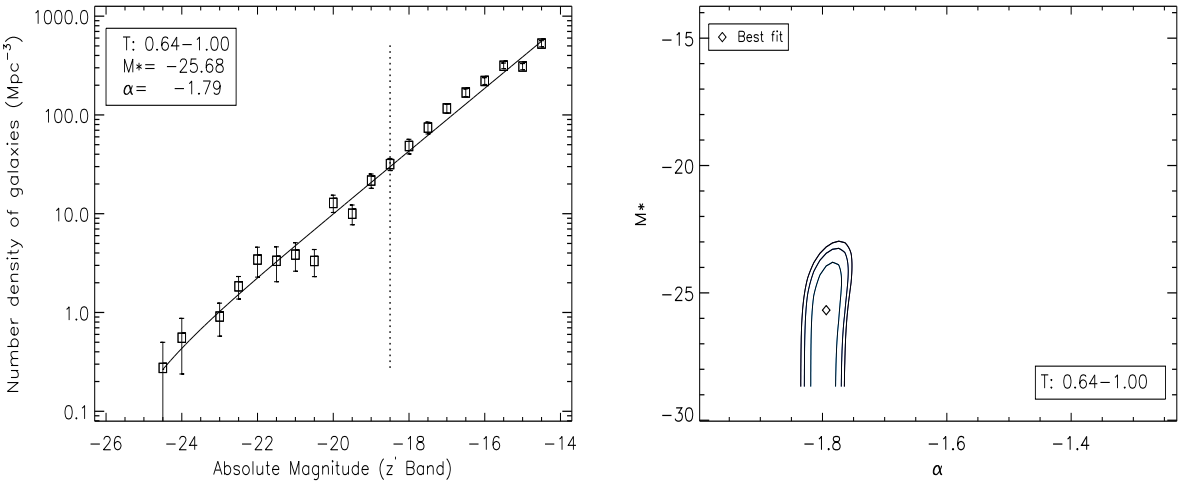

(a) Temperature: 0.64-1.00 (z' band)

Figure 4.14: LFs of the stacked clusters for 5 temperature ranges and the associated 1σ, 2σ and 3σ contours for z' band. All stacked clusters contributed to all magnitude bins are at the left side (brighter side) of the vertical dotted line which is at the faintest common magnitude bin of the clusters. Whereas at the right side (fainter side) of it, some clusters did not have data in some magnitude bins because they already reached their faintest magnitude limit.

4.4 Discussion

4.4.1 Faint-end slope of the luminosity function

In this chapter we have studied the LFs of the individual clusters in the C1 sample from XMM-LSS. A Schechter function provided a reasonable fit across most of the LF for most clusters, especially in the z' band. But the bright end was poorly-fitted for nearly half of the sample (6 out of 14) and M^* values were often not well constrained. The faint-end slope ranges are $-1.03 \leq \alpha \leq -2.1$, $-1.19 \leq \alpha \leq -1.89$ and $-1.06 \leq \alpha \leq -1.77$ with averages -1.70 ± 0.10, -1.64 ± 0.04 and -1.43 ± 0.03 for the g', r' and z' passbands respectively. The mean faint-end slope, averaging over all the three filters, is $\alpha_{avg} = -1.59 \pm 0.05$.

Comparison of fitted Schechter parameters from different studies should take into account the passband, cluster redshift, and the procedure used in constructing the LF, including the methods used to determine the cluster membership and the background subtraction, since all of these factors may affect the results and therefore the accuracy of comparison.

Previous studies of galaxy cluster LFs have found a wide range for α, from $\alpha \sim -1$ (Paolillo et al. 2001) to $\alpha \sim -2$ (Popesso et al. 2006), but generally, LFs of clusters (both high-mass and

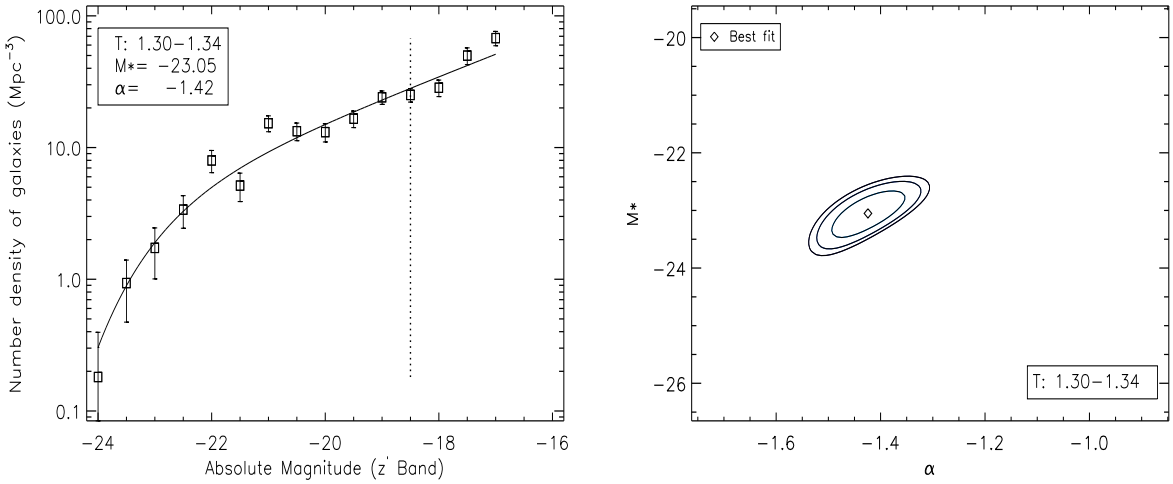

(b) Temperature: 1.30-1.34 (z' band)

Figure 4.14: (*continued*)

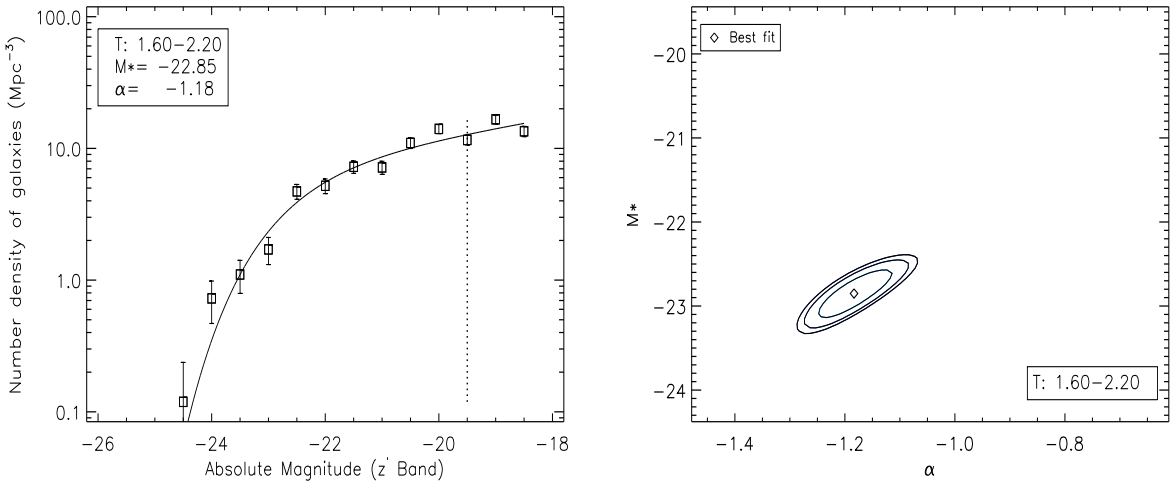

(c) Temperature: 1.60-2.20 (z' band)

Figure 4.14: (*continued*)

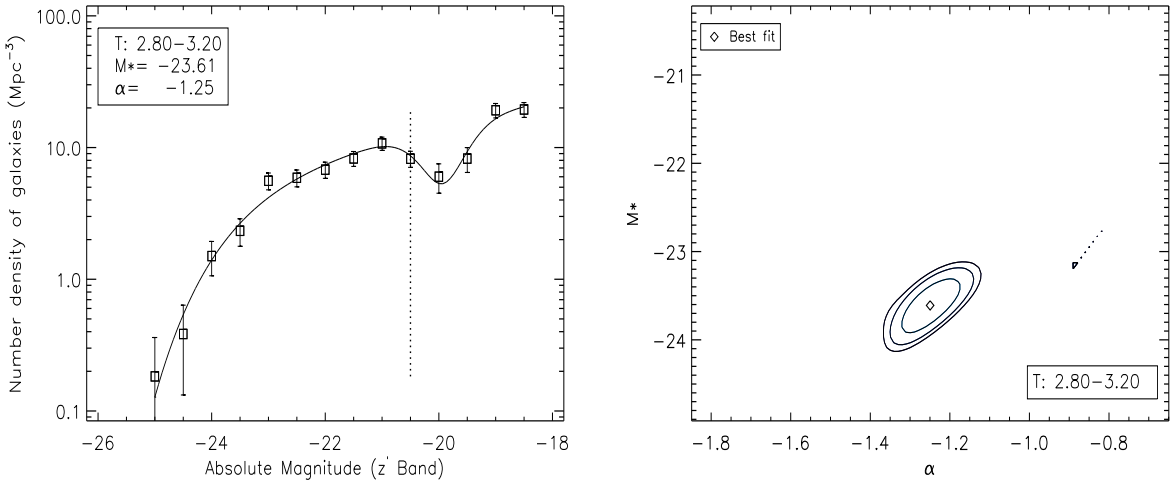

(d) Temperature: 2.80-3.20 (z' band)

Figure 4.14: (*continued*)

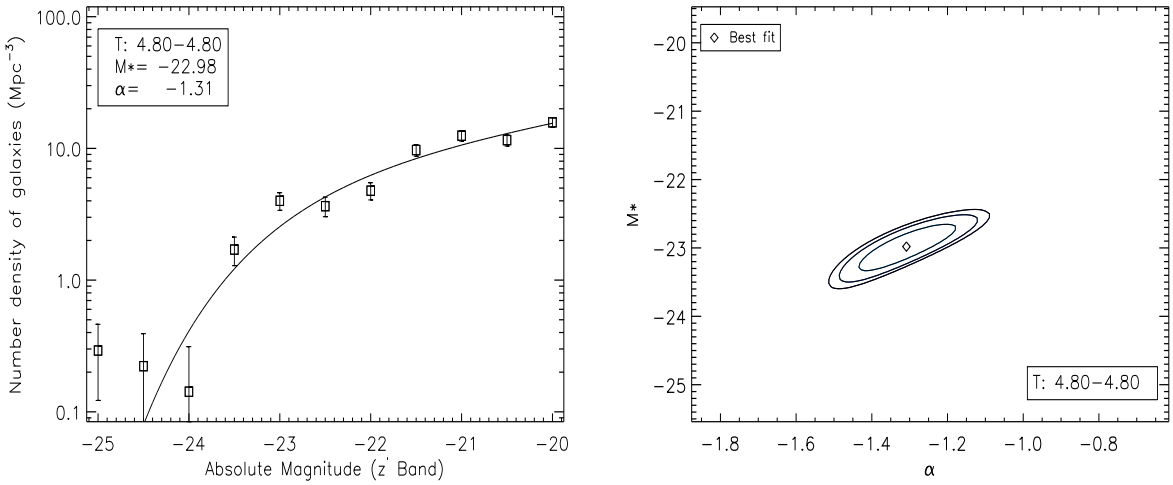

(e) Temperature: 4.80-4.80 (z' band)

Figure 4.14: (*continued*)

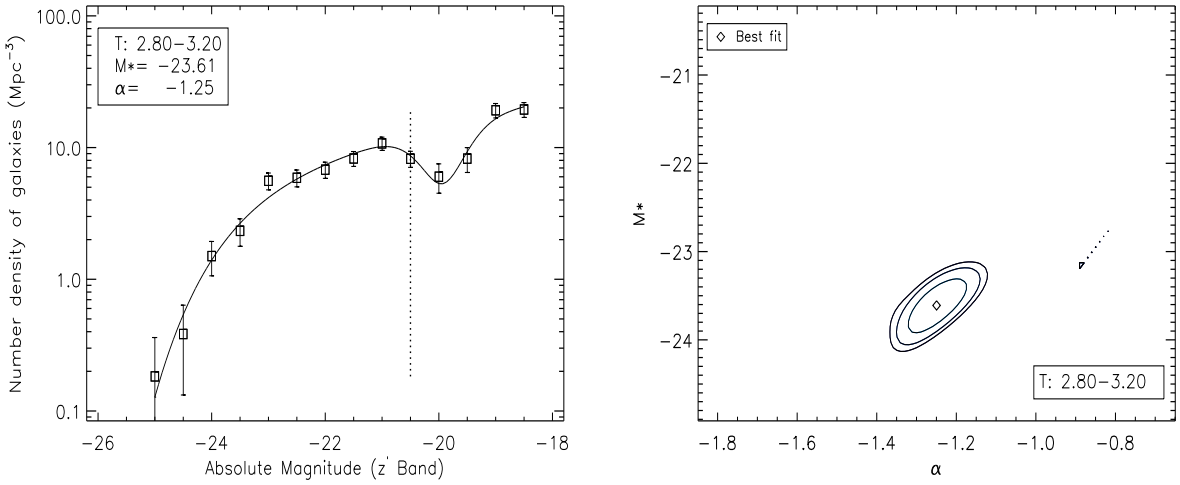

Figure 4.15: LF of the stacked clusters 1 and 27 (fourth temperature bin: $2.80 \leq T \leq 3.20$) with plot of the 1σ, 2σ and 3σ confidence contours in the α-M^* plane. The line is the fit of a Schechter function plus a Gaussian dip. The fitted dip position is -19.9 ± 0.1 (z' filter). The vertical dotted line marks the faintest magnitude at which both stacked clusters contribute.

low-mass systems) are found to have steeper slopes than field galaxy LFs, which usually span values $\alpha \sim -0.7$ (Lin et al. 1996) to -1 (Loveday et al. 1995). The values we obtain for α fall into the cluster LF range. The mass (M_{500}) range of the C1 clusters is 0.6-19 $\times 10^{13} M_{\odot}$ (Pacaud et al. 2007) and this puts the C1 sample in the lower-mass class of galaxy clusters (poor clusters and groups). This indicates that low-mass systems have almost the same range of faint-end LF slopes as more massive systems.

Moreover, Gonzàlez et al. (2006) studied LFs of galaxy clusters with a virial mass range $0.01 - 20 \times 10^{13} M_{\odot}$ and redshift $0.03 < z < 0.06$ and found slopes of $-1.9 < \alpha < -1.6$ at the faint end ($M_r \geq -18$). This is consistent with our result for clusters with comparable redshift; clusters 11 and 21, which have estimated masses of 0.6 and 0.9 $\times 10^{13} M_{\odot}$ and redshifts 0.05 and 0.08, show faint-end slopes of -1.80 ± 0.05 and -1.89 ± 0.06 in the r' band, with magnitude limits of -14.5 and -15 respectively.

The study of Popesso et al. (2005a) on X-ray selected rich clusters with $z \leq 0.25$ also gave a steep faint-end ($M_g \geq -16$) slope: $-2.1 \leq \alpha \leq -1.6$ in the SDSS g band. C1 clusters with redshifts ≤ 0.26, namely clusters 11, 21, 25, 41 and 44, have a g' band slope range of $-2.1 \leq \alpha \leq -1.67$, which agrees well with Popesso et al. (2005a). The redshift-stacked clusters with redshift $z \leq 0.32$ (the first four redshift bins) gave a slope range of $-1.79 \leq \alpha \leq -1.59$ in the g' band which is also consistent with Popesso et al. (2005a). The C1 clusters are low-mass

systems, whilst the Popesso et al. (2005a) systems are rich clusters. The steep faint end slopes seen in both indicate a larger fraction of dwarf galaxies in both groups and clusters, compared with the shallower LF slopes usually found in the field.

However, as is the case with richer clusters, the results from different studies of the luminosity function of group galaxies arrive at different results. For instance, Miles et al. (2004) derived a very flat ($\alpha \sim -1$) Schechter slope for X-ray bright groups – though they found a faint upturn in X-ray dim systems – and Zandivarez et al. (2006) derived similarly low faint end slopes for SDSS groups. Miles et al. (2004) used photometric data of X-ray selected systems and used all galaxies with B-R < 1.7 from the regions outside a radius of R_{500} from the centre of the group as the background for subtraction, whilst Zandivarez et al. (2006) used spectroscopic data for membership determination for their friends-of-friends selected clusters. Robotham et al. (2006) extracted LFs for 2PIGG groups, derived from the 2dF galaxy redshift survey, and obtained good fits with Schechter functions, with faint end slopes which increased from $\alpha \sim -1$ for red galaxies to $\alpha \sim -1.5$ for blue galaxies.

These discrepancies in the faint-end slope from different studies could arise from a variety of causes: different cluster selection methods (X-ray selected clusters in our case), spectroscopic or photometric selection of cluster galaxies, different galaxy background subtraction techniques (see discussion in section 4.3), and possibly because different clusters have different faint-end slopes depending on their large-scale environment, which will affect the incidence of infalling galaxies.

4.4.2 The absence of the upturn in the faint end of LFs

Both Popesso et al. (2005a) and Gonzàlez et al. (2006) reported an upturn at the faint end of their stacked LF, and required a sum of two Schechter functions, rather than a single Schechter, to obtain reasonable fits. Popesso et al. (2005a) located the upturn at -16 in the g' band, and -18.5 in z'; the upturn of Gonzàlez et al. (2006) was found at a similar magnitude: -18 in the r' band. In our sample, only the LFs for clusters 11, 21 and 41 extend to the faint magnitudes in which Popesso et al. (2005a) and Gonzàlez et al. (2006) found their upturns. The composite LF for these systems is the first in the redshift-stacked LFs, see Figs 4.3, 4.4 and 4.5. Although our results agree with Popesso et al. (2005a) and Gonzàlez et al. (2006) regarding the steep values

of the faint-end slope, we do not find any evidence for a departure from a simple power law at the faint end.

Other studies gave steep slopes at the faint end of cluster LFs but without evidence of sudden upturns, see for example Durret et al. (2002). Garilli et al. (1999) studied composite LFs of 65 clusters ranging in redshift from 0.05 to 0.25 and did not find upturns in their composite LFs. Popesso et al. (2005a) argued that Garilli et al. (1999) did not see this upturn in their stacked LF because they used a weighting for the individual LFs which depends strongly on the cluster magnitude limit, such that clusters with fainter magnitude limits, which contribute to the faint magnitude bins of the stacked LF, were heavily down-weighted. We did not apply any weighting method that depends on the magnitude limit and although faint-end slopes are steep in all three bands for the stacked LF of clusters 11, 21 and 41, they lack any upturn at the locations found by Popesso et al. (2005a) and Gonzàlez et al. (2006). Furthermore, individual LFs of these three clusters do not show any obvious upturn in the faint-end part of the LF that can be distinguished from the scatter of the data relative to the fitted Schechter function.

Popesso et al. (2006) decomposed their LF by galaxy type and showed that the late-type galaxies LF was well fitted by a single Schechter function with a steep slope ($\alpha = 2.0$), while the early-type galaxies LF could not be fitted by a single Schechter function, and a composite of two Schechter functions was needed, such that the faint-end upturn of the global cluster LF was due to the early-type cluster galaxies. This suggests one way of reconciling our results with those of Popesso et al. (2006). If in our poorer clusters late-type galaxies outnumber early-types in the intermediate and faint magnitude ranges then the LF would be steep and without any upturns. This needs to be further investigated by studying the early-type and the late-type LF separately. Another possibility for the difference between our results and those of Popesso et al. (2006) lies in the techniques used to remove non-cluster galaxies, as we discuss in the next section.

4.4.3 Membership determination methods: Effects on α

The steepness of the faint end of the luminosity function reflects the number of dwarf galaxies within a cluster. Estimates of this number are very sensitive to the method used to estimate and remove the contribution of background and foreground galaxies before constructing the cluster

luminosity function.

Rines & Geller (2008) compared methods of membership determination based on spectroscopic data and on photometric data (which we used) with regard to the resulting LF. They highlighted the advantages of spectroscopic identification of cluster members. Where automated photometric methods are used, they found, for example, that many large galaxies, especially those with low surface brightnesses, may be detected as many small separate objects, and warned that if these pieces of galaxies are not removed, they can produce an artificial excess of faint galaxies in cluster fields.

However, we have to emphasise that although spectroscopic data can give precise information on the cluster membership, their use to study cluster LFs is limited to relatively nearby clusters, since for higher-redshift clusters, spectroscopy is feasible only for the bright cluster galaxies. Boué et al. (2008) used deep multicolour photometry to study the LF of A496, using colour selection to reduce contamination by red background galaxies, and did not find the large fraction of dwarf galaxies ($\alpha = 2.0$) inferred by some other authors, including Popesso et al. (2006). They suggested that this excess of dwarf galaxies in some studies might arise from inadequate removal of background, due to use of inadequate (or no) colour cuts. They claimed that the red sequence used by Popesso et al. (2006) was polluted by field galaxies because they used $u^* - r'$ vs i' in their CMD which Boué et al. (2008) showed was not efficient in rejecting background galaxies.

In our study, we did not use $u^* - r'$ vs i' to define the colour cuts. Instead, we used $u^* - g'$ vs g' for the g' band, $g' - r'$ vs r' for the r' band and $i' - z'$ vs z' for the z' band. Moreover, our method of field LF subtraction is based on global background LF constructed by using the whole $1^\circ \times 1^\circ$ field of the cluster. Therefore, we don't see any obvious reason why we might have contaminated the red sequence with field galaxies in such away as to give a false steep faint-end slope.

4.4.4 Origin of the faint galaxies

Our results indicate that larger numbers of faint galaxies exist in cluster environments than in the field. It is not straightforward to understand this result, since various dynamical processes that can destroy dwarfs act more effectively in dense environments. Several ideas have been proposed to explain the excess of dwarfs in clusters. Babul & Rees (1992) argued that a primordial

population of dwarf galaxies is preserved in high-pressure environments, whilst it fades away in low-pressure regions.

Alternatively, dwarfs could be formed by galaxies that fell into clusters from the surrounding field and were morphologically transformed. The transformation mechanism could be tidal fragmentation or so-called harassment of infalling late-type spiral galaxies by the cluster potential or by close encounters (Moore et al. 1996) or ram pressure stripping of dwarf irregular galaxies (e.g., van Zee et al. 2004).

Boselli et al. (2008) showed that both simulations and observations are consistent regarding the scenario of recent accretion and transformation of low-luminosity star-forming galaxies in the Virgo cluster into quiescent dwarfs due to ram pressure gas stripping and galaxy starvation. They also showed that this process of transformation results in galaxies with structural and spectrophotometric properties similar to those of dwarf ellipticals. If the whole star-forming dwarf galaxy population dominating the faint end of the field luminosity function were accreted, it could be totally transformed by the cluster environment into dwarf ellipticals on timescales as short as 2 Gyr. These vigorous forces acting in cluster environments may explain the steepness of LFs faint-end slopes in nearby clusters.

4.4.5 The evolution of α

Our results show an evolutionary trend of the faint-end slope, α, in all bands used: g', r' and z'. Liu et al. (2008) examined the faint-end slope of the V-band LF of *field* galaxies with redshifts $z < 0.5$ and found that it becomes shallower with increasing redshift: their α changed from -1.24 for the lowest redshift bin $0.02 \leq z < 0.1$ to -1.12 for the highest redshift bin $0.4 \leq z < 0.5$. In clusters, a recent study by Lu et al. (2009) of an optically selected cluster sample found steepening of the faint end with decreasing redshift since $z \sim 0.2$, and that the relative number of red-sequence dwarf galaxies had increased by a factor of ~ 3.

It is possible that this LF slope trend with redshift is linked to the finding of Harsono & De Propris (2007) that the 'upturn' in the LF faint end (i.e. the excess of galaxies above a single Schechter function) is found only in low redshift clusters. They attributed this to the recent infall of star-forming field galaxies or the whittling down of formerly more massive objects.

The impact of recent infall of galaxies into clusters is also supported by the work of Lisker et

al. (2007), who showed that dEs in the Virgo cluster fall into two major morphological subclasses: a) dEs with blue centres, thick disks or features reminsiscent of late-type galaxies, such as spiral arms or bars; this class showed no central clustering, suggesting that they are an unrelaxed population formed from infalling galaxies. The second subclass is b) nucleated dEs – a fairly relaxed population of spheroidal galaxies indicating that they have resided in the cluster for a long time, or were formed along with it. Lisker et al. (2007) also pointed to other studies deriving similar results (see references therein), indicating that this subclassification is not specific to the Virgo cluster.

4.4.6 Colour trends

The faint-end slopes, α, of the redshift-stacked groups are steeper in bluer bands in almost all redshift bins. However, this trend is significant ($> 1\sigma$) only for the redshift range $0.29 \leq z \leq 0.32$. The redshift bin in which this effect seems to be absent is the first bin: $0.05 \leq z \leq 0.14$. This suggests that the fraction of faint blue galaxies in clusters of redshift $z \sim 0.3$ are higher than in local systems. Fig. 4.8 further illustrates this and it also shows that these blue faint galaxies appear to have reddened and moved upwards in the colour-magnitude diagram. This is consistent with the findings of Wilman et al. (2005a) who compared the fractions of passive (red and quiescent) and blue star-forming galaxies in cluster at $0.3 \leq z \leq 0.55$ with nearby ($z \simeq 0$) clusters. They found that the fraction of passive galaxies declined strongly with redshift to at least $z \simeq 0.45$. These results are also consistent with the well-known Butcher-Oemler effect in clusters and support the idea that dense environments are responsible for galaxy transformation from blue to red because these trends are less obvious in field environments, see Wilman et al. (2005b).

Our result is also consistent with Yee et al. (2005) who studied the colours of galaxies as a function of luminosity and environment using the Red Sequence Cluster Survey and the SDSS. They found a higher incidence of faint to moderate luminosity galaxies in high density environments at $z > 0.2$ compared to lower redshifts and lower density environments. They interpreted this as arising from the shut-down of star formation in low mass galaxies within clusters at $z < 0.3$, in contrast to the situation in the field (cf. Balogh et al. 2004).

The fact that such transformations are observed in low-mass clusters like our C1 sample, as

well as in richer clusters, favours mechanisms for suppression of star formation which operate in shallower potential wells, such as strangulation, tidal interactions and galaxy mergers, rather than ram pressure stripping, which is effective mostly in rich environments with high velocity dispersions.

4.4.7 Correlation between global properties of clusters

The optical luminosity is a good indicator of cluster richness, and hence should be closely related to cluster mass, velocity dispersion and temperature (Popesso et al. 2005b). Assuming that cluster mass is directly proportional to the optical light (i.e. M/L_{OPT} is constant), that the ICM is in hydrostatic equilibrium and that X-ray luminosity L_X scales with gas temperature T as $L_X \propto T^3$ (Xue & Wu 2000), it is expected that $L_{OPT} \propto T^{1.5}$, and that $L_{OPT} \propto L_X^{0.5}$.

Our scaling results for L_{OPT} with L_X and T mostly agree well with these expectations. For the $L_{OPT} - L_X$ relation, the logarithmic slopes are 0.47 ± 0.07 (g' band), 0.43 ± 0.08 (r' band) and 0.50 ± 0.07 (z' band). While for the $L_{OPT} - T$ relation, we have 1.57 ± 0.17 (g' band), 1.51 ± 0.17 (r' band) and 1.79 ± 0.12 (z' band).

Popesso et al. (2004) found 0.38 ± 0.02 for the $L_{OPT} - L_X$ relation and 1.12 ± 0.08 for the $L_{OPT} - T$ relation in the z SDSS band within a cluster radius of 0.5 Mpc (chosen to minimise the scatter in their scaling relations). The systems they used for their analysis, the RASS-SDSS sample, were X-ray selected, and ranged from low-mass systems of $10^{12.5} M_\odot$ to massive clusters of $10^{15} M_\odot$, over a redshift range from 0.002 to 0.45. Their logarithmic slope value for the $L_{OPT} - L_X$ relation is not inconsistent with our value (within the errors), however, their $L_{OPT} - T$ value is lower than ours. They attributed the departure of their results from the expected values to a breakdown in the assumption of constant mass-to-light ratio. More precisely, they argued that if the assumption of hydrostatic equilibrium was retained, their results would be in a good agreement with $M/L \propto L^{0.33 \pm 0.03}$, as found by Girardi et al. (2002).

However, we note that extracting L_{OPT} within a fixed *metric* radius, will include a smaller fraction of the virial radius for higher mass clusters. Hence it should be no surprise if the $L_{OPT} - T$ relation is flattened below the expected slope of 1.5 for self-similar clusters. Using clusters from the RASS-SDSS sample, Popesso et al. (2005b) calculated L_{OPT} within R_{500} and R_{200}. Their R_{200} results were (we used $1.5 \times R_{500}$): 0.57 ± 0.03 (g band), 0.58 ± 0.03 (r band)

and 0.58 ± 0.03 (z band) for the $L_{OPT} - L_X$ relation and 1.62 ± 0.10 (g' band), 1.64 ± 0.09 (r' band) and 1.62 ± 0.10 (z' band) for $L_{OPT} - T$ relation. These are in better agreement with our results than Popesso et al. (2004), and demonstrate the importance of the radius used to estimate the L_{OPT}.

4.5 Conclusions

We have studied the luminosity functions of 14 Class 1 (C1) XMM-LSS galaxy clusters in three CFHTLS MegaCam bands: g', r' and z'. The X-ray selected clusters have masses ranging from 0.6 to 19 $\times 10^{13} M_{\odot}$, a redshift range of 0.05 to 0.61, and ICM temperature range of 0.64 to 4.80 keV. We used colour-magnitude lower and upper cuts to reduce contamination by cluster non-members, and performed background subtraction using the $1^{\circ} \times 1^{\circ}$ field of view in which the cluster lies. K-corrected luminosity functions of galaxies within $1.5 \times R_{500}$ were constructed for each cluster and fitted with a Schechter function. Total optical luminosities of the individual clusters were also computed by integrating over the fitted Schechter functions. The individual LFs were also stacked together into five redshift and five temperature bins. The main findings are:

- A Schechter function provides a good fit across most of the LF for the majority of clusters in our sample. The value of α range from -1.03 to -2.1, but no evidence is found for upturns at the faint end of the Schechter function, even in the lowest redshift systems, for which our LFs extend well into the dwarf regime.

- M^* ranges from -19.66 to -24.31. However, for many (nearly a third) of the clusters' M^* values are not well-constrained.

- The redshift-stacked LFs confirm that α becomes shallower with increasing redshift. The value of α is -1.75 ± 0.02 at low redshift (0.05-0.14), flattening to -1.22 ± 0.06 at high redshift (0.43-0.61) in the z' band. Similar trends are present in the other two bands.

- α, also steepens significantly from the red (z') to the blue (g') band for clusters at redshift ~ 0.3. This effect is not present in our local clusters ($z \sim 0$), suggesting reddening of the faint blue galaxies from $z \sim 0.3$ to $z \sim 0$.

- After removing the effects of redshift (correcting for the Malmquist effect), the temperature-stacked LFs do not exhibit any strong evidence for trends of the Schechter parameters with ICM temperature.

- Total optical luminosities for our sample range from 1.0 to 56.3 $\times 10^{11} L_{\odot}$, and correlate strongly with X-ray luminosity. The logarithmic slopes of the $L_{OPT} - L_X$ relation are 0.47 ± 0.07, 0.43 ± 0.08 and 0.50 ± 0.07 for the g', r' and z' bands respectively.

- Also, L_{OPT} correlate strongly with the X-ray gas temperature, T. The logarithmic slopes of the $L_{OPT} - T$ relation are 1.57 ± 0.17, 1.51 ± 0.17 and 1.79 ± 0.12 for the g', r' and z' bands respectively.

- The slopes of the $L_{OPT} - L_X$ and $L_{OPT} - T$ relations are consistent with the established, non-self-similar, cluster $L_X - T$ relation and constant mass-to-light ratio, except for the z' band value of the $L_{OPT} - T$ relation which is higher than the expected value (1.5) by ~ 0.3.

- Some of our stacked LFs show dips, but these appear to be artefacts arising where clusters with different faintest magnitude limits are stacked together. We therefore we conclude there is no evidence for real dips in the optical LFs of the C1 clusters.

Chapter 5

Conclusions and Future Work

5.1 Summary of conclusions

In this thesis, X-ray and optical properties of galaxy clusters are explored. A sample consisting of 27 X-ray selected galaxy clusters is used for the investigation. The sample is derived from the CLASS 1 (C1) *XMM-LSS* survey which guarantee negligible contamination of point-like sources in the selected clusters. These clusters are mostly groups and poor clusters, with temperatures 0.6 to 4.8 keV and masses (M_{500}) in the range 0.6 to 19 $\times 10^{13} M_{\odot}$. They have redshift in the range of 0.05 to 1.05. With this redshift range, these systems are some of the highest redshift X-ray selected groups to have been studied.

In chapter 3, radial profiles of intracluster media are extracted up to $3\times R_{500}$ and corrected for vignetting before they are fitted with β-models. The models are blurred to account for the limited resolution of the *XMM-Newton* cameras. 54% of the cluster sample show evidence for cool cores (CCs), in the form of central excesses in the X-ray surface brightness profiles. Stacked and individual profiles for our sample of poor galaxy clusters show that the CCs do not disappear at high redshift, but rather become more prominent, in contrary to what was observed in the case of rich clusters. The slope parameter, β, shows a positive trend with both redshift and temperature in our data and by combining this result with previous findings, we incline towards a trend with temperature rather than redshift. Previous results found this β-T trend in low z clusters. Our findings, thus, confirm this trend, for the first time, in groups and clusters at higher redshift.

A study of optical luminosity function (LF) of 14 of *XMM-LSS* galaxy clusters in three CFHTLS MegaCam bands (g', r' and z') is presented in chapter 4. The LFs are derived within $1.5 \times R_{500}$ of the clusters and are background-subtracted and K-corrected, before fitted with

Schechter function. The redshift-stacked LFs show that the faint-end slope, α, becomes shallower with increasing redshift. This trend is observed in all three bands, though it is stronger in the z' band. α is also found to steepen significantly from the red (z') band to the blue (g') band for clusters at redshift ~ 0.3. This effect is not present in our local clusters ($z \sim 0$), suggesting reddening of the faint blue galaxies from $z \sim 0.3$ to $z \sim 0$.

Total optical luminosities for the 14 clusters range from 1.0 to 56.3 $\times 10^{11} L_{\odot}$, and correlate strongly with X-ray luminosity. The logarithmic slopes of the $L_{OPT} - L_X$ relation are 0.47 ± 0.07, 0.43 ± 0.08 and 0.50 ± 0.07 for the g', r' and z' bands respectively. Also, L_{OPT} correlate strongly with the X-ray gas temperature, T. The logarithmic slopes of the $L_{OPT} - T$ relation are 1.57 ± 0.17, 1.51 ± 0.17 and 1.79 ± 0.12 for the three bands g', r' and z' bands respectively. This correlation is expected for non-self-similar clusters with constant mass-to-light ratios.

5.2 Future work

The most interesting results in the X-ray part of this thesis is that the central excess in the X-ray surface brightness profiles corresponding to cuspy cores become more prominent with increasing redshift in our sample of poor clusters. This evolution in CCs is opposite to what was previously reported in the case of rich clusters (Vikhlinin et al. 2007 and Santos et al. 2008). It is possible that the central excess could result from the presence of Active Galactic Nuclei (AGN) in the cluster cores, rather than from cool cores. We have ruled out this possibility by extracting profiles in hard X-ray band (2.0-4.5 keV) and noticing the absence of the central excess. Giving that AGN generally have much harder spectra than cool cores, this test suggests that the central excesses are not generated by AGN. To confirm our results, further observations of clusters with CCs in our sample needs to be performed by, for example, the *Chandra* satellite which has a sharper resolution than *XMM-Newton*.

It would be interesting to check the possibility that *Chandra* will detect X-ray bright AGN in some of the clusters in our sample that have strong cuspy cores, like clusters 2, 1, 10 and 40 which all have very large excess in the central X-ray emission indicating strong CCs. The incidence of AGN in rich clusters has been found (Martini, Sivakoff & Mulchaey 2009) to increase strongly with redshift (by a factor of ~ 8 from $z = 0.2$ to $z = 0.7$). If this is true for poor clusters, which contain a higher fraction of AGN than rich clusters at low redshifts (Arnold et al. 2009

and Koulouridis & Plionis 2010), then it is very likely that clusters in our sample harbour AGN in their central regions.

This proposed future work is important because confirmation that cores of groups evolve in the opposite sense to cores of rich clusters will provide very strong constraints on models of cosmic feedback. This confirmation would immediately rule out models based on widespread preheating of the ICM , which have been much used to produce the observed similarity breaking in clusters (Muanwong, Kay & Thomas 2006, McCarthy et al. 2008 and Short et al. 2010), and would provide strong constraints to meet alternative feedback models.

As to the optical LF study of cluster (chapter 4), we found that the faint-end slope, α, becomes shallower with increasing redshift. Various studies gave very different values for α and a trend with redshift needs to be confirmed. The value of α is very sensitive to the method used to determine the cluster membership of faint galaxies. Since we don't have spectral data for all galaxies in our optical catalogues, we used the photometric data to remove the contribution of the background and foreground galaxies. Future observatories, for example, VLT, should have better capabilities to obtain spectroscopic data of cluster individual galaxies with redshifts larger than local systems and thus construct better-constrained LFs.

Though *XMM-LSS* C1 sample contains clusters with high redshifts ($z > 0.7$), we constructed LFs for clusters up to redshift of 0.61 only because optical data of clusters with higher redshifts are too poor to produce adequate LFs. Further optical surveys that are more sensitive to dim galaxies ($M > -14.5$) are necessary to confirm trends in α with redshift.

References

Abell, G. O. 1958, ApJS, 3, 211

Adami C., Durret F., Mazure A., Pello R., Picat J. P., West M., Meneuk B., 2007, A&A, 462, 411

Akritas M. G., Bershady M. A., 1996, ApJ, 470, 706

Andreon S., Willis J., Quintana H., Valtchanov I., Pierre M., Pacaud F., 2004, MNRAS, 353, 353

Alshino A. et al., 2010, MNRAS, 401, 941

Andreon S., Valtchanov I., Jones L. R., Altieri B., Bremer M., Willis J., Pierre M., Quintana H., 2005, MNRAS, 359, 1250

Arnaud M., 2009, A&A, 500, 103

Arnaud M. et al., 2002, A&A, 390, 27

Arnaud M., Evrard A. E., 1999, MNRAS, 305, 631

Arnold T., Martini P, Mulchaey J., 2009, ApJ, 707, 1691

Babul A., Rees M. J., 1992, MNRAS, 255, 346

Bahcall N. A., Cen R., 1993, ApJ, 407, L49

Bahcall N., Lubin L., 1994, ApJ, 426, 513

Bagnasco G., et al., 1999, ESA Bulletin, 100, 21

Bahcall J. N., Sarazin C. L., 1977, ApJ, 213, L99

Bahcall J. N., Sarazin C. L., 1978, ApJ, 219, 781

Baldry I. K., Glazebrook K., Brinkmann J., Ivezi Ž.,Lupton R. H., Nichol R. C., Szalay A. S., 2004, ApJ, 600, 681

Balogh M. L., Baldry I. K., Nichol R., Miller C., Bower R., Glazebrook K., 2004, ApJ, 615, L101

Barnes J., Murdin P., 2000, Ency. Astron. Astrophys., article 1671

Barré H., Nye H., Janin G., 1999, ESA Bulletin, 100, 15

Bauer F. E., Fabian A. C., Sanders J. S., Allen S. W., Johnstone R. M., 2005, MNRAS, 359, 1481

Bekki K., Couch W. J., Shioya Y., 2002, ApJ, 577, 651

Bell E. F. et al., 2004, ApJ, 608, 752

Bertin, E., Arnouts, S. 1996, A&AS, 117, 393

Binggeli B., Sandage A., Tammann G. A., 1988, ARA&A, 26, 509

Blanton M. R., 2006, ApJ, 648, 268

Böhringer H., et al., 2001 ,A& A 369, 826

Bond J. R., Cole S., Efstathiou G., Kaiser N., 1991, ApJ, 379, 440

Borgani S., Finoguenov A., Kay S. T., Ponman T. J., Springel V., Tozzi P., Voit G. M., 2005, MNRAS, 361, 233

Boselli A., Boissier S., Cortese L., Gavazzi G., 2008, ApJ, 674, 742

Boselli A., Gavazzi G., 2006, PASP, 118, 517

Boué, G., Adami, C., Durret, F., Mamon, G. A., Cayatte, V. 2008, A&A, 479, 335

Bower R. G., Benson A. J., Malbon R., Helly J. C., Frenk C. S., Baugh C. M., Cole S., Lacey C. G., 2006, MNRAS, 370, 645

Branchesi M., Gioia I. M., Fanti C., Fanti R., 2007, A&A, 472, 739

Branduardi-Raymont G., Fabricant D., Feigelson E., Gorenstein P., Grindlay J., Soltan A., Zamorani G., 1981, ApJ, 248, 55

Bremer M. N. et al., 2006, MNRAS, 371, 1427

Brough S., Forbes D. A., Kilborn V. A., Couch W., Colless M., 2006, MNRAS, 369, 1351

Butcher H., Oemler A., Jr, 1978, ApJ, 219, 18

Burenin, R. A., Vikhlinin, A., Hornstrup, A., et al. 2007, ApJS, 172, 561

Burns J. O., Hallman E. J., Gantner B., Motl P. M., Norman M. L., 2008, ApJ, 675, 1125

Cavaliere A., Fusco-Femiano R., 1976, A&A, 49, 137

Cavaliere A., Fusco-Femiano R., 1981, A&A, 100, 194

Chen Y., Reiprich T. H., Böhringer H., Ikebe Y., Zhang Y.-Y., 2007, A&A, 466, 805

Chung A., van Gorkom J. H., Kenney J. D. P., Vollmer B., 2007, ApJ, 659, L115

Cohn J. D., White M., 2005, Astropart. Phys., 24, 316

Coles P., Lucchin F., 1995, Cosmology: The Origin and Evolution of Cosmic Structure, Wiley

Crawford S. M., Bershady M. A., Hoessel J. G., 2009, ApJ, 690, 1158

Croston J. H. et al., 2008, A&A, 487, 431

Dekel A., Silk J., 1986, ApJ, 303, 39

De Propris R., Stanford S. A., Eisenhardt P. R., Dickinson M., Elston R., 1999, AJ, 118, 719

Donahue M., Voit G. M., 2004, in Mulchaey J. S., Dressler A., Oemler A., eds, Clusters of Galaxies: Probes of Cosmological Structure and Galaxy Evolution, Cool Gas in Clusters of Galaxies. Cambridge University Press, Cambridge, UK, p. 143

Dressler A., Gunn J. E., 1992, ApJS, 78, 1

Durret, F., Adami, C., Lobo, C. 2002, A&A, 393, 439

Edge A. C., Stewart G. C., 1991, MNRAS, 252, 428

Edge A. C., Stewart G. C., Fabian A. C., 1992, MNRAS, 258, 177

Ellingson E., Lin H., Yee H. K. C., Carlberg R. G., 2001, ApJ, 547, 609

Ettori S. et al., 2004a, MNRAS, 354, 111

Ettori S., Tozzi P., Borgani S., Rosati P., 2004b, A&A, 417, 13

Fabian A. C., 1994, ARA&A, 32, 277

Finoguenov A. et al., 2007, ApJS, 172, 182

Finoguenov A., Reiprich T. H., Böhringer H., 2001, A&A, 368, 749

Frei, Z., Gunn, J. E. 1994, AJ, 108, 1476

Garilli B., Maccagni D., Andreon S., 1999, A&A, 342, 408

Geller M. J., Huchra J. P., 1983, ApJS, 52, 61

Gerke B. F. et al., 2007, MNRAS, 376, 1425

Giacconi, R., Murray, S., Gursky, H., Kellogg, E., Schreier, E., Tananbaum, H., 1972, ApJ, 178, 281

Gilbank, D. G., et al., 2008, ApJ, 673, 742

Giocoli C., Tormen G., Sheth R. K., van den Bosch F. C., 2010, MNRAS, 404, 502

Gioia, I. M., Henry, J. P., Maccacaro, T., et al. 1990, ApJ, 356, L35

Girardi M., Manzato P., Mezzetti M., Giuricin G., Limboz F., 2002, ApJ, 569, 720

González R. E., Lares M., Lambas D. G., Valotto C., 2006, A&A, 445, 51

Gonzalez A. H., Zaritsky D., Zabludoff A. I., 2007, ApJ, 666, 147

Gorenstein P., Fabricant D., Topka K., Harnden F. R., Jr, Tucker W. H., 1978, ApJ, 224, 718

Goto T. et al., 2003, PASJ, 55, 739

Gunn J. E., Gott J. R. I., 1972, ApJ, 176, 1

Gursky, H., Kellogg, E., Murray, S., Leong, C., Tananbaum, H., Giacconi, R, 1971, Ap J, 167

Guzzo L. et al., 1999, The Messenger, 95, 27

Haarsma, D. B. et al. 2010, ApJ, 713, 1037

Harsono D., De Propris R., 2007, MNRAS, 380, 1036

Harsono D., De Propris R., 2009, AN, 330, 937

He J.-H., Wang B., 2008, J. Cosmol. Astropart. Phys., 0806, 010

Helsdon S. F., Ponman T. J., 2000a, MNRAS, 315, 356

Helsdon S. F., Ponman T. J., 2000b, MNRAS, 319, 933

Hickson P., 1982, ApJ, 255, 382

Hinshaw G. et al., 2009, ApJS, 180, 225

Hoekstra H. et al., 2006, ApJ, 647, 116

Horner, D. J., R. F. Mushotzky, and C. A. Scharf, 1999, Astrophys. J. 520, 78

Hubble E., 1929, Proc. Natl. Acad. Sci., 15, 168

Huchra J. P., Geller M. J., 1982, ApJ, 257, 423

Huo Z. Y., Xia X. Y., Xue S. J., Mao S., Deng Z. G., 2004, ApJ, 611, 208

Jansen F., 1999, ESA Bulletin, 100, 9

Jeltema T. E., Canizares C. R., Bautz M. W., Buote D. A., 2005, ApJ, 624, 606

Jeltema T. E. et al., 2009, MNRAS, 399, 715

Jeltema T. E., Mulchaey J. S., Lubin L. M., Fassnacht C. D., 2007, ApJ, 658, 865

Jeltema T. E., Mulchaey J. S., Lubin L. M., Rosati P., Böhringer H., 2006, ApJ, 649, 649

Jones M., et al, 2004, An Introduction to Galaxies and Cosmology, Cambridge Uni. Press, p. 169-211

Jones C., Forman W., 1984, ApJ, 276, 38

Johnson R., Ponman T. J., Finoguenov A., 2009, MNRAS, 395, 1287

Kaastra J. S., Mewe R., 1993, A&AS, 97, 443

Kaiser N., 1986, MNRAS, 222, 323

Kauffmann G., 1995, MNRAS, 274, 161

Kay S. T., da Silva A. C., Aghanim N., Blanchard A., Liddle A. R., Puget J.-L., Sadat R., Thomas P. A., 2007, MNRAS, 377, 317

Khochfar S., Silk J., Windhorst R. A., Ryan R. E., 2007, ApJ, 668, L115

King, C. R., Ellis, R. S. 1985, ApJ, 288, 456

Kofman L., Gnedin N., Bahcall N., 1993, ApJ, 413, 1

Koulouridis E., Plionis M., 2010, arXiv1003.0753

Krick J. E., Surace J. A., Thompson D., Ashby M. L. N., Hora J. L., Gorjian V., Yan L., 2008, ApJ, 686, 918

Krumpe, M., Miyaji, T., Coil, A. L. 2010, ApJ, 713, 558

Liedahl D. A., Osterheld A. L., Goldstein W. H., 1995, ApJ, 438, L115

Lin H., Kirshner R. P., Shectman S. A., Landy S. D., Oemler A., Tucker D. L., Schechter P. L., 1996, ApJ, 464, 60

Lisker T., Grebel E. K., Binggeli B., Glatt K., 2007, ApJ, 660, 1186

Liu C. T., Capak P., Mobasher B., Paglione T. A. D., Rich R. M., Scoville N. Z., Tribiano S. M., Tyson N. D., 2008, ApJ, 672, 198

Loveday J., Maddox S. J., Efstathiou G., Peterson B. A., 1995, ApJ, 442, 457

Lu T., Gilbank D. G., Balogh M. L., Bognat A., 2009, MNRAS, 399, 1858

Mahdavi A., Böhringer H., Geller M. J., Ramella M., 2000, ApJ, 534, 114

Martini P., Sivakoff G. R., Mulchaey J. S., 2009, ApJ, 701, 66

Marzke R. O., Geller M. J., Huchra J. P., Corwin H. G., 1994, AJ, 108, 437

Maughan B. J., Jones C., Forman W., Van Speybroeck L., 2008, ApJS, 174, 117

McCarthy I. G., Balogh M. L., Babul A., Poole G. B., Horner D. J., 2004, ApJ, 613, 811

McCarthy I. G., Babul A., Bower R. G., Balogh M. L., 2008, MNRAS, 386, 1309

Mewe R., Gronenschild E. H. B. M., van den Oord G. H. J., 1985, A&AS, 62, 197

Miles T. A., Raychaudhury S., Forbes D. A., Goudfrooij P., Ponman T. J., Kozhurina-Platais V., 2004, MNRAS, 355, 785

Moore B., Katz N., Lake G., Dressler A., Oemler A., 1996, Nat, 379, 613

Morandi A., Ettori S., Moscardini L., 2007, MNRAS, 379, 518

Muanwong O., Kay S. T., Thomas P. A., 2006, ApJ, 649, 640

Mulchaey, J. S. 2000, ARA&A, 38, 289

Mulchaey J. S., Davis D. S., Mushotzky R. F., Burstein D., 2003, ApJS, 145, 39

Mulchaey J. S., Lubin L. M., Fassnacht C., Rosati P., Jeltema T. E., 2006, ApJ, 646, 133

Mushotzky, R. F., 1984, Phys. Scr. T, 7, 157

Muzzin A., Wilson G., Lacy M., Yee H. K. C., Stanford S. A., 2008, ApJ, 686, 966

Naab T., Burkert A., 2003, ApJ, 597, 893

Navarro J. F., Frenk C. S., White S. D. M., 1996, ApJ, 462, 563

Navarro J. F., Frenk C. S., White S. D. M., 1997, ApJ, 490, 493

Neumann D. M., Arnaud M., 1999, A&A, 348, 711

Ortiz-Gil A., Guzzo L., Schuecker P., Böhringer H., Collins C. A., 2004, MNRAS, 348, 325

Osmond J. P. F., Ponman T. J., 2004, MNRAS, 350, 1511

Ota N., Mitsuda K., 2004, A&A, 428, 757

Pacaud F. et al., 2006, MNRAS, 372, 578

Pacaud, F., et al., 2007, MNRAS, 382, 1289

Paolillo M., Andreon S., Longo G., Puddu E., Gal R. R., Scaramella R., Djorgovski S. G., De Carvalho R., 2001, A&A, 367, 59

Peacock J., 1999, Cosmological Physics, Cambridge Univ. Press

Peebles P., 1993, Physical Cosmology, Princeton Univ. Press

Peres C. B., Fabian A. C., Edge A. C., Allen S. W., Johnstone R. M., White D. M., 1998, MNRAS, 298, 416

Perez-Gonzalez P. G. et al., 2008, ApJ, 675, 234

Peterson J. R. et al., 2001, A&A, 365, L104

Peterson J. R., Kahn S. M., Paerels F. B. S., Kaastra J. S., Tamura T., Bleeker J. A. M., Ferrigno C., Jernigan J. G., 2003, ApJ, 590, 207

Peterson J. R., Fabian A. C., 2006, Phys. Rep., 427, 1

Piccinotti, G., Mushotzky, R.F., Boldt, E.A., Holt, S.S., Marshall, F.E., et al. 1982, ApJ, 253, 485

Pierre, M. et al., 2004, JCAP, 09, 011

Plionis M., Tovmassian H. M., 2004, A&A, 416, 441

Ponman T.J., et al, 1996, MNRAS, 283, 690

Ponman T. J., Cannon D. B., Navarro J. F., 1999, Nat, 397, 135

Ponman T. J., Sanderson A. J. R., Finoguenov A., 2003, MNRAS, 343, 331

Popesso P., Böhringer H., Brinkmann J., Voges W., York D. G., 2004, A&A, 423, 449

Popesso P., Böhringer H., Romaniello M., Voges W., 2005a, A&A, 433, 415

Popesso P., Biviano A., Böhringer H., Romaniello M., 2006, A&A, 445, 29

Popesso P., Biviano A., Böhringer H., Romaniello M., Voges W., 2005b, A&A, 433, 431

Pratt G. W., Arnaud M., 2002, A&A, 394, 375

Pratt G. W., et al., 2007, A&A, 461, 71

Pratt G. W., et al., 2009, A&A, 498, 361

Quilis V., Moore B., Bower R., 2000, Sci, 288, 1617

Rakos K. D., Schombert J. M., 1995, ApJ, 439, 47

Rasmussen J., Ponman T. J., 2004, MNRAS, 349, 722

Refregier A., Valtchanov I., Pierre M., 2002, A&A, 390, 1

Rines08 Rines K., Diaferio A., Natarajan P., 2008, ApJ, 679

Rines, K., Geller, M. J. 2008, AJ, 135, 1837

Robotham A., Wallace C., Phillipps S., De Propris R., 2006, ApJ, 652, 1077

Rosati P., Borgani S., Norman C., 2002, Ann. Rev. Astron. Astrophys., 40, 539

Rothschild, R., et al., 1979, Space Sci. Instr., 4

Sandage A., 1961, Hubble Atlas of Galaxies. Carnegie Inst. Washington, Washington ,DC ,p. 618

Sanderson A. J. R., Ponman T. J., 2003, MNRAS, 345, 1241

Sanderson A. J. R., Ponman T. J., O'Sullivan E., 2006, MNRAS, 372, 1496

Santos J. S., Rosati P., Tozzi P., Böhringer H., Ettori S., Bignamini A., 2008, A&A, 483, 35

Sarazin C. L., Bahcall J. N., 1977, ApJS, 34, 451

Sarazin C. L., 1986, Rev. Mod. Phys., 58, 1

Schechter, P. 1976, ApJ 203, 297

Schuecker P., Böhringer H., Reiprich T. H., Feretti L., 2001, A&A, 378, 408

Sharples R., et al., 2009, CfA, NASA

Short C., et al., 2010, arXiv1002.4539S

Sparke L. S., Gallagher J. S., 2007, Galaxies in the Universe: An Introduction, 2nd Ed., Cambridge Uni. Press

Spergel, D. N., et al., 2007, ApJ, 170, 377

Strazzullo V. et al., 2006, A&A, 450, 909

Strüder L. et al., 2001, A&A, 365, L18

Sun M., Voit G. M., Donahue M., Jones C., Forman W., Vikhlinin A., 2009, ApJ, 693, 1142

Tolman R. C., 1930, Proc. Natl. Acad. Sci., 16, 511

Trümper J., 1992, QJRAS, 33, 165

Tully R.B., 1987, ApJ, 321, 280

Turner M. J. L. et al., 2001, A&A, 365, L27

Urquhart, S.A., Willis, J.P., Hoekstra H. and Pierre, M., 'An environmental Butcher-Oemler effect in intermediate redshift X-ray clusters', submitted, 2010, MNRAS

Valtchanov I. et al., 2004, A&A, 423, 75

van Zee L., Barton E. J., Skillman E. D., 2004, AJ, 128, 2797

Vikhlinin A., Burenin R., Forman W. R., Jones C., Hornstrup A., Murray S. S., Quintana H., 2007, in Böhringer H., Pratt G. W., Finoguenov A., Schuecker P., eds, Eso Astro. Symp., Heating versus Cooling in Galaxies and Clusters of Galaxies. Springer-Verlang, Berlin, p. 48

Vikhlinin A., Forman W., Jones C., 1999, ApJ, 525, 47

Vikhlinin A., Markevitch M., Murray S. S., Jones C., Forman W., Van Speybroeck L., 2005, ApJ, 628, 655

Vogt N. P., Haynes M. P., Giovanelli R., Herter T., 2004, ApJ, 127, 3300

Voit G. M., 2005a, Rev. Mod. Phys., 77, 207

Voit G. M., 2005b, Adv. Space Res., 36, 701

Voit G. M., Kay S. T., Bryan G. L., 2005, MNRAS, 364, 909

Vrtilek J., et al., 2002, CfA, NASA

Willis J. P. et al., 2005, MNRAS, 363, 675

Wilman D. J. et al., 2005a, MNRAS, 358, 88

Wilman D. J., Balogh M. L., Bower R. G., Mulchaey J. S., Oemler A., Carlberg R. G., Morris S. L., Whitaker R. J., 2005b, MNRAS, 358, 71

White S. D. M., Efstathiou G., Frenk C. S., 1993, MNRAS, 262, 1023

White D. A., Jones C., Forman W., 1997, MNRAS, 292, 419

Wu K. K. S., Fabian A. C., Nulsen P. E. J., 2000, MNRAS, 318, 889

Xue Y.-J., Wu X.-P., 2000, ApJ, 538, 65

Yee H. K. C., Hsieh B. C., Lin H., Gladders M. D., 2005, ApJ, 629, L77

Yee, H.K.C., Ellingson, E., Carlberg, R.G., 1996, ApJ., Suppl., 102, 269

Zabludoff A. I., Mulchaey J. S., 1998, ApJ, 496, 39

Zandivarez A., Martnez H. J., Merchn M. E., 2006, ApJ, 650, 137

Zwicky, I. F. 1942, ApJ, 95, 555

Appendix A

Optical CFHTLS images of C1 clusters with X-ray contours.

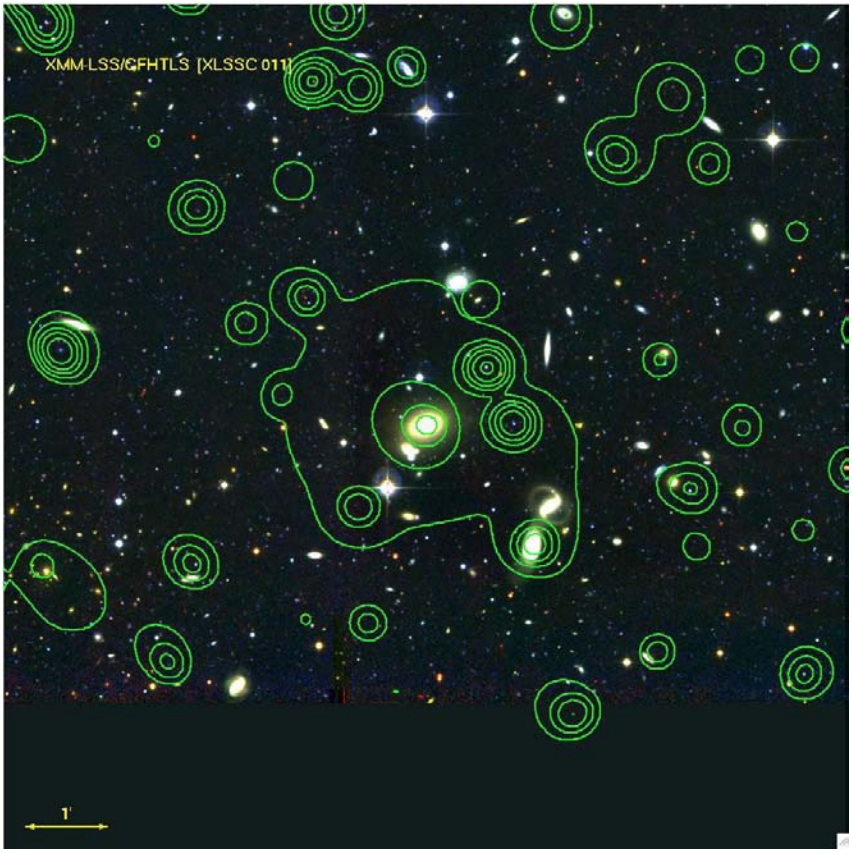

Figure A.1: Cluster 11.

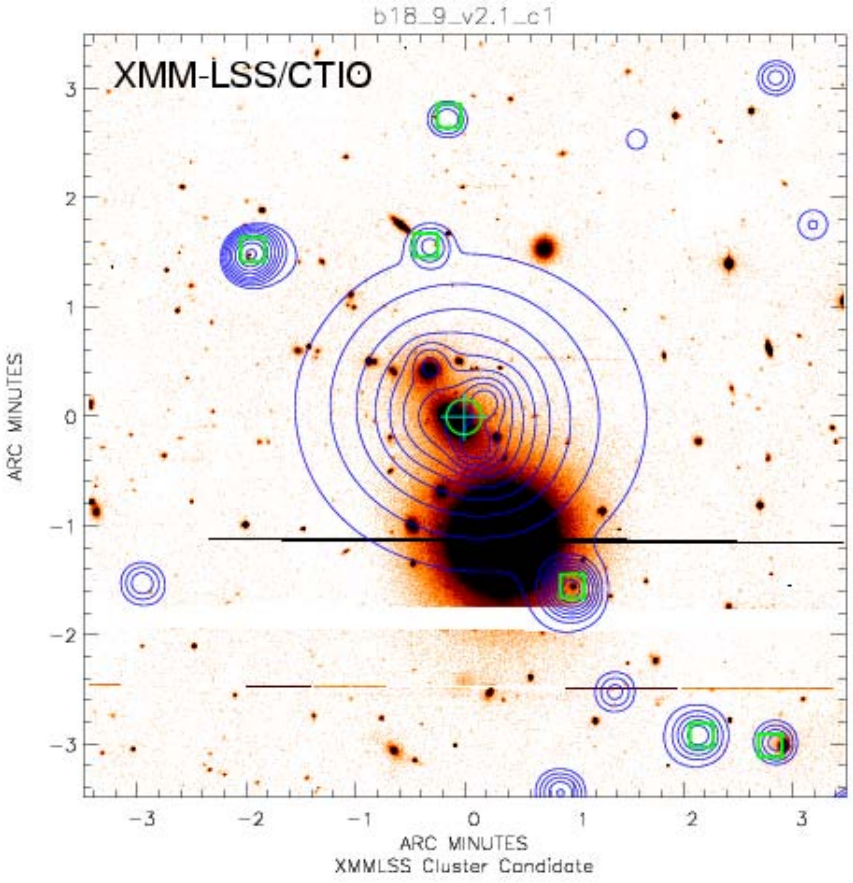

Figure A.2: Cluster 52.

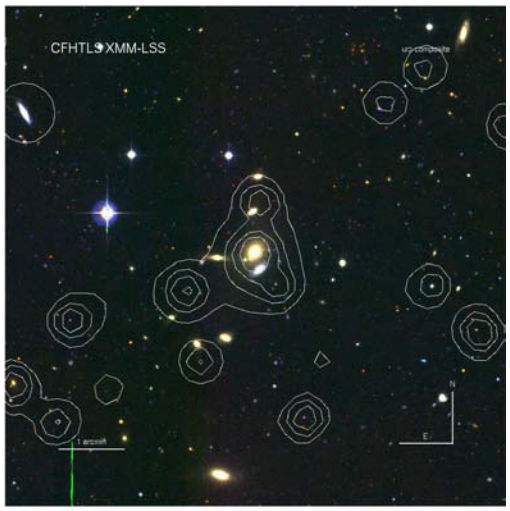

Figure A.3: Cluster 21.

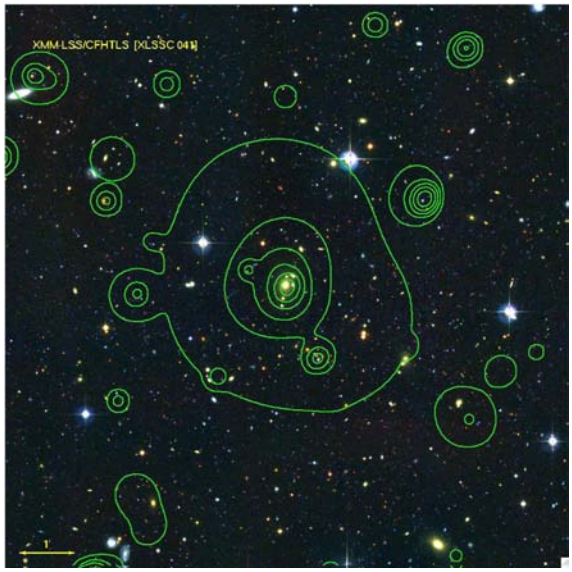

Figure A.4: Cluster 41.

Figure A.5: Cluster 50.

Figure A.6: Cluster 35.

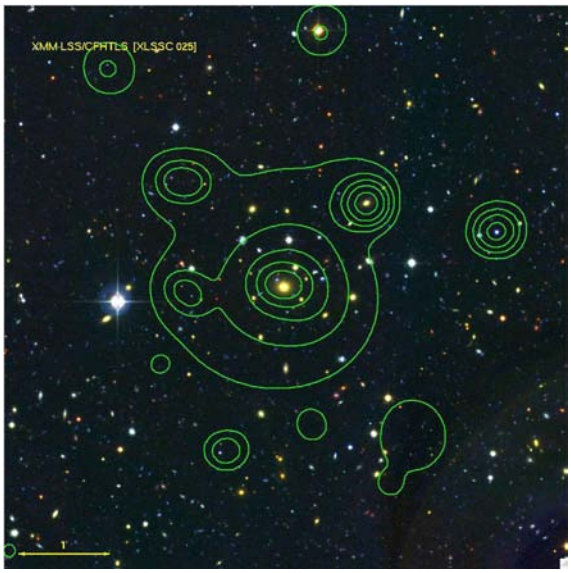

Figure A.7: Cluster 25.

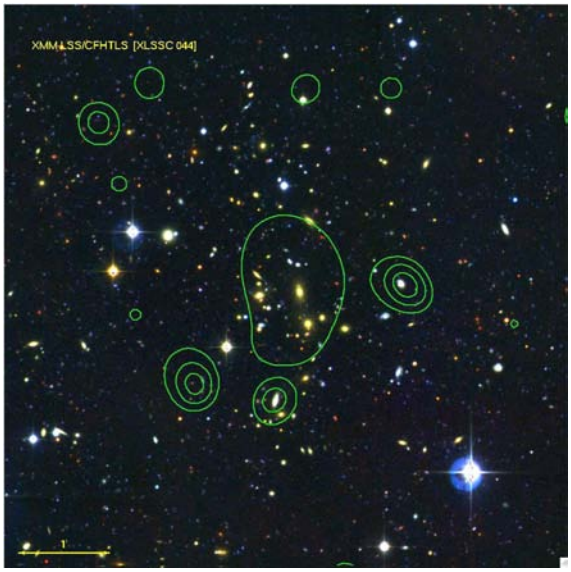

Figure A.8: Cluster 44.

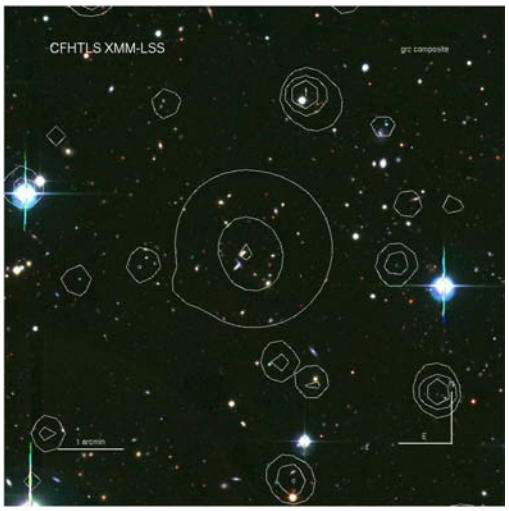

Figure A.9: Cluster 51.

Figure A.10: Cluster 22.

Figure A.11: Cluster 27.

Figure A.12: Cluster 8.

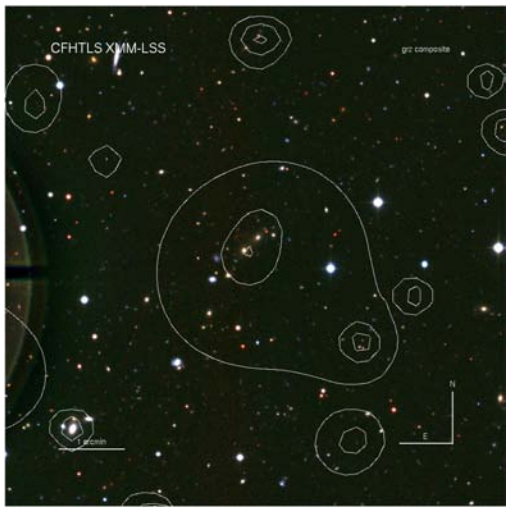

Figure A.13: Cluster 28.

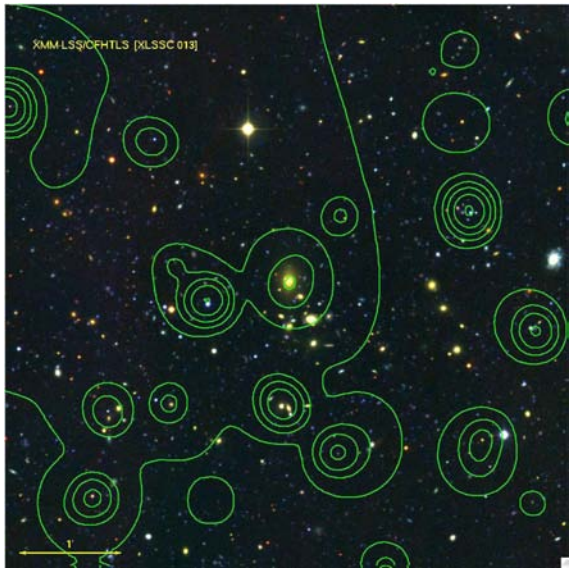

Figure A.14: Cluster 13.

Figure A.15: Cluster 18.

Figure A.16: Cluster 40.

Figure A.17: Cluster 10.

Figure A.18: Cluster 23.

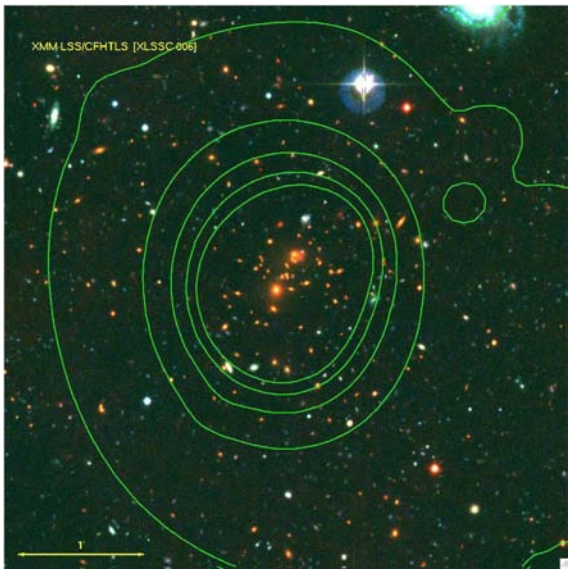

Figure A.19: Cluster 6.

Figure A.20: Cluster 36.

Figure A.21: Cluster 49.

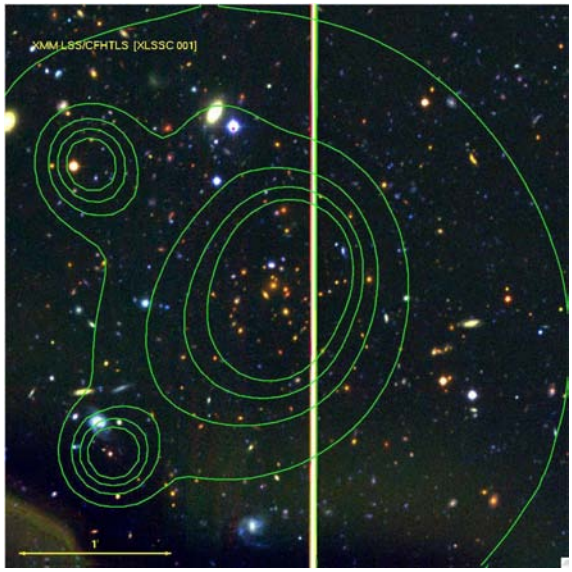

Figure A.22: Cluster 1.

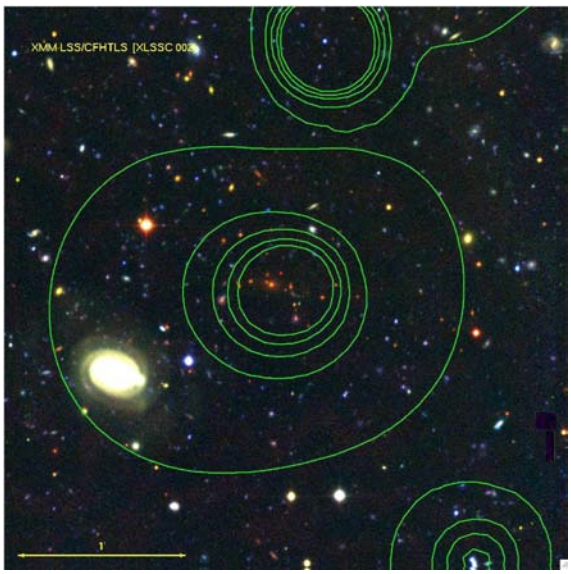

Figure A.23: Cluster 2.

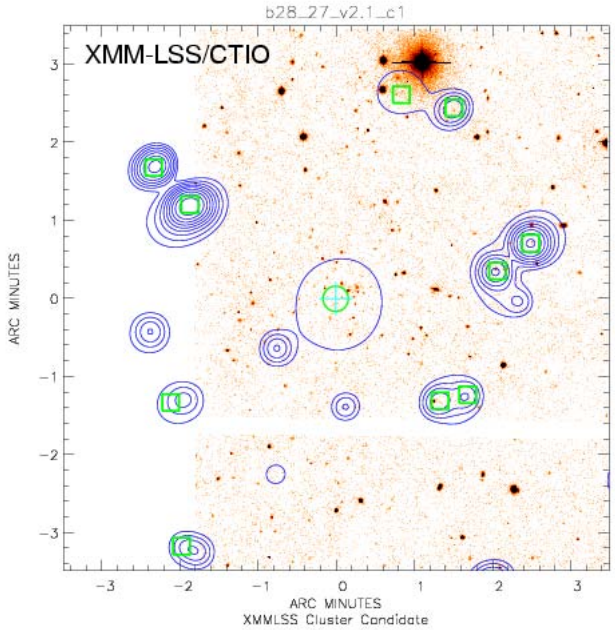

Figure A.24: Cluster 47.

Figure A.25: Cluster 3.

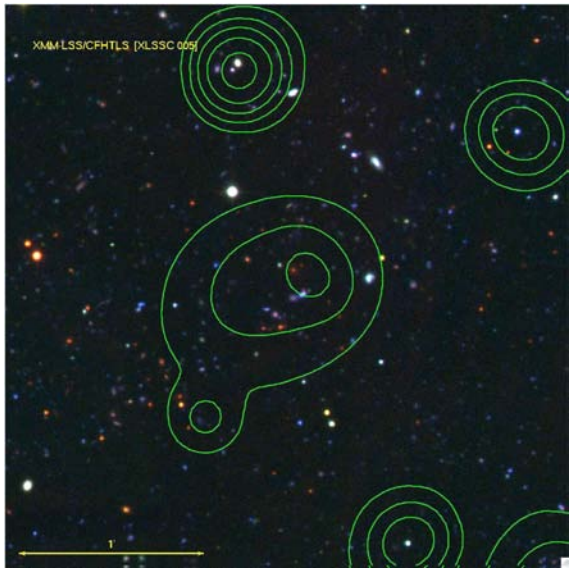

Figure A.26: Cluster 5.

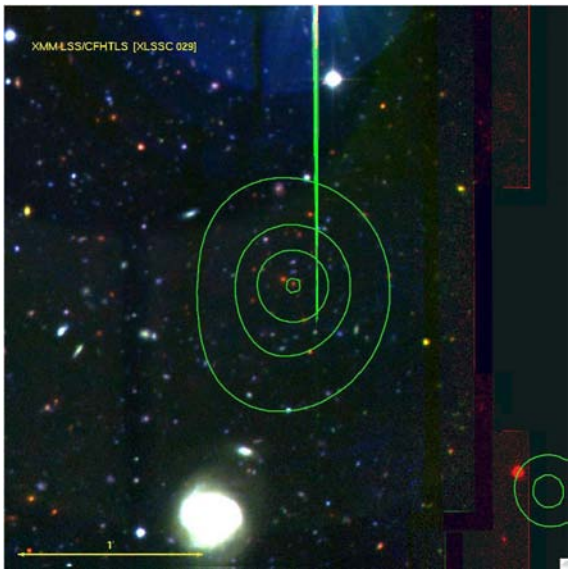

Figure A.27: Cluster 29.

Appendix B

Standard Error on Weighted Mean in Presence of Real Scatter

When averaging data of variable statistical quality, a more robust mean is obtained by weighting the averaged values by their inverse variances. Standard formulae for the standard error on such a weighted mean assume that statistical errors represent the *only* source of variance. For our application, this is not true, since there are real cluster-to-cluster variations, in additional to statistcal scatter. Here we derive an expression for the standard error of a weighted mean in these circumstances.

For a data set $x_i = x_1, x_2, .., x_n$ with variable statistical errors $\sigma_i = \sigma_1, \sigma_2, .., \sigma_n$, the weighted mean $\bar{x}$ is

$$\bar{x} = \frac{\sum_{i=1}^{n} w_i x_i}{\sum_{i=1}^{n} w_i}, \tag{B.1}$$

where $w_i = 1/\sigma_i^2$ are the weights. This weighted mean will properly take into account the varying statistical quality of the data.

The variance in this weighted mean, $var(\bar{x})$, is

$$var(\bar{x}) = \frac{\sum_{i=1}^{n} w_i^2 var(x_i)}{\left(\sum_{i=1}^{n} w_i\right)^2}. \tag{B.2}$$

In the presence of real, non-statistical scatter in the x_i values, the expected variance for the

ith data point is

$$var(x_i) = \left\langle (x_i - \mu)^2 \right\rangle = \sigma_i^2 + \sigma_t^2, \tag{B.3}$$

where σ_t is the *true* (non-statistical) variance of the population and

$$\left\langle (x_i - \mu)^2 \right\rangle = \frac{n}{n-1} \left\langle (x_i - \bar{x})^2 \right\rangle. \tag{B.4}$$

So an estimate $\hat{\sigma}_t^2$ of σ_t^2 is obtained from

$$\hat{\sigma}_t^2 = \frac{1}{n-1} \sum_{i=1}^{n} \left[(x_i - \bar{x})^2 - \sigma_i^2 \right], \tag{B.5}$$

and the variance of the weighted mean becomes

$$var(\bar{x}) = \frac{\displaystyle\sum_{i=1}^{n} w_i^2 \left[\sigma_i^2 + \frac{1}{n-1} \sum_{i=1}^{n} \left[(x_i - \bar{x})^2 - \sigma_i^2 \right] \right]}{\left(\displaystyle\sum_{i=1}^{n} w_i \right)^2}. \tag{B.6}$$

Substituting for $w_i = 1/\sigma_i^2$ we get

$$var(\bar{x}) = \frac{\displaystyle\sum_{i=1}^{n} \left[\frac{1}{\sigma_i^2} + \frac{\hat{\sigma}_t^2}{\sigma_i^4} \right]}{\left(\displaystyle\sum_{i=1}^{n} \frac{1}{\sigma_i^2} \right)^2}, \tag{B.7}$$

and finally the standard error of the weighted mean (SEWM), $SE_{\bar{x}}$, is

$$SE_{\bar{x}} = \sqrt{\frac{var(\bar{x})}{n}} = \sqrt{\frac{\displaystyle\sum_{i=1}^{n} \left[\frac{1}{\sigma_i^2} + \frac{\hat{\sigma}_t^2}{\sigma_i^4} \right]}{n \left(\displaystyle\sum_{i=1}^{n} \frac{1}{\sigma_i^2} \right)^2}}. \tag{B.8}$$

Appendix C

Individual Luminosity Functions of C1 Clusters in r' Band

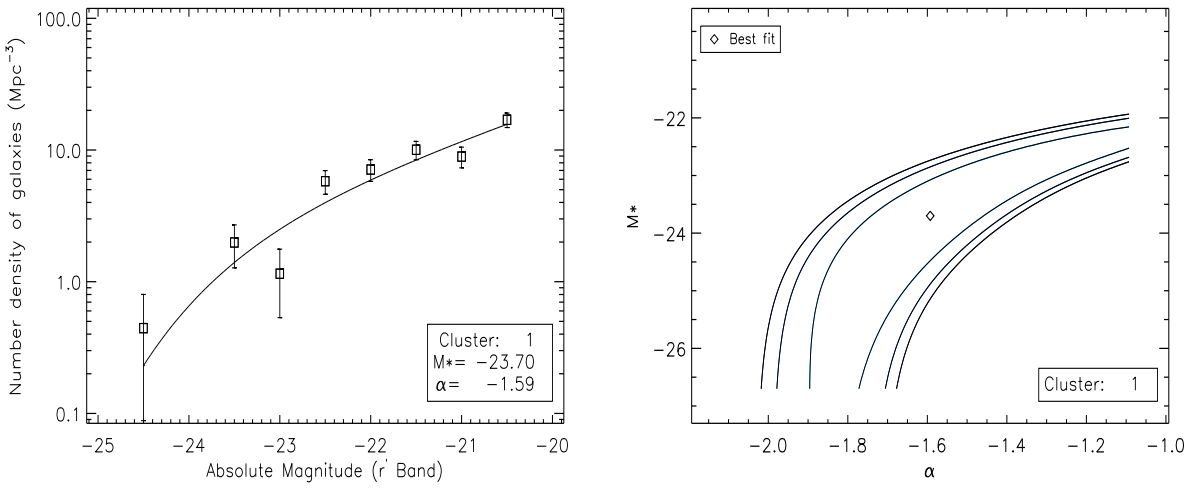

(a) Cluster 1 (r' band)

Figure C.1: LFs of the 14 individual C1 clusters and contours of the well-fitted clusters for the r' band. Contours plots of the 1σ, 2σ and 3σ confidence levels of α and M^* are placed next to their associated LF. Clusters with unconstrained M^* (and no contours) were placed at the end.

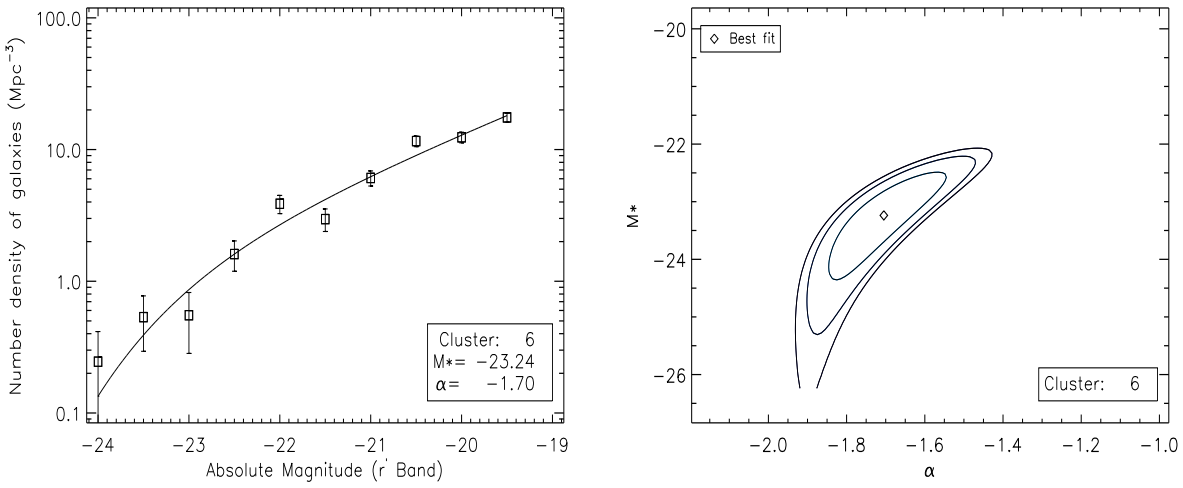

(b) Cluster 6 (r' band)

Figure C.1: (*continued*)

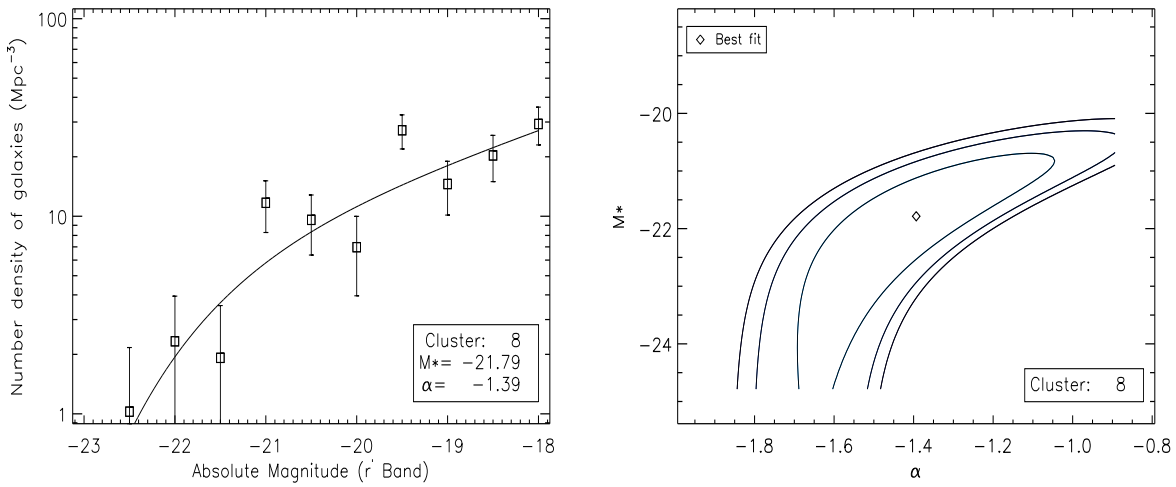

(c) Cluster 8 (r' band)

Figure C.1: (*continued*)

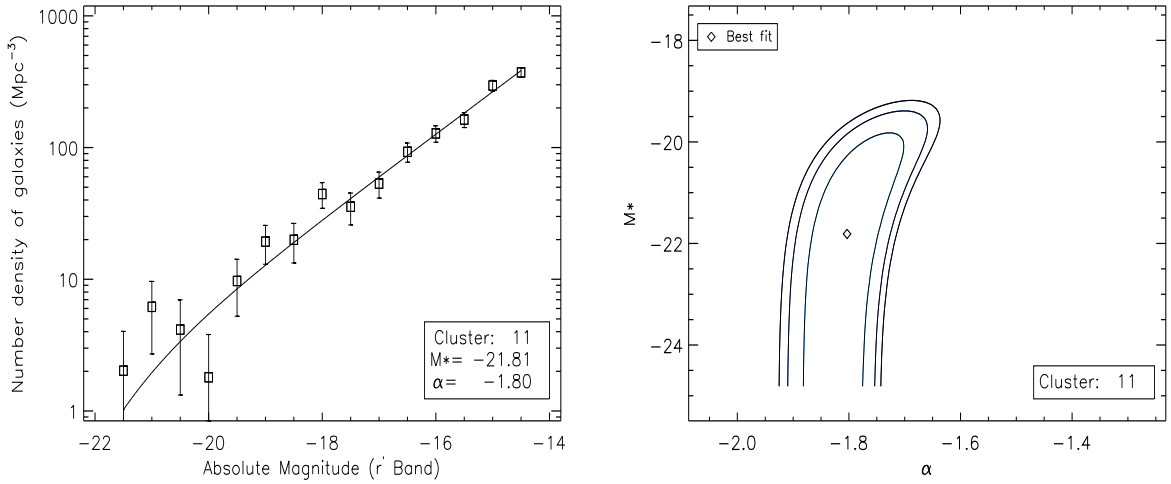

(d) Cluster 11 (r' band)

Figure C.1: (*continued*)

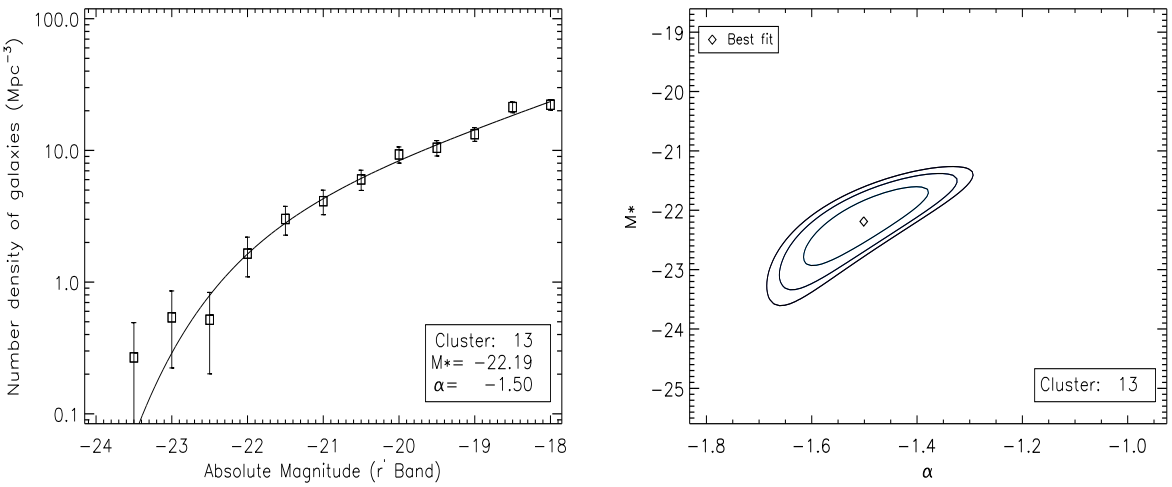

(e) Cluster 13 (r' band)

Figure C.1: (*continued*)

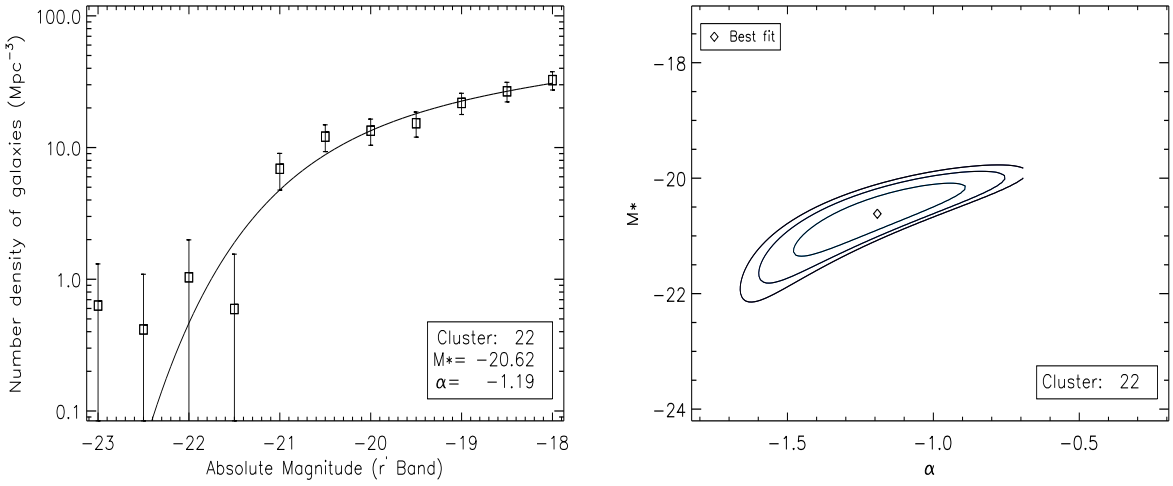

(f) Cluster 22 (r' band)

Figure C.1: (*continued*)

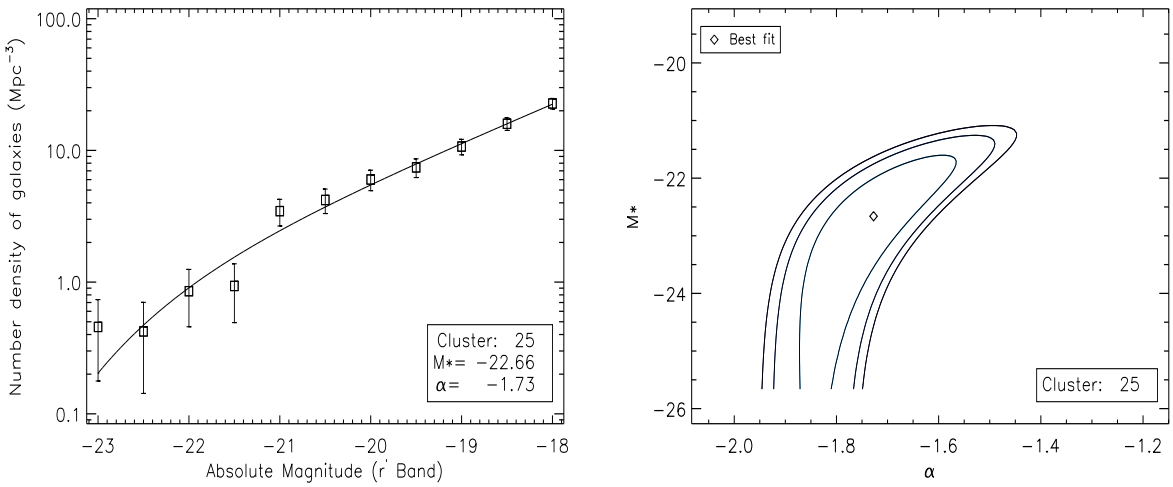

(g) Cluster 25 (r' band)

Figure C.1: (*continued*)

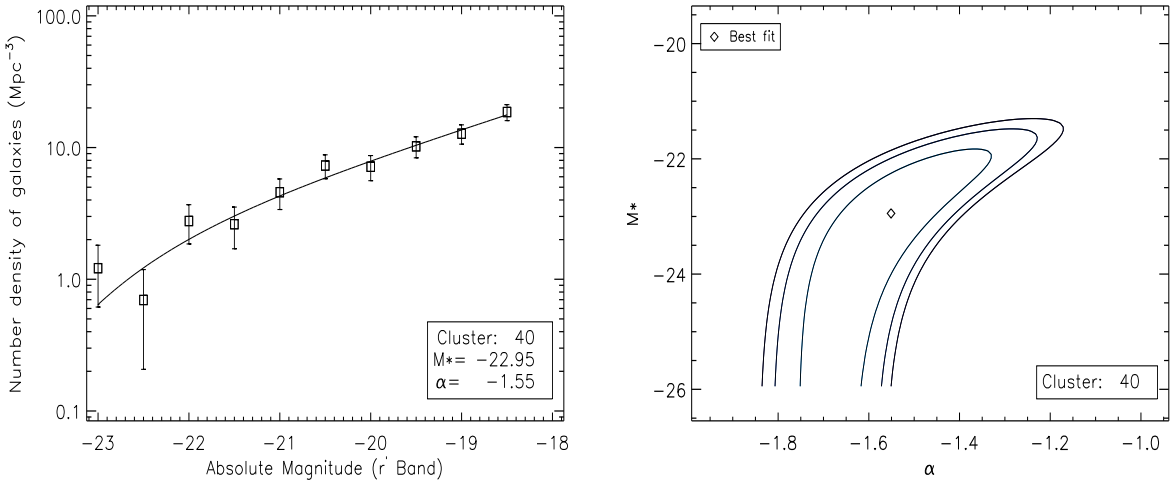

(h) Cluster 40 (r' band)

Figure C.1: (*continued*)

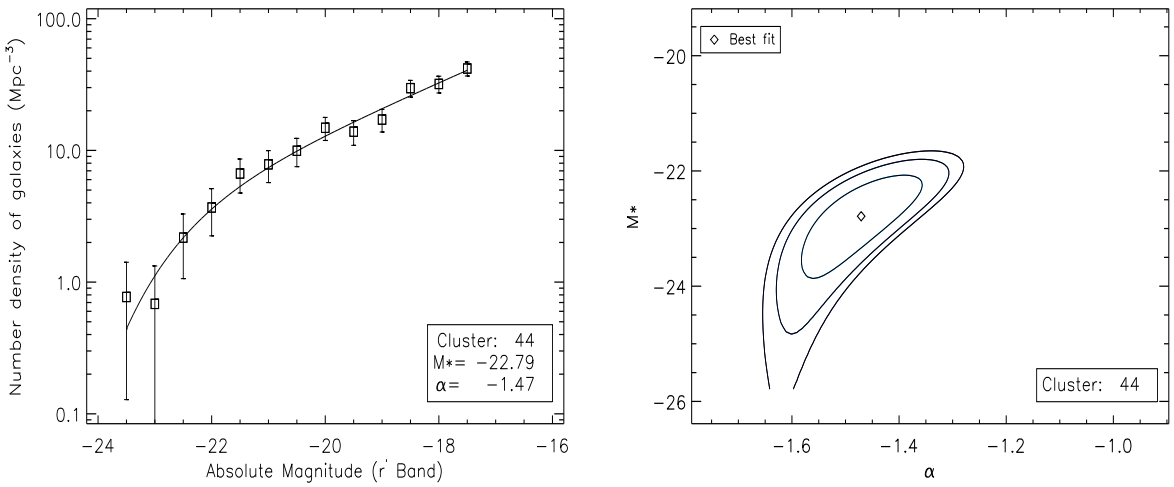

(i) Cluster 44 (r' band)

Figure C.1: (*continued*)

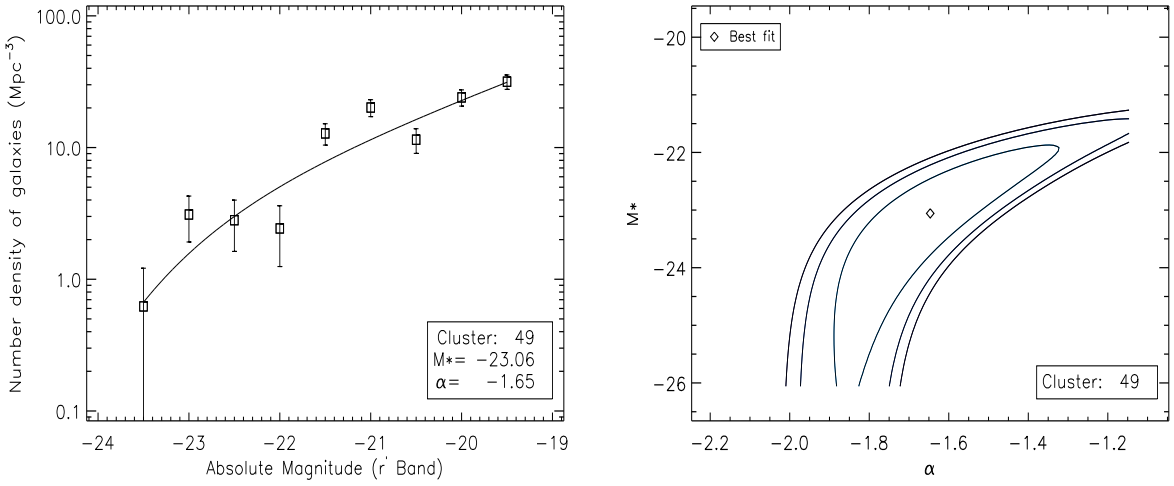

(j) Cluster 49 (r' band)

Figure C.1: (*continued*)

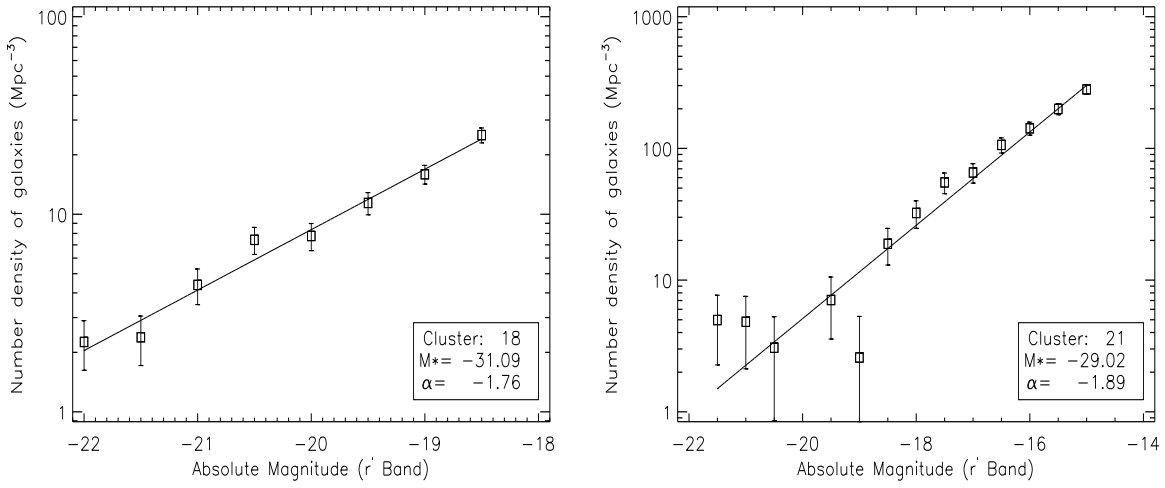

(k) Cluster 18 and 21 (r' band)

Figure C.1: (*continued*)

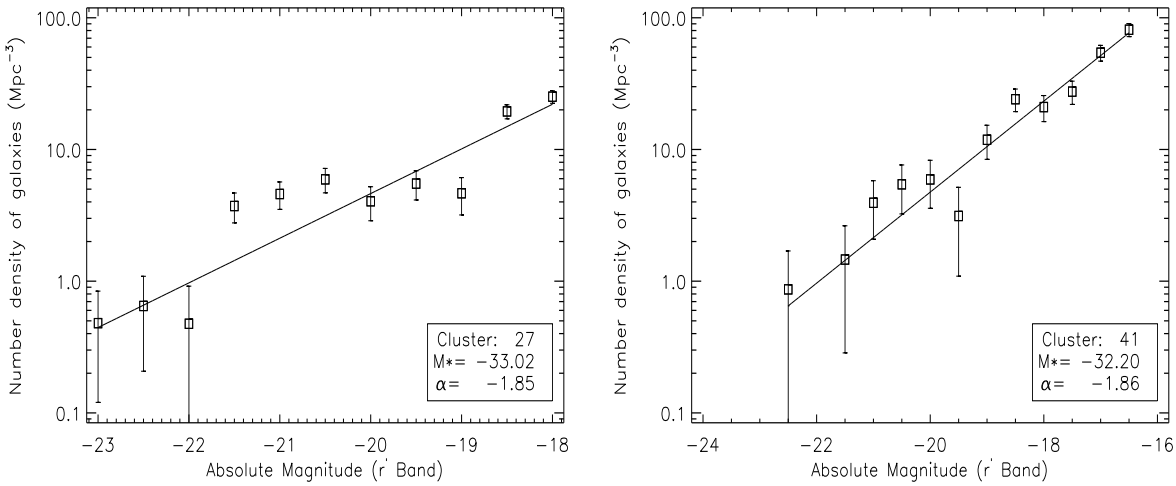

(m) Cluster 27 and 41 (r' band)

Figure C.1: (*continued*)

Appendix D

Individual Luminosity Functions of C1 Clusters in z' Band

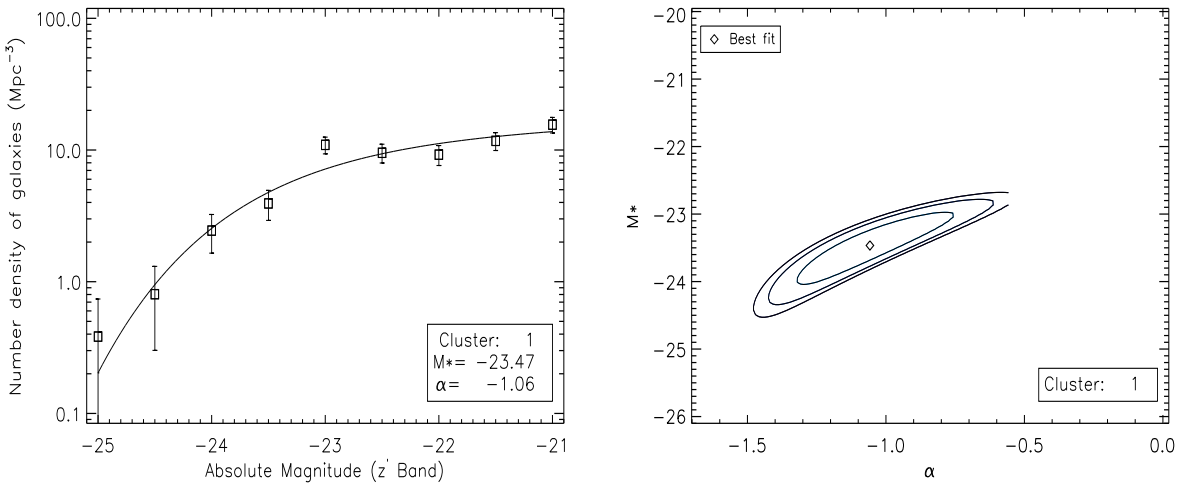

(a) Cluster 1 (z' band)

Figure D.1: LFs of the 14 individual C1 clusters and contours of the well-fitted clusters for the z' band. Contours plots of the 1σ, 2σ and 3σ confidence levels of α and M^* are placed next to their associated LF. Clusters with unconstrained M^* (and no contours) were placed at the end.

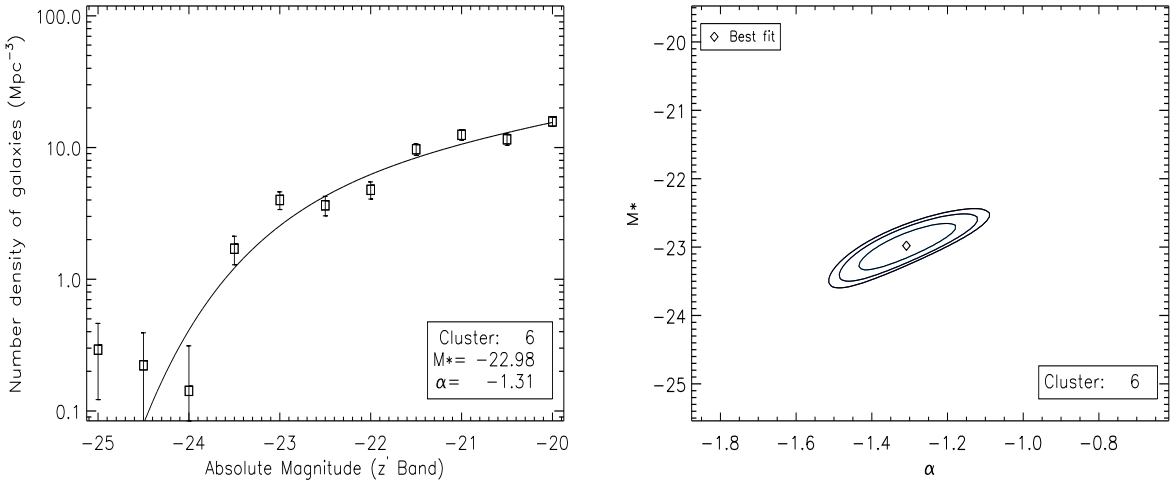

(b) Cluster 6 (z' band)

Figure D.1: (*continued*)

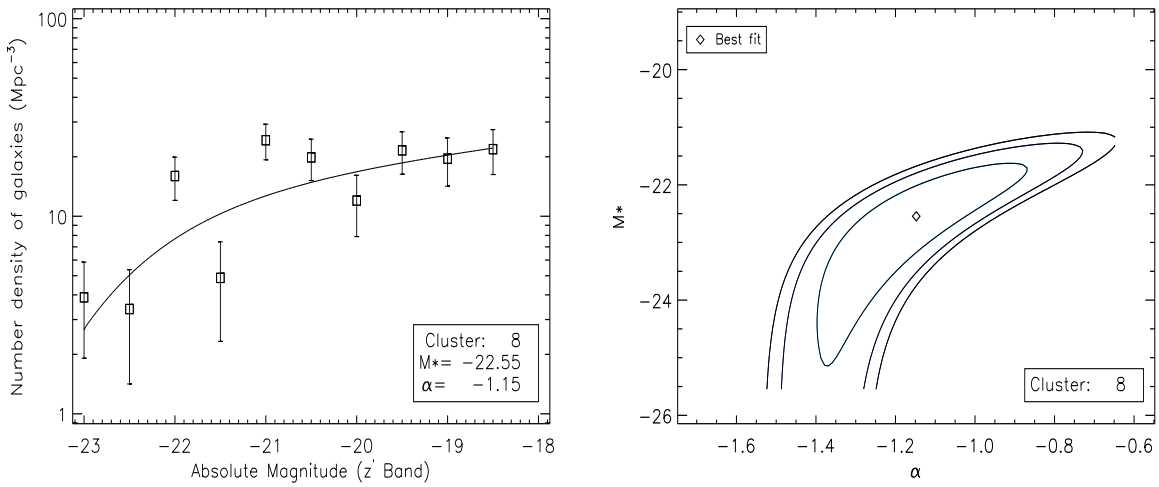

(c) Cluster 8 (z' band)

Figure D.1: (*continued*)

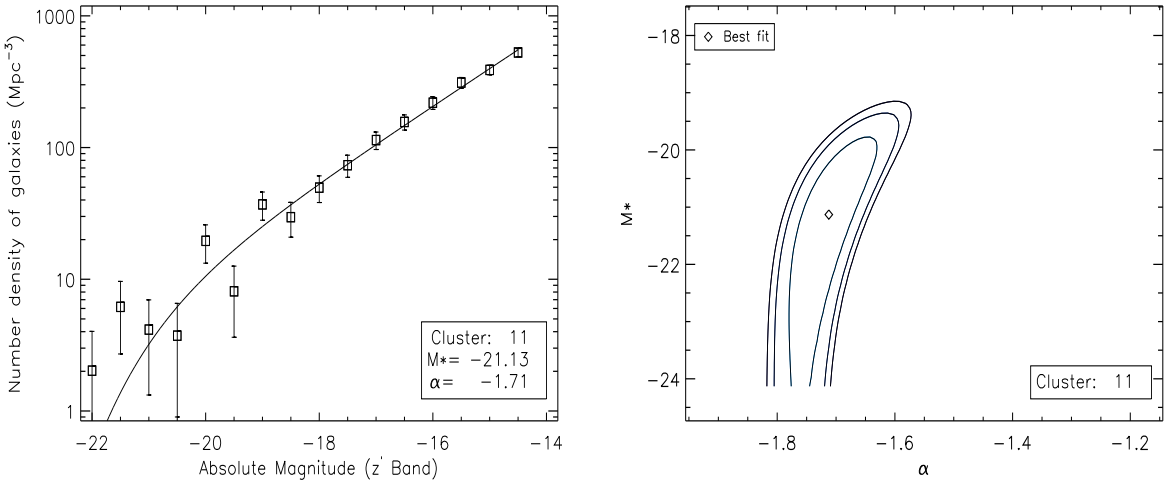

(d) Cluster 11 (z' band)

Figure D.1: (*continued*)

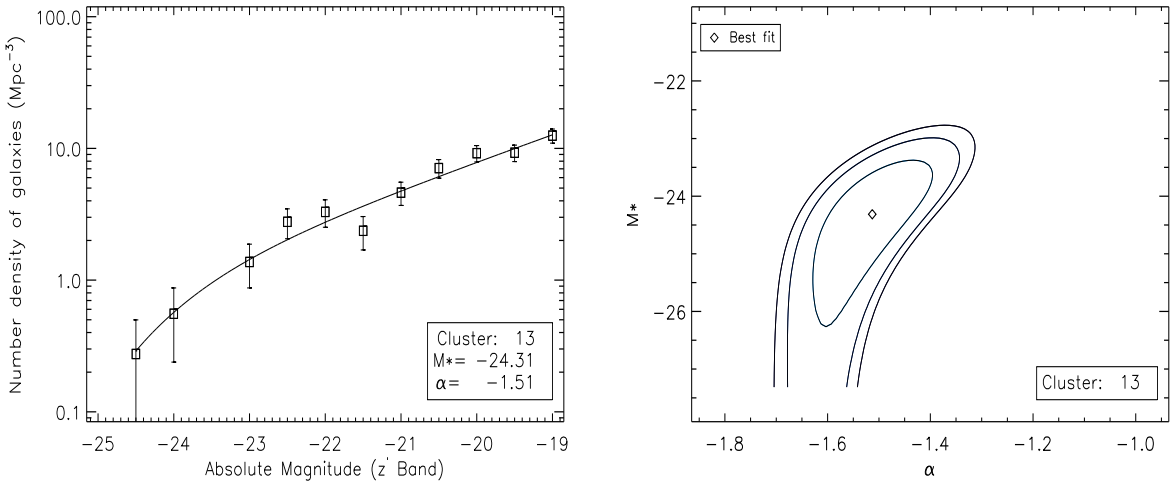

(e) Cluster 13 (z' band)

Figure D.1: (*continued*)

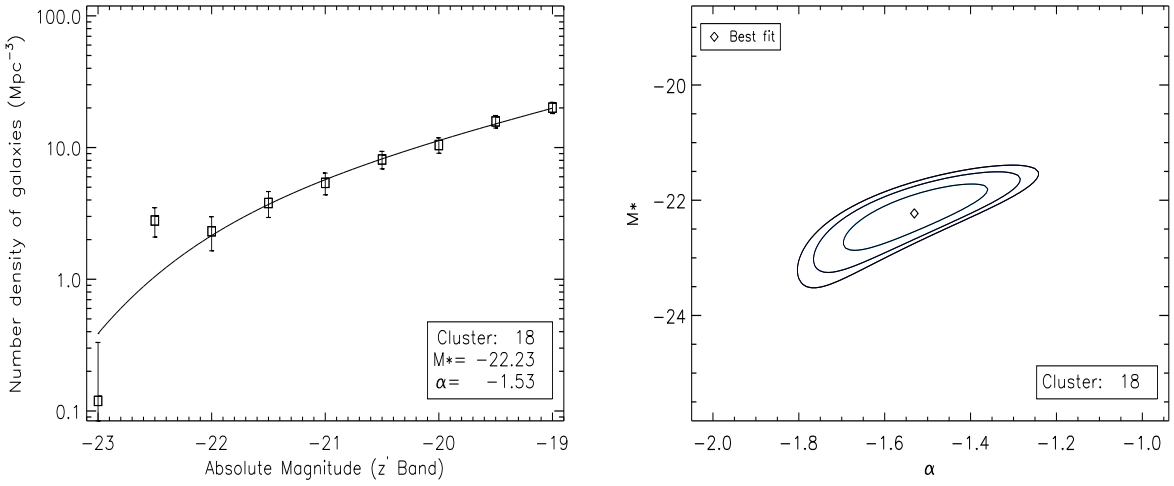

(f) Cluster 18 (z' band)

Figure D.1: (*continued*)

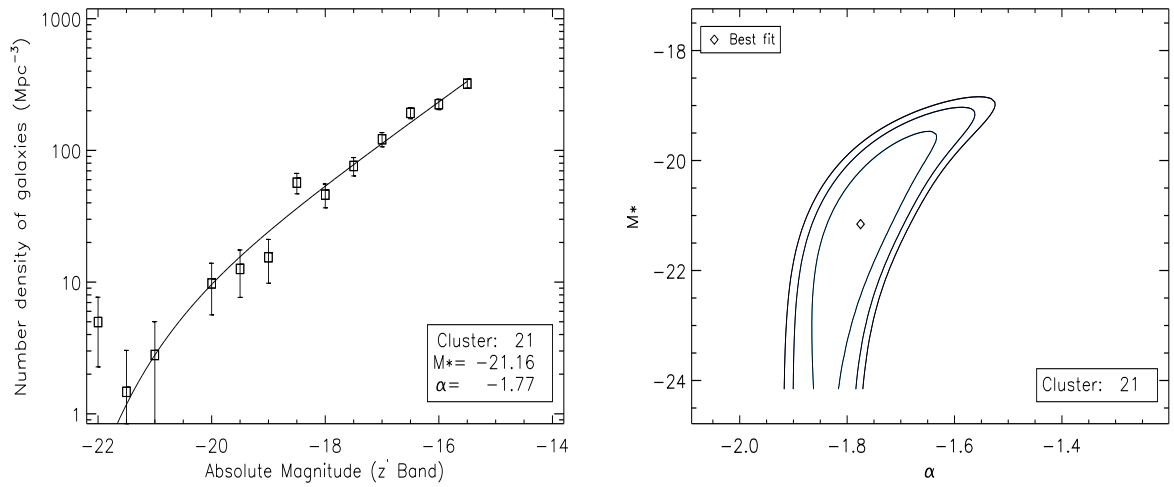

(g) Cluster 21 (z' band)

Figure D.1: (*continued*)

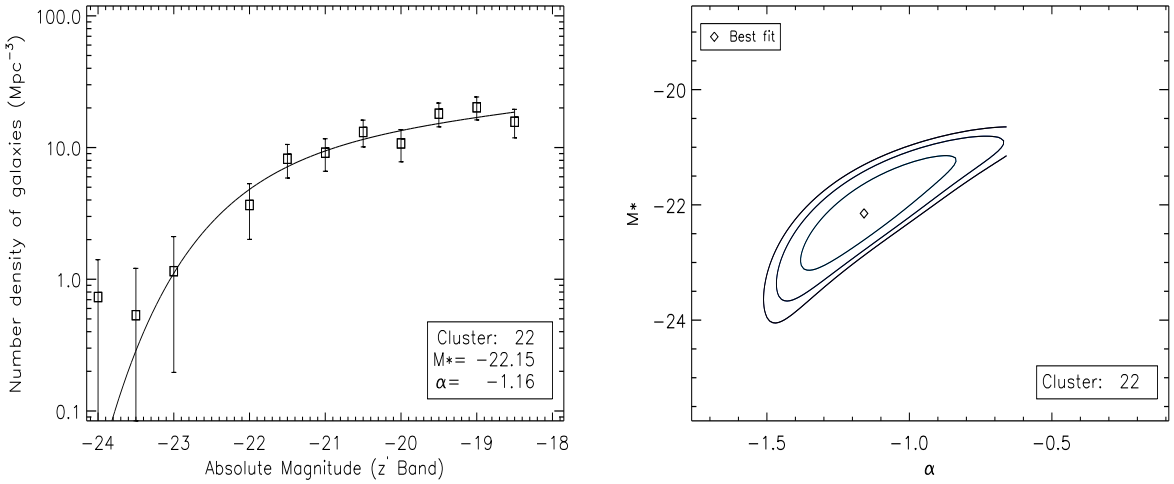

(h) Cluster 22 (z' band)

Figure D.1: (*continued*)

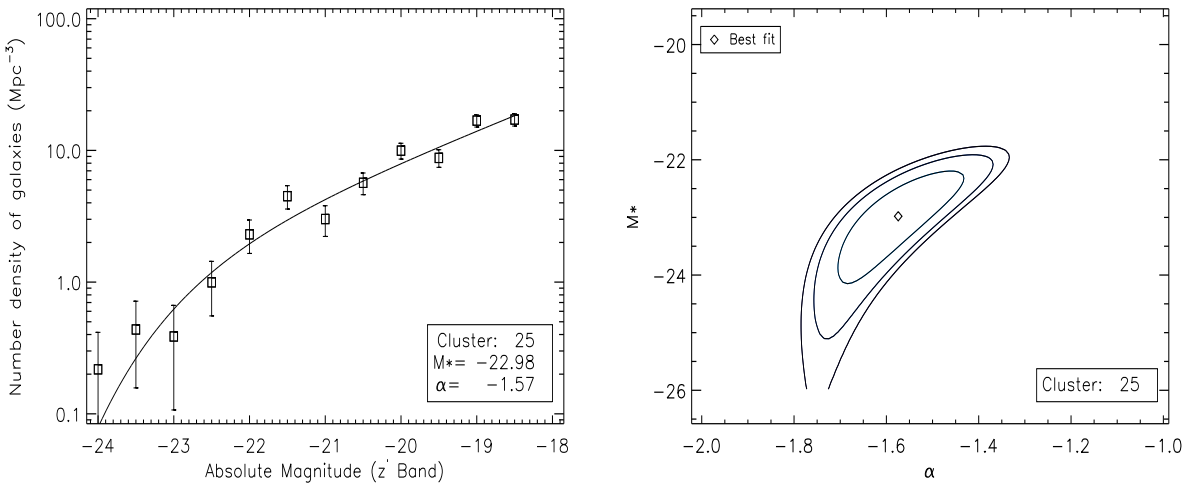

(i) Cluster 25 (z' band)

Figure D.1: (*continued*)

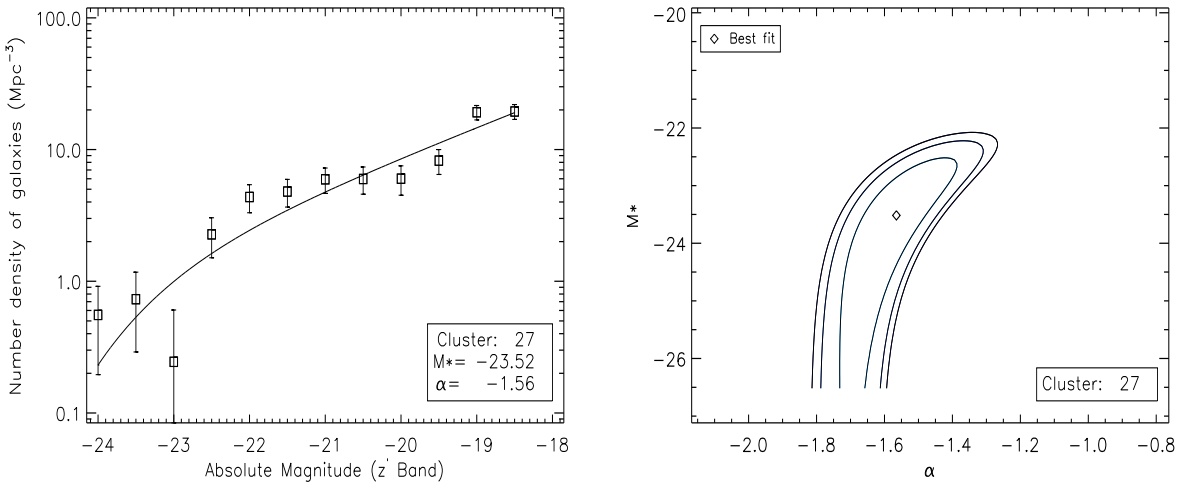

(j) Cluster 27 (z' band)

Figure D.1: (*continued*)

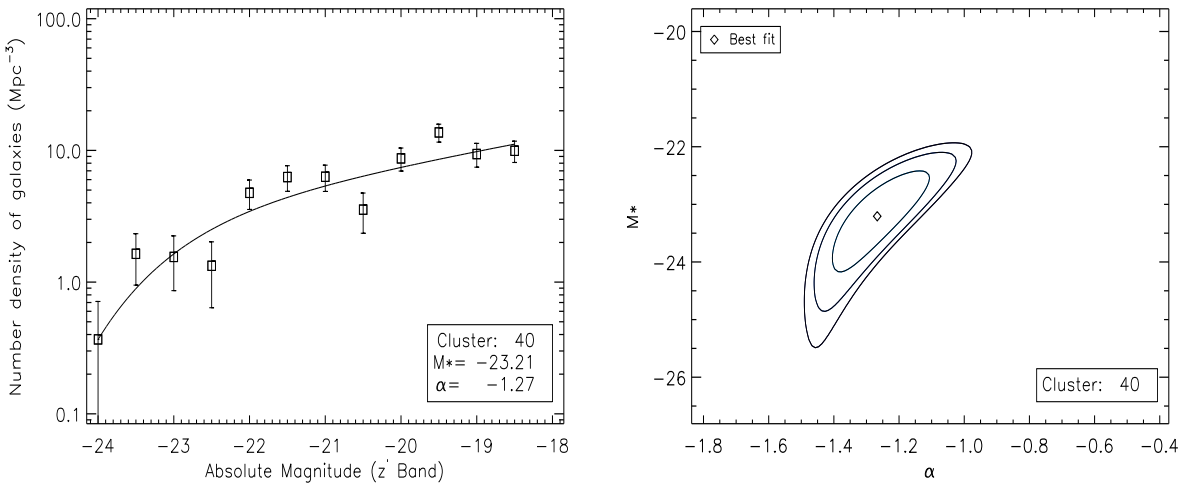

(k) Cluster 40 (z' band)

Figure D.1: (*continued*)

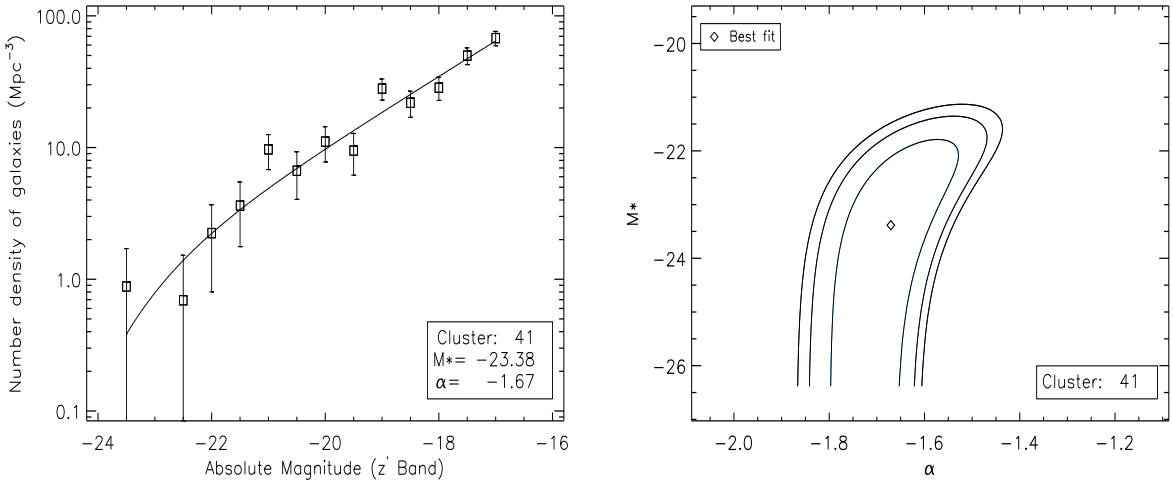

(l) Cluster 41 (z' band)

Figure D.1: (*continued*)

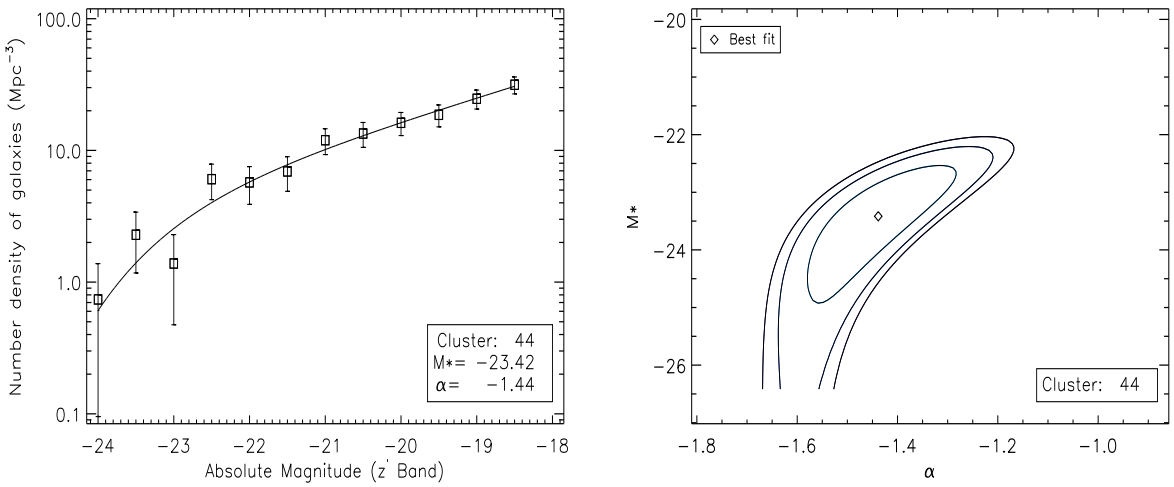

(m) Cluster 44 (z' band)

Figure D.1: (*continued*)

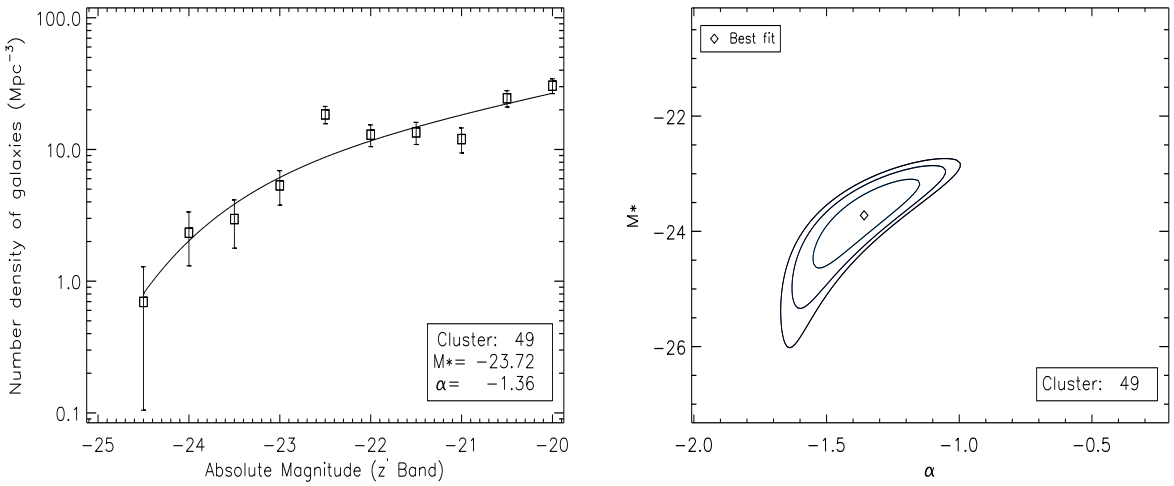

(n) Cluster 49 (z' band)

Figure D.1: (*continued*)